Spiral galaxies

de Jong, Roelof Sybe

RIJKSUNIVERSITEIT GRONINGEN

Spiral Galaxies

The light and color distributions in the optical and near-infrared

Proefschrift

ter verkrijging van het doctoraat in de
Wiskunde en Natuurwetenschappen
aan de Rijksuniversiteit Groningen
op gezag van de
Rector Magnificus Dr. F. van der Woude
in het openbaar te verdedigen op
vrijdag 24 maart 1995
des namiddags te 2.45 uur precies

door

Roelof Sybe de Jong

geboren op 26 mei 1965

te Leeuwarden

Promotor: Prof. Dr. P.C. van der Kruit

‘I love this place at night
. . . the stars. . .
There is no right
or wrong in them
They’re just there’

Willem Dafoe as Sgt. Elias
in Vietnam-movie Platoon

On the cover:

A true color image of spiral galaxy Messier 100 (NGC 4321 or UGC 7450) with its companion, composed from B, V and I images obtained with the William Herschel telescope at La Palma. The bright circular dots around the galaxy are foreground stars from our own Galaxy, the Milky Way, the fuzzy orange features are background galaxies.

Bij de omslag:

Een kleurenfoto van het spiraal sterrenstelsel Messier 100 (ook wel NGC 4321 of UGC 7450 genoemd) met een begeleidend stelsel. De foto werd gemaakt van afzonderlijke rode, gele en blauwe afbeeldingen, welke werden gemaakt met de William Herschel teleskoop op La Palma. De heldere punten om het sterrenstelsel heen zijn voorgrond sterren behorend tot ons eigen sterrenstelsel, de Melkweg, de vage oranje vlekjes zijn sterrenstelsels op de achtergrond.

Contents

Voorwoord

Preface

Bijna niemand kan ontsnappen aan de mystieke aantrekkingskracht van het heelal. De mensheid is altijd al gefascineerd geweest door het oneindige van het heelal en is nog immer nieuwsgierig naar de oorsprong der dingen. Dit proefschrift getuigt van die fascinatie. Toch kon ik als astronoom niet alleen maar stevig met beide benen in de lucht staan, ik was vooral afhankelijk van de mensen op de grond. Een aantal mensen verdient bijzondere dank voor hun bewuste of onbewuste hulp bij het tot stand komen van dit proefschrift.

Allereerst zijn er natuurlijk mijn ouders. Zij hebben mij opgevoed met een vrije, edoch kritische geest. Heit en Mem, tige tank foar dat jimme der altyd wienen.

Van sterrenkunde alleen kun je niet leven, maar gelukkig is er meer te doen in Groningen. Mijn dank gaat uit naar mijn USVA foto kameraden en met name naar Ton Broekhuis. Dankzij hen was mijn kamera niet alleen maar naar boven gericht en werd mijn ruimtelijk denken aangevuld met een wijde blik. Met mijn Cirkeltijgers handbal vrienden kon ik me lichamelijk altijd goed afreageren, om vervolgens 's avonds met een gerstennat en een goed gesprek inwendig weer aan te sterken.

Het Kapteynlab was een erg plezierige werkomgeving. Van veel mensen heb ik op één of andere manier steun ontvangen. Allereerst van een vaak zwaar onderschatte groep mensen, het niet-wetenschappelijk personeel. George, Nanne, Gineke, Jantina, Willemien, Jackie, Wim, Jaap, Hans, Martin, Coby, allemaal bedankt. Het gewauwel van promovendi onderling deed me vaak beseffen dat ik niet de enige was die het soms niet meer zag zitten. Om er vervolgens nog maar weer een schepje bovenop te gooien. De koffiehoek, de open deuren en de wandelgangen hadden een vergelijkbare funktie en een aantal mensen wil ik met name noemen. Op het gevaar af dat ik mensen vergeet: Olaf, Marc, Ronald, Kor, Gerard, Erwin, Thijs, David, Yannis, Renzo, Jeroen, Marijn, Penny, Dolf, Jurjen, Tjeerd, Roelof, Peter, Edwin, Marc, Ger, Griet, Huug bedankt. Een aantal mensen verliet het lab al voor mij, maar ik ben ze nog niet vergeten, gegroet Reynier, Johan, Richard, Brian, Richard, Edwin, Adrick en Renée.

Een speciale dank geldt natuurlijk voor mijn promotor Piet van der Kruit. Jij startte dit projekt op en hoewel je me regelmatig gewoon maar in het diepe gooide, gaf je me wel genoeg blijk van vertrouwen en zo nu en dan handige tips om de overkant te halen.

Het roemruchte "kamer 183 gevoel" nadert zijn einde nu de inwoners aan het promoveren zijn. Op het Kapteynlab lopen nogal wat niet-"kamer 183" bewoners van het promoverende soort rond die een licht masochistisch genoegen aan zelf-kastijding ontlenen, want waarom zouden ze anders elke keer maar weer massaal langs komen op kamer 183? Kortom, Arpad Szomoru en René Oudmaijer hartstikke bedankt voor jullie cynisme, geouwehoer, luisterend oor, goede adviezen en al dat soort dingen.

Zoals gewoonlijk, maar daarom niet minder gemeend, als laatste het dankwoord aan de levensgezel. Gerda, met jou in de buurt, word ik er er konstant aan herinnerd dat mijn fascinatie voor het leven nog groter is dan mijn fascinatie voor het heelal. Tút Tov.

Groningen, 5 februari 1995

The Jacobus Kapteyn Telescope and the Isaac Newton Telescope are operated on the island of La Palma by the Royal Greenwich Observatory in the Spanish Observatorio del Roque de los Muchachos of the Instituto de Astrofisica de Canarias on behalf of the Particle Physics and Astronomy Research Council (PPARC) and the Netherlands Organization for Scientific Research (NWO). The United Kingdom Infrared Telescope at Mauna Kea, Hawaii is operated by the Royal Observatory Edinburgh on behalf of the PPARC. Many thanks to the staff of these observatories for their support.

This research was supported under grant no. 782-373-044 from the Netherlands Foundation for Research in Astronomy (ASTRON), which receives its funds from the Netherlands Foundation for Scientific Research (NWO).

Dit onderzoek heeft geprofiteerd van financiële ondersteuning door het Leids Kerkhoven Bosscha fonds.

This research has made use of the NASA/IPAC Extragalactic Database (NED) which is operated by the Jet Propulsion Laboratory, Caltech, under contract with the National Aeronautics and Space Administration.

This research has made use of NASA's Astrophysics Data System Astrophysics Science Information and Abstract Service.

Samenvatting

Summary in Dutch

Sterren, elke heldere nacht weer die mysterieuze flikkeringen aan de hemel. Ze staan daar niet zo eenzaam als het op het eerste gezicht lijkt. De sterren die we 's avonds zien, zitten samen met miljarden soortgenoten in de Melkweg en met elkaar zijn ze op een maanloze nacht zichtbaar als een vage veeg over de hemel. De Melkweg is een sterrenstelsel, een groep van zo'n 1 tot 500 miljard sterren met daartussen "gas en stof [1] ". De Melkweg is niet het enige sterrenstelsel in het heelal, er zijn er tientallen miljarden. Over deze sterrenstelsels, en hun relatie met bloemen en konijnen, gaat deze samenvatting van dit proefschrift.

Sterrenstelsels

Sterrenstelsels zijn er in allerlei soorten en maten, zoals hiernaast te zien is. Astronomen hebben de sterrenstelsels ingedeeld in verschillende soorten aan de hand van hun uiterlijk, net zo als biologen hun dieren- en plantensoorten hebben en chemici hun verschillende molekulen. De belangrijkste indeling van sterrenstelsels is de tweedeling in elliptische en spiraal sterrenstelsels. De bovenste foto hiernaast toont een elliptisch stelsel, de drie andere stelsels zijn spiraalstelsels. De elliptische stelsels kunnen we meteen weer vergeten, want ik ga het alleen over spiraalstelsels hebben.

Een spiraalstelsel bestaat voornamelijk uit een grote platte schijf van sterren, gas en stof, draaiend om het centrum zoals een CD (grammafoon plaat voor de oudere generatie). De prachtige spiraal struktuur waar deze stelsels hun naam aan te danken hebben is goed te zien op de omslag foto . Bekijken we zo'n spiraalstelsel van opzij, zoals in figuur 1b, dan zien we in het centrum een bolvormige verdikking die we de *bulge* noemen. De Melkweg is ook een spiraalstelsel en wij bevinden ons met onze eigen ster de Zon in één van de spiraalarmen ergens in de buitengebieden van ons stelsel.

De spiraal sterrenstelsels zijn weer verder onderverdeeld in zogenaamde Hubble typen afhankelijk van de vorm van de spiraalarmen en de grootte van de bulge t.o.v. de schijf. Uit historische overwegingen worden de sterrenstelsels met kleine, strak opgewonden spiraalarmen "vroeg" type stelsels genoemd (zie bijvoorbeeld figuur 1c) en de stelsels met wijde grove armen "laat" type stelsels (figuur 1d).

Na 70 jaar onderzoek speuren astronomen nog steeds naar het hoe en waarom van die uiterlijke verschillen van sterrenstelsels. Mijn onderzoek vormt een onderdeel van die speurtocht.

Waarnemingen

Eén van de belangrijkste stappen in astronomische speurtochten bestaat uit het doen van waarnemingen. Voor dit onderzoek

a

b

c

d

Figuur 1. Sterrenstelsels.

[1] Het gas bestaat voornamelijk uit waterstof gas, iets anders dus dan het methaangas dat uit het fornuis komt. Ook het stof is anders dan het huis- tuin- en keukenstof waar ik zo allergisch voor ben, het lijkt nog het meest op verpulverd zand.

heb ik een groot aantal “afbeeldingen” van 86 speciaal geselekteerde spiraalstels gemaakt om de preciese lichtverdeling in deze stelsels in kaart te brengen. Niet zoals vroeger (10-15 jaar geleden) met grote fotografische platen, maar met gevoelige digitale kamera’s, waarvan de gegevens direkt met een komputer verwerkt kunnen worden.

De afbeeldingen maakte ik door gekleurde filters, zodat alleen de lichtverdeling in één bepaalde kleur op de afbeeldingen staan. Op de één of andere manier liggen de beste astronomische waarneemplekken op mooie exotische bergtoppen en daarom reisde ik af naar een teleskoop op het eiland La Palma om blauwe, gele en rode afbeeldingen te maken en naar een grote teleskoop op Hawaii om de infrarode (roder dan rood in de regenboog) opnamen te maken. De infrarode techniek is nog maar enkele jaren in gebruik en dankzij deze nieuwe techniek kon ik enkele nieuwe vindingen doen.

Statistiek en konijnen

Na het doen van de waarnemingen begint het echte astronomische werk pas, het inpassen van de waarnemingen in een theorie. Natuurlijk zijn astronomen met de indeling van sterrenstelsels in verschillende soorten alleen nog niet tevreden. Ze willen ook graag weten hoeveel van elk soort er zijn in een bepaald gebied. Ze zijn wat dat betreft net als bijvoorbeeld biologen, die niet alleen willen weten dat er vossen en konijnen zijn, maar ook willen weten hoeveel van elke soort er zijn in een bepaald gebied en vooral waarom.

Het bepalen van de hoeveelheden sterrenstels lijkt eenvoudig. Neem foto’s van de hele hemel en tel hoeveel stelsels van elke soort er zijn. Zo eenvoudig is het helaas niet, want niet alle stelsels staan even ver weg. Sommige staan zo ver weg dat ze te klein zijn om meegeteld te worden. Laat ik even een vergelijking trekken met een konijnen tellende bioloog. Een in de grazige weilanden staande bioloog zal witte konijnen veel gemakkelijker en tot op veel grotere afstand kunnen zien dan hun goed gekamoufleerde bruine soortgenoten. Hoe groter het kontrast met de omgeving, des te gemakkelijker is de langoor te zien en onze bioloog zou simpelweg kunnen denken dat er veel meer witte konijnen zijn dan bruine. Hetzelfde geldt voor grote en kleine konijnen. Onze bioloog herkent een groot konijn tot op veel grotere afstand en ziet daarom vanuit zijn schuilplaats veel meer grote dan kleine konijnen. Simpel geredeneerd denkt onze bioloog dat er voornamelijk grote witte konijnen in het weiland rondlopen en weinig kleine bruine. Het is wel even schrikken voor de bioloog als er plotseling een keer sneeuw ligt.

Onze bioloog heeft echter één enorm voordeel boven alle astronomen. Biologen kunnen het veld inlopen en de konijnen van verschillende afstanden bekijken, opzoeken en zelfs meten. Astronomen zitten aan de aarde vast. Ik moest altijd vanaf mijn plekje op aarde naar het heelal kijken en kon nooit naar een ander sterrenstelsel gaan om te bekijken hoe het er van dichtbij uitziet. Zelfs al kon ik reizen met de snelheid van het licht, dan zou het nog miljoenen jaren duren voor ik bij andere sterrenstelsels aan zou komen.

Net als bij de konijnen zijn er twee faktoren die bepalen of we een sterrenstelsel goed kunnen zien: een schalings- en een helderheidsfaktor. De schalingsfaktor bepaalt hoe groot een stelsel is en hoe groter een sterrenstelsel werkelijk is, des te groter het aan de hemel lijkt en des te meer kans natuurlijk dat ik het bekeken heb. De tweede faktor wordt bepaald door de oppervlakte helderheid van het stelsel. Hoe meer licht er uit één gebiedje komt, oftewel hoe dichter de sterren opelkaar staan, des te meer kontrast het stelsel heeft tegen de hemelachtergrond en des te meer kans weer dat ik er naar heb staan kijken. Kortom, er bestaat meer kans dat ik grote heldere stelsels heb waargenomen dan kleine lichtzwakke.

De Australische astronoom Freeman ontdekte in 1970 in een belangrijke studie dat, van de 36 spiraal sterrenstelsels die hij bestudeerd had, er 28 ongeveer dezelfde helderheid hadden in hun binnen gebied. Dit suggereert dat heel veel sterrenstelsels ongeveer evenveel sterren in hun centrale gebied hebben staan en dat is niet eenvoudig te verklaren met de tot nu toe bestaande theorieën over het onstaan en de ontwikkeling van sterrenstelsels. De afgelopen 25 jaar zijn er talloze verklaringen geopperd voor de vondst van Freeman. Eén van de belangrijkste zal ik hier maar de Grote Witte Konijnen theorie noemen. Freeman zou voornamelijk grote witte konijnen gezien hebben en had daarbij de kleine witte en de meeste bruine over het hoofd gezien. Een belangrijk deel van mijn onderzoek ging over de helderheidswet van Freeman en de Grote Witte Konijnen theorie.

Dankzij de snelle komputers van tegenwoordig kon ik een nieuwe techniek ontwikkelen om de helderheden en schaalgrootten van sterrenstelsels in één keer van de gemaakte afbeeldingen te bepalen. De metingen werden gekorrigeerd voor het Grote Witte Konijnen effect en daarna ontdekte ik dat er welliswaar een bovenlimiet is aan de centrale helderheid van spiraalstelsels, maar ook dat er bijna evenveel stelsels zijn met een lage als met een hoge centrale helderheid. Verder vond ik dat er veel kleine heldere stelsels zijn, maar de waarnemingen waren niet gevoelig genoeg om te kunnen zeggen of er veel of weinig kleine, lichtzwakke sterrenstelsels zijn. Of anders uitgedrukt, er zijn naast grote witte konijnen ook veel kleine witte konijnen in het heelal, maar veel belangrijker, ook een redelijke populatie grote bruine konijnen. Van de kleine bruine konijntjes kan helaas nog niet zoveel gezegd worden, maar het is duidelijk dat de Grote Witte Konijnen theorie serieus genomen moet worden.

Kleuren en bloemen

De omslag foto laat direkt zien dat sterrenstelsels niet overal dezelfde kleur hebben. Ook tussen sterrenstelsels onderling bestaan er grote kleurverschillen. Twee grondslagen voor de kleurverschillen heb ik onderzocht: sterren en stof. Het blijkt dat de kleuren te maken hebben met hoe zwaar een sterrenstelsel is en hoe oud het is, dingen die voor astronomen erg belangrijk zijn.

Sterrenstelsels zijn vaak al miljarden jaren oud en hun leeftijd kan dus niet even met een stopwatch bepaald worden. Om uit te leggen hoe ik met de kleur van een sterrenstelsel

zijn leeftijd kan bepalen, grijp ik weer even naar een voorbeeld uit de biologie. Een kollega veldonderzoeker van de bioloog van zonet krijgt de opdracht te bepalen hoe lang bepaalde weilandjes op de toppen van de Andes bergen al in bloei staan en hoe dit beïnvloed wordt door lokale omstandigheden op de berg. Er zijn echter een paar problemen. Haar onderzoeks instituut heeft alleen maar genoeg geld om haar voor twee weken naar Chili te sturen en de Chileense autoriteiten staan haar alleen maar toe om aan het eind van de zomer in de Andes rond te stappen. Goede raad is duur, hoe bepaalt onze bioloog in het najaar wanneer de weilanden in het voorjaar begonnen te bloeien?

Zij heeft geluk. Kollega biologen hebben ontdekt dat er in het gebied eigenlijk maar twee soorten bloemen voorkomen, die tegelijk beginnen te groeien en bloeien. Van de ene soort zijn er niet zoveel, maar ze bloeien uitbundig met grote blauwe bloembladeren. Na zo'n paar weken verwelkt deze soort, wordt nog even rood maar sterft dan af. Van de andere soort ontstaan er tegelijk veel meer en deze soort bloeit het hele seizoen door in kleine rode bloemetjes. Als een bergweide begint te bloeien, lijkt het vanuit het dal eerst blauw, omdat de grote blauwe bloemen de kleur volledig domineren. Maar na verloop van tijd beginnen steeds meer blauwe bloemen af te sterven en lijkt het veldje steeds roder. Het verhaal wordt gekompliceerder als er alsmaar nieuwe generaties bloemen beginnen te bloeien. Er komen dan steeds meer rode bloemetjes (die sterven het hele seizoen immers niet af), terwijl de hoeveelheid blauwe bloemen nauwelijks toeneemt omdat de oudere bloemen steeds afsterven. Verder moet de bioloog ook nog rekening houden met het feit dat de kleur van de bloemen enigszins samenhangt met de grond waarop ze groeien, vooral met de hoeveelheid metalen die er in de grond zit. De leeftijd is echter de bepalende faktor waardoor je kunt stellen, hoe blauwer een veldje, des te korter geleden zijn veel bloemen (rood en blauw) beginnen te bloeien.

Onze bioloog moet nu gaan kiezen wat zij die twee weken in Chili zal gaan doen. In die tijd kan zij misschien net naar één veldje toeklimmen om de bloemetjes van dichtbij te bekijken. Ze weet dan welliswaar veel van dat ene veldje, maar weet nog niets van de systematiek binnen het dal. Beginnen bijvoorbeeld de bloemen aan de regenachtige kant van het dal eerder te bloeien of ontstaan er meer generaties bloemen als een veldje lang in de zon ligt? Zij kan in die twee weken één dal uitgebreid bestuderen om daar meer inzicht in te krijgen, maar heeft dan nog steeds geen idee of de grondsoort of de grootte van het dal er toe doet. Ze besluit in die twee weken 86 dalen te bezoeken en van ieder dal ruwweg de kleur van een aantal veldjes rondom op de toppen te bepalen. Door nu alleen naar de kleuren te kijken kan ze zien of de veldjes aan de zonnige of de regenachtige kant het eerst en het meest bloeien, of de grootte van de dalen er toe doet en of twee nabij gelegen dalen elkaar beïnvloeden omdat de kruisbestuivende bijen gemakkelijk van het ene dal naar het andere dal kunnen vliegen. Zij kan nu ook de verschillende planten massa's gaan schatten. Ze moet wel rekening houden met het feit dat de grote blauwe bloemen dan wel de kleur bepalen, maar dat de vele kleine rode bloemetjes samen veel zwaarder zijn. Nu maar hopen dat ze in haar twee weken waarneemtijd geen slecht weer heeft en vanuit het dal de veldjes kan zien liggen.

Wat heeft dit nu allemaal te maken met de kleur van sterrenstelsels. Je zou de Chileense dalen met sterrenstelsels kunnen vergelijken en de bloemen zijn dan de sterren. Net als de bloemen, hebben niet alle sterren dezelfde kleur, iets wat 's avonds trouwens met het blote oog al waarneembaar is. Grote zware sterren verbranden hun gasvoorraad in hoog tempo en zijn blauw-wit heet. Aan het eind van hun leven zwellen ze op en koelen ze tegelijk af, ze zijn dan roodgloeiend. Hun leven eindigen ze daarna met een grote knal, een supernova explosie, en dan is het over en uit. Kleine sterren daarentegen zijn veel zuiniger met hun gas voorraad, ze zijn koeler en geel (zoals de Zon) of rood. Deze sterren worden veel ouder, vele kunnen nog ouder worden dan dat het heelal nu oud is.

Sterren zijn gezelligheidsdieren en ze worden net als de bloemen van zonet in groepen geboren. In zo'n nestje jonge sterren zitten altijd een paar grote jongens en heel veel kleintjes. Als je de totale kleur van zo'n groep sterren in de tijd zou kunnen volgen, dan zou die in het begin erg blauw lijken. Er zitten welliswaar maar een paar grote blauwe sterren in de groep, maar deze verstoken zoveel energie en geven zoveel licht dat ze de totale groep domineren. Na verloop van tijd beginnen de grote sterren uit te sterven en wordt de groep sterren eerst geel en vervolgens langzaam rood. Net als de bioloog die maar twee weken naar Chili mag, kunnen we de kleurverandering nooit in werkelijkheid zien, omdat het hele proces vele miljarden jaren duurt. Deze kleurveranderingstechniek heb ik gebruikt om de leeftijden van de sterren in de sterrenstelsels te schatten.

Er is echter nog een tweede faktor die invloed heeft op de kleur van sterren, namelijk het gasmateriaal waaruit ze opgebouwd zijn. Bevatten de sterren meer zwaardere elementen zoals koolstof en zuurstof (door astronomen meestal metalen genoemd), dan zal dit de kleur beïnvloeden.

Nieuwe groepen van sterren worden nog steeds geboren. Bekijken we de omslag foto, dan zien we dat de spiraal armen blauw zijn, met soms erg heldere blauwe gebieden. In deze gebieden worden nieuwe sterren geboren. Het binnengebied van het stelsel is rood en in het algemeen wordt aangenomen dat de sterren hier gemiddeld veel ouder zijn.

Er is helaas nog een ander verschijnsel dat ook invloed heeft op de kleur van een sterrenstelsel: "verroding" door stof. Ook dit effect is op de omslag foto te zien. De donkere banden en vlekken die langs de spiraal armen lopen worden veroorzaakt door stof en zijn duidelijk roder van kleur. Stof houdt namelijk blauw licht beter tegen dan rood licht en het gevolg is dat als we door stof naar iets kijkt het niet alleen minder helder, maar ook roder wordt. Hetzelfde zien we bij een zonsondergang. Het stof in de atmosfeer houdt voornamelijk blauw licht tegen en zonsondergangen zijn dan ook prachtig rood, vooral als er veel stof in de atmosfeer zit na een recente vulkaanuitbarsting.

Bijna alle 86 sterrenstelsels ("86 dalen") die ik bekeken heb worden blauwer naar buiten toe. Op het eerste gezicht kan dit dus twee dingen betekenen: 1) of de buiten gebieden van sterrenstelsel bevatten veel meer jonge sterren of 2) de binnen gebieden lijken veel roder door de grote hoeveelheid stof die het blauwe licht tegenhoudt.

Door nu alle blauwe, gele, rode en infrarode kleuren van de stelsels tegelijk met de modellen te vergelijken kon ik onderscheid maken tussen de effekten van ster evolutie en stof. Mijn nieuwe stofmodellen laten namelijk zien dat sterrenstelsels op een andere manier rood worden door stof dan door het ouder worden van sterren. Het “oude bloemen” rood is anders dan het stof (“ondergaande zon”) rood. Sterrenstelsels zijn bejaard in hun binnengebied en jong van buiten. Ook blijkt dat sterren stelsels met een “laat” Hubble type in het algemeen veel jonger zijn en minder metalen bevatten dan de “vroege” types. Die leeftijden zijn dus precies tegengesteld aan de betekenis van de historische naamgeving uit de jaren twintig.

Deze metingen hebben ook konsekwenties voor de berekeningen van massaverdelingen in sterrenstelsels. De massaverdeling kan op twee manieren berekend worden. Ten eerste kunnen we zeggen dat bij een bepaalde hoeveelheid licht een bepaald aantal sterren hoort en dus een zekere massa. We kunnen de massa ook berekenen uit de ronddraaiende beweging van het gas en de sterren rondom het centrum van het stelsel m.b.v. de zwaartekrachtswetten van Newton. Uit dit soort vergelijkingen was al gebleken dat de hoeveelheid “zwaartekracht massa” in de buitengebieden van stelsels veel groter is dan de hoeveelheid “zichtbare massa”, en dat er dus geheimzinige “donkere materie” moet zijn. Nu ik heb laten zien dat de buitengebieden van spiraalstelsels jong zijn, en dat de heldere jonge blauwe sterren daar dus wel heel veel licht geven maar samen niet zo zwaar zijn, is het verschil alleen maar groter geworden. Er is nog meer donkere materie nodig om het verschil te verklaren.

Er bestaan verschillende plannen om de verschillende effekten van sterevolutie en stof verder uit te zoeken. Nieuwe grote teleskopen worden momenteel gebouwd, nieuwe meetinstrumenten ontwikkeld en een nieuwe infrarood satelliet staat op het punt om gelanceerd te worden. Hiermee kunnen nieuwe waarnemingen gedaan worden die direkter het stof en de sterren in kaart kunnen brengen (we zullen minder afhankelijk zijn van de bloemenperkjes). Waarschijnlijk zullen deze toekomstige waarnemingen alleen maar nieuwe vragen oproepen en zal ik ’s avonds (en velen met mij) nog steeds in verwondering omhoog kijken.

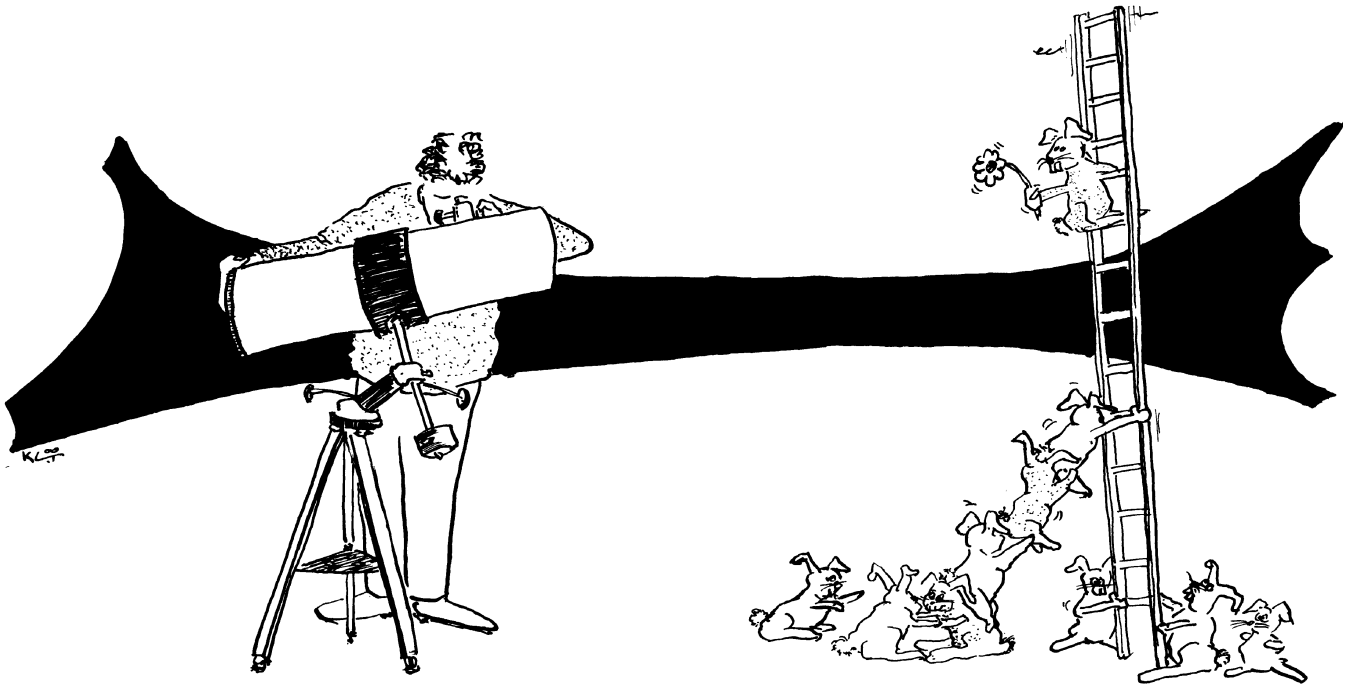

Chapter 1

Selection, observations and data reduction

Abstract. We present accurate surface photometry in the B, V, R, I, H and K passbands of 86 spiral galaxies. The galaxies in this statistically complete sample of undisturbed spirals were selected from the UGC to have minimum diameters of $2'$ and minor over major axis ratios larger than 0.625. This sample has been selected in such a way that it can be used to represent a volume limited sample.
The observation and reduction techniques are described in detail, especially the not often used driftscan technique for CCDs and the relatively new techniques using near-infrared (near-IR) arrays. For each galaxy we present radial profiles of surface brightness. Using these profiles we calculated the integrated magnitudes of the galaxies in the different passbands.
We performed internal and external consistency checks for the magnitudes as well as the luminosity profiles. The internal consistency is well within the estimated errors. Comparisons with other authors indicate that measurements from photographic plates can show large deviations in the zero-point magnitude. Our surface brightness profiles agree within the errors with other CCD measurements. The comparison of integrated magnitudes shows a large scatter, but a consistent zero-point.
These measurements will be used in a series of forthcoming papers to discuss central surface brightnesses, scalelengths, colors and color gradients of disks of spiral galaxies.

1 Introduction

In recent years there have been several investigations into the global optical properties of spiral galaxies (Grosbøl 1985; van der Kruit 1987; Valentijn 1990). In his review of 1959 de Vaucouleurs already mentioned that spiral galaxies have a radial luminosity profile which can reasonably accurately be described by a combination of a bulge and an exponential disk. Generally bulges are, in resemblance to profiles of elliptical galaxies, described by $R^{1/4}$ profiles:

$$\Sigma(r) = \Sigma_{\rm e} {\rm e}^{-7.67((r/r_{\rm e})^{1/4}-1)} \tag{1}$$

which in magnitudes translates to

$$\mu(r) = \mu_{\rm e} + 8.325((r/r_{\rm e})^{1/4} - 1) \tag{2}$$

with $r_{\rm e}$ the effective radius, the radius which encloses half the total light of the bulge and $I_{\rm e}$ the surface intensity ($\mu_{\rm e}$ in magnitudes) at this radius. The formula for the exponential light profile of the disk is:

$$\Sigma(r) = \Sigma_0 {\rm e}^{-r/h} \tag{3}$$

or in magnitudes

$$\mu(r) = \mu_0 + 1.086 r/h \tag{4}$$

with μ_0 the central surface brightness (Σ_0 surface intensity) and h the scalelength of the exponential disk.

This chapter is a slightly modified version of an article that appeared in A&AS 106, p.451, co-authored by P.C. van der Kruit.

One of the most remarkable results of a study by Freeman (1970) was the constancy of μ_0 in the B passband among galaxies. For his subsample of 28 (out of 36) galaxies he found $\langle \mu_0 \rangle = 21.65 \pm 0.3$ B-mag arcsec^{-2}. If M/L is more or less constant among galaxies, this translates directly to a constant central surface density of matter associated with luminous material. This has of course serious implications for theories on galaxy formation and evolution.

Several authors have tried to explain this effect. Disney & Phillipps (1983, see also Davies 1990) have proposed it could be the result of a selection effect. Catalogs of galaxies have been selected by eye from photographic plates. Therefore one might select against very compact galaxies with very high central surface brightness, because they appear to be stellar. Likewise, galaxies with very low surface brightness might have been missed due to the low contrast with the sky background. Disney and Phillipps define a visibility for a galaxy, which enables one to correct a sample for selection effects if a careful selection is made beforehand. Using this correction on a statistically complete sample of 51 galaxies, van der Kruit (1987) still found a small range in μ_0, with $\langle \mu_0 \rangle = 22.7 \pm 0.9$ J-mag arcsec^{-2} (the photographic J passband is very near the B passband).

Another explanation of the constancy might be dust absorption, as proposed by Jura (1980), Valentijn (1990) and Phillipps et al. (1991). If galaxies are optically thick in the B passband, we always see the same outer layer of galaxies. The solution to the dust problem is to move to longer wavelengths. The absorption by dust is expected to be less at these wavelengths, as in our own galaxy (Rieke & Lebofsky 1985) and the Sombrero galaxy (Knapen et al. 1991). A study of Grosbøl (1985) done on the red Palomar Observatory Sky Survey-plates (POSS) indeed shows no constant μ_0. His sample is incomplete, because he selected his galaxies from the incomplete RC2 (de Vaucouleurs et al. 1976). Reanalyzing a statistically complete

subsample, we still found a larger standard deviation in μ_0 than the previously found values (van der Kruit 1989). Further analysis of this sample is difficult, because Grosbøl did not provide the profiles to check his analysis.

If absorption has an important effect on the shape of the global profiles of spiral galaxies, one can expect a change of scalelength with wavelength for a galaxy (Phillipps et al. 1991; Han 1992a). Knapen and van der Kruit (1991) have shown that scalelengths found by different authors can differ by a substantial amount. This means that comparisons of scalelengths at different wavelengths can only be done on a homogeneous dataset reduced and analyzed with the same procedures.

If one has a set of observations at different wavelengths of a galaxy, one can make radial color profiles. These color profiles can be an important tool in finding dust absorption. Dust absorption will tend to redden the profiles. A complicating factor in this analysis is the change in colors of stellar populations as function of radius. The color profiles are expected to redden near the nucleus, because of the redder stellar populations in the bulge compared to the disk.

To investigate the global properties of spiral galaxies, the constancy of μ_0, the dust absorption and the distribution of stellar populations, we have observed and analyzed a sample of 86 spiral galaxies at several wavelengths. To have a practically unobscured view of the galaxies, we have observed the galaxies in the near-IR, where the obscuration by dust is much smaller than in the optical. This enables us to analyze the constancy of μ_0, without having to take dust absorption into account. Additionally, older stellar populations of a galaxy, which contain most of the mass, are more luminous in the near-IR. To investigate the dust and stellar populations distribution, we have also observed the galaxies in several optical passbands.

We describe the selection of our sample in Section 2. The observations and data reduction, split in an optical and a near-IR part, are described in Section 3 and a short discussion of the results can be found in Section 4.

2 The sample selection

When defining a sample for a statistical study extra care has to be taken to avoid unwanted selection biases. One needs a sample with objects most suited for the type of study, but still correctable for selection effects. For our study a large homogeneous catalog of galaxies was needed, from which we could select our sample. We used the Uppsala General Catalogue of Galaxies (UGC, Nilson 1973), because it contains a large number of galaxies, that were selected and parameterized in a uniform way. All of the selection was done using the parameters available in the UGC, even though more accurate parameters were available for some of the galaxies in other catalogs (for instance isophotal diameters), to avoid inhomogeneities in the sample.

As we are interested in disk systems of spiral galaxies we first had to select the spiral galaxies from the UGC. We used only galaxies classified equal or later than S1 or SB1 and earlier or equal to DWARF (which means we excluded S0-S1, SB0-SB1, IRR, DWRF IRR, S3-IRR etc.). Furthermore all galaxies classified as SB3+CMP, DBL SYS, etc. were excluded, while systems classified simply as S or SB were selected. This resulted in a sample of galaxies which are clearly disk dominated.

For this study we are interested in undisturbed spiral galaxies. The ideal case would be a complete volume limited sample of undisturbed spiral galaxies. Defining a volume limited sample using a redshift limit will introduce incompleteness, since it is likely that the smallest galaxies near the redshift limit are not catalogued. Using a smaller limit so as not to miss any galaxies, will leave a small uninteresting sample, which will contain very few large galaxies. Using galaxies belonging to one cluster would be another way to define a volume limited sample, but galaxies belonging to a cluster are more likely to be disturbed and thus not suited for our investigation.

We therefore decided to use a diameter limited sample, which can easily be corrected to represent a volume limited sample (Davies 1990). When calculating number densities one gives each galaxy a weight inversely proportional to $V_{\rm max}$, the volume associated with the maximum distance at which one can place a galaxy, while still being included in the sample (d_{max}). Each galaxy gets a weight

$$w = (V_{\rm max})^{-1} = \frac{3}{4\pi}(d_{\rm max})^{-3} = \frac{3}{4\pi}(D_{\rm maj}^{\rm lim}/dD_{\rm maj})^3 \qquad (5)$$

with d the true distance to the galaxy, $D_{\rm maj}$ major axis diameter of the galaxy, $D_{\rm maj}^{\rm lim}$ the diameter limit of the sample. To obtain real volume densities one should make sure to correct also for other selection criteria (in our case an inclination limit and RA and DEC limits).

We used a red major axis diameter limit of 2 arcmin, a diameter at which the UGC is still expected to be complete, which can be checked with a $V/V_{\rm max}$-test (Schmidt 1968; Thuan & Seitzer 1979). The $V/V_{\rm max}$ of a galaxy is just the volume associated with the distance of a galaxy divided by $V_{\rm max}$ as defined in Eq.(5), thus $V/V_{\rm max} = (D_{\rm maj}^{\rm lim}/D_{\rm maj})^3$. Note that this quantity is distance independent. For objects distributed randomly in space the average value of $V/V_{\rm max}$ should be $0.5 \pm 1/\sqrt{12 \times N}$, where N is the number of objects in the test. The UGC is statistically complete to red diameters of $1.4'$, as can be seen in Fig. 1. For selection limits larger than $4'$ there seem to be too many big galaxies, which might be a signature of the non-random distribution of galaxies in space. We used the red instead of the blue UGC diameters to minimize the effect of dust and strong spiral arm features on the selection.

The next selection criterion we used was an inclination limit. The reason for this is twofold, both concerning the unknown projection effects of the light distribution on the sky:

1. We are examining radial distributions of light, which have a different scaling in the plane and perpendicular to the plane. For galaxies seen at an angle between 50 and 85 degrees this light projects in a difficult and unknown way. There are two ideal cases, face-on or edge-on disk systems, of which we are examining face-on galaxies, because the effect of dust is in these systems minimized.
2. Another effect of the projection might be the change in diameter as function of inclination, if galaxies are optically

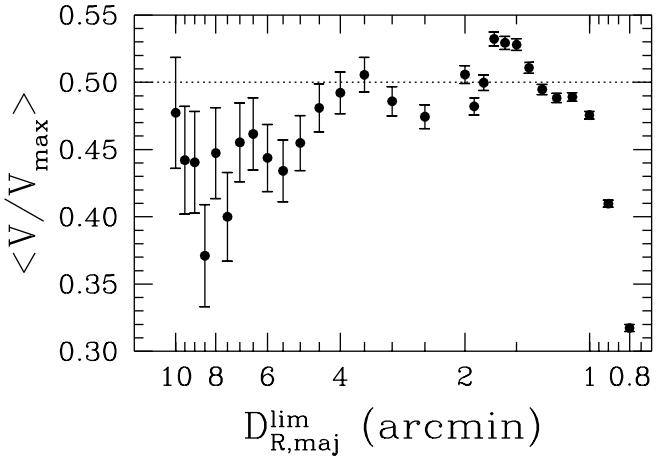

Fig. 1. $\langle V/V_{max} \rangle$ values for the UGC using different red major axis diameter limits. The expected value of 0.5 for galaxies randomly distributed in space is indicated by a dotted line.

thin. Looking through a galaxy, the pathlength grows with inclination angle, the surface brightness will increase and a galaxy seems to be larger. So samples containing all inclinations might have an inclination dependent selection effect in their diameters. As the pathlength increases inversely proportionally with the cosine of inclination, this effect is less severe for the low inclination galaxies examined here. This effect might be also less important for the UGC diameters as they were measured by eye. The diameters were measured out to the faintest structures belonging to the galaxy seen on the photographic plate, which are likely to be bright H II regions. Their surface brightness probably doesn't change with inclination and therefore are diameters measured by eye less inclination dependent than isophotal diameters (Huizinga 1994).

The galaxies selected for our sample have a red minor axis diameter over major axis diameter larger than 0.625 and a UGC inclination class less or equal to 4. This roughly corresponds to an inclination less than 51 degrees.

To avoid selection problems because of unknown Galactic foreground extinction and to avoid excessive amounts of foreground stars in our images we decided to select only galaxies at Galactic latitude $|b| \geq 25^{\rm o}$. Further selections depended only on the position on the sky of the galaxy, and assuming that our position in the universe is not exceptional, this should not create any biases.

These criteria result in a sample of 368 galaxies. To check the completeness of this sample we have performed a $V/V_{\rm max}$-test. For our sample we have $\langle V/V_{\rm max} \rangle = 0.496 \pm 0.015$ and we conclude that our sample is at least statistically complete.

In summary: we have selected all spiral galaxies of the UGC with $D_{\rm maj,red} \geq 2'$, $D_{\rm min,red}/D_{\rm maj,red} > 0.625$, $|b| > 25^{\rm o}$, which resulted in a sample of 368 galaxies. A $V/V_{\rm max}$-test shows that this sample is statistically complete.

The choice of the 86 galaxies observed out of this sample of 368 galaxies depended only on allocated observing time, after the POSS plates were checked against disturbed and interacting galaxies. We selected only galaxies with declination $\delta \leq 60^{\rm o}$, because one of the intended telescopes (UKIRT) is unable to observe at higher declinations. The ranges in declination and hour angle were chosen in such a way that we had roughly an equal number of galaxies all through the night. This procedure can not have produced unwanted biases. The total selected area was 1.57 steradian or 12.5% of the sky. Table 1 shows the global parameters of all observed galaxies.

3 Observations and reduction

As the observations and data reduction techniques for the optical and the near-IR differ substantially, each will be treated separately until the stage where we have created calibrated images. Once we have these, extraction of the galaxy parameters is the same for both kind of observations and will be treated together.

Because we are primarily interested in the central surface brightness and scalelengths of the galaxies, we decided to observe only along the major axes of the galaxies that were too large for the field of view (FOV) of the telescope/camera combinations. This is especially important for the near-IR observations, where the FOV of UKIRT/IRCAM2 is about 1 arcmin square.

3.1 Creating calibrated optical images

The original goal of our survey was to obtain photometric B, V, R and I observations for the full sample of galaxies. Due to weather conditions we did not succeed completely, but for 83 galaxies at least one calibrated optical image has been obtained and in general a B and an R or I image is available. For 57 galaxies we have obtained the full photometric B, V, R and I observations. For the remaining 29 galaxies often non-photometric observations are available, so we can at least compare scalelengths in different passbands.

3.1.1 The observations

The optical data were obtained using three different techniques. First of all we used the normal direct imaging mode on the 1m Jacobus Kapteyn Telescope (JKT) on La Palma, equipped with a GEC CCD. For the second technique we used the driftscan mode on the JKT, which enabled us to observe a larger area in spite of the small FOV. And finally we obtained data using service observations and archived material of the Isaac Newton Group of telescopes on La Palma. We used the Kitt Peak B, V, R and I filters available on La Palma (RGO/La Palma Technical Notes 1987). As galaxies are not all oriented East-West on the sky, the CCD camera was rotated halfway the observing run to have an image field better suited for galaxies which are oriented North-South. A full observation log of objects, telescopes, techniques, CCDs, pixelsizes, filters, exposure times, seeing and quality of the observations can be found in Table 2.

Table 1. Global parameters of the galaxies in the observed sample. The positions and the V_{GSR} receding velocities are obtained from the RC3, D_{maj} is the red UGC major axis diameter, b/a is the red UGC minor over major axis diameter ratio.

name		RA	DEC	galactic		classification		D_{maj}	b/a	V_{GSR}
		(1950)		$l(^\circ)$	$b(^\circ)$	UGC	RC3	$(')$		km/s
UGC 89	NGC 23	0 07 18.6	25 38 42	111.4	-36.0	SB1	.SBS1..	2.2	0.68	4733
UGC 93		0 07 47.0	30 34 16	112.6	-31.2	S IV	.SA.8..	2.0	0.85	5124
UGC 242		0 22 52.6	19 57 39	114.7	-42.2	SB3	.SX.7..	2.1	0.86	4449
UGC 334	A 0031+31	0 31 16.6	31 10 33	118.6	-31.3	DWRF SP	.S..9..	2.0	1.00	4800
UGC 438	NGC 214	0 38 48.9	25 13 33	120.1	-37.3	S3	.SXR5..	2.2	0.77	4685
UGC 463	NGC 234	0 40 55.6	14 04 10	120.1	-48.5	S3	.SXT5..	2.0	1.00	4577
UGC 490	NGC 251	0 45 12.0	19 18 00	121.8	-43.3	S3	.S..5..	2.3	0.78	4732
UGC 508	NGC 266	0 47 05.6	32 00 23	122.5	-30.6	SB1	.SBT2..	3.5	0.94	4823
UGC 628		0 58 18.0	19 13 00	126.0	-43.3	DWRF SP	.S..9*.	2.0	0.80	5574
UGC 1305	NGC 691	1 47 55.8	21 30 45	140.7	-39.1	S2/S3	.SAT4..	3.7	0.70	2769
UGC 1455	NGC 765	1 55 58.7	24 38 56	141.8	-35.5	SB2/S3	.SXT4..	3.0	1.00	5224
UGC 1551		2 00 48.4	23 50 03	143.4	-35.9	SB IV-V	.SB?...	3.0	0.67	2773
UGC 1559	IC 1774	2 01 12.0	15 04 00	147.6	-44.1	S3/SB3	.SXS7..	2.1	0.81	3705
UGC 1577		2 02 32.3	30 56 14	141.0	-29.1	SB2	.SB?...	2.3	0.70	5393
UGC 1719	IC 213	2 11 18.0	16 14 00	150.0	-42.0	S2	.SXT3..	2.2	0.73	8297
UGC 1792		2 16 58.2	28 48 27	145.3	-30.0	SB3	.SXR5..	2.2	0.64	5092
UGC 2064		2 32 18.0	20 38 00	153.2	-35.9	SB2/S3	.SXS4..	2.1	0.71	4338
UGC 2081		2 33 27.1	0 12 08	169.6	-52.7	S3	.SXS6..	2.5	0.72	2626
UGC 2124	NGC 1015	2 35 38.9	-1 32 00	172.2	-53.7	SB1	.SBR1*.	3.0	1.00	2639
UGC 2125	IC 1823	2 35 36.9	31 51 14	148.0	-25.5	SB3	.SBR5..	2.3	0.87	5288
UGC 2197		2 40 25.8	31 15 34	149.3	-25.6	S3	.S..6*.	2.0	0.70	5195
UGC 2368	IC 267	2 51 06.1	12 38 43	163.5	-40.2	SB2	PSBS3..	2.1	0.71	3610
UGC 2595	IC 302	3 10 13.9	4 31 06	175.4	-43.3	SB2/SB3	.SBT4..	2.5	0.92	5907
UGC 3066		4 28 18.2	5 26 00	189.9	-27.8	S3/SB3	.SXR7*.	2.0	0.75	4594
UGC 3080	A 0429+01	4 29 21.8	1 05 27	194.1	-30.0	S3	.SXT5..	2.2	1.00	3481
UGC 3140	NGC 1642	4 40 20.1	0 31 35	196.4	-27.9	S3	.SAT5*.	2.0	1.00	4564
UGC 4126	NGC 2487	7 55 19.0	25 17 08	196.3	25.2	SB2	.SB.3..	2.5	0.92	4771
UGC 4256	NGC 2532	8 07 03.2	34 06 20	187.6	30.2	S3	.SXT5..	2.2	0.82	5228
UGC 4308	A 0814+21	8 14 29.9	21 50 20	201.6	28.1	SB3	.SBT5..	2.2	0.77	3486
UGC 4368	NGC 2575	8 19 46.2	24 27 32	199.2	30.2	S3	.SAT6*.	2.5	0.80	3800
UGC 4375	A 0820+22	8 20 12.0	22 49 00	201.1	29.7	S3	.SX.5*.	2.5	0.68	1983
UGC 4422	NGC 2595	8 24 46.7	21 38 40	202.7	30.3	SB2/S3	.SXT5..	3.2	0.88	4250
UGC 4458	NGC 2599	8 29 15.4	22 44 00	201.9	31.7	S1	.SA.1..	2.0	1.00	4672
UGC 5103	NGC 2916	9 32 07.6	21 55 45	208.7	45.2	S	.SAT3$.	2.3	0.74	3649
UGC 5303	NGC 3041	9 50 22.5	16 54 53	217.7	47.6	S3	.SXT5..	3.8	0.63	1317
UGC 5510	NGC 3162	10 10 45.5	22 59 16	211.0	54.1	S3	.SXT4..	3.2	0.88	1231
UGC 5554	NGC 3185	10 14 53.2	21 56 20	213.2	54.7	SB1	RSBR1..	2.8	0.64	1159
UGC 5633	A 1021+15	10 21 54.0	15 00 00	225.3	53.7	SB IV-V	.SB.8..	2.5	0.64	1287
UGC 5842	NGC 3346	10 40 59.0	15 08 03	228.8	57.9	SB3	.SBT6..	3.0	0.87	1169
UGC 6028	NGC 3455	10 51 51.6	17 33 08	226.9	61.3	S2	PSXT3..	2.6	0.65	1029
UGC 6077	NGC 3485	10 57 24.0	15 06 43	232.6	61.3	SB2	.SBR3*.	2.3	1.00	1350
UGC 6123	NGC 3507	11 00 46.3	18 24 25	227.1	63.6	SB2	.SBS3..	3.4	0.82	906
UGC 6277	NGC 3596	11 12 27.9	15 03 38	236.9	64.4	S3	.SXT5..	3.6	0.78	1111
UGC 6445	NGC 3681	11 23 52.6	17 08 22	236.1	67.8	S2/S3	.SXR4..	2.3	1.00	1171
UGC 6453	NGC 3684	11 24 34.4	17 18 20	236.0	68.1	S3	.SAT4..	2.5	0.68	1097
UGC 6460	NGC 3686	11 25 07.3	17 29 56	235.7	68.3	SB2/SB3	.SBS4..	3.0	0.83	1089
UGC 6536	NGC 3728	11 30 36.0	24 43 00	217.2	72.2	S2	.S..3..	2.0	0.75	6941
UGC 6693	NGC 3832	11 40 54.0	23 00 00	225.2	74.0	SB3	.SBT4..	2.2	0.95	6869
UGC 6746	NGC 3884	11 43 37.0	20 40 11	233.8	73.6	S1	.SAR0..	2.1	0.81	6897
UGC 6754	NGC 3883	11 44 11.5	20 57 16	233.1	73.9	S2	.SAT3..	3.3	0.91	6979
UGC 7169	NGC 4152	12 08 04.6	16 18 42	260.4	75.4	S3	.SXT5..	2.2	0.86	2112
UGC 7315	NGC 4237	12 14 38.2	15 36 08	267.2	75.8	S2	.SXT4..	2.2	0.64	813
UGC 7450	NGC 4321	12 20 23.3	16 06 00	271.1	76.9	S3	.SXS4..	6.8	0.88	1540
UGC 7523	NGC 4394	12 23 24.7	18 29 30	268.2	79.3	SB2	RSBR3..	3.9	0.90	884
UGC 7594	NGC 4450	12 25 58.0	17 21 40	273.9	78.6	S2	.SAS2..	6.5	0.69	1918
UGC 7876	NGC 4635	12 40 09.5	20 13 12	286.8	82.5	S3	.SXS7..	2.0	0.80	938

Table 1. -continued.

name		RA	DEC	galactic		classification		D_{maj}	b/a	V_{GSR}
		(1950)		$l(^\circ)$	$b(^\circ)$	UGC	RC3	$(')$		km/s
UGC 7901	NGC 4651	12 41 12.5	16 40 05	293.1	79.1	S3	.SAT5..	4.0	0.68	772
UGC 8279	NGC 5016	13 09 42.6	24 21 42	1.0	84.4	S2-3	.SXT5..	2.0	0.75	2622
UGC 8289	NGC 5020	13 10 11.0	12 51 53	322.9	74.6	S2/SB3	.SXT4..	3.3	0.85	3331
UGC 8865	NGC 5375	13 54 40.7	29 24 26	44.8	75.4	SB2	.SBR2..	3.7	0.81	2435
UGC 9024		14 04 24.0	22 16 00	20.4	72.2	S	.S?....	2.0	1.00	2338
UGC 9061	IC 983	14 07 42.4	17 58 08	9.7	69.6	SB1/SB2	.SBR4..	4.5	0.78	5466
UGC 9481	NGC 5735	14 40 23.5	28 56 15	43.2	65.5	SB2	.SBT4..	2.2	0.82	3817
UGC 9915	NGC 5957	15 33 00.9	12 12 51	19.7	48.8	SB2	PSXR3..	2.8	1.00	1889
UGC 9926	NGC 5962	15 34 14.1	16 46 23	26.3	50.5	S3	.SAR5..	2.8	0.71	2034
UGC 9943	NGC 5970	15 36 08.1	12 20 53	20.4	48.2	SB3	.SBR5..	2.9	0.66	2030
UGC 10083	NGC 6012	15 51 54.6	14 44 55	26.0	45.8	SB1	RSBR2*.	2.0	0.65	1944
UGC 10437		16 29 36.0	43 27 00	68.2	43.2	S	.S?....	2.0	0.85	2759
UGC 10445		16 31 48.6	29 05 19	48.9	41.4	S3	.S..6?.	2.3	0.87	1102
UGC 10584	NGC 6246A	16 49 12.0	55 28 00	83.8	39.1	S3/SB3	.SXR5P*	2.3	0.91	5451
UGC 11628	NGC 6962	20 44 45.4	0 08 13	47.4	-25.4	S1	.SXR2..	3.0	0.77	4370
UGC 11708	NGC 7046	21 12 24.1	2 37 38	54.0	-29.9	SB	.SBT6..	2.0	0.65	4326
UGC 11872	NGC 7177	21 58 18.6	17 29 50	75.4	-29.0	S2	.SXR3..	2.7	0.70	1343
UGC 12151		22 39 00.0	0 08 00	69.0	-48.4	DWARF	.IBS9*.	3.0	0.67	1896
UGC 12343	NGC 7479	23 02 26.8	12 03 06	86.3	-42.8	SB2	.SBS5..	4.0	0.83	2544
UGC 12379	NGC 7490	23 05 01.0	32 06 18	98.7	-25.6	S2	.S..4..	2.3	1.00	6416
UGC 12391	NGC 7495	23 06 24.0	11 46 00	87.2	-43.6	S3	.SXS5..	2.0	0.85	5050
UGC 12511	NGC 7610	23 17 09.8	9 54 40	89.0	-46.6	S3	.S..6*.	2.5	0.84	3708
UGC 12614	NGC 7678	23 25 58.2	22 08 50	98.9	-36.5	S3/SB3	.SXT5..	2.8	0.68	3665
UGC 12638	NGC 7685	23 28 00.2	3 37 31	87.7	-53.3	S3	.SXS5*.	2.0	0.85	5775
UGC 12654	NGC 7691	23 29 53.0	15 34 28	96.6	-42.9	SB2/S3	.SXT4..	2.0	0.80	4224
UGC 12732		23 38 09.1	25 57 30	103.7	-34.0	DWRF SP	.S..9*.	3.0	1.00	929
UGC 12754	NGC 7741	23 41 22.7	25 47 53	104.5	-34.4	SB3	.SBS6..	4.3	0.70	935
UGC 12776		23 43 41.4	33 05 26	107.6	-27.6	SB2	.SBT3..	2.7	0.81	5127
UGC 12808	NGC 7769	23 48 31.5	19 52 25	104.2	-40.5	S1-2	RSAT3..	2.5	0.84	4380
UGC 12845		23 53 11.0	31 37 23	109.4	-29.5	S3	.S..7..	2.4	0.75	5064

3.1.2 Direct imaging reduction

The direct imaging mode on the JKT is the standard one using a CCD camera. We used the GEC CCD with 385x578 pixels and a pixel size of $0.3''$. We used the M 67 calibration fields to check the pixelsizes, which is described in Sect 3.1.5. Bias subtraction was performed using the average value of the overscan region on the CCD. We did not use the bias frames we obtained, because there was no obvious structure in them. We created for each filter and for each night flatfields by averaging 2-4 evening and morning twilight flats. Large scale flatfielding was stable at the 1% level through one observing run, but on small scales this could go up to 4% because of dust particles on the CCD window, which seemed to move around with telescope position. Therefore flatfields of the night before or after the observation were sometimes used to flatfield object frames, if these seemed to fit the dust pattern better. As we are interested in the large scale structure of galaxies, the dust patches don't influence our measurements significantly, except that it made our calibration less secure. We often made two shorter exposures at the same position to be able to remove cosmic ray events.

3.1.3 Driftscan reduction

For the driftscan observations the same telescope/CCD combination as described in the previous paragraph was used. The driftscan technique takes advantage of the way CCDs are designed, making use of the shift and readout technique of the CCD. In contrast to the normal observing mode, the CCD is shifted under the telescope (that keeps tracking the object) while it is read out row by row. Each time the CCD has been shifted one row up with respect to the observed field, the electrons in the bottom row are read out and the electrons in all other rows of the CCD are shifted one row down. In effect the image of the sky (and the electrons in the CCD associated with it) stays at the same place, while the CCD is shifted underneath it.

The first time the bottom row of the CCD is read out it contains electrons associated with an exposure time of only one step time, the second time two step times, et cetera, until we have shifted the CCD a full chiplength. From then on each readout contains electrons associated with an effective exposure time of #pixels (578) time intervals. When finished, the top row of the CCD has just been exposed one time interval to a new part of the sky and the bottom row contains flux of a full 578 times time steps exposure. The full scan looks like

Table 2. The observation log of the optical observations. All galaxies were observed with the JKT at La Palma with a GEC CCD having a pixelsize of 0.3″, unless otherwise indicated at the notes. Exp.time indicates the number of positions and the exposure time per position in seconds. Q denotes the photometric quality, estimated errors are 1: photometric, 2: 0.0-0.2 mag, 3: 0.2-0.5 mag, 4: 0.5-1.0 mag and 5: >1.0 mag. The FWHM seeing estimate is in arcseconds.
Notes to the table: (1) Driftscan, (2) Internal calibration, (3) Calibrated using Longo and de Vaucouleurs (1983), (4) Mosaic, (5),(7) JKT, GEC CCD, 0.6″ pixels, (6),(8) JKT, RCA CCD, 0.41″ pixels, (9) INT, GEC CCD, 0.54″ pixels, (10) INT, EEV CCD, 0.53″ pixels, (11) 1.3m MDM observatory, Thomson CCD, 0.48″ pixels.

UGC	band	date	exp.time	Q	seeing	notes
89	B	13 Sep '91	578.0	1	1.9	1
	V	13 Sep '91	404.6	1	1.6	1
	R	13 Sep '91	289.0	1	1.8	1
	I	13 Sep '91	404.6	1	1.6	1
93	B	10 Sep '91	2×500.0	1	1.8	
	V	10 Sep '91	2×350.0	1	1.6	
	R	10 Sep '91	2×300.0	1	1.2	
	I	10 Sep '91	2×300.0	1	1.6	
242	B	8 Sep '91	2×300.0	1	1.5	
	V	8 Sep '91	2×250.0	1	1.3	
	R	8 Sep '91	2×200.0	1	1.2	
	I	8 Sep '91	2×250.0	1	1.2	
334	B	16 Sep '91	2×700.0	1	2.5	
	V	16 Sep '91	2×400.0	1	2.4	
	R	16 Sep '91	2×400.0	1	2.1	
	I	16 Sep '91	2×400.0	1	2.1	
438	B	14 Sep '91	578.0	1	1.7	1
	V	14 Sep '91	404.6	1	1.7	1
	R	14 Sep '91	289.0	1	1.6	1
	I	15 Sep '91	346.8	1	1.7	1
	B	9 Sep '91	578.0	1	2.2	1
	V	9 Sep '91	346.8	1	1.6	1
	R	9 Sep '91	289.0	1	1.5	1
	I	9 Sep '91	289.0	1	1.6	1
463	B	11 Nov '88	918.2	1	1.7	5
	I	11 Nov '88	800.0	1	1.7	5
490	B	7 Sep '91	578.0	1	1.5	1
	V	7 Sep '91	404.6	1	1.3	1
	R	7 Sep '91	289.0	1	1.3	1
	I	7 Sep '91	289.0	1	1.2	1
508	B	13 Sep '91	578.0	1	1.7	1
	V	13 Sep '91	346.8	1	1.7	1
	R	13 Sep '91	346.8	1	1.9	1
	I	13 Sep '91	404.6	1	1.7	1
628	B	15 Sep '91	2×600.0	1	1.6	
	V	15 Sep '91	2×450.0	1	1.6	
	R	15 Sep '91	2×350.0	1	1.7	
	I	15 Sep '91	2×300.0	1	1.6	
1305	B	8 Sep '91	578.0	1	1.6	1
	V	8 Sep '91	404.6	1	1.6	1
	R	8 Sep '91	404.6	1	1.6	1
	I	8 Sep '91	404.6	1	1.6	1
1455	B	9 Sep '91	693.6	1	1.5	1
	V	9 Sep '91	404.6	1	1.5	1
	R	9 Sep '91	346.8	1	1.5	1
	I	9 Sep '91	346.8	1	1.4	1

Table 2. -continued.

UGC	band	date	exp.time	Q	seeing	notes
1551	B	14 Sep '91	693.6	1	1.4	1
	V	14 Sep '91	404.6	1	1.5	1
	R	14 Sep '91	346.8	1	1.6	1
	I	14 Sep '91	346.8	1	1.5	1
1559	B	13 Sep '91	2×300.0	1	1.5	
	V	13 Sep '91	404.6	1	1.5	1
	R	13 Sep '91	289.0	1	1.7	1
	I	13 Sep '91	404.6	1	1.6	1
1577	B	9 Sep '91	693.6	1	1.6	1
	V	10 Sep '91	462.4	1	1.8	1
	R	9 Sep '91	346.8	1	1.7	1
	I	10 Sep '91	404.6	1	1.8	1
1719	B	14 Sep '91	693.6	1	1.6	1
	V	14 Sep '91	404.6	1	1.3	1
	R	14 Sep '91	346.8	1	1.4	1
	I	13 Sep '91	300.0	1	1.5	
1792	B	16 Sep '91	2×600.0	1	2.1	
	V	16 Sep '91	2×300.0	1	2.2	
	R	16 Sep '91	2×250.0	1	2.1	
	I	16 Sep '91	2×300.0	1	2.1	
2064	B	15 Sep '91	2×400.0	1	1.5	
	V	15 Sep '91	2×450.0	1	1.4	
	R	15 Sep '91	2×350.0	1	1.5	
	I	15 Sep '91	400.0	1	1.4	
2081	B	10 Sep '91	3×350.0	1	1.6	
	V	16 Sep '91	600.0	1	2.3	
	R	16 Sep '91	250.0	1	2.1	
	I	10 Sep '91	500.0	1	1.6	
2124	B	7 Sep '91	578.0	1	1.5	1
	V	8 Sep '91	404.6	1	1.4	1
	R	8 Sep '91	404.6	1	1.4	1
	I	8 Sep '91	404.6	1	1.4	1
2125	B	15 Sep '91	751.4	1	1.3	1
	V	15 Sep '91	462.4	1	1.6	1
	R	15 Sep '91	404.6	1	1.6	1
	I	15 Sep '91	346.8	1	1.4	1
2197	B	16 Sep '91	2×600.0	1	2.6	
	V	16 Sep '91	2×350.0	1	2.2	
	R	16 Sep '91	2×300.0	1	2.2	
	I	16 Sep '91	2×350.0	1	2.1	
2368	B	15 Nov '90	1000.0	1	1.2	6
	V	15 Nov '90	800.0	1	1.3	6
	R	15 Nov '90	600.0	1	1.3	6
	I	15 Nov '90	600.0	1	1.2	6
2595	V	6 Mar '92	2×200.0	1	2.7	
	R	6 Mar '92	2×200.0	1	2.8	
	I	5 Mar '92	3×300.0	1	1.8	
3066	B	4 Mar '92	600.0	1	1.6	
	V	4 Mar '92	500.0	1	1.7	
	R	4 Mar '92	2×150.0	1	1.5	
	I	4 Mar '92	2×150.0	1	1.4	
3080	B	4 Mar '92	2×300.0	1	1.9	
	V	4 Mar '92	2×200.0	1	1.9	
	R	4 Mar '92	2×150.0	1	2.1	
	I	5 Mar '92	3×150.0	1	1.5	
3140	B	5 Oct '88	800.0	1	2.1	7
	I	5 Oct '88	600.0	1	2.1	7
4126	B	4 Mar '92	601.1	1	1.4	1
	V	6 Mar '92	400.0	1	2.5	3

Table 2. -continued.

UGC	band	date	exp.time	Q	seeing	notes
	R	4 Mar '92	300.6	1	1.3	1
	I	4 Mar '92	300.6	1	1.3	1
4256	B	9 Mar '92	2×600.0	1	1.9	3
	V	9 Mar '92	2×300.0	1	1.8	3
	R	9 Mar '92	600.0	3	1.6	
	I	9 Mar '92	2×300.0	3	1.6	
4308	B	7 Apr '91	400.0	1	3.0	
	V	7 Apr '91	2×250.0	1	2.6	
	R	7 Apr '91	300.6	1	2.4	1
	I	7 Apr '91	398.8	1	2.1	1
4368	B	5 Mar '92	601.1	1	1.7	1
	V	8 Apr '91	4×200.0	1	2.1	4
	R	8 Apr '91	4×200.0	1	1.9	4
	I	5 Mar '92	300.6	1	1.6	1
4375	B	8 Mar '92	4×400.0	1	1.8	4
	R	8 Mar '92	2×400.0	1	1.8	4
4422	B	7 Apr '91	4×300.0	1	2.5	4
	V	8 Apr '91	5×200.0	1	1.7	4
	R	7 Apr '91	4×200.0	1	2.0	4
	I	7 Apr '91	4×200.0	1	2.0	4
4458	B	3 Apr '91	4×600.0	1	1.8	4
	V	5 Mar '92	352.6	1	1.7	1
	R	5 Mar '92	352.6	1	1.7	1
	I	3 Apr '91	2×500.0	1	1.6	
5103	B	8 Mar '92	2×350.0	1	1.8	
	R	8 Mar '92	400.0	1	1.7	
5303	B	4 Apr '91	601.1	1	2.5	1
	V	4 Mar '92	300.6	1	1.6	1
	R	4 Mar '92	300.6	1	1.5	1
	I	4 Apr '91	502.9	1	3.2	1
5510	B	7 Apr '91	2×300.6	1	2.2	1
	V	9 Apr '91	398.8	3	1.8	1
	R	7 Apr '91	398.8	1	1.9	1
	I	7 Apr '91	398.8	1	1.9	1
5554	B	4 Mar '92	578.0	1	1.6	1
	V	6 Mar '92	2×250.0	2	3.2	
	R	4 Mar '92	289.0	1	1.6	1
	I	4 Mar '92	289.0	1	1.5	1
5633	B	8 Mar '92	3×600.0	1	1.8	3
	V	9 Mar '92	2×400.0	1	2.5	3
	R	8 Mar '92	2×250.0	1	2.5	3
	I	9 Mar '92	600.0	3	2.6	
5842	B	4 Apr '91	601.1	1	2.8	1
	V	6 Apr '91	400.0	4	1.8	
	R	6 Mar '92	200.0	1	3.9	
	I	4 Apr '91	502.9	1	3.2	1
6028	B	5 Mar '92	601.1	1	1.1	1
	V	5 Mar '92	352.6	1	1.3	1
	R	5 Mar '92	300.6	1	1.4	1
	I	9 Apr '91	398.8	1	1.4	1
6077	B	8 Apr '91	2×300.0	1	1.8	
	V	8 Apr '91	2×200.0	1	1.8	
	R	7 Apr '91	398.8	1	1.8	1
	I	7 Apr '91	398.8	1	2.0	1
6123	B	9 Mar '92	3×400.0	3	6.0	
	R	9 Mar '92	2×300.0	3	4.9	
6277	B	4 Mar '92	601.1	1	1.1	1
	V	6 Mar '92	3×300.0	2	1.9	
	R	4 Mar '92	300.6	1	1.3	1

Table 2. -continued.

UGC	band	date	exp.time	Q	seeing	notes
	I	4 Mar '92	352.6	1	1.3	1
6445	B	5 Mar '92	601.1	1	1.5	1, 2
	V	5 Mar '92	300.6	1	1.3	1, 2
	R	30 May '87	1000.0	1	1.8	8
	I	30 May '87	1000.0	1	2.7	8
6453	B	3 Apr '91	4×600.0	1	1.8	4
	V	5 Apr '91	2×250.0	1	1.3	3
	R	5 Apr '91	2×250.0	4	1.3	
	I	3 Apr '91	2×500.0	1	1.3	
6460	B	9 Mar '92	3×400.0	1	3.0	4
	R	9 Mar '92	2×250.0	1	3.1	4
6536	B	8 Mar '92	2×400.0	2	1.3	4
	R	8 Mar '92	2×300.0	2	1.6	
6693	B	4 Mar '92	601.1	1	1.3	1
	V	6 Mar '92	2×250.0	1	1.8	3
	R	4 Mar '92	300.6	1	1.2	1
	I	4 Mar '92	352.6	1	1.4	1
6746	B	8 Mar '92	2×300.0	1	1.6	
	V	1 Mar '87	180.0	1	1.4	9
	R	1 Mar '87	45.0	1	1.4	9
6754	B	9 Mar '92	4×600.0	1	7.1	4
	R	9 Mar '92	4×300.0	1	7.1	4
7169	B	5 Mar '92	2×400.0	1	0.9	3
	V	5 Mar '92	2×250.0	1	0.8	3
	R	5 Mar '92	2×200.0	1	0.9	2
	I	5 Mar '92	2×200.0	4	0.8	
7315	B	4 Apr '91	601.1	1	1.0	1
	B	5 Mar '92	601.1	1	1.0	1
	V	5 Mar '92	300.6	1	1.0	1
	R	5 Mar '92	300.6	1	1.2	1
	I	4 Apr '91	500.0	1	2.3	
7450	B	2 May '92	600.0	1	2.2	2, 10
	V	2 May '92	300.0	1	2.1	2, 10
	R	2 May '92	300.0	1	2.1	2, 10
	I	2 May '92	300.0	1	2.1	2, 10
7523	B	4 Mar '92	601.1	1	1.6	1
	V	6 Mar '92	4×250.0	1	1.2	3, 4
	R	4 Mar '92	300.6	1	1.5	1
	I	4 Mar '92	300.6	1	1.3	1
7594	B	8 Mar '92	549.1	1	1.8	1
	R	8 Mar '92	289.0	1	1.8	1
7876	B	9 Apr '91	2×300.0	2	1.4	
	V	9 Apr '91	2×200.0	2	1.3	
	R	9 Apr '91	2×200.0	2	1.3	
	I	9 Apr '91	2×200.0	2	1.3	
7901	B	5 Mar '92	502.9	1	1.3	1
	V	8 Apr '91	398.8	1	1.6	1
	R	8 Apr '91	352.6	1	1.7	1
	I	4 Apr '91	502.9	1	2.1	1
8279	B	3 Apr '91	3×500.0	1	1.4	4
	V	5 Apr '91	2×250.0	2	1.6	
	R	5 Apr '91	2×250.0	2	1.6	
	I	3 Apr '91	2×500.0	1	1.1	4
8289	B	8 Apr '91	2×300.6	1	1.5	1
	R	8 Apr '91	300.6	1	1.6	1
	I	8 Apr '91	398.8	1	1.6	1
8865	B	8 Mar '92	601.1	1	1.9	1
	R	8 Mar '92	300.6	1	1.9	1
	I	8 Mar '92	300.6	1	1.7	1

Table 2. -continued.

UGC	band	date	exp.time	Q	seeing	notes
9024	B	30 Jan '92	1806.0	1	1.7	11
	R	9 Mar '92	2×600.0	2	1.8	
	I	30 Jan '92	900.0	1	1.7	11
9061	B	4 Mar '92	601.1	1	1.6	1
	V	5 Apr '91	502.9	2	1.3	1
	R	4 Mar '92	300.6	1	1.6	1
	I	6 Apr '91	3×300.0	1	1.5	2
9481	B	7 Apr '91	4×300.0	1	1.6	4
	R	7 Apr '91	4×200.0	1	1.5	4
	I	7 Apr '91	4×200.0	1	1.5	4
9915	B	9 Mar '92	4×600.0	3	1.8	4
	V	9 Apr '91	300.0	1	1.4	
	R	5 Apr '91	398.8	2	1.9	1
	I	9 Apr '91	352.6	1	1.4	1
9926	B	3 Apr '91	6×500.0	1	2.8	4
	V	9 Apr '91	300.6	1	1.5	1
	R	6 Apr '91	398.8	2	1.6	1
9943	B	5 Mar '92	601.1	1	1.4	1
	V	5 Mar '92	300.6	1	1.3	1
	R	5 Mar '92	300.6	1	1.4	1
	I	5 Mar '92	300.6	1	1.2	1
10083	B	7 Apr '91	2×300.0	1	1.4	
	V	7 Apr '91	2×200.0	1	1.5	
	R	7 Apr '91	2×200.0	1	1.6	
	I	8 Apr '91	2×300.0	1	1.3	
10437	B	14 Sep '91	2×500.0	1	1.6	
	V	14 Sep '91	2×400.0	1	1.4	
	R	14 Sep '91	300.0	1	1.5	
	I	14 Sep '91	2×400.0	1	1.5	
10445	B	13 Sep '91	809.2	1	1.5	1
	V	15 Sep '91	2×400.0	1	1.8	
	R	13 Sep '91	2×300.0	1	1.5	
	I	15 Sep '91	2×400.0	1	1.3	
	B	3 Apr '91	2×500.0	1	1.8	
	V	8 Apr '91	2×300.0	1	1.6	
	R	8 Apr '91	2×300.0	1	1.4	
10584	B	10 Sep '91	578.0	1	1.8	1
	V	10 Sep '91	404.6	1	1.8	1
	R	10 Sep '91	404.6	1	1.9	1
	I	10 Sep '91	404.6	1	1.7	1
11628	B	9 Sep '91	578.0	1	1.6	1
	V	10 Sep '91	404.6	1	1.6	1
	R	10 Sep '91	289.0	1	1.7	1
	I	8 Sep '91	289.0	1	1.8	1
11708	B	9 Sep '91	2×350.0	1	1.4	4
	V	9 Sep '91	2×250.0	1	1.5	
	R	9 Sep '91	2×250.0	1	1.3	
	I	9 Sep '91	2×250.0	1	1.3	
11872	B	7 Sep '91	578.0	1	1.3	1
	V	7 Sep '91	289.0	1	1.4	1
	R	7 Sep '91	289.0	1	1.4	1
	I	7 Sep '91	289.0	1	1.4	1
12151	B	16 Sep '91	600.0	1	2.7	
	V	16 Sep '91	2×400.0	1	2.8	
	R	16 Sep '91	2×400.0	1	2.8	
	I	16 Sep '91	2×400.0	1	2.4	
12343	B	14 Sep '91	578.0	1	1.8	1
	V	14 Sep '91	346.8	1	1.6	1
	R	14 Sep '91	289.0	1	1.6	1

Table 2. -continued.

UGC	band	date	exp.time	Q	seeing	notes
	I	14 Sep '91	289.0	1	1.6	1
12379	B	8 Sep '91	578.0	1	1.3	1
	V	8 Sep '91	404.6	1	1.4	1
	R	8 Sep '91	404.6	1	1.6	1
	I	8 Sep '91	289.0	1	1.4	1
12391	B	15 Sep '91	2×400.0	1	1.6	
	V	15 Sep '91	2×350.0	1	1.6	
	R	15 Sep '91	2×350.0	1	1.7	
	I	15 Sep '91	2×300.0	1	1.6	
12511	B	8 Sep '91	800.0	1	1.3	
	V	8 Sep '91	404.6	1	1.7	1
	R	8 Sep '91	300.0	1	1.3	
	I	8 Sep '91	404.6	1	1.4	1
12614	B	13 Sep '91	578.0	1	1.8	1
	V	13 Sep '91	346.8	1	1.7	1
	R	13 Sep '91	289.0	1	1.7	1
	I	13 Sep '91	289.0	1	1.7	1
12638	B	14 Sep '91	578.0	1	1.4	1
	V	14 Sep '91	346.8	1	1.5	1
	R	14 Sep '91	289.0	1	1.6	1
	I	14 Sep '91	289.0	1	1.4	1
12654	B	7 Sep '91	2×350.0	1	1.4	
	V	7 Sep '91	2×200.0	1	1.5	
	R	7 Sep '91	2×200.0	1	1.5	
	I	7 Sep '91	2×200.0	1	1.5	
12732	B	9 Sep '91	751.4	1	1.9	1
	V	9 Sep '91	578.0	1	1.8	1
	R	9 Sep '91	2×300.0	1	1.9	
	I	9 Sep '91	578.0	1	1.8	1
12754	B	15 Sep '91	578.0	1	1.6	1
	V	15 Sep '91	404.6	1	1.7	1
	R	15 Sep '91	289.0	1	1.6	1
	I	15 Sep '91	289.0	1	1.5	1
12776	B	10 Sep '91	693.6	1	1.9	1
	R	10 Sep '91	404.6	1	2.1	1
	I	10 Sep '91	404.6	1	1.8	1
12808	B	9 Sep '91	578.0	1	2.1	1
	V	9 Sep '91	404.6	1	1.6	1
	R	9 Sep '91	289.0	1	1.6	1
	I	9 Sep '91	404.6	1	1.5	1
12845	B	10 Sep '91	693.6	1	1.7	1
	V	10 Sep '91	462.4	1	1.6	1
	R	10 Sep '91	404.6	1	1.7	1
	I	10 Sep '91	2×300.0	1	1.4	

a linear ramp up from bias level to a normal 578× step time exposure, a constant exposure which can be longer than the normal chiplength(!) and a linear ramp down part. A crosscut of a few columns from top to bottom through such an image is shown in Fig. 2.

The driftscan method has several advantages and disadvantages. Advantages are:

– Only a one dimensional flatfield is needed. As the flux in one pixel in the final image is the result of the average

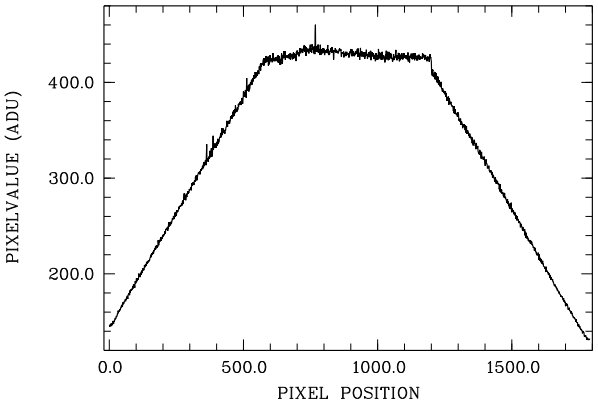

Fig. 2. The average intensity of 50 columns of a driftscan image. From row 1 to 577 the flux is still building up, rows 578 to 1200 have been exposed to the sky for the full chiplength (there is a hint of the outskirts of a galaxy), row 1201 to 1790 have been read out after the shutter was closed and the scantable was stopped. Notice the clear drop in bias level after scanning has stopped.

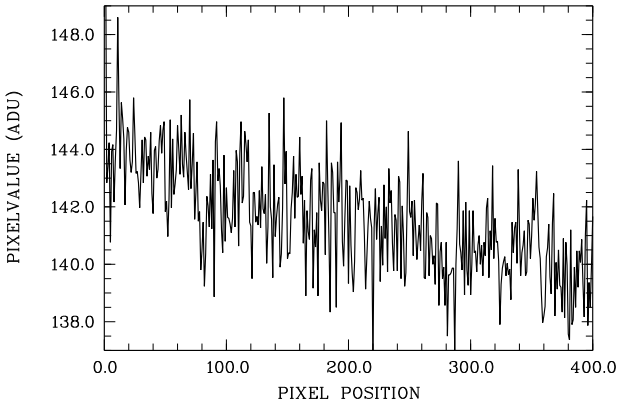

Fig. 3. The average intensity of the first ten rows of a driftscan image. Notice that the bias level is not a constant perpendicular to the scandirection.

quantum efficiency of all the detector elements in a column, local problems in flatfielding (low efficiency pixels, moving dust patches) are canceled out to a high degree.

– Larger field of view. We can continue scanning as far as the scantable and the telescope optics permit us. In case of the JKT the maximum scanlength is 650 arcsec, much more than the 114x173 arcsec FOV of the JKT in the direct imaging mode.

Disadvantages are:

– Photometric nights are needed. It is obvious that if the circumstances change during a scan, it is impossible to correct the image. In direct imaging one still can do relative photometry within one image.
– The data reduction requires more effort. In the standard data reduction packages no routines are available to reduce scan data, so one has to write one's own routines. It also turned out that the scan data had some unexpected side effects in bias level and flatfielding for which we had to correct. These will be described below.

During scanning the bias level was higher and not constant in the cross-scan direction. This was obvious by examining the first few rows of the ramp up part, which contain essentially no flux (see Fig. 3). After scanning stopped and the ramp down part was read out, the bias level was constant again in cross-scan direction and the bias level dropped as could be determined from the overscan region.

To determine the bias level accurately, the first half of the ramp up part was iteratively clipped and median filtered to remove star images. Next a first order polynomial was fitted column by column and the flux in the first row of the fit indicated the exact bias level of that column. We preferred this complicated method over simply using the first few rows, because these rows had low quantum efficiency. In addition this method introduced very little new noise and avoided problems with accidental stars in the first few rows.

Flatfielding was done column by column, using one dimensional flatfields (flatlines?), created by averaging the normal flatfields in column direction. The ramp up and down parts were corrected for the shorter exposure time, expanding the FOV even further. At this stage the quality of the bias subtraction could be checked, by comparing the flux of the scan region with the flux in the ramp down part, where a constant bias level was used, determined from the overscan region.

3.1.4 Archive reduction

The La Palma data archive was examined for galaxies that had not been observed in certain optical passbands during the JKT observing runs or for which we only obtained non-photometric data. Six galaxies were found in the archive to fill up the gaps in our sample. Data reduction was essentially the same as for the direct imaging. We used the overscan region for bias subtraction and the average of the available twilight frames as flatfield. McGaugh (1992) provided us calibrated B and I images of UGC 9024, which were also used to extract profiles. The telescope, CCD and pixelsize varied from observation to observation for the archive galaxies and are indicated in Table 2.

3.1.5 Calibration of the optical observations

In order to calibrate our images, we observed a number of fields with standard stars. The standard fields used were M 67 (Schild 1983), M 92 (Heasley & Christian 1986; Christian et al. 1985), NGC 4147, NGC 7006 and NGC 7790 (Odewahn et al. 1992; Christian et al. 1985). The calibration of all these fields can be traced back to Landolt (1983) stars, so in principle everything is calibrated to Johnson B and V and Kron-Cousins R and I. During each night at least five measurements of standard fields were made in a range of airmasses for each filter. With DAOphot (Stetson 1987) instrumental magnitudes of all standard stars on the frames were determined. All magnitudes of one observing run were combined and spurious values and data from (partly) non-photometric nights were eliminated. Next the data of the nights with the same characteristics were combined to fit zero-point magnitudes and color and extinction

coefficients of the form:

$$\begin{aligned} b &= B + c_{0,B} + c_{1,B}(B-V) + c_{2,B}X \\ v &= V + c_{0,V} + c_{1,V}(B-V) + c_{2,V}X \\ r &= R + c_{0,R} + c_{1,R}(V-R) + c_{2,R}X \\ i &= I + c_{0,I} + c_{1,I}(R-I) + c_{2,I}X \end{aligned}$$

where B, V, R and I are the standard magnitudes, b, v, r and i the instrumental magnitudes per second, X the airmass of the observation and $c_{i,J}$ the unknown transformation coefficients. The resulting parameters can be found in Table 3. The calibration of the September 1991 observing run was of lower quality because of the faint standard star fields used and the small scale flatfielding problems due to dust patches on the CCD window.

Table 3. Calibration coefficients determined for the different observing runs on the JKT telescope.

passband	zero-point (c_0)	color coef. (c_1)	airmass coef. (c_2)
	April 3-9, 1991		
B	-22.251 ± 0.065	-0.062 ± 0.011	0.251 ± 0.027
V	-22.791 ± 0.032	-0.013 ± 0.007	0.216 ± 0.030
R	-22.883 ± 0.030	-0.001 ± 0.010	0.179 ± 0.020
I	-22.060 ± 0.045	-0.012 ± 0.015	0.058 ± 0.058
	September 7-10, 1991		
B	-21.757 ± 0.111	-0.161 ± 0.044	0.238 ± 0.065
V	-22.215 ± 0.067	-0.048 ± 0.024	0.135 ± 0.025
R	-22.438 ± 0.073	-0.016 ± 0.046	0.141 ± 0.020
I	-21.709 ± 0.081	-0.034 ± 0.057	0.081 ± 0.082
	September 13-16, 1991		
B	-21.977 ± 0.122	-0.161 ± 0.044	0.279 ± 0.052
V	-22.322 ± 0.072	-0.048 ± 0.024	0.121 ± 0.030
R	-22.558 ± 0.064	-0.016 ± 0.046	0.126 ± 0.026
I	-21.833 ± 0.068	-0.034 ± 0.057	0.023 ± 0.027
	March 4-9, 1992		
B	-22.157 ± 0.041	-0.067 ± 0.013	0.294 ± 0.011
V	-22.697 ± 0.019	-0.033 ± 0.005	0.198 ± 0.005
R	-22.768 ± 0.036	-0.002 ± 0.018	0.170 ± 0.010
I	-22.063 ± 0.038	-0.008 ± 0.027	0.118 ± 0.012

Galaxy observations taken under non-photometric conditions were calibrated by using photometric observations of other nights if available. This was of course only done if the flatfield quality of the non-photometric image allowed us to go to fainter magnitudes than the photometric image. Aperture photometry from Longo and de Vaucouleurs (1983) provided another means to calibrate non-photometric observations. We first determined our magnitude of a galaxy within a synthetic aperture of the size of the literature photometry, using the calibration from Table 3. This magnitude was compared with the Longo and de Vaucouleurs value. If the offset between our observation and the literature value was greater than 1.5 times the expected error, all magnitude parameters were corrected with this zero-point offset.

To calibrate the archive observations we used synthetic aperture photometry on Landolt (1983) stars observed on the same night. The standard airmass extinction curve for La Palma was used but no color coefficient was calculated. At least three observations of standard stars had to agree to within the expected errors to make sure that the night was photometric (there were no observation logs for the archive observations available).

Another point of calibration was the determination of pixelsize and the position angle (PA) orientation of the chip. The standard star field of M67 proved to be well suited for this. A least squares fit was made for pixel positions of 7 stars against the sky positions as found in the Guide Star Catalog (Russell et al. 1990). The average measured pixelsize was $0.303'' \pm 0.004''$, not depending on filter, observing run or CCD, but with a hint of dependence on North-South versus East-West pixelsize. As the measured pixelsize was equal within the errors to the instrumental specification we have used the $0.3''$ pixelsize throughout this study.

With the same fit of standard star positions the North-South alignment of the CCD could be tested. The PA was never exactly NS, the discrepancies varying between 0.9 and 1.75 degrees depending on the observation run and the NS or EW orientation of the CCD within one observing run. The PAs measured for the galaxies were corrected for this effect.

3.1.6 Last reduction steps

All images were cleaned from cosmic ray hits by an automatic routine. The routine looked for pixels above the expected noise and checked if they had a point spread function smaller than the estimated seeing. Faulty pixels were replaced by the median value of the surrounding area. The selection limits were taken conservatively, in order to avoid removal of real structure. Remaining cosmics were removed by hand using a polygon editor.

When necessary, images were mosaiced together using common stars in the frames to determine the spatial offsets. The overlapping area was used to determine the offset in skylevel. If there were more than two frames of one object, all combinations of frames were used to determine spatial and intensity offsets. A least squares fit was made through these values to obtain the best match. All frames were put in one image using the mean value in the overlapping areas.

If after flatfielding some large scale residual of more than 1% was left in the sky background, this was subtracted by fitting a 1^{st} order polynomial to the area free of objects. This correction was necessary on about 30% of the images, mostly on images taken with some moonlight.

Finally the skylevel in the images was determined using the box method. On several places free of objects around the galaxy the mean value of the sky was determined in a small rectangular area. The skylevel was determined as the average of these mean values. For the estimated error in the sky we used half the difference between the minimum and the maximum of these mean values.

3.2 Creating calibrated near-IR images

3.2.1 The near-IR observations

The near-IR observations were obtained in two observing runs of three nights with the IRCAM2 camera on the UKIRT telescope on Hawaii. An InSb Santa Barbara array of 58x62 pixels was used, with pixel size 1.2″. During the Sep. '91 run we used the standard Johnson H filter and a K' filter (Wainscoat & Cowie 1992) equipped with an extra red leak blocking filter. For the run of Feb. '92 we used the standard Johnson H and K filters. All 86 galaxies were observed in either K or K' (except UGC 12808) and 39 galaxies were also observed through a H filter. The K passband observations of UGC 2125 and UGC 2595 were of such a poor quality that they could not be used.

The FOV with IRCAM2 was only about one arcmin square, so we decided to mosaic the selected galaxies along the major axis. Depending on size we imaged about 3-7 positions along the major axis with 10-15″ overlap for offset determinations. In general first two images, each on one side of the nucleus, were taken. Next to these two images were first on the one side, then on the other side, two slightly shifted positions near the outside of the galaxy observed. Using this technique we have spent twice as much time on the low surface brightness regions of the galaxy compared to the bright center.

As the sky in the near-IR is fluctuating very much and is about 10^4 times brighter than the faint outskirts of the galaxies we wanted to measure, it is evident that we had to observe it regularly to obtain good flatfielding and skysubtraction. A sky frame, taken with a few arcminutes offset from the object, was made after each second object exposure, beginning and ending each observation of a galaxy with a sky exposure. So the complete observing cycle was SOOSOOSOOS.

Because of the many sky photons the full well capacity of the near-IR array is reached quickly. Therefore one makes several short exposures at the same position, which are averaged on line at the telescope. In general we used 2x30 s per position for K', 6x15 s for K and 2x25 s for H exposures. Every two hours dark exposures were taken with the same integration time as the object exposures.

The full observation log can be found in Table 4.

3.2.2 Near-IR reduction

As flux levels at a level 10^4 times lower than the sky had to be determined, great care went into flatfielding and mosaicing. As a first step all frames (sky and object) were dark subtracted by the average of the two dark frames taken nearest in time. The sky frames observed around a galaxy (normally 4 or 5) were combined to make a flatfield. The sky frames were first normalized to one and then the median for each pixel position was taken to make a flatfield. In this way we eliminated hot pixels and stars from the flatfield. If rapid changes in skylevel had occurred during the observation, this flatfielding showed no satisfactory result. In such a case sky frames taken immediately before and after the object exposure were combined to be used as a flatfield. In the resulting flatfielded images hot and dead pixels were put to undefined by a bad pixel mask and spurious

Table 4. The observation log of the near-IR observations. All observations were performed on UKIRT equipped with IRCAM2. Pixelsize was 1.2″ and exp.time indicates the number of positions and the exposure time per position in seconds. Q denotes the photometric quality, estimated errors are 1: photometric, 2: 0.0-0.2 mag, 3: 0.2-0.5 mag, 4: 0.5-1.0 mag and 5: >1.0 mag. The FWHM seeing estimate is in arcseconds.
Notes: (2) Internal calibration (3) Calibrated using Gezari et al. (1990).

UGC	band	date	exp.time	Q	seeing	notes
89	H	30 Sep '91	5×60	1	1.5	
	K'	29 Sep '91	5×90	1	1.4	
93	K'	28 Sep '91	8×60	1	1.7	
242	K'	28 Sep '91	8×60	1	1.8	
334	K'	29 Sep '91	8×60	1	1.6	
438	K'	28 Sep '91	5×60	1	2.3	
463	K'	28 Sep '91	4×60	1	1.8	
490	K	Aug '92	5×120	1	1.7	
508	K'	28 Sep '91	6×120	1	1.7	
628	H	30 Sep '91	7×90	1	1.4	
	K'	30 Sep '91	7×90	1	1.7	
1305	K'	29 Sep '91	6×120	1	1.3	
1455	K'	29 Sep '91	5×120	1	1.7	
1551	K'	29 Sep '91	5×120	1	1.6	
1559	K'	28 Sep '91	8×60	1	2.3	
1577	K'	29 Sep '91	5×120	1	1.8	
1719	K'	28 Sep '91	11×60	1	1.8	
1792	K'	28 Sep '91	10×60	1	1.6	
2064	K'	30 Sep '91	10×60	1	2.0	
2081	K'	30 Sep '91	5×60	1	2.0	
2124	K'	30 Sep '91	5×60	1	1.6	
2197	K'	30 Sep '91	5×90	1	1.6	
2368	H	22 Feb '92	6×50	1	1.6	
	K	22 Feb '92	12×90	1	1.7	
2595	H	22 Feb '92	6×50	1	1.8	
3066	H	22 Feb '92	6×50	1	1.6	
	K	20 Feb '92	6×90	1	1.7	
3080	H	21 Feb '92	6×50	1	1.7	
	K	21 Feb '92	6×90	1	1.8	
3140	H	22 Feb '92	6×50	1	2.0	
	K	21 Feb '92	8×90	1	2.0	
4126	H	22 Feb '92	6×50	1	1.7	
	K	22 Feb '92	6×90	1	1.6	
4256	H	22 Feb '92	6×50	1	1.6	
	K	21 Feb '92	6×90	1	1.8	
4308	H	22 Feb '92	6×50	1	2.0	
	K	20 Feb '92	6×90	1	1.8	
4368	K	21 Feb '92	6×90	1	1.6	
4375	H	21 Feb '92	6×50	1	1.7	
	K	20 Feb '92	6×90	1	1.8	
4422	H	22 Feb '92	6×50	1	2.1	
	K	20 Feb '92	6×90	1	2.1	
4458	H	20 Feb '92	6×50	1	1.4	
	K	20 Feb '92	6×90	1	1.7	
5103	H	22 Feb '92	6×50	1	1.2	
	K	22 Feb '92	6×90	1	1.6	
5303	H	20 Feb '92	6×50	1	1.7	
	K	20 Feb '92	6×90	1	1.8	
5510	K	20 Feb '92	6×90	1	1.7	
5554	H	21 Feb '92	6×50	1	2.0	

Table 4. -continued.

UGC	band	date	exp.time	Q	seeing	notes
	K	21 Feb '92	6×90	1	1.8	
5633	H	21 Feb '92	6×50	1	1.8	
	K	21 Feb '92	4×90	1	1.8	
5842	H	22 Feb '92	6×50	1	1.4	
	K	20 Feb '92	6×90	1	1.7	
6028	H	22 Feb '92	6×50	1	1.7	
	K	21 Feb '92	8×90	1	1.8	
6077	K	20 Feb '92	6×90	1	1.6	
6123	H	22 Feb '92	6×50	1	2.4	
	K	20 Feb '92	6×90	1	2.1	
6277	H	22 Feb '92	6×50	1	1.3	
	K	20 Feb '92	6×90	1	1.4	
6445	K	21 Feb '92	6×90	1	1.7	
6453	K	21 Feb '92	6×90	1	1.6	
6460	K	21 Feb '92	6×90	1	2.1	
6536	K	21 Feb '92	6×90	1	1.8	
6693	K	21 Feb '92	6×90	1	2.0	
6746	H	21 Feb '92	6×50	1	2.0	
	K	21 Feb '92	6×90	1	2.0	
6754	K	22 Feb '92	6×90	1	1.8	
7169	K	22 Feb '92	6×90	1	1.7	
7315	K	22 Feb '92	6×90	1	1.4	
7450	K	22 Feb '92	14×90	1	1.8	
7523	K	22 Feb '92	6×90	1	1.6	
7594	K	22 Feb '92	8×90	1	2.0	
7876	K	22 Feb '92	6×90	1	2.0	
7901	H	22 Feb '92	6×50	1	1.6	
	K	22 Feb '92	6×90	1	1.8	
8279	K	22 Feb '92	6×90	1	2.0	
8289	H	22 Feb '92	6×50	1	1.7	
	K	22 Feb '92	6×90	1	1.7	
8865	H	20 Feb '92	6×50	1	2.3	
	K	20 Feb '92	6×90	1	2.0	
9024	H	21 Feb '92	4×50	1	1.6	
	K	21 Feb '92	4×90	1	1.5	
9061	K	20 Feb '92	8×90	1	1.7	
9481	H	22 Feb '92	6×50	1	2.0	
	K	20 Feb '92	6×90	1	1.6	
9915	H	21 Feb '92	6×50	1	1.7	
	K	21 Feb '92	6×90	1	1.7	
9926	K	20 Feb '92	6×90	1	1.8	
9943	H	20 Feb '92	6×50	1	1.8	
	K	20 Feb '92	6×90	1	1.8	
10083	H	22 Feb '92	6×50	1	1.6	
	K	22 Feb '92	6×90	1	1.6	
10437	K'	30 Sep '91	7×75	2	1.6	
10445	K'	30 Sep '91	4×50	1	1.7	2
	H	21 Feb '92	6×50	1	1.7	
	K	21 Feb '92	6×90	1	1.6	
10584	K'	28 Sep '91	5×100	1	1.7	
11628	H	30 Sep '91	5×50	4	1.8	
	K'	28 Sep '91	5×125	1	2.0	
11708	H	30 Sep '91	4×75	3	1.8	
	K'	30 Sep '91	4×75	2	2.3	
11872	H	30 Sep '91	5×50	2	1.7	
	K'	28 Sep '91	5×100	1	1.7	
12151	K'	28 Sep '91	5×150	1	2.0	
12343	H	30 Sep '91	6×50	1	1.8	3
	K'	30 Sep '91	6×75	1	1.7	3

Table 4. -continued.

UGC	band	date	exp.time	Q	seeing	notes
12379	K'	28 Sep '91	5×125	1	1.6	
12391	K'	29 Sep '91	8×60	1	1.7	
12511	K'	28 Sep '91	5×125	1	1.7	
12614	K'	29 Sep '91	5×90	1	2.0	
12638	K'	28 Sep '91	8×75	1	1.6	
12654	K'	28 Sep '91	8×75	1	1.6	
12732	H	30 Sep '91	5×50	2	1.7	
	K'	30 Sep '91	5×100	2	1.6	
12754	H	30 Sep '91	6×60	2	1.7	
	K'	30 Sep '91	6×90	2	1.6	
12776	K'	28 Sep '91	6×125	1	1.6	
12808	H	30 Sep '91	5×60	1	1.4	3
12845	H	30 Sep '91	4×60	2	1.4	
	K'	30 Sep '91	5×90	2	1.7	

values by hand. These undefined pixels were not used in the rest of the calculations. The large scale flatfielding was in general better than 1 in 10^5.

To determine the spatial offset between the different object exposures we used a 2D correlation technique. This technique "scans" the images for corresponding structure like foreground stars, H II regions and spiral arms. From the object frames a median filtered version was subtracted to remove the large scale structure. The partly overlapping areas were 2D cross correlated, resulting in an image with a peak on the position where the two frames have similar structure. To this peak a Gaussian was fitted to determine spatial offsets in X and Y. Tests on artificial images showed the high accuracy that can be reached by this method. If necessary, signal to noise could be improved by indicating with a cursor the region in the images with the most structure. Telescope offsets were only used when the images did not contain enough structure to use the 2D correlation. Offsets were determined for all combinations of overlapping frames. A least squares fit was made through all relative offset values to obtain the best match.

In the next step the calculated spatial offsets were used to determine the offset in skylevel in the overlapping area. Again all combinations of frames were used to determine the intensity offsets and a least squares fit was also made through these values to obtain the best match. All frames were combined into one image using the calculated spatial and intensity offsets, while in the overlapping areas the mean values were used.

3.2.3 Calibrating the near-IR observations

We used the list of standard stars of Elias et al. (1982) to calibrate our near-IR observations. The corrections supplied by Wainscoat and Cowie (1992) were used to transform the K' measurements to the K passband. Each standard star was measured on four different positions on the array. This measurement was repeated at least five times each night. The photometric observations of one run were combined to determine zero-point offsets and airmass coefficients. The resulting parameters can be found in Table 5. During the September run,

Table 5. Calibration coefficients determined for the different observing runs on the UKIRT telescope.

color	zero point (c_0)	airmass coefficient (c_2)
September 28-30, 1991		
H	-20.500±0.200	—
K'	-20.018±0.040	0.087±0.032
February 20-22, 1992		
H	-20.704±0.032	0.147±0.048
K	-20.497±0.032	0.119±0.047

the H filter was only used during a partly non-photometric night, which explains the large error.

While making the mosaics it was already found that the calculated offsets were much better fitted by assuming a pixel-size of 1.2″ instead of the 1.24″ quoted in the instrumental documentation. As we had no frames with several stars on it with accurately known positions, we used the scaling factor needed to align the near-IR images with the optical images (see next paragraph) to estimate the pixelsize. Using the calibrated optical pixelsize we found that the actual pixelsize of the IRCAM2 was 1.203″± 0.009″ and decided to use a value of 1.2″ throughout this study.

3.3 Profile extraction

Now that we have reduced and calibrated the near-IR and optical images, they can be treated in the same way to extract the profiles. The images taken through the different filters were aligned using foreground stars common in the frames. We avoided using the center of the galaxy, as the morphology might be different in the different passbands because of dust obscuration. On the frame with the highest signal to noise level (usually the R passband frame), we masked out pixels contaminated by foreground star light, using a polygon editor. This mask was transferred to the images of the other passbands, thus making sure that further analysis was done on exactly the same area for the different passbands. For several larger galaxies the optical profiles were determined twice, once with the full image and once using only the overlapping area with the narrower near-IR images. The first profiles will be used to get the best values for global properties, while the profiles extracted from the reduced images are better suited to determine colors and color profiles.

The center of the galaxy was determined using ellipse fitting to the highest peak of the galaxy in the R passband frame. This center was used as center for the ellipses that were fitted at the 23.5, 24.0 and 24.5 R-magnitude. The median values for the fitted minor/major axis ratios (b/a) and position angles (PA) were used in the next routine, where average flux values were determined on elliptical rings with the above found center, b/a and PA, but with varying major axis radius. We preferred the method of fixed b/a and PA for each radius above fitting this for each radius, because this enable us to compare the profiles measured in the different passbands. The resulting luminosity profiles are presented in Fig. 12 and are available in FITS table format or Postscript format upon request. As several

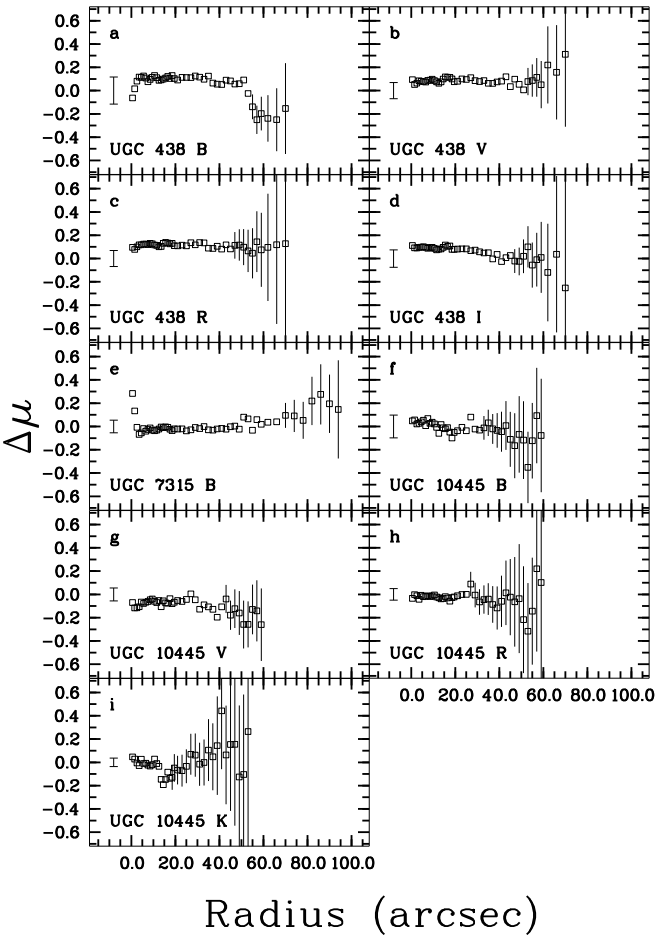

Fig. 4. The difference between two surface brightness profiles as function of radius for galaxies observed on two different nights with independent determinations of the calibration coefficients. The errorbar in front of the profiles indicates the 1σ-error in the zero point, the error bars on the profile indicate the maximum error due to a wrong determination of the skylevel. **(a-d)** UGC 438 14/15 Sept.'91 minus 9 Sept.'91, **(e)** UGC 7316 4 Apr.'91 minus 5 Mar.'92, **(f-h)** UGC 10445 13/15 Sept.'91 minus 3/8 Apr.'91, **(i)** UGC 10445 30 Sept.'91 minus 21 Feb.'92.

profiles are dropping rather rapidly at large radii, one could get the impression that sky subtraction was wrong in these cases. This is in fact an artifact resulting from scanning only the major axis of the large galaxies. After passing a spiralarm the surface brightness drops rapidly and fades in the sky. Next to the surface brightness profiles presented in Fig. 12 we show the grayscale/contour representation of the galaxies. This enables the reader to trace back certain features in the profiles from the original images. The values of the b/a ratios and the PAs can be found in Table 6. These values are hard to determine for our low inclination systems, therefore we estimate the error in PA about 5° for the more inclined galaxies increasing to 20° for the almost face-on galaxies.

Some galaxies were observed more than once through the same filter on different nights to provide internal consistency checks. The difference profiles in Fig. 4 show that the internal consistency is well within the estimated zero-point and sky errors. The fact that UGC 438 was observed once in NS and once in EW direction doesn't show up in the difference profiles.

Table 6. The PA and the major over minor axis ratio (b/a), as determined on the R frames, used to calculate the radial luminosity profiles and total extrapolated apparent magnitude, calculated from the luminosity profiles. Indicated errors were calculated using the maximum error estimate of the skylevel. Errors in the zero-point were not included.

UGC	PA ($^\circ$)	b/a	m$_B$ (B-mag)	m$_V$ (V-mag)	m$_R$ (R-mag)	m$_I$ (I-mag)	m$_H$ (H-mag)	m$_K$ (K-mag)
89	168.8	0.67	12.63 ± 0.06	11.85 ± 0.08	11.36 ± 0.06	10.88 ± 0.07	9.23 ± 0.07	8.85 ± 0.05
93	64.8	0.64	14.26 ± 0.13	13.58 ± 0.17	12.89 ± 0.30	12.42 ± 0.29	—	11.04 ± 0.30
242	114.5	0.77	13.92 ± 0.06	13.12 ± 0.06	12.59 ± 0.09	12.03 ± 0.11	—	10.30 ± 0.19
334	53.8	0.76	15.24 ± 0.20	14.28 ± 0.17	14.11 ± 0.20	13.88 ± 0.49	—	12.07 ± 0.95
438	47.7	0.78	12.95 ± 0.04	12.20 ± 0.04	11.65 ± 0.06	11.01 ± 0.06	—	9.10 ± 0.05
463	69.0	0.83	13.35 ± 0.02	—	—	11.53 ± 0.01	—	9.62 ± 0.04
490	99.7	0.71	13.48 ± 0.09	12.60 ± 0.06	12.05 ± 0.04	11.44 ± 0.06	—	9.46 ± 0.15
508	165.8	0.88	12.69 ± 0.05	11.71 ± 0.03	11.13 ± 0.03	10.55 ± 0.04	—	8.49 ± 0.04
628	128.3	0.63	15.58 ± 0.13	14.96 ± 0.16	14.47 ± 0.19	13.83 ± 0.36	12.81 ± 0.64	12.52 ± 0.47
1305	95.4	0.81	12.75 ± 0.10	11.76 ± 0.03	11.16 ± 0.04	10.38 ± 0.13	—	8.65 ± 0.05
1455	125.6	0.94	13.36 ± 0.15	12.47 ± 0.07	11.96 ± 0.04	11.30 ± 0.12	—	9.46 ± 0.07
1551	100.9	0.89	13.70 ± 0.12	12.99 ± 0.09	12.52 ± 0.10	12.03 ± 0.22	—	10.31 ± 0.21
1559	100.7	0.87	14.25 ± 0.14	13.61 ± 0.12	13.29 ± 0.08	12.54 ± 0.45	—	11.73 ± 0.68
1577	68.2	0.79	13.79 ± 0.20	12.82 ± 0.05	12.18 ± 0.06	11.75 ± 0.09	—	9.90 ± 0.13
1719	154.1	0.73	14.08 ± 0.15	13.20 ± 0.14	12.58 ± 0.08	12.05 ± 0.14	—	10.09 ± 0.13
1792	178.9	0.59	14.10 ± 0.04	13.17 ± 0.05	12.75 ± 0.04	12.27 ± 0.08	—	10.15 ± 0.14
2064	167.2	0.70	14.20 ± 0.09	13.22 ± 0.11	12.70 ± 0.10	11.98 ± 0.18	—	10.18 ± 0.09
2081	73.6	0.60	14.50 ± 0.20	13.96 ± 0.11	13.63 ± 0.23	12.81 ± 0.29	—	11.55 ± 0.48
2124	8.2	0.88	13.47 ± 0.07	12.47 ± 0.04	11.61 ± 0.09	10.93 ± 0.14	—	9.33 ± 0.11
2125	148.4	0.96	14.23 ± 0.09	13.28 ± 0.10	12.71 ± 0.10	12.28 ± 0.21	—	—
2197	161.7	0.62	14.76 ± 0.10	13.90 ± 0.11	13.43 ± 0.13	12.81 ± 0.15	—	11.00 ± 0.25
2368	163.1	0.92	13.89 ± 0.04	13.09 ± 0.02	12.53 ± 0.02	11.92 ± 0.06	9.96 ± 0.08	9.77 ± 0.10
2595	67.2	0.78	—	13.05 ± 0.09	12.48 ± 0.06	11.78 ± 0.11	9.87 ± 0.12	—
3066	111.3	0.73	14.60 ± 0.06	13.71 ± 0.05	13.07 ± 0.06	12.37 ± 0.07	10.36 ± 0.12	10.06 ± 0.28
3080	149.1	0.91	14.05 ± 0.17	13.33 ± 0.09	12.76 ± 0.08	12.17 ± 0.15	10.51 ± 0.12	10.46 ± 0.21
3140	117.3	0.94	13.34 ± 0.04	—	—	11.57 ± 0.04	9.77 ± 0.05	9.51 ± 0.05
4126	106.3	0.85	13.25 ± 0.09	12.58 ± 0.08	12.01 ± 0.06	11.35 ± 0.09	9.83 ± 0.09	9.63 ± 0.07
4256	11.8	0.86	13.26 ± 0.04	12.73 ± 0.04	—	—	9.86 ± 0.06	9.36 ± 0.07
4308	129.8	0.77	13.17 ± 0.07	12.54 ± 0.04	12.07 ± 0.05	11.41 ± 0.08	10.05 ± 0.04	9.83 ± 0.10
4368	140.2	0.80	13.57 ± 0.09	12.98 ± 0.09	12.46 ± 0.08	11.77 ± 0.07	—	10.21 ± 0.11
4375	175.8	0.66	13.28 ± 0.09	—	12.06 ± 0.04	—	9.67 ± 0.08	9.53 ± 0.07
4422	56.8	0.82	12.85 ± 0.17	12.35 ± 0.13	11.55 ± 0.13	11.01 ± 0.24	9.29 ± 0.07	8.83 ± 0.13
4458	96.2	0.87	13.04 ± 0.06	12.17 ± 0.05	11.61 ± 0.12	11.02 ± 0.05	9.28 ± 0.14	9.01 ± 0.10
5103	14.7	0.61	12.77 ± 0.04	—	11.89 ± 0.03	—	9.35 ± 0.05	9.22 ± 0.03
5303	91.2	0.59	12.24 ± 0.02	11.57 ± 0.05	11.02 ± 0.05	10.50 ± 0.02	8.91 ± 0.05	8.67 ± 0.07
5510	48.1	0.81	12.36 ± 0.04	—	11.41 ± 0.02	10.94 ± 0.02	—	9.24 ± 0.04
5554	129.3	0.69	12.88 ± 0.07	—	11.59 ± 0.03	11.01 ± 0.10	9.25 ± 0.12	9.10 ± 0.04
5633	177.0	0.63	14.24 ± 0.49	13.60 ± 0.41	13.11 ± 0.27	—	11.04 ± 0.37	11.28 ± 0.30
5842	110.8	0.85	12.48 ± 0.03	—	11.47 ± 0.04	10.95 ± 0.04	9.32 ± 0.05	9.19 ± 0.03
6028	73.1	0.58	13.14 ± 0.08	12.73 ± 0.06	12.30 ± 0.04	11.88 ± 0.04	10.60 ± 0.11	10.19 ± 0.19
6077	90.9	0.82	12.84 ± 0.07	12.24 ± 0.05	11.67 ± 0.03	11.14 ± 0.05	—	9.43 ± 0.01
6123	90.0	0.93	—	—	—	—	8.59 ± 0.04	8.42 ± 0.05
6277	139.2	0.88	11.77 ± 0.07	—	10.74 ± 0.07	10.08 ± 0.11	8.70 ± 0.42	8.35 ± 0.57
6445	103.6	0.84	12.58 ± 0.05	11.93 ± 0.04	11.36 ± 0.02	10.66 ± 0.04	—	9.08 ± 0.07
6453	110.5	0.75	12.45 ± 0.06	11.55 ± 0.34	—	10.88 ± 0.04	—	9.18 ± 0.05
6460	13.1	0.75	11.87 ± 0.03	—	10.83 ± 0.02	—	—	8.62 ± 0.04
6536	22.6	0.62	—	—	—	—	—	9.90 ± 0.11
6693	106.8	0.85	13.47 ± 0.09	12.78 ± 0.17	12.39 ± 0.06	11.71 ± 0.08	—	10.09 ± 0.06
6746	21.9	0.76	13.35 ± 0.16	12.54 ± 0.04	11.86 ± 0.04	—	9.71 ± 0.04	9.39 ± 0.06
6754	180.5	0.89	13.42 ± 0.14	—	12.09 ± 0.09	—	—	9.59 ± 0.15
7169	131.8	0.81	12.72 ± 0.06	12.20 ± 0.06	11.62 ± 0.05	—	—	9.63 ± 0.04
7315	104.3	0.67	12.55 ± 0.09	11.84 ± 0.04	11.17 ± 0.04	10.50 ± 0.05	—	8.62 ± 0.02
7450	153.0	0.89	10.17 ± 0.10	9.56 ± 0.08	9.01 ± 0.10	8.56 ± 0.11	—	6.47 ± 0.23
7523	97.7	0.81	11.80 ± 0.05	11.09 ± 0.08	10.54 ± 0.03	9.85 ± 0.06	—	8.08 ± 0.06
7594	171.4	0.69	10.54 ± 0.18	—	9.23 ± 0.09	—	—	6.91 ± 0.08
7876	166.0	0.73	—	—	—	—	—	10.30 ± 0.07

Table 6. -continued.

UGC	PA (°)	b/a	m$_B$ (B-mag)	m$_V$ (V-mag)	m$_R$ (R-mag)	m$_I$ (I-mag)	m$_H$ (H-mag)	m$_K$ (K-mag)
7901	73.9	0.67	11.46 ± 0.05	10.82 ± 0.02	10.27 ± 0.02	9.67 ± 0.02	8.05 ± 0.03	7.90 ± 0.03
8279	61.8	0.77	13.07 ± 0.08	—	—	11.37 ± 0.05	—	9.74 ± 0.07
8289	60.8	0.89	12.33 ± 0.07	—	11.38 ± 0.05	10.82 ± 0.12	9.40 ± 0.05	9.19 ± 0.03
8865	3.8	0.76	12.62 ± 0.08	—	11.37 ± 0.07	10.90 ± 0.08	9.10 ± 0.19	8.98 ± 0.09
9024	164.8	0.90	14.90 ± 0.22	—	—	13.74 ± 0.06	12.31 ± 0.61	12.29 ± 0.93
9061	118.9	0.91	12.04 ± 0.14	—	10.92 ± 0.07	10.09 ± 0.27	—	7.95 ± 0.26
9481	42.5	0.74	13.31 ± 0.07	—	12.23 ± 0.12	11.74 ± 0.15	10.13 ± 0.13	10.00 ± 0.07
9915	89.8	0.90	—	12.25 ± 0.06	—	11.07 ± 0.04	9.48 ± 0.09	9.33 ± 0.04
9926	96.1	0.71	12.17 ± 0.12	11.51 ± 0.02	—	—	—	8.45 ± 0.02
9943	86.3	0.64	12.30 ± 0.08	11.61 ± 0.04	11.06 ± 0.03	10.46 ± 0.04	8.90 ± 0.02	8.67 ± 0.02
10083	167.9	0.82	12.37 ± 0.33	11.92 ± 0.17	11.38 ± 0.14	10.97 ± 0.12	9.17 ± 0.09	9.19 ± 0.06
10437	34.8	0.92	14.37 ± 0.36	14.08 ± 0.19	13.53 ± 0.58	12.97 ± 0.37	—	—
10445	133.0	0.77	13.10 ± 0.40	12.95 ± 0.18	12.61 ± 0.40	11.90 ± 0.24	10.92 ± 0.17	10.81 ± 0.36
10584	103.3	0.88	13.10 ± 0.17	12.49 ± 0.09	12.08 ± 0.10	11.34 ± 0.18	—	10.05 ± 0.10
11628	73.3	0.70	12.82 ± 0.10	11.77 ± 0.05	11.25 ± 0.05	10.86 ± 0.09	—	8.54 ± 0.11
11708	105.6	0.81	13.41 ± 0.17	12.68 ± 0.22	11.99 ± 0.31	11.39 ± 0.46	—	—
11872	80.6	0.74	12.03 ± 0.04	11.13 ± 0.02	10.58 ± 0.01	9.87 ± 0.03	—	8.11 ± 0.02
12151	0.0	0.87	14.43 ± 0.69	13.83 ± 0.52	13.75 ± 0.55	12.99 ± 0.48	—	11.32 ± 0.60
12343	40.5	0.77	11.87 ± 0.03	10.85 ± 0.03	10.35 ± 0.03	9.80 ± 0.06	8.14 ± 0.04	7.807 ± 0.04
12379	69.7	0.91	13.56 ± 0.20	12.69 ± 0.09	11.92 ± 0.04	11.26 ± 0.07	—	9.41 ± 0.09
12391	4.7	0.89	13.80 ± 0.10	13.12 ± 0.10	12.51 ± 0.13	11.93 ± 0.18	—	10.25 ± 0.22
12511	71.0	0.82	13.81 ± 0.08	13.06 ± 0.17	12.31 ± 0.36	11.65 ± 0.34	—	10.58 ± 0.16
12614	14.5	0.73	12.64 ± 0.02	11.88 ± 0.03	11.39 ± 0.03	10.86 ± 0.05	—	9.12 ± 0.04
12638	172.2	0.81	13.95 ± 0.11	13.13 ± 0.10	12.61 ± 0.08	12.05 ± 0.13	—	9.99 ± 0.18
12654	171.4	0.82	13.65 ± 0.07	12.85 ± 0.06	12.43 ± 0.05	11.88 ± 0.06	—	10.28 ± 0.20
12732	12.5	0.89	14.73 ± 0.80	13.17 ± 0.57	12.12 ± 1.41	12.52 ± 0.65	—	—
12754	170.8	0.70	11.87 ± 0.08	11.29 ± 0.06	10.78 ± 0.10	10.42 ± 0.14	—	—
12776	94.6	0.88	13.17 ± 0.07	—	11.94 ± 0.11	11.41 ± 0.15	—	9.44 ± 0.20
12808	140.7	0.93	12.52 ± 0.09	11.79 ± 0.07	11.17 ± 0.06	10.60 ± 0.10	9.18 ± 0.06	—
12845	59.0	0.81	14.12 ± 0.10	13.18 ± 0.06	12.68 ± 0.05	12.30 ± 0.23	—	—

In this case the scanning of only a part of the galaxy has clearly not a great effect on the shape of the profile.

3.4 Integrated magnitudes

The integrated magnitudes of the galaxies were calculated from the radial profiles, given that we only imaged the part of the galaxies along the major axis in many cases. The total magnitude was calculated by summing the average flux determined on the elliptical rings multiplied with the area of the rings. The radial profile was extended to "infinity" by fitting a linear function to the last 6 points deemed reliable in the radial profile. The errors were estimated using the maximum error estimate of the skylevel subtraction, errors in the zero-point were not included. Resulting total magnitudes can be found in Table 6.

3.5 Comparison with other measurements

Comparing luminosity profiles of different authors is not straightforward as different techniques are employed to extract the profile from the images. The older surface photometry using photographic plates has in general profiles extracted in a similar way as ours, using averages on elliptical rings with a fixed ellipticity and PA. Interpolating the surface brightness data to the radii where we measured our brightnesses was sufficient to make the comparison. Later CCD photometry has profiles determined by fitting ellipses to the isophotes. In order to compare this data with ours, we extracted the profiles again, using ellipticities and PAs given by the authors. The first five panels in Fig. 5 show the difference between our and the other photographic plate measurement. The other panels show the same for the CCD comparisons with remeasured profiles with shifting ellipticities and PAs. If we had not observed a galaxy in the same passband, we used for the comparison the nearest passband available.

It is immediately clear that the comparison with the older photographic photometry is not very good, especially the zero-points show some large discrepancies. The bright inner regions of galaxies were most likely overexposed on the photographic plates, which explains the drop in the difference profiles in the inner few arcsec. For the comparisons with the CCD photometry it can be readily seen that our measurements had in general a better seeing, as the observed differences also become more negative in the inner few arcseconds. UGC 6754 is the clear exception, which we measured with a seeing of about $7''$. The photometric zero-points of our photometry agree very well with the measurements of Han (1992b). The differences $\Delta\mu$ are in general less than 0.1 mag, except for UGC 4368, where his I passband image was out of focus.

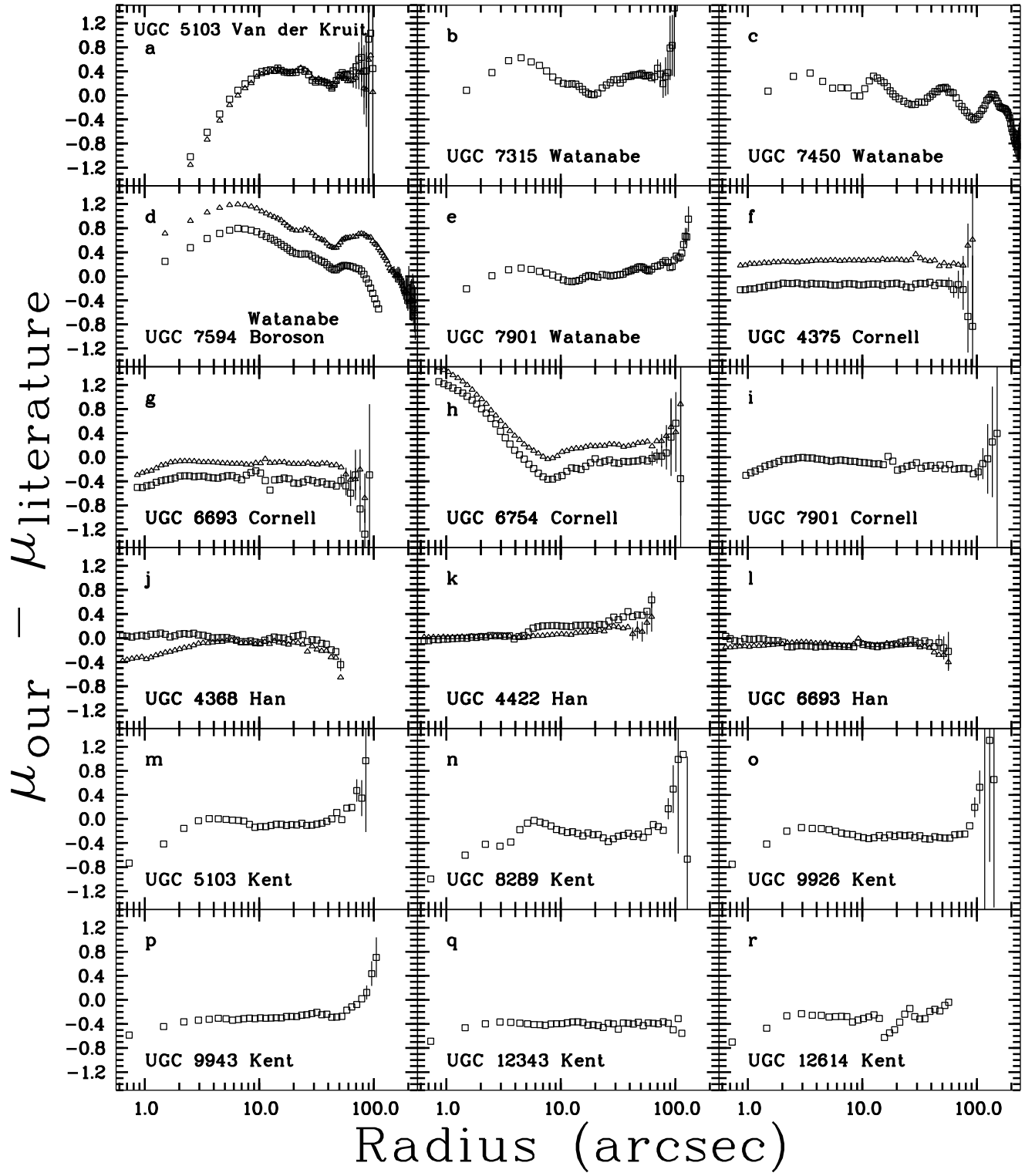

Fig. 5. The difference between our derived surface brightness profiles and literature profiles. The errorbars indicate the maximum errors in our profiles due to errors in sky subtraction. **(a)** $B_{our} - J$ Van der Kruit (1987), **(b,c,e)** $V_{our} - V$ Watanabe (1983), **(d)** $\triangle$ $B_{our} - V$ Watanabe (1983), $\square$ $R_{our} - I$ Boroson (1983), **(f-i)** $\square$ $B_{our} - B$, $\triangle$ $R_{our} - R$ Cornell (1987, private communication), **(j-l)** $\square$ $V_{our} - V$, $\triangle$ $I_{our} - I$ Han (1992b, private communication), **(m-r)** $R_{our} - r$ Kent (1984)

The shapes of the profiles of Cornell et al. (1987) agree well with ours, but the zero-points are off. They calibrated their observations with the aperture photometry of Bothun et al. (1985), so we compared this photometry with ours using synthetic apertures. Using 7 galaxies in common in our samples, we find that the mean difference and rms error between our photometry and theirs is –0.005 ± 0.188 B-mag, –0.005 ± 0.081 V-mag and 0.204 ± 0.067 R-mag. We excluded their UGC 6693 measurement, which clearly deviates from our and Han's measurement. The discrepancy in the R passband is surprising, especially because the rms error is the lowest for R. It is unclear whether Bothun et al. used Johnson or Cousins R. They refer for their calibration to Landolt (1973), but this contains only UBV standards and no R.

Kent (1984) reduced his photometry to the photometric system of Thuan and Gunn (1976) and states that his r passband measurement of UGC 12343 is non-photometric, while our R passband measurement of UGC 9926 is non-photometric. We find a mean difference of –0.3 mag with a r.m.s. of 0.05 mag. This is a little bit less than the ~ -0.344 mag expected from the transformation formulas given by Bell and VandenBerg (1987) for transforming Gunn r to Cousins R. A bit worrying are the systematic lower sky values found by Kent (showing up as an upturn at large radii in the difference profiles). We used mean values in boxes around the galaxy to determine sky intensities, while Kent used median intensities, which might explain the difference. Even though median values might give a better estimate for the true sky brightness (the effect of very small cosmic ray events and stars is reduced), one uses the *means* on ellipses to determine the luminosity profiles. So the luminosity profiles will also contain the effect of small cosmic ray events and stars and these should be subtracted from the profile as well. Of the galaxies in common between Kent and us there is only one other measurement in the literature, which is of UGC 5103 by van der Kruit (1987). His measurements from deep photographic plates seem to agree better with our profile at large radii than with Kent's profile. There seems to be no systematic trend in sky level difference with the measurements of the other authors.

We compared our integrated magnitudes with the values in the RC3 (de Vaucouleurs et al. 1991) as depicted in Figs 6a and b. The weighted mean difference between our value and the RC3 value for B_T is 0.046 B-mag with an rms error of 0.255, for $(B-V)_T$ we find a difference of 0.023 ± 0.178 mag. The zero-point differences are within the expected errors, but the high rms error values are somewhat disturbing. The B_T and the $(B-V)_T$ in the RC3 are for a large fraction derived from extrapolated photoelectric aperture photometry of all kinds of sources, which might explain the high rms.

Figure 6c shows the difference between our and Grosbøl's (1985) measurements for the integrated R magnitude. He determined his magnitude within the 23.5 R-magnitude isophote, using scanned POSS plates. One zero-point was used, even though many different plates were used, and Grosbøl estimated an internal uncertainty of 0.3 magnitudes. We find that the weighted mean difference between our and his measurement is –0.041 R-mag with an rms of 0.493, more than the 0.3 magnitudes error estimated by Grosbøl. It is clear that the high rms error results from a few outlying points. Remember also that our magnitudes are extrapolated magnitudes, while Grosbøl measured his magnitudes within the 23.5 R-mag arcsec^{-2} isophote.

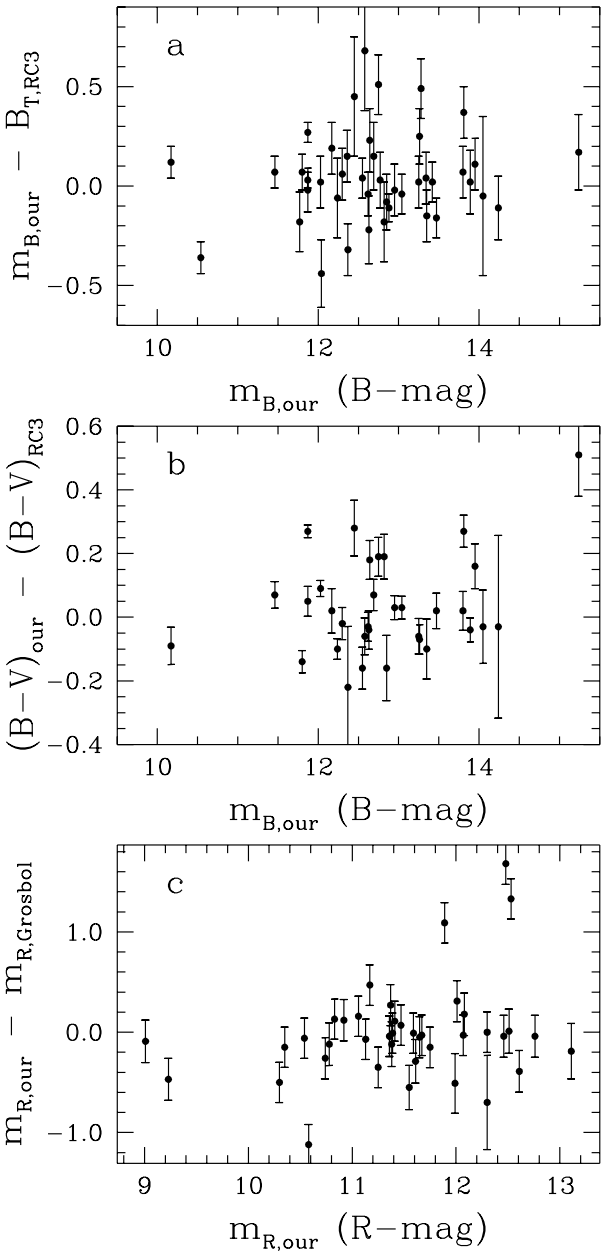

Fig. 6. Differences between our extrapolated integrated magnitudes and the literature values, as function of integrated magnitude. **(a)** Our m_B values minus B_T of the RC3, **(b)** our $(B–V)$ minus $(B–V)_T$ of the RC3 and **(c)** our m_R minus Grosbøl's m_R (1985)

There are no near-IR profiles in the literature yet, so we could only check the zero-points, using the aperture photometry collected by De Vaucouleurs and Longo (1988) and by Gezari et al. (1993). We excluded measurements with apertures equal or smaller than 5″, as these were probably influenced by seeing. Using 29 measurements we find a mean difference between our synthetic aperture values and the literature values of –0.011 H-mag with an rms of 0.073. The 33 measurements

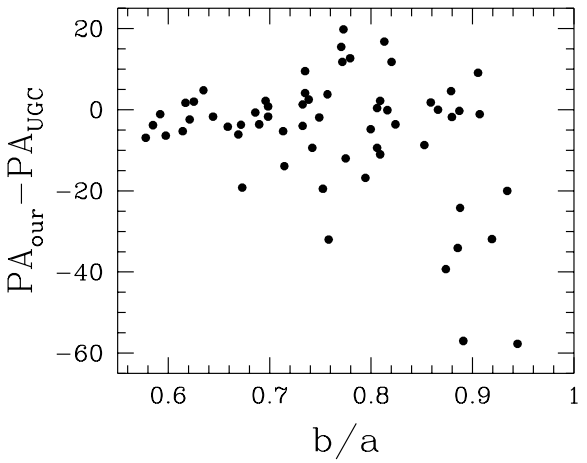

Fig. 7. The difference between the PAs as determined by us at approximately the 23.5 R-mag arcsec^{-2} isophote and the UGC PAs as function of axis ratio.

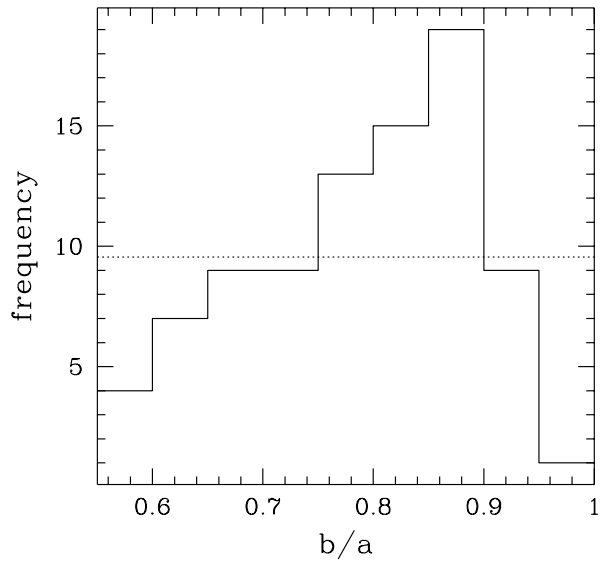

Fig. 8. The distribution of the minor over major axis ratios (b/a) as determined by us from the R passband images at approximately the 23.5 R-mag arcsec^{-2} isophote. The dotted line indicates the normal frequency for randomly orientated disks.

in the K passband have a mean difference of 0.007 K-mag with an rms of 0.093 K-mag. The zero-points agree quite well, the high rms values can again be ascribed to the many different sources of the literature values. Many different techniques were used to produce them.

One final comparison we made was between our and the UGC PAs, which is shown in fig. 7. The determination of the PA gets of course more difficult when getting closer to face-on, but in general our PAs agree within the expected errors with the UGC values.

4 Discussion

To get an impression of the quality of the data reduction we performed some statistical tests. First of all we checked if our

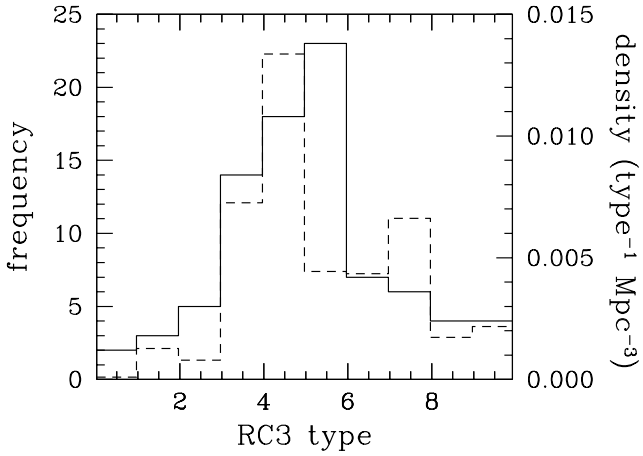

Fig. 9. The distribution of morphological (RC3) types, before (full drawn) and after (dashed) V_{max} volume correction as described in the text.

PAs were uniformly distributed. Using a Kolmogorov-Smirnov test this was found to be indeed the case as the chance of erroneously rejecting this hypothesis was more than 10%. The distribution of the b/a ratios are not randomly distributed, as can be seen in Fig. 8. Some galaxies are below the 0.625 b/a selection limit, as could be expected, but more significant is the lack of galaxies in the 0.95-1.0 bin, which moved to the 0.75-0.9 bins. This just means that galaxies are not circular in the outer regions, a conclusion earlier drawn by several other authors (Binney & de Vaucouleurs 1981; Grosbøl 1985; Huizinga & van Albada 1992).

Figure 9 shows the distribution of types before and after volume correction (using Eq.(5), distances were calculated using the V_{GSR} of Table 1 and $H_0 = 100$ km s^{-1} Mpc^{-1}). The volume correction was done taking the 0.625 inclination limit and the 12.5% sky coverage into account. The volume correction did not change the distribution of types significantly. The same volume correction can be used to create a luminosity function (Fig. 10). Our luminosity function is slightly lower than the one of Kirshner et al. (1983), but ours does not include ellipticals and irregulars. It's clear that our treatment of volume correction results in a luminosity function which is consistent with the one of Kirshner et al. .

The surface brightnesses at the blue and red UGC diameters as well as the isophotal diameters at 25 B-mag arcsec^{-2} and 23.5 R-mag arcsec^{-2} were determined from the radial surface brightness profiles. They were determined by linearly interpolating between the two nearest points in radius or in surface brightness respectively. The measured values can be found in Table 7. Following Paturel et al. (1991) we plot the UGC diameter versus our isophotal diameters in a log-log plot (Fig. 11). It is clear that the UGC diameters of the latest type galaxies were estimated differently from the other types. The reason for this difference is hard to trace. These late-type galaxies have a lower overall surface brightness, so maybe Nilson tried harder to find the faintest structures belonging to the galaxies when making the UGC. And even though their overall surface brightness is very low, they have a flocculent

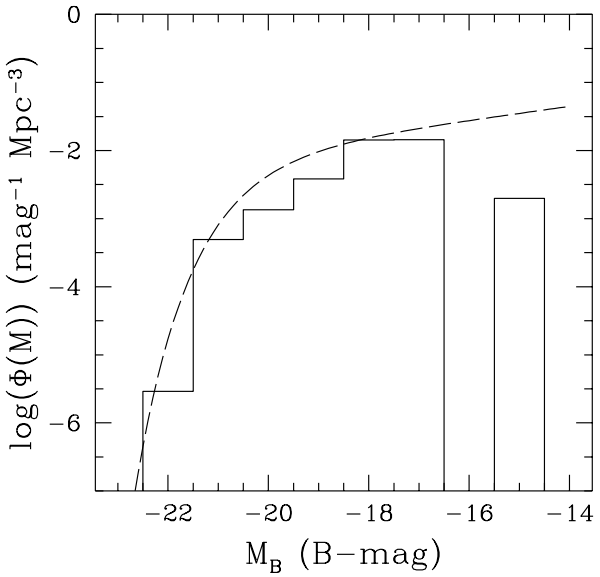

Fig. 10. The luminosity function for our sample using the $V_{\rm max}$ correction. The dashed line is a Schechter luminosity function as determined by Kirshner et al. (1983), using the correction to the B passband by Felten (1985).

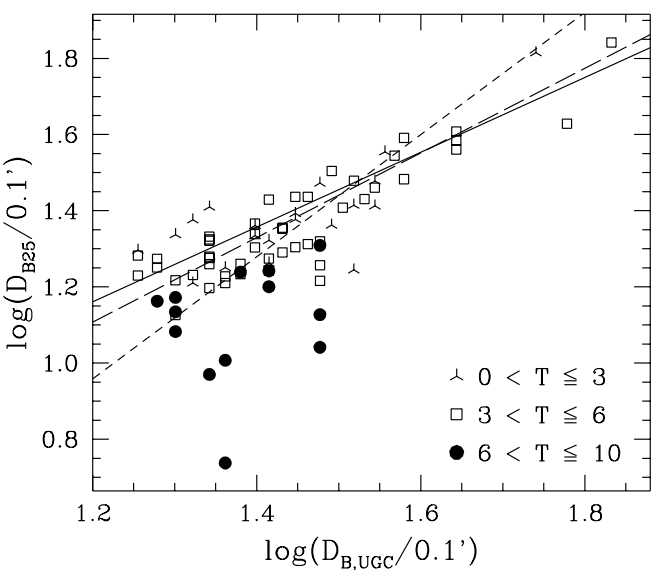

Fig. 11. The blue UGC diameter versus our isophotal diameter at 25 B-mag arcsec^{-2}, the symbols indicate different RC3 types. The short dashed line indicates the double regression least squares fit for all points, the long dashed line for all points with RC3 type T<6 and the full drawn line for all points with RC3 type T<6 and $\log(D_{B25}) > 1.27$.

appearance with a few H II regions in their outer parts, which can be seen to larger radii.

Like Paturel et al. (1991) we have tried to establish a relation between UGC and isophotal diameters. Using a double regression least squares fit, assuming equal errors in UGC and our diameters, we find for the B passband:

$$\begin{aligned} \log(D_{B25}) &= 1.603\log(D_{B,\rm UGC}) - 0.965 \\ n &= 81 \qquad\qquad \sigma = 0.131 \end{aligned}$$

When using only morphological RC3 types earlier than 6 we have:

$$\begin{aligned} \log(D_{B25}) &= 1.110\log(D_{B,\rm UGC}) - 0.224 \\ n &= 61 \qquad\qquad \sigma = 0.072 \end{aligned}$$

If we, like Paturel et al., in addition take the selection effects into account by using a cutoff of the form $\log(D_{B25}) > 1.27$ we find:

$$\begin{aligned} \log(D_{B25}) &= 0.981\log(D_{B,\rm UGC}) - 0.017 \\ n &= 45 \qquad\qquad \sigma = 0.057 \end{aligned}$$

These lines are also indicated in Fig. 11. The same fits can be determined for the R passband which result in:

$$\begin{aligned} \log(D_{R23.5}) &= 1.589\log(D_{R,\rm UGC}) - 0.969 \\ n &= 75 \qquad\qquad \sigma = 0.109 \end{aligned}$$

using only RC3 types earlier than 6:

$$\begin{aligned} \log(D_{R23.5}) &= 1.130\log(D_{R,\rm UGC}) - 0.279 \\ n &= 56 \qquad\qquad \sigma = 0.053 \end{aligned}$$

and in addition $\log(D_{R23.5}) > 1.24$:

$$\begin{aligned} \log(D_{R23.5}) &= 1.055\log(D_{R,\rm UGC}) - 0.016 \\ n &= 44 \qquad\qquad \sigma = 0.050 \end{aligned}$$

It is only allowed to use the $V_{\rm max}$ correction if the slope of the fit is close to one, otherwise one has a selection effect as function of angular diameter. Within the errors this is at least true for the early-type galaxies. For the late-type galaxies we have too short a range in diameters and too large a scatter to be able to tell whether this influences our statistics.

We conclude from our tests that we have obtained accurate surface brightness profiles for a large number of spiral galaxies. These observations of this statistically complete sample have many purposes. Especially the near-IR surface photometry is the first of its kind. The distribution of scalelengths and central surface brightnesses, as well as the colors and radial color profiles of these galaxies will be discussed in the forthcoming papers of this series.

Acknowledgements. The authors would like to thank Stacy McGaugh for providing his B and I image of UGC 9024 and Mark Cornell and Mingsheng Han for providing their radial surface brightness profiles. We thank Arpad Szomoru, René Oudmaijer and Leslie Hunt for useful comments on the manuscript. Andrew Pickles brought our attention to the driftscan technique. Special thanks to Paul Wesselius, without whom this work would not have been possible. The research of RSJ was supported under grant no. 782-373-044 from the Netherlands Foundation for Research in Astronomy (ASTRON), which receives its funds from the Netherlands Foundation for Scientific Research (NWO). The luminosity profiles presented in this paper are available in FITS format at the CDSARC anonymous ftp facility (cdsarc.u-strasbg.fr), maintained by the Centre de Donnees Astronomiques, Strasbourg, France.

Table 7. The surface brightnesses measured at the blue and red UGC diameters and the isophotal major axis diameters at 25 B-mag arcsec^{-2} and 23.5 R-mag arcsec^{-2}. Non-photometric measurements were not used and some profiles did not extend far enough to provide reliable measurements and are also not quoted. The errors were determined by using the estimate of the maximum error in the sky subtraction. Errors in the zero-point were not included.

UGC	$\mu_{D_{B\,\mathrm{UGC}}}$ B-mag arcsec^{-2}	$\mu_{D_{R\,\mathrm{UGC}}}$ R-mag arcsec^{-2}	D_{B25} ($''$)	$D_{R23.5}$ ($''$)
89	24.65 ± 0.07	23.69 ± 0.10	154.2 ± 6.6	121.0 ± 3.4
93	27.83 ± 1.19	24.15 ± 0.44	104.8 ± 3.6	90.4 ± 9.8
242	26.55 ± 0.75	24.92 ± 0.41	89.2 ± 3.2	83.4 ± 1.0
334	27.21 ± 1.36	25.92 ± 1.37	72.6 ± 6.4	44.4 ± 6.0
438	25.60 ± 0.27	24.52 ± 0.68	118.4 ± 2.8	110.2 ± 4.2
463	25.45 ± 0.06	—	101.8 ± 0.6	—
490	26.02 ± 0.41	24.34 ± 0.15	120.8 ± 6.2	112.2 ± 1.4
508	26.52 ± 0.48	26.15 ± 1.70	155.2 ± 2.4	152.6 ± 1.6
628	29.24 ± 1.99	25.93 ± 0.78	61.0 ± 2.8	51.0 ± 5.4
1305	26.55 ± 1.23	24.58 ± 0.19	182.4 ± 7.0	181.2 ± 2.0
1455	26.42 ± 0.78	25.45 ± 0.38	125.2 ± 3.4	116.4 ± 3.2
1551	27.30 ± 6.51	26.00 ± 1.62	122.2 ± 5.2	107.2 ± 5.0
1559	25.82 ± 0.41	25.25 ± 0.33	87.2 ± 3.8	72.8 ± 1.8
1577	25.69 ± 0.82	24.65 ± 0.36	102.8 ± 8.4	102.4 ± 4.8
1719	26.21 ± 0.51	24.55 ± 0.19	106.8 ± 6.0	99.6 ± 1.2
1792	28.70 ± 1.21	25.45 ± 0.49	104.8 ± 2.4	96.6 ± 1.4
2064	26.22 ± 0.29	24.29 ± 0.21	97.4 ± 1.0	97.4 ± 2.2
2081	—	26.29 ± 1.04	98.6 ± 3.4	72.4 ± 2.8
2124	26.42 ± 0.69	24.64 ± 0.24	105.4 ± 2.6	121.6 ± 2.4
2125	26.88 ± 0.65	25.15 ± 0.65	101.4 ± 1.2	98.0 ± 3.6
2197	26.37 ± 0.30	25.42 ± 0.72	80.2 ± 2.0	69.2 ± 1.4
2368	26.46 ± 0.28	25.30 ± 0.14	97.4 ± 2.0	86.6 ± 0.4
2595	—	25.62 ± 0.74	—	101.0 ± 1.8
3066	26.76 ± 0.39	26.35 ± 1.11	81.8 ± 4.0	78.2 ± 1.6
3080	26.94 ± 0.85	25.84 ± 1.12	94.4 ± 2.8	88.6 ± 2.4
3140	25.96 ± 0.24	—	102.2 ± 3.8	—
4126	25.93 ± 0.33	24.90 ± 0.27	129.6 ± 3.0	117.4 ± 3.0
4256	26.24 ± 0.65	—	109.2 ± 2.0	—
4308	25.21 ± 0.25	24.21 ± 0.18	126.8 ± 4.4	114.2 ± 1.8
4368	26.62 ± 0.90	25.17 ± 0.42	112.8 ± 5.0	95.8 ± 2.0
4375	26.01 ± 0.63	24.24 ± 0.13	136.0 ± 4.8	122.2 ± 2.0
4422	26.36 ± 2.96	24.48 ± 0.62	153.4 ± 6.0	145.2 ± 3.8
4458	25.63 ± 0.15	23.81 ± 0.17	109.8 ± 1.8	108.6 ± 3.8
5103	25.53 ± 0.28	24.49 ± 0.15	137.8 ± 3.2	119.6 ± 1.0
5303	25.42 ± 0.12	24.31 ± 0.21	210.2 ± 2.0	204.6 ± 3.2
5510	26.75 ± 0.92	25.41 ± 0.25	161.8 ± 2.6	143.2 ± 0.8
5554	24.79 ± 0.09	24.75 ± 0.15	130.4 ± 5.0	119.4 ± 1.4
5633	26.20 ± 1.02	24.69 ± 0.45	95.2 ± 11.4	80.4 ± 4.8
5842	24.74 ± 0.08	25.07 ± 0.43	161.2 ± 1.8	149.0 ± 1.8
6028	26.19 ± 0.82	24.90 ± 0.24	143.0 ± 5.2	98.0 ± 1.8
6077	25.82 ± 0.49	24.28 ± 0.11	126.0 ± 4.8	117.2 ± 1.4
6123	—	—	—	—
6277	25.48 ± 0.24	23.94 ± 0.15	243.4 ± 16.2	168.4 ± 6.8
6445	25.82 ± 0.35	24.16 ± 0.06	135.2 ± 5.2	118.4 ± 1.0
6453	26.43 ± 0.70	—	173.4 ± 6.0	—
6460	24.84 ± 0.12	23.46 ± 0.05	191.6 ± 2.8	181.0 ± 1.2
6536	—	—	—	—
6693	25.69 ± 0.31	24.64 ± 0.20	114.2 ± 3.0	102.6 ± 1.2
6746	24.84 ± 0.24	23.88 ± 0.04	117.6 ± 4.8	111.2 ± 0.8
6754	26.66 ± 0.99	25.70 ± 0.80	138.2 ± 6.2	119.8 ± 3.6
7169	25.30 ± 0.40	24.61 ± 0.45	125.6 ± 4.4	109.6 ± 4.8
7315	25.09 ± 0.21	23.65 ± 0.11	129.0 ± 5.4	126.0 ± 3.2
7450	24.91 ± 0.16	23.74 ± 0.17	417.0 ± 14.8	385.8 ± 8.8
7523	25.03 ± 0.16	24.34 ± 0.18	215.2 ± 4.6	198.8 ± 3.0
7594	24.40 ± 0.15	23.60 ± 0.18	392.0 ± 14.8	377.8 ± 10.2
7876	—	—	—	—
7901	24.79 ± 0.20	24.23 ± 0.13	234.0 ± 5.8	210.2 ± 2.8
8279	25.04 ± 0.21	—	112.6 ± 2.0	—
8289	26.20 ± 0.61	25.60 ± 0.84	180.8 ± 2.8	146.0 ± 3.2
8865	26.07 ± 0.48	25.02 ± 0.59	180.4 ± 7.0	166.6 ± 4.4
9024	26.75 ± 0.14	—	32.8 ± 0.4	—
9061	—	24.32 ± 0.15	255.0 ± 7.4	202.2 ± 7.6
9481	26.74 ± 0.92	24.38 ± 0.33	121.0 ± 4.2	105.4 ± 2.6
9915	—	—	—	—
9926	25.07 ± 0.62	—	163.8 ± 9.6	—
9943	25.35 ± 0.64	24.07 ± 0.17	163.8 ± 6.2	157.0 ± 2.4
10083	24.77 ± 0.22	23.70 ± 0.11	142.6 ± 8.8	113.4 ± 2.0
10437	27.04 ± 0.86	25.70 ± 1.02	56.0 ± 4.0	41.0 ± 4.4
10445	26.03 ± 0.87	24.96 ± 0.21	123.2 ± 19.2	89.6 ± 1.0
10584	26.07 ± 1.07	24.45 ± 0.31	130.8 ± 6.4	108.8 ± 4.0
11628	25.10 ± 0.28	23.97 ± 0.22	178.0 ± 4.4	171.2 ± 1.8
11708	24.84 ± 0.23	23.75 ± 0.63	115.0 ± 9.8	114.4 ± 20.2
11872	25.92 ± 0.37	23.99 ± 0.08	155.8 ± 3.0	147.4 ± 1.2
12151	26.95 ± 1.41	24.03 ± 0.51	80.4 ± 16.6	53.0 ± 11.4
12343	—	23.54 ± 0.10	218.0 ± 4.4	227.0 ± 8.0
12379	26.36 ± 0.94	24.25 ± 0.12	108.4 ± 10.8	112.8 ± 1.6
12391	26.27 ± 1.15	24.85 ± 1.03	99.0 ± 3.2	93.4 ± 4.8
12511	26.01 ± 0.19	24.13 ± 0.57	117.2 ± 3.4	109.0 ± 26.6
12614	25.11 ± 0.09	24.39 ± 0.20	139.4 ± 1.8	134.2 ± 2.2
12638	25.47 ± 0.37	24.49 ± 0.34	107.0 ± 3.6	102.6 ± 3.0
12654	26.86 ± 1.84	24.24 ± 0.16	109.4 ± 2.0	104.4 ± 1.4
12732	25.20 ± 1.09	—	66.0 ± 17.6	102.0 ± 49.4
12754	25.54 ± 0.60	24.84 ± 1.36	230.8 ± 8.2	218.8 ± 7.4
12776	25.54 ± 0.21	24.61 ± 0.47	148.2 ± 2.4	135.8 ± 4.6
12808	24.77 ± 0.10	23.92 ± 0.10	118.8 ± 5.2	108.2 ± 2.8
12845	26.50 ± 0.46	24.83 ± 0.13	104.0 ± 1.8	99.8 ± 1.2

References

Bell R.A., VandenBerg D.A. 1987, ApJS 63, 335

Binney J., de Vaucouleurs G. 1981, MNRAS 194, 679

Boroson T.A., Strom K.M., Strom S.E. 1983, ApJ 274, 39

Bothun G.D., Aaronson M., Schommer B., Mould J., et al. 1985, ApJ 57, 423

Christian C.A., Adams M., Barnes J.V., Butcher H., Hayes D.S., Mould J.R., Siegel M. 1985, PASP 97, 363

Cornell M., E., Aaronson M., Bothun G., Mould J. 1987, ApJS 64, 507

Davies J.I. 1990, MNRAS 244, 8

de Vaucouleurs A., Longo G. 1988, Catalogue of Visual and Infrared Photometry of Galaxies from 0.5 μ m to 10 μ m (1961-1985). Univ. of Texas Press, Austin

de Vaucouleurs G. 1959, Hdb. d. Physik 53, 311

de Vaucouleurs G., de Vaucouleurs A., Corwin H.G. 1976, Second Reference Catalog of Bright Galaxies (Univ. of Texas Press, Austin) (RC2)

de Vaucouleurs G., de Vaucouleurs A., Corwin H.G., Buta R.J. et al. 1991, Third Reference Catalog of Bright Galaxies (Springer-Verlag, New York) (RC3)

Disney M.J., Phillipps S. 1983, MNRAS 205, 1253

Elias J.H., Frogel J.A., Matthews K., Neugebauer G. 1982, AJ 87, 1029

Felten J.E. 1985, Comments on Astrophysics 11 No.2, 53

Freeman K.C. 1970, ApJ 160, 811

Gezari D.Y., Schmitz M., Pitts P.S., Mead J.M. 1993, Catalog of Infrared Observations, Third edition, NASA Reference Publication, p. 1294

Grosbøl P.J. 1985, A&AS 60, 261

Han M. 1992a ApJ 391, 617

Han M. 1992b ApJS 81, 35

Heasley J.N., Christian C.A. 1986, ApJ 307, 738

Huizinga J.E. 1994, Ph.D. Thesis, University of Groningen, The Netherlands

Huizinga J.E., van Albada T.S. 1992, MNRAS 254, 677

Jura M. 1980, ApJ 238, 499

Kent S.M. 1984, ApJS 56, 105

Kirshner R.P., Oemler Jr., A., Schechter P.L., Shectman S.A. 1983, AJ 88, 1285

Knapen J.H., van der Kruit P.C. 1991, A&A 248, 57

Knapen J.H., Hes R., Beckman J.E., Peletier R.F. 1991, A&A 241, 42

Landolt A.U. 1973, AJ 78, 959

Landolt A.U. 1983, AJ 88, 439

Longo G., de Vaucouleurs A. 1983, A general catalog of photoelectric magnitudes and colors in the UBV system of 3,578 galaxies brighter than the 16^{th} V-magnitude (Univ. of Texas, Austin)
McGaugh S.S. 1992, Ph.D. Thesis, University of Michigan, USA
Nilson P. 1973, Uppsala General Catalog of Galaxies (Roy. Soc. Sci., Uppsala) (UGC)
Odewahn S.C., Bryja C., Humphreys R.M. 1992, PASP 104, 553
Paturel G., Fouqué P., Buta R., Garcia A.M. 1991, A&A 243, 319
Phillipps S., Evans Rh., Davies J.I., Disney M.J. 1991, MNRAS 253, 496
Rieke G.H., Lebofsky M.J. 1985, ApJ 288, 618
RGO/La Palma Technical Notes No.37, 1987, Isaac Newton Group, La Palma
Russell J.L., Lasker B.M., McLean B.J., Sturch C.R., Jenkner H. 1990, AJ 99, 2059
Schild R.E. 1983, PASP 95, 1021
Schmidt M. 1968, ApJ 151 393
Stetson P.B. 1987, PASP 99, 191
Thuan T.X., Gunn J.E. 1976, PASP 88, 543
Thuan T.X., Seitzer P.O. 1979, ApJ 231, 680
Valentijn E.A. 1990, Nat 346, 153
van der Kruit P.C. 1987, A&A 173, 59
van der Kruit P.C. 1989, The distribution of properties of galaxies. In: Gilmore G., King I., van der Kruit P.C., The Milky Way as a Galaxy (Geneva Observatory, Sauverny-Versoix, Switzerland), p.263
Wainscoat R.J., Cowie L.L. 1992, AJ 103 332
Watanabe M. 1983, Ann. Tokyo Astrom. Obs. 2nd Series 19, 121

UGC 89, contours at 19.0, 24.0, 0.5 R-mag arcsec^{-2}.

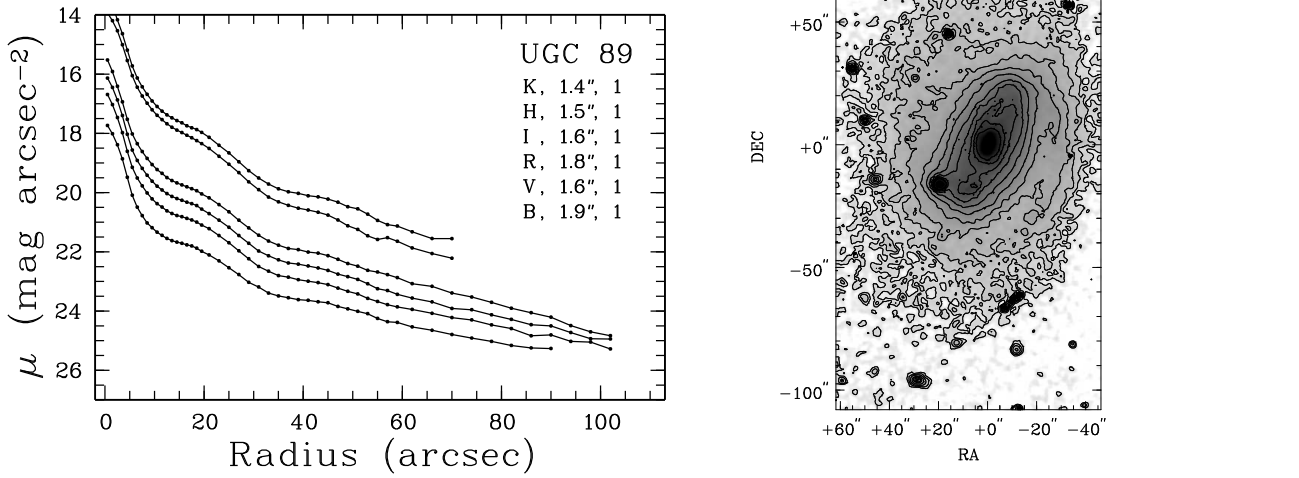

UGC 93, contours at 21.0, 24.0, 0.5 R-mag arcsec^{-2}.

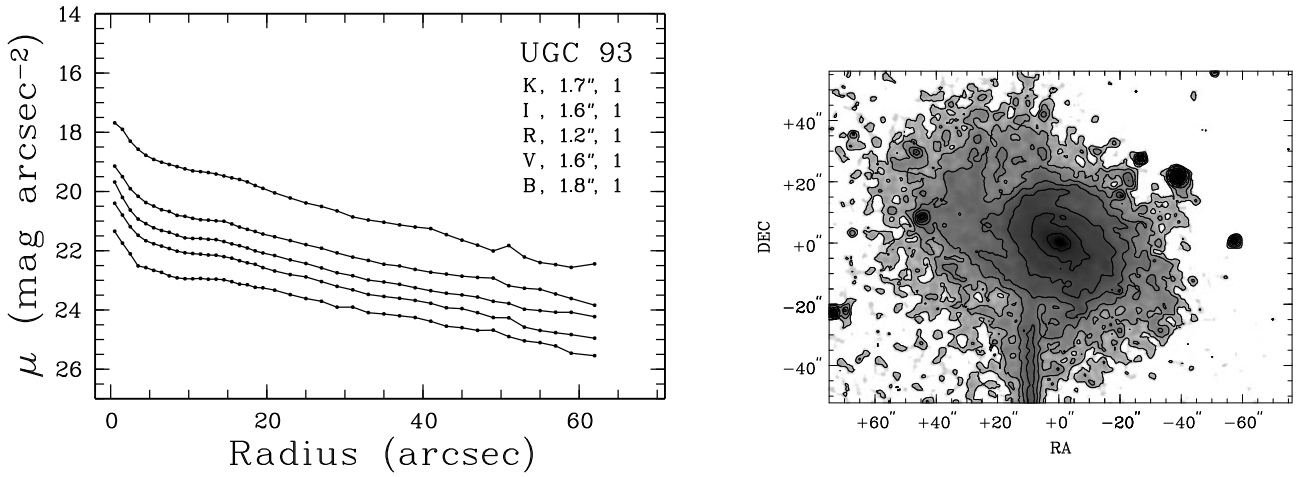

Fig. 12. The surface brightness as function of radius for all galaxies are presented in the left panels. In the top right corner of these graphs are indicated the galaxy name and the observed passbands, with their seeing and photometric quality estimate. The estimated photometric errors are 1: photometric, 2: 0.0-0.2 mag, 3: 0.2-0.5 mag, 4: 0.5-1.0 mag and 5: >1.0 mag. The FWHM seeing estimate is in arcseconds. UGC 436n2 and UGC 10445n2 indicate the second independent observation of these galaxies. The grayscale/contour images are presented in the right panels. Generally the images are much larger (especially the driftscans), but only the areas with the galaxies are displayed here. The lowest and highest contour levels of each image are indicated, with the stepsize between each contour level.

UGC 242, contours at 20.0, 24.0, 0.5 R-mag arcsec^{-2}.

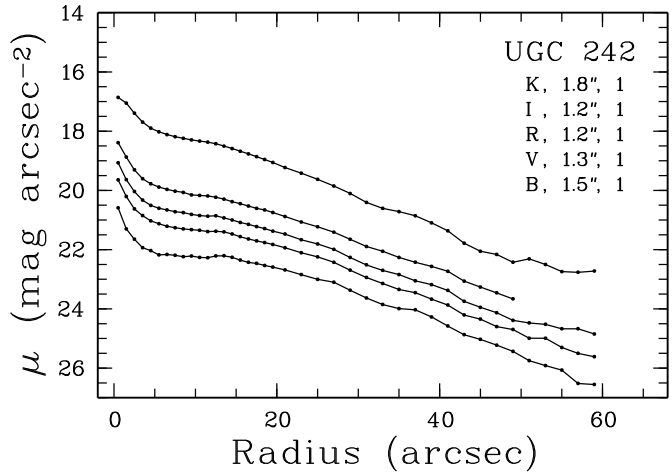

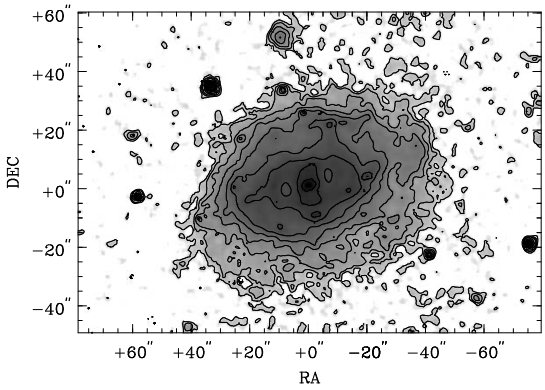

UGC 334, contours at 21.5, 24.5, 0.5 R-mag arcsec^{-2}.

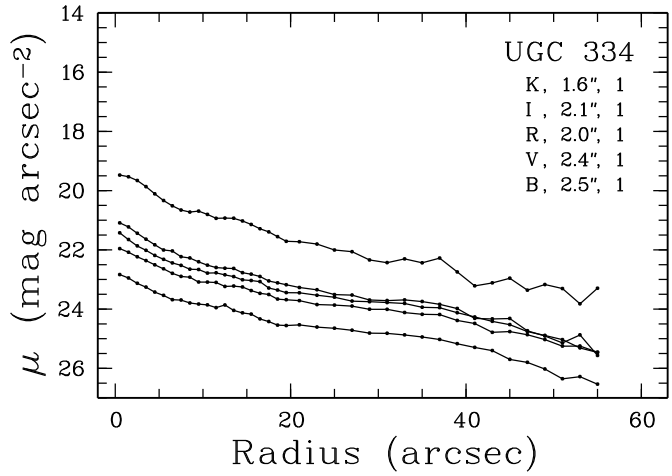

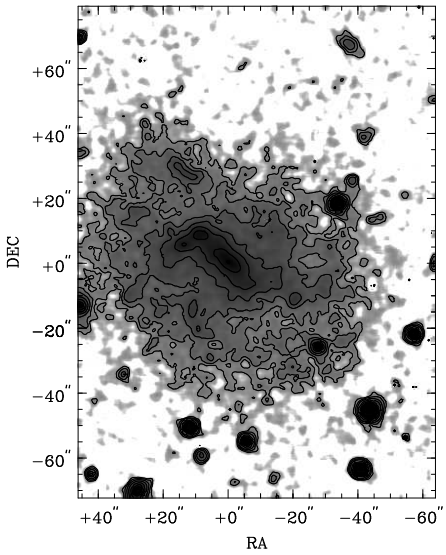

UGC 438, contours at 19.0, 24.5, 0.5 R-mag arcsec^{-2}.

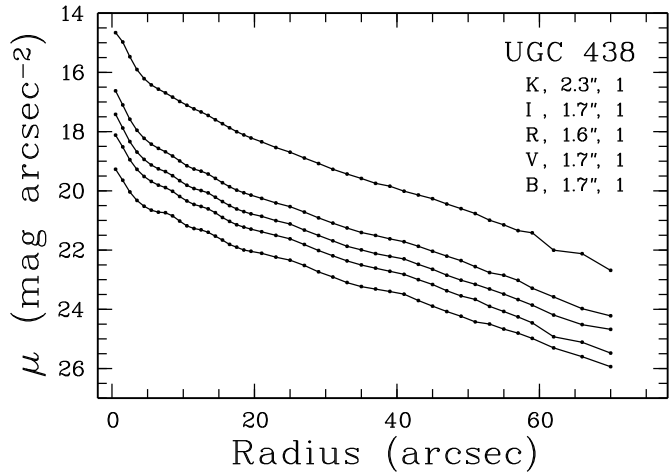

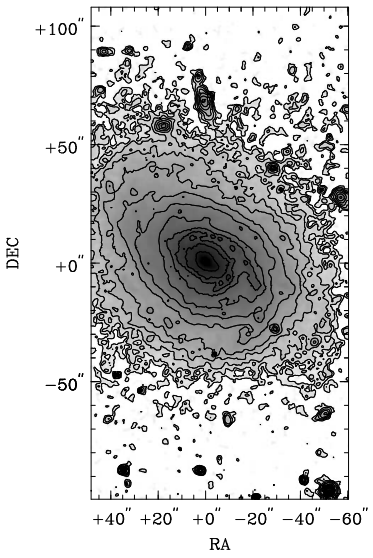

Fig. 12. -Continued.

UGC 438, contours at 19.0, 24.0, 0.5 R-mag arcsec^{-2}.

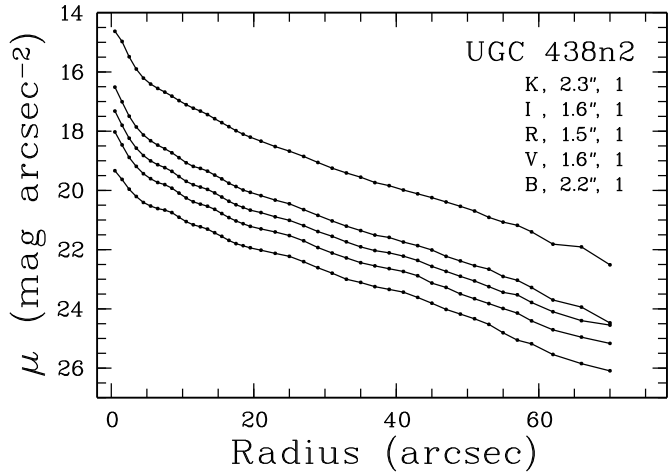

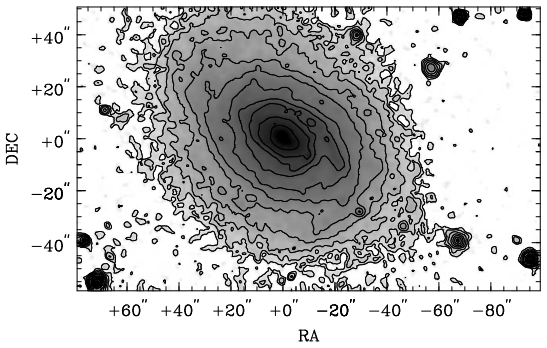

UGC 463, contours at 19.5, 24.0, 0.5 I-mag arcsec^{-2}.

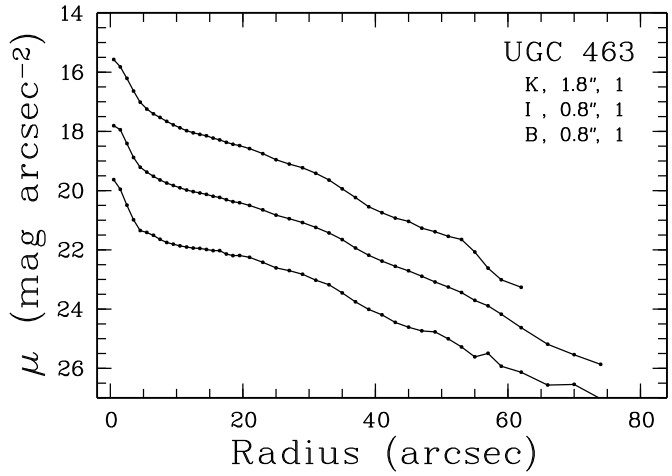

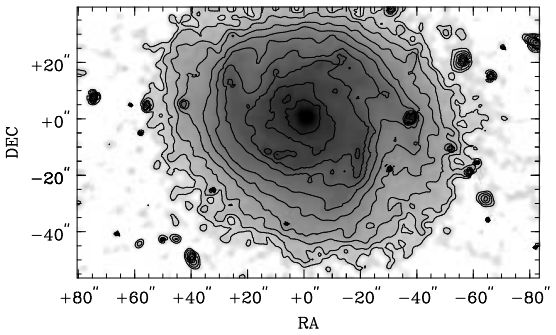

UGC 490, contours at 19.5, 24.0, 0.5 R-mag arcsec^{-2}.

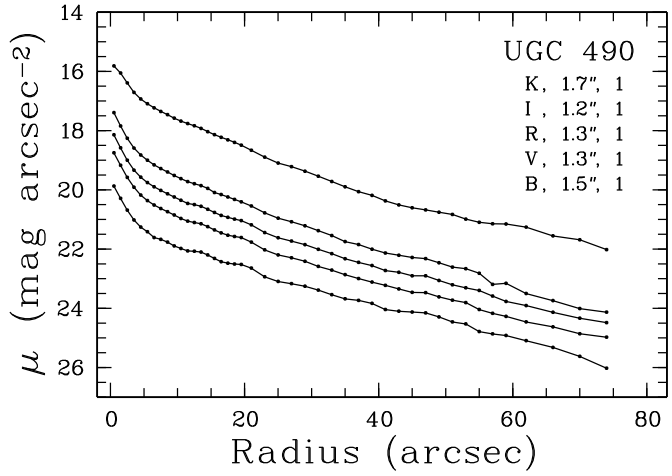

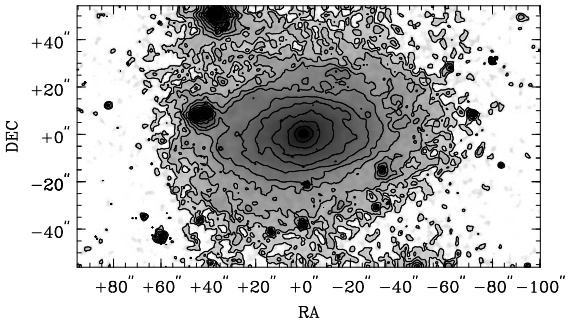

Fig. 12. -Continued.

UGC 508, contours at 19.0, 24.0, 0.5 R-mag arcsec^{-2}.

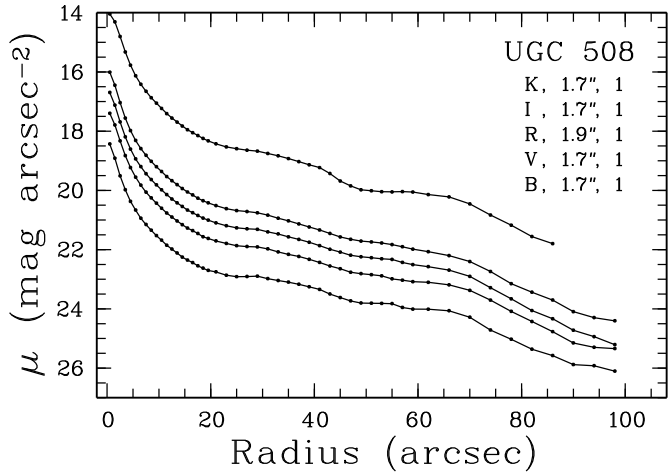

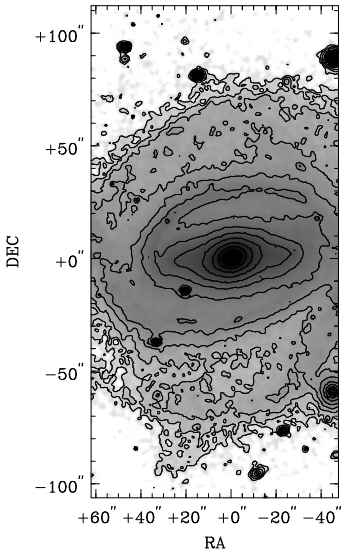

UGC 628, contours at 20.5, 24.5, 0.5 R-mag arcsec^{-2}.

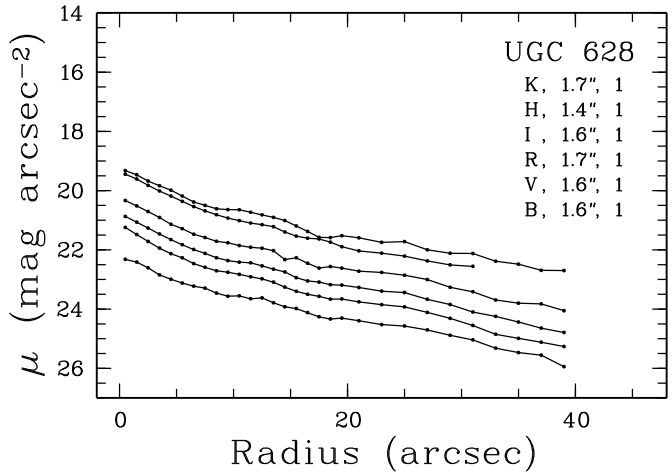

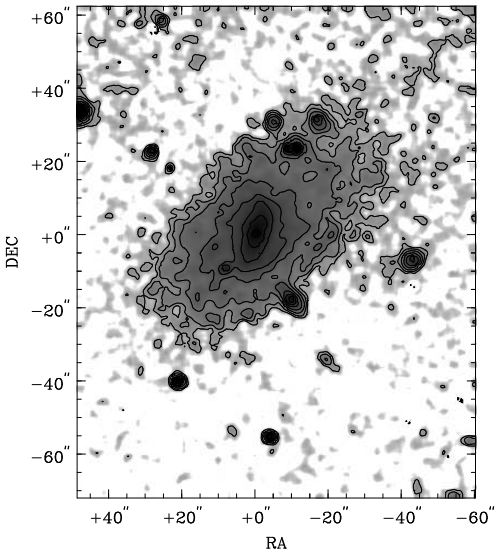

UGC 1305, contours at 19.0, 23.5, 0.5 R-mag arcsec^{-2}.

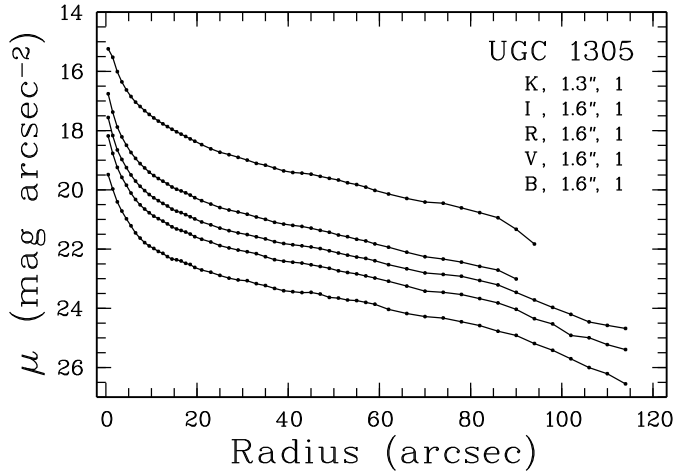

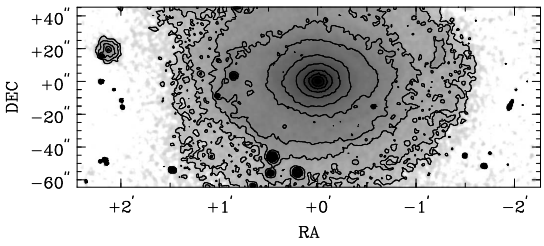

Fig. 12. -Continued.

UGC 1455, contours at 20.0, 24.0, 0.5 R-mag arcsec^{-2}.

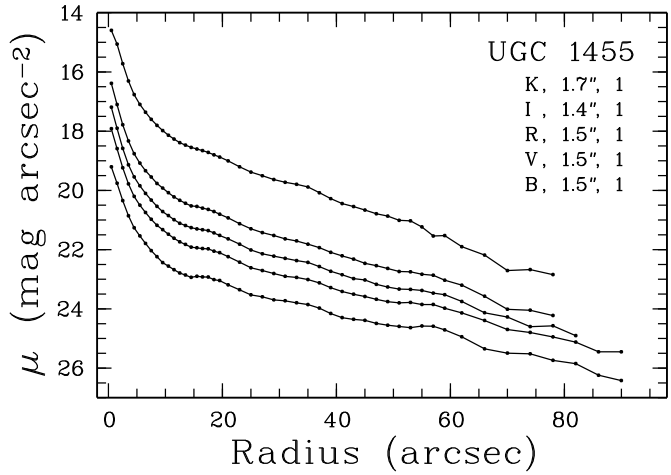

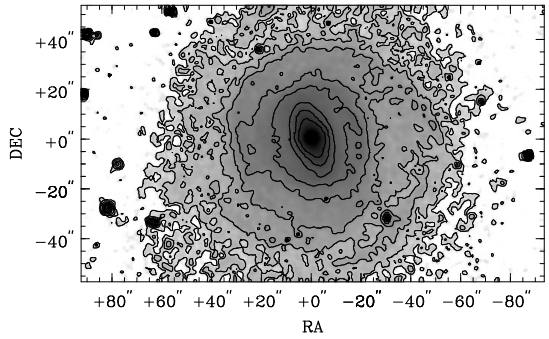

UGC 1551, contours at 21.0, 24.5, 0.5 R-mag arcsec^{-2}.

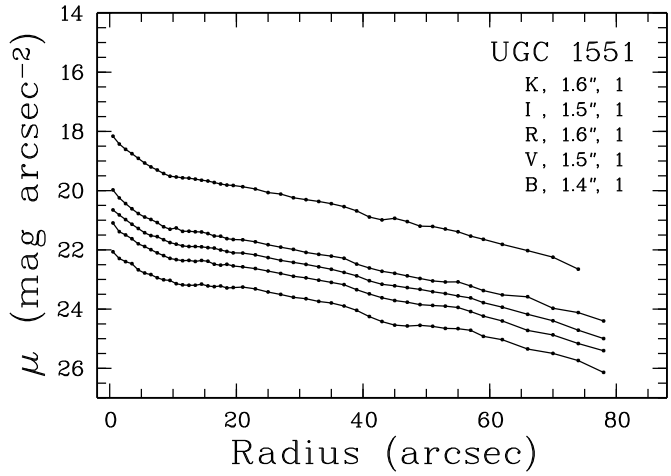

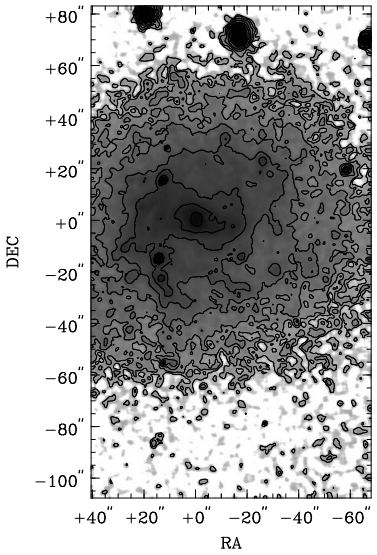

UGC 1559, contours at 21.0, 24.5, 0.5 R-mag arcsec^{-2}.

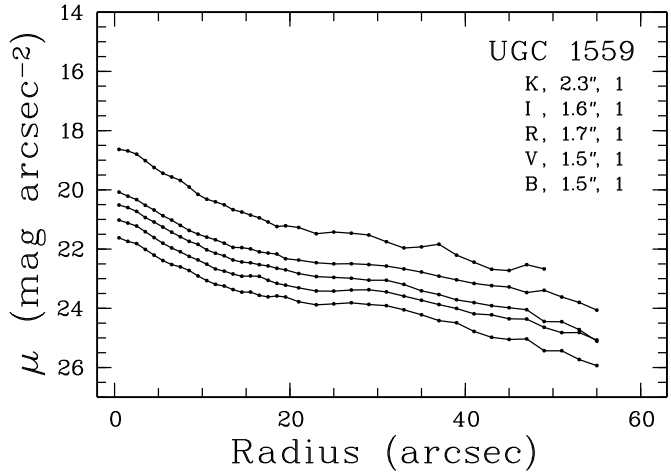

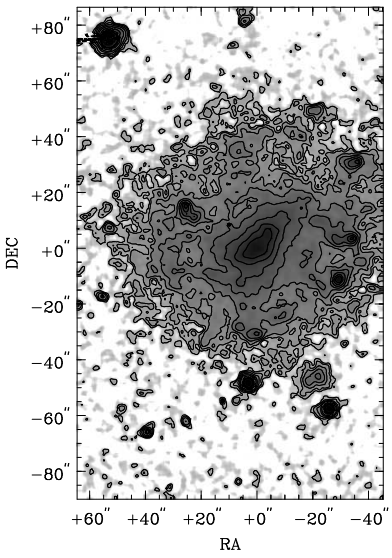

Fig. 12. -Continued.

UGC 1577, contours at 20.0, 23.5, 0.5 R-mag arcsec^{-2}.

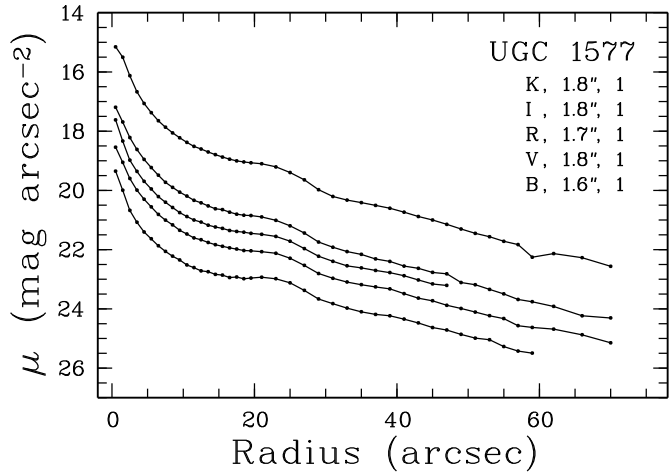

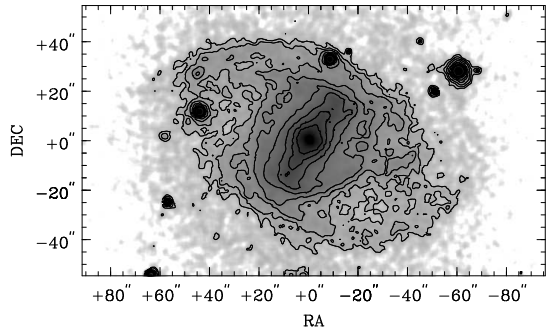

UGC 1719, contours at 20.5, 24.0, 0.5 R-mag arcsec^{-2}.

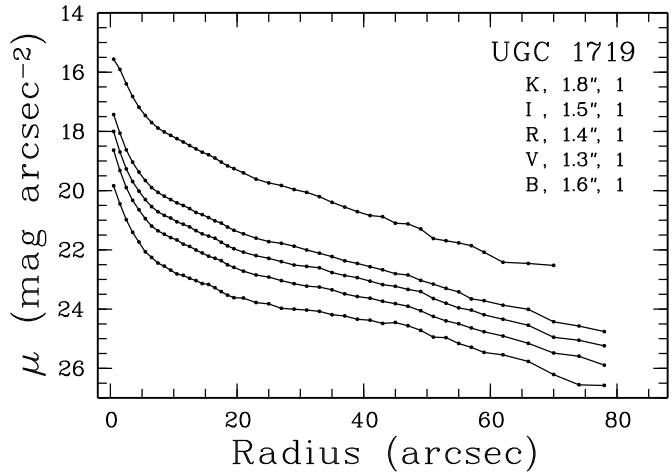

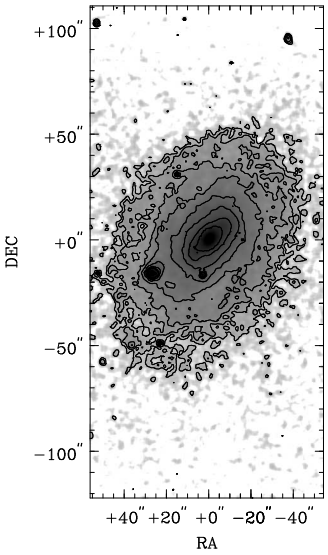

UGC 1792, contours at 20.0, 24.5, 0.5 R-mag arcsec^{-2}.

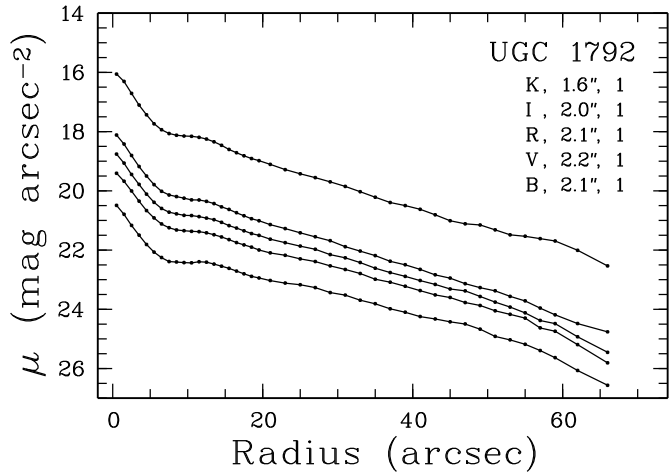

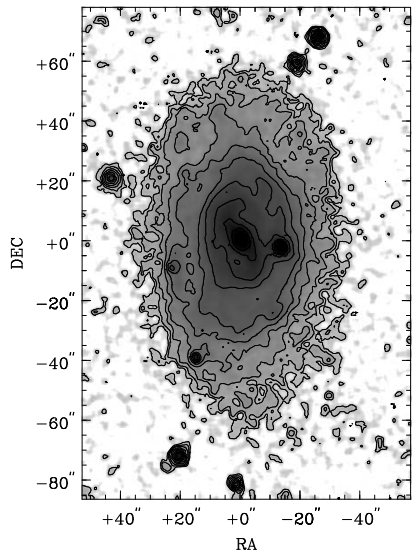

Fig. 12. -Continued.

UGC 2064, contours at 20.5, 24.5, 0.5 R-mag arcsec^{-2}.

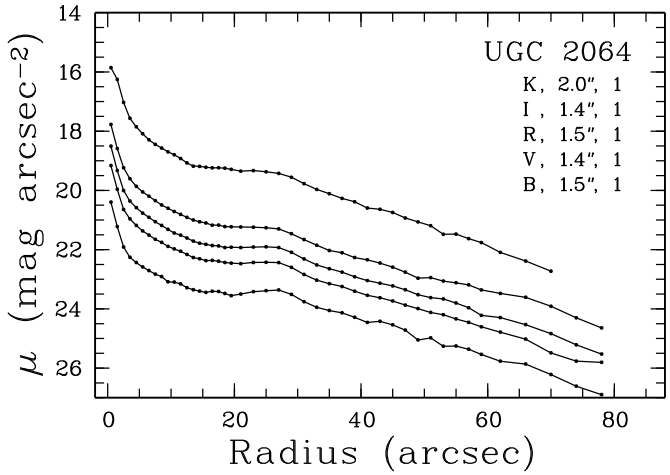

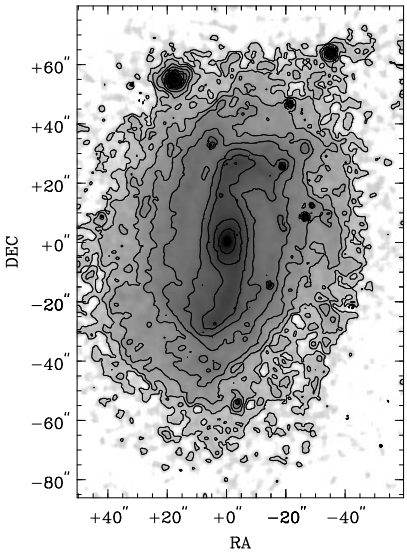

UGC 2081, contours at 20.5, 24.5, 0.5 R-mag arcsec^{-2}.

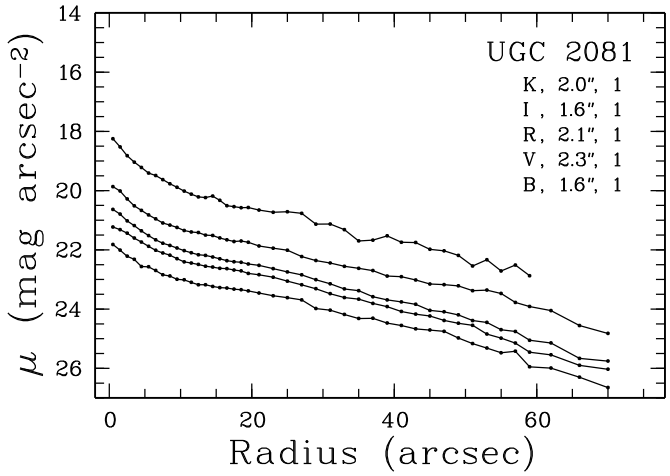

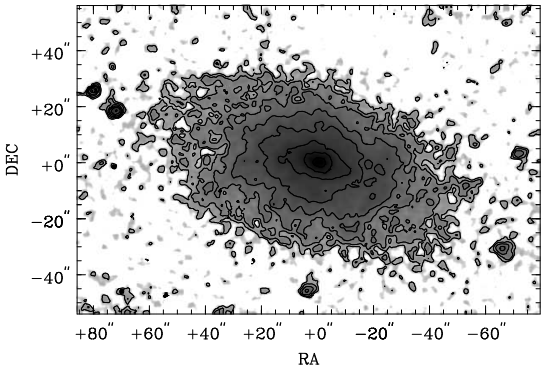

UGC 2124, contours at 20.0, 24.0, 0.5 R-mag arcsec^{-2}.

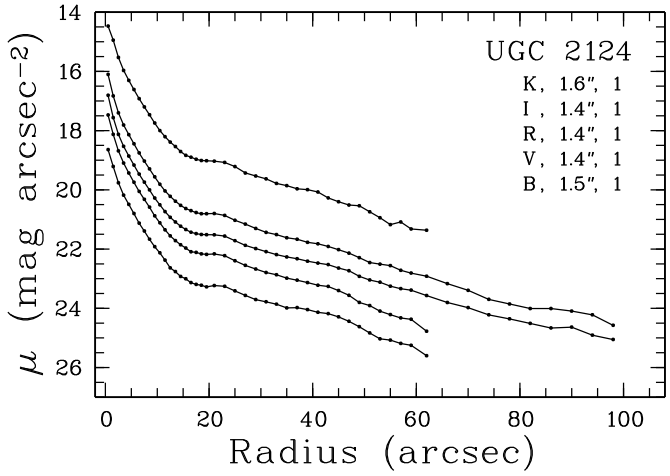

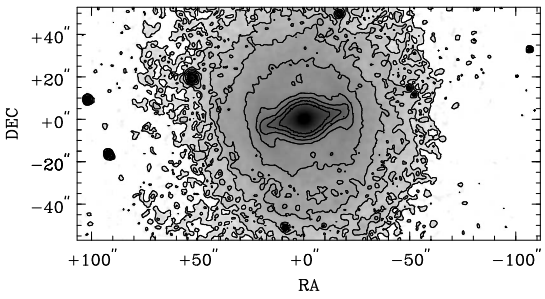

Fig. 12. -Continued.

UGC 2125, contours at 20.5, 24.0, 0.5 R-mag arcsec^{-2}.

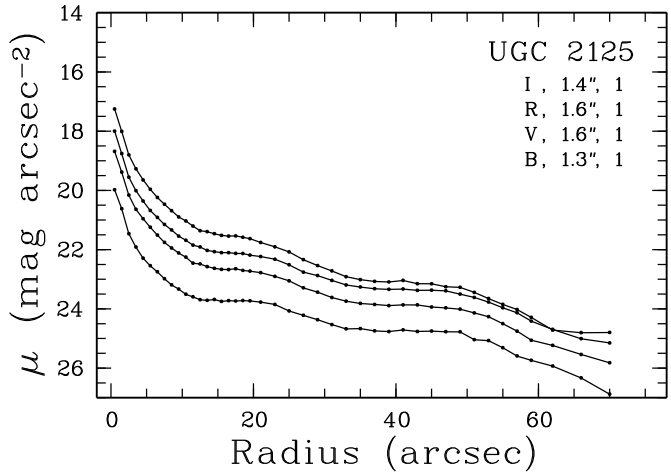

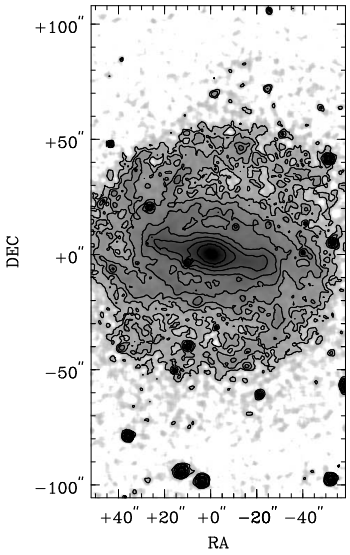

UGC 2197, contours at 21.0, 24.5, 0.5 R-mag arcsec^{-2}.

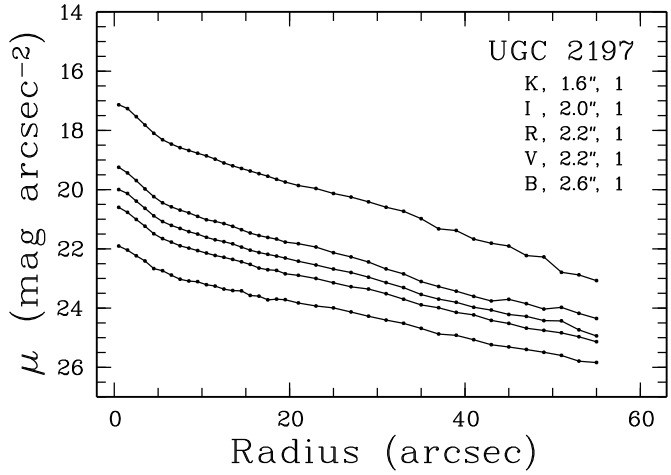

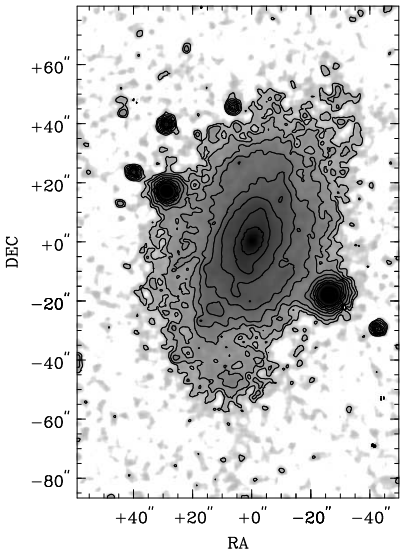

UGC 2368, contours at 20.5, 25.0, 0.5 R-mag arcsec^{-2}.

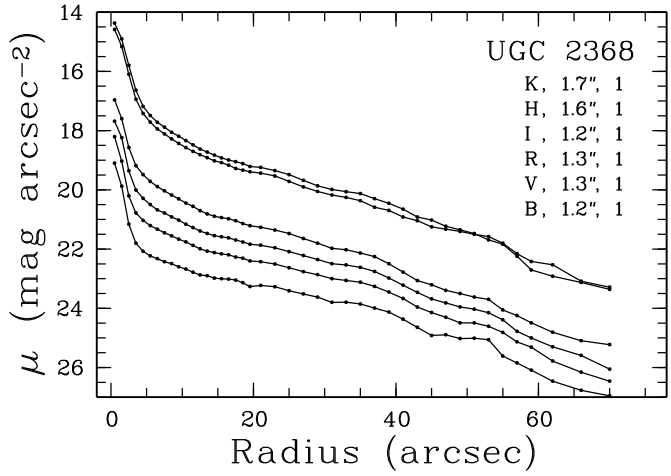

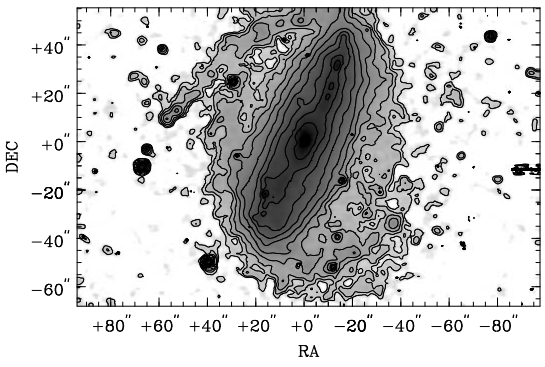

Fig. 12. -Continued.

UGC 2595, contours at 20.5, 24.5, 0.5 R-mag arcsec^{-2}.

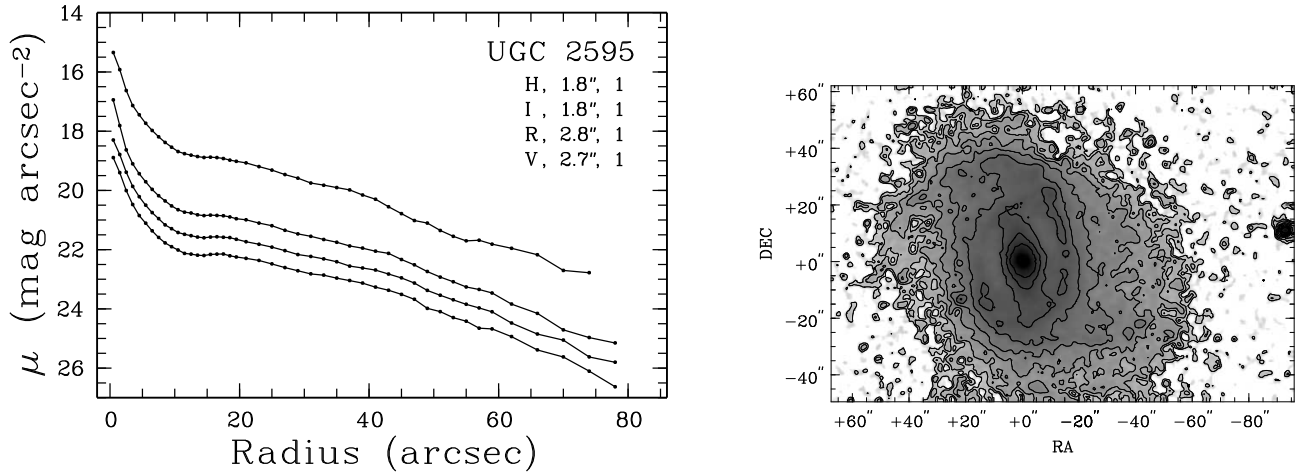

UGC 3066, contours at 20.5, 24.0, 0.5 R-mag arcsec^{-2}.

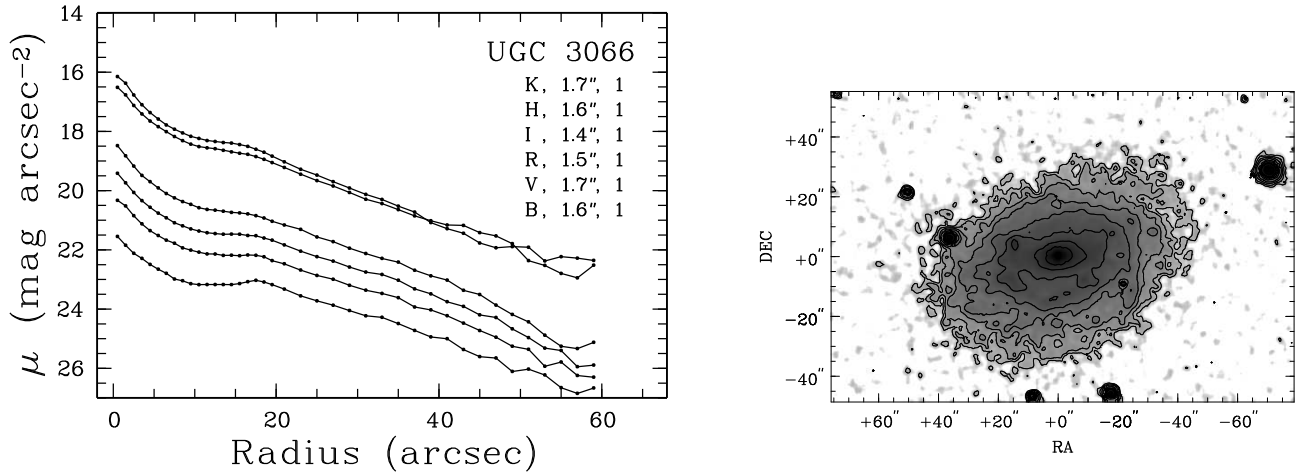

UGC 3080, contours at 20.0, 24.0, 0.5 R-mag arcsec^{-2}.

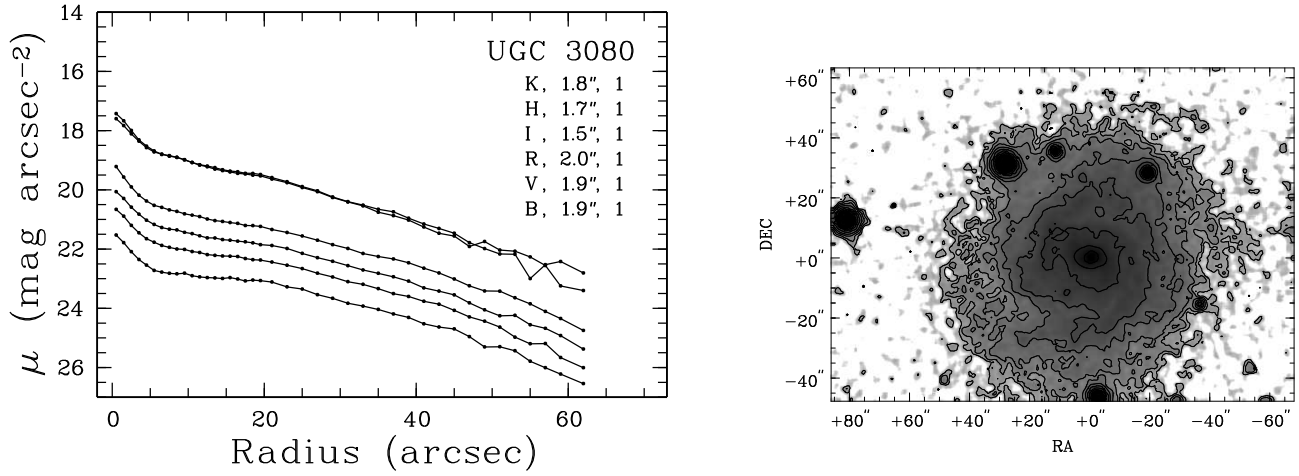

Fig. 12. -Continued.

UGC 3140, contours at 20.0, 24.5, 0.5 I-mag arcsec^{-2}.

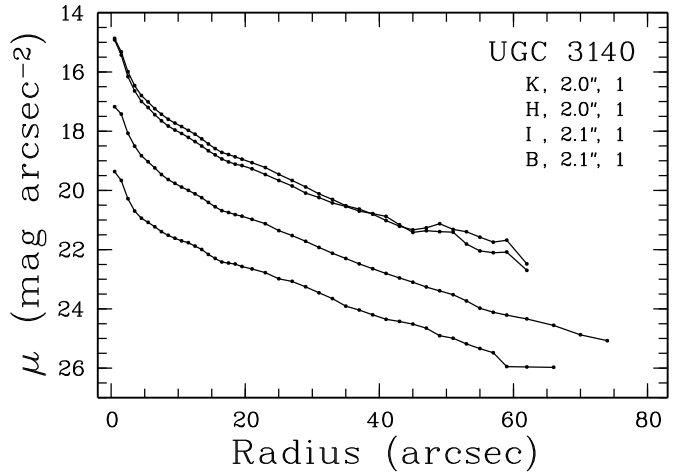

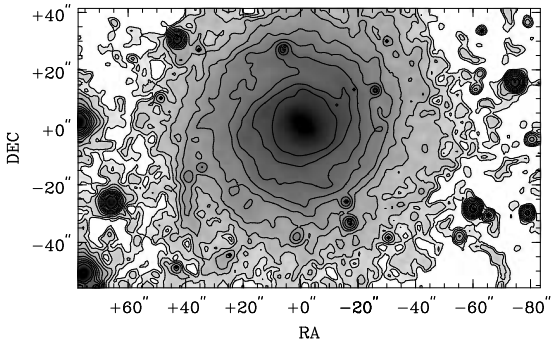

UGC 4126, contours at 20.0, 24.0, 0.5 R-mag arcsec^{-2}.

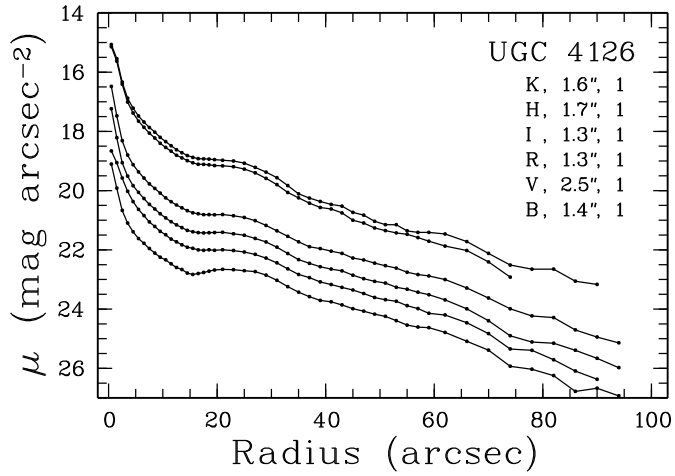

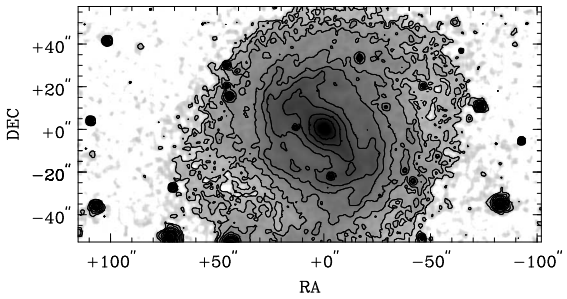

UGC 4256, contours at 20.5, 24.0, 0.5 R-mag arcsec^{-2}.

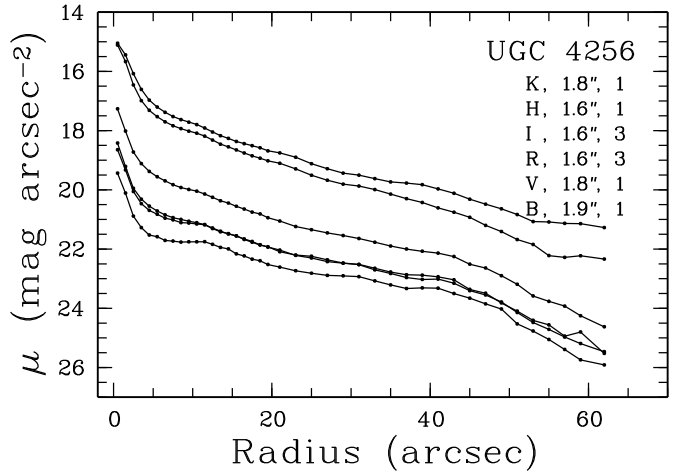

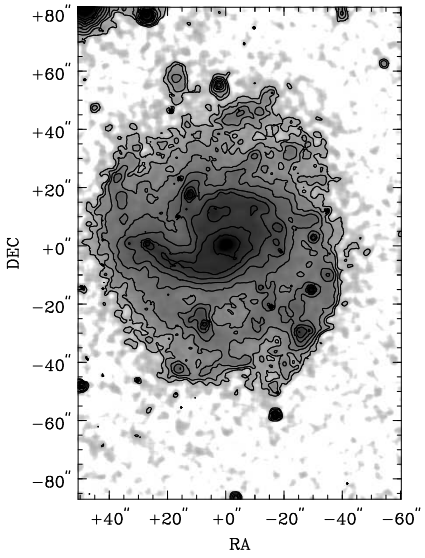

Fig. 12. -Continued.

UGC 4308, contours at 20.5, 24.0, 0.5 R-mag arcsec^{-2}.

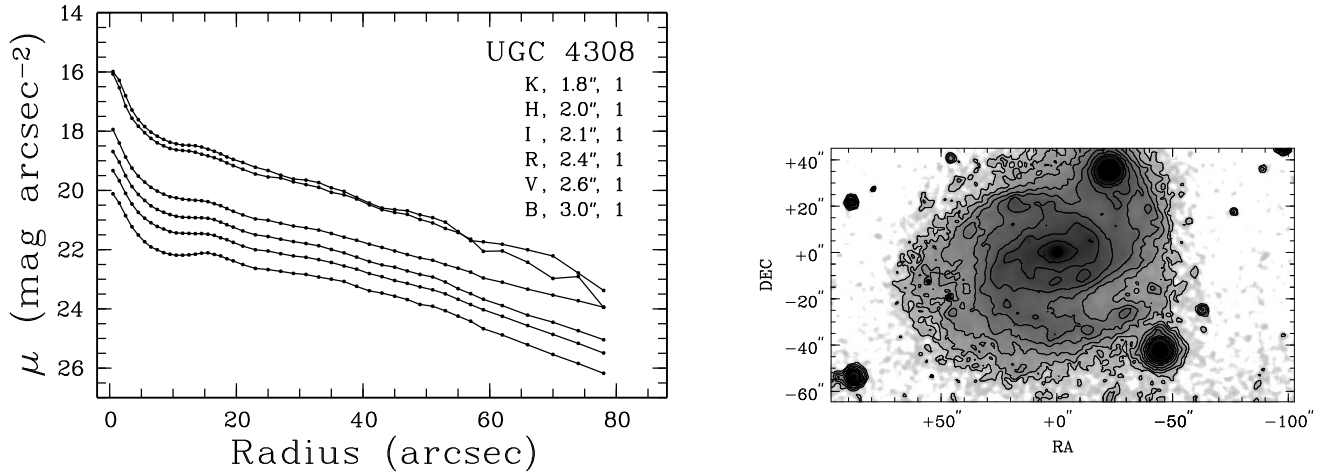

UGC 4368, contours at 20.5, 24.0, 0.5 R-mag arcsec^{-2}.

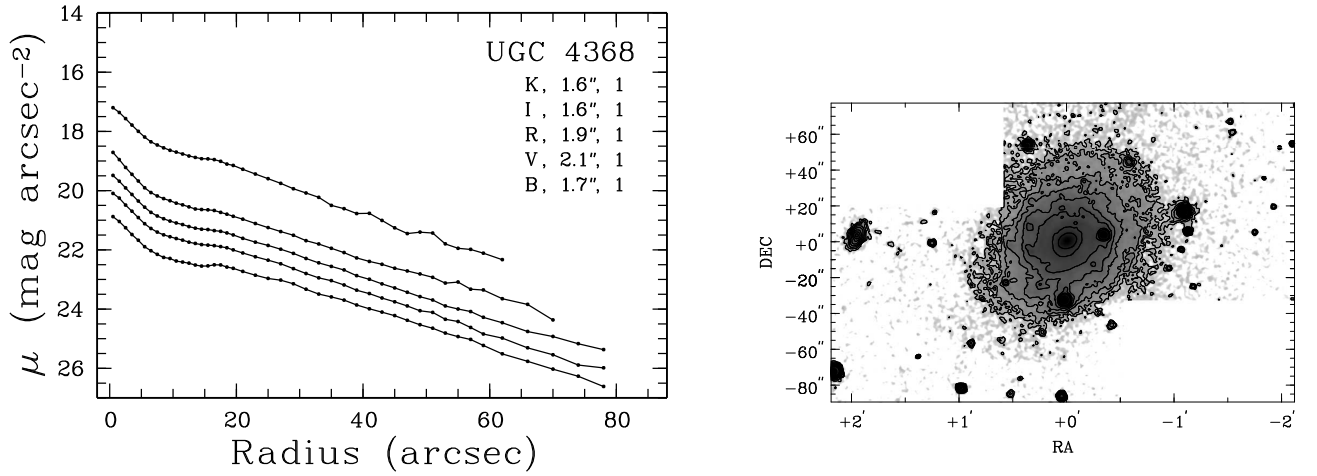

UGC 4375, contours at 20.0, 24.0, 0.5 R-mag arcsec^{-2}.

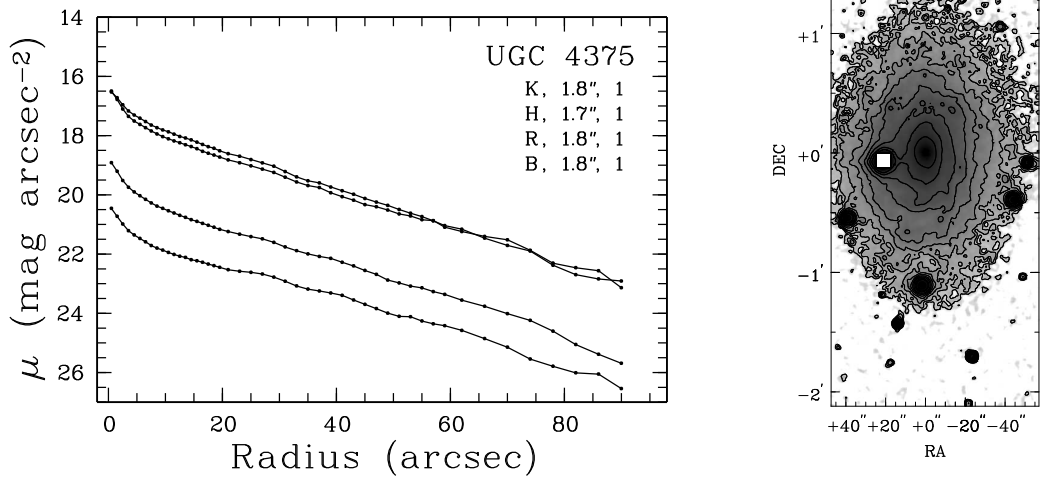

Fig. 12. -Continued.

UGC 4422, contours at 20.0, 24.0, 0.5 R-mag arcsec^{-2}.

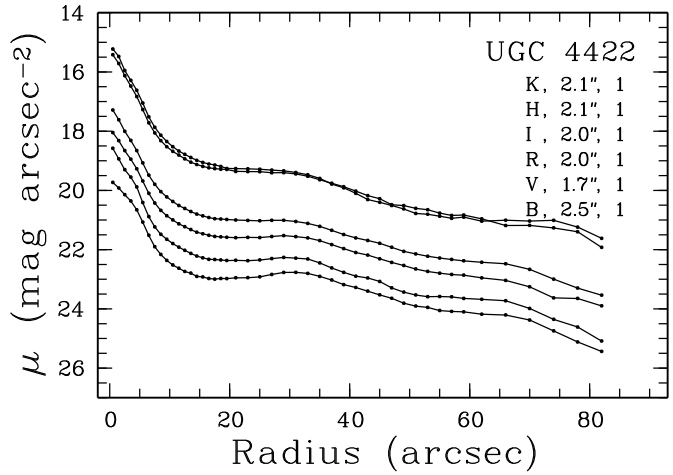

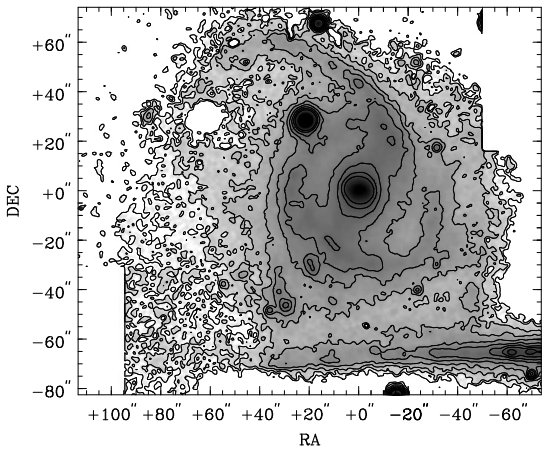

UGC 4458, contours at 19.0, 23.5, 0.5 I-mag arcsec^{-2}.

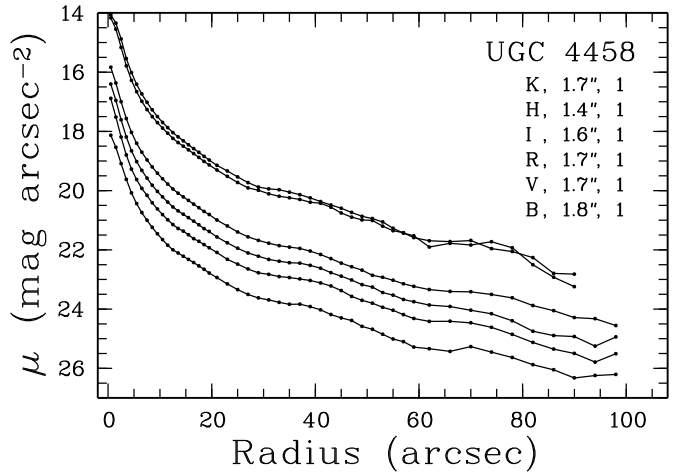

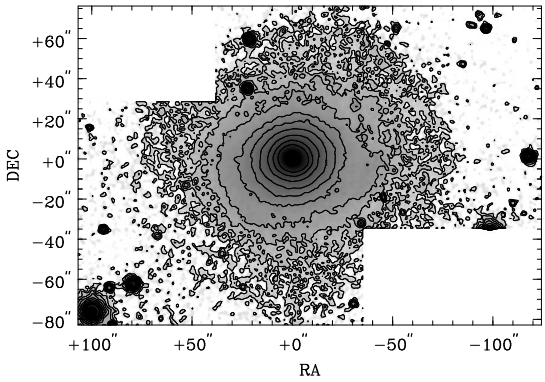

UGC 5103, contours at 20.0, 24.0, 0.5 R-mag arcsec^{-2}.

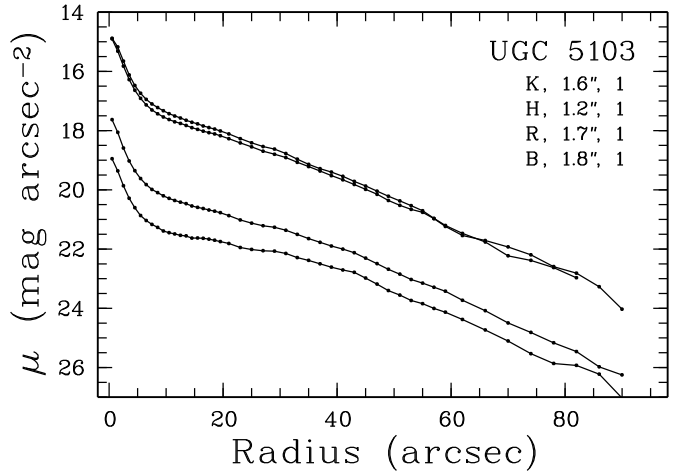

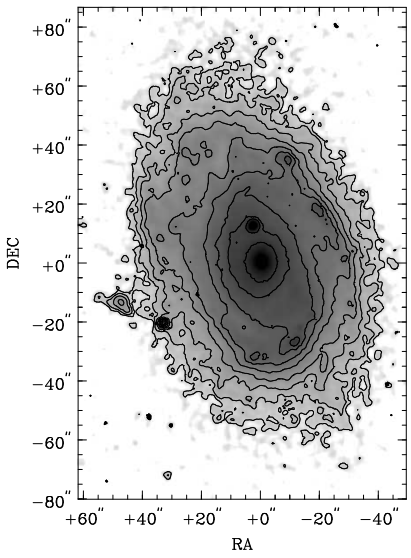

Fig. 12. -Continued.

UGC 5303, contours at 20.5, 24.5, 0.5 R-mag arcsec^{-2}.

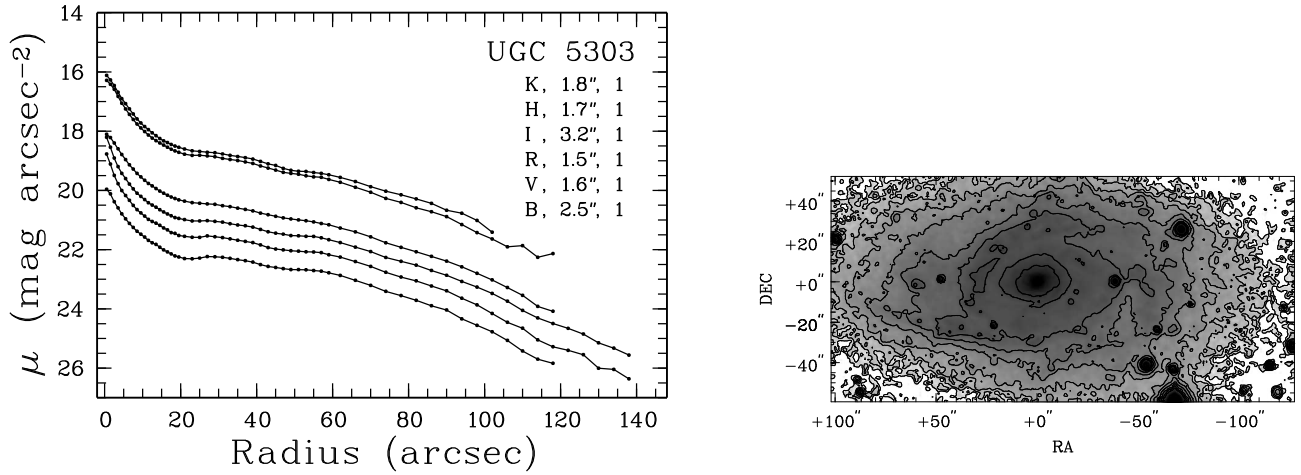

UGC 5510, contours at 19.5, 24.5, 0.5 R-mag arcsec^{-2}.

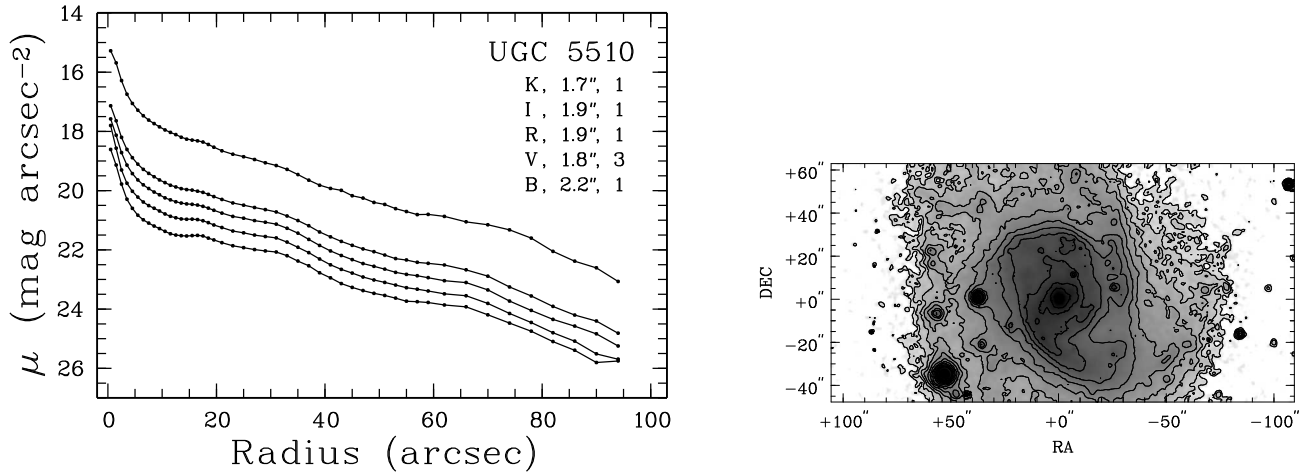

UGC 5554, contours at 20.0, 24.0, 0.5 R-mag arcsec^{-2}.

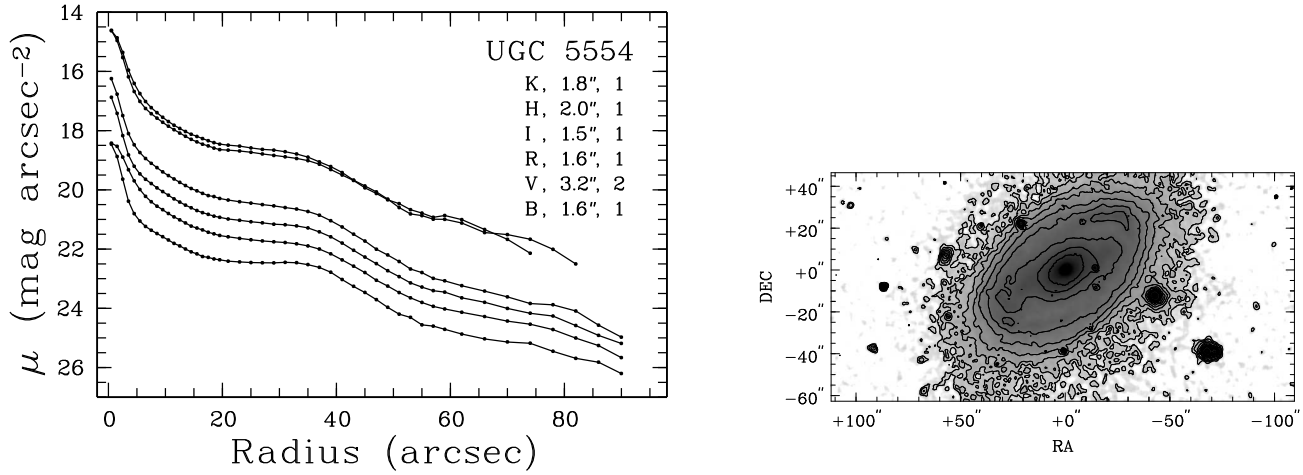

Fig. 12. -Continued.

UGC 5633, contours at 21.0, 24.5, 0.5 R-mag arcsec^{-2}.

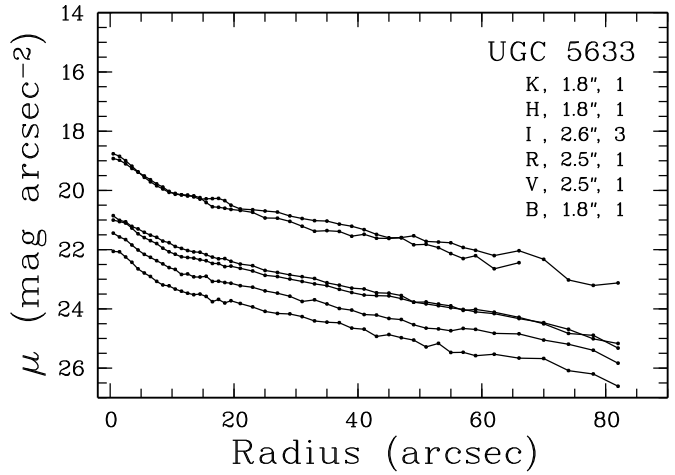

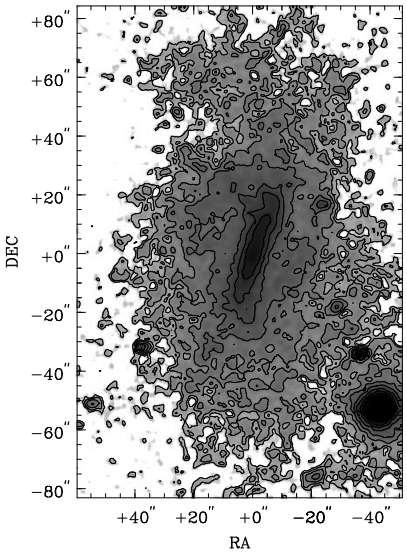

UGC 5842, contours at 20.5, 24.5, 0.5 R-mag arcsec^{-2}.

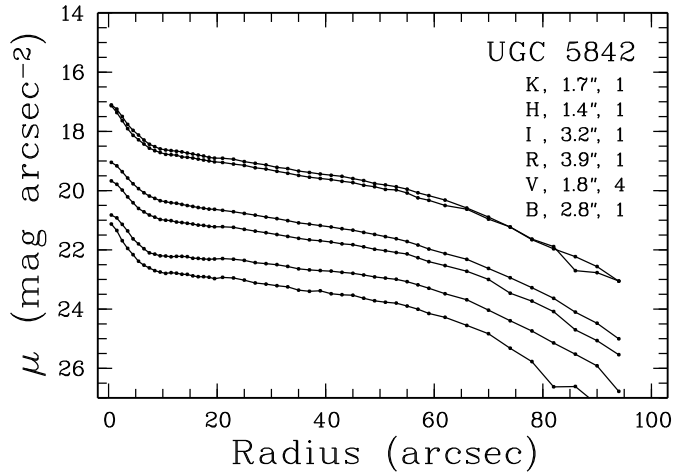

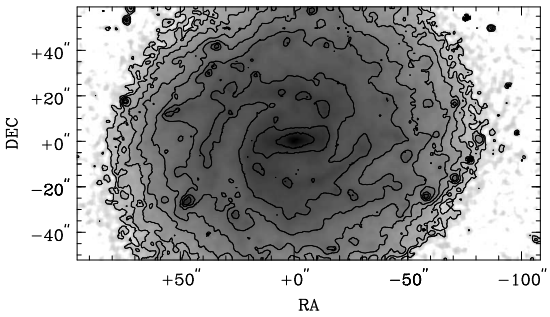

UGC 6028, contours at 20.0, 24.5, 0.5 R-mag arcsec^{-2}.

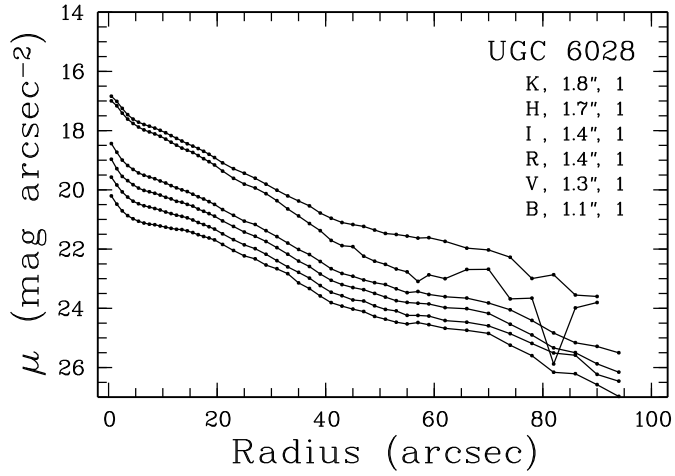

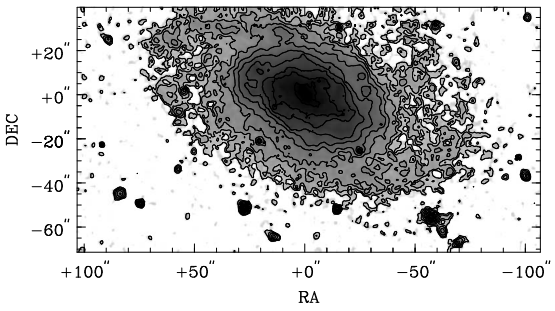

Fig. 12. -Continued.

UGC 6077, contours at 20.5, 24.5, 0.5 R-mag arcsec^{-2}.

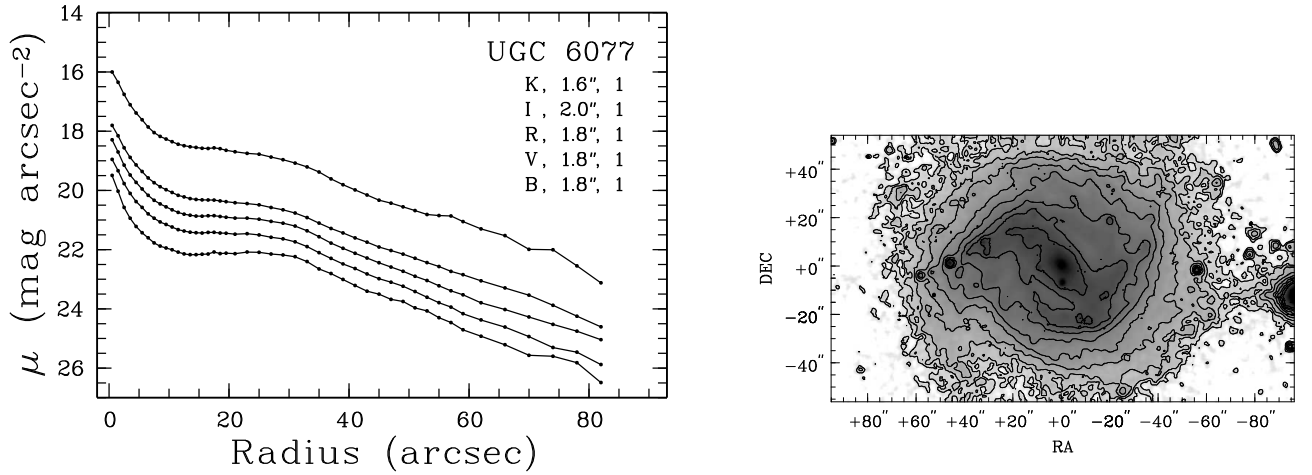

UGC 6123, contours at 19.0, 24.0, 0.5 R-mag arcsec^{-2}.

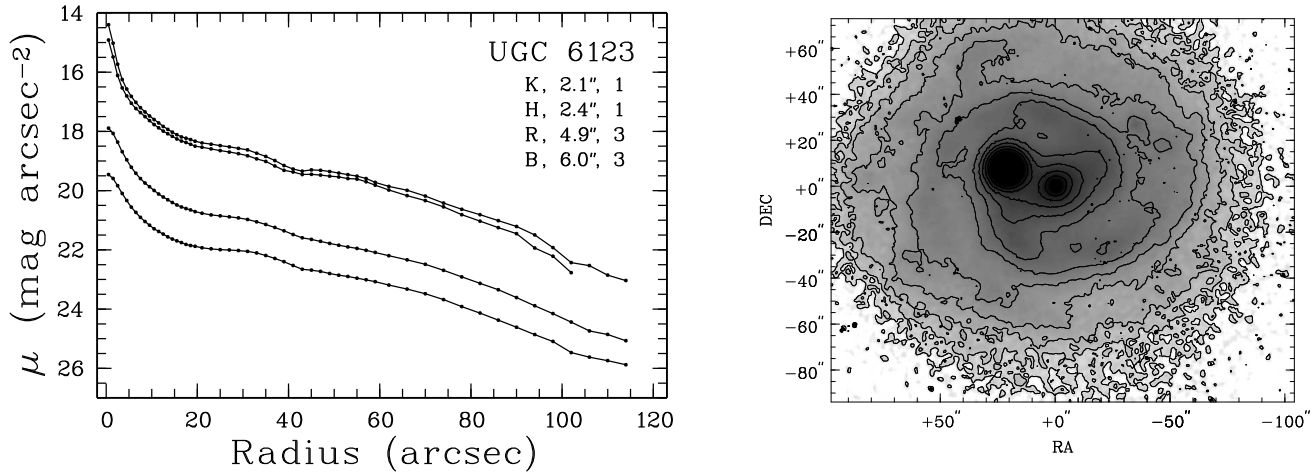

UGC 6277, contours at 19.0, 24.0, 0.5 R-mag arcsec^{-2}.

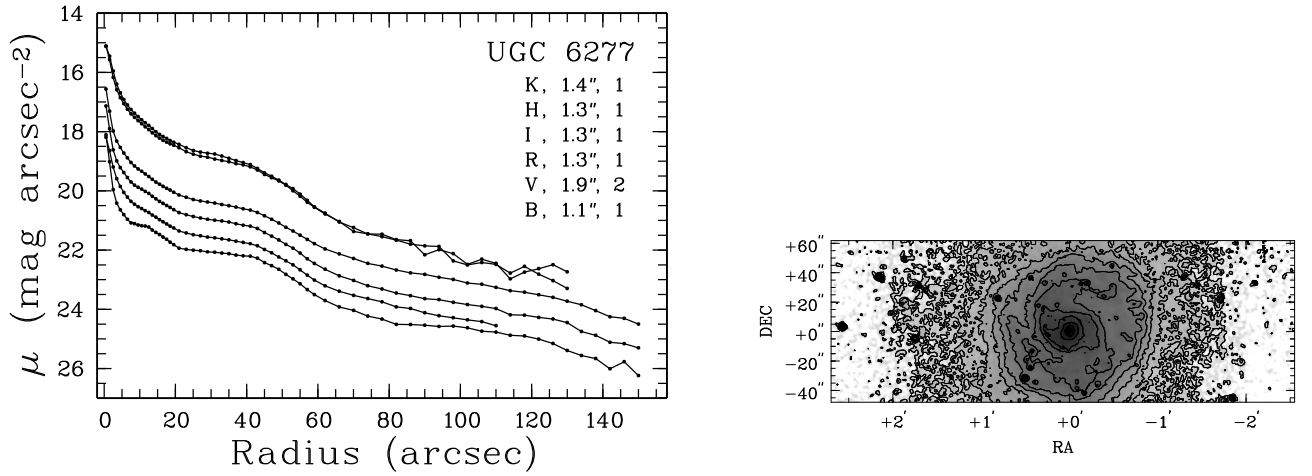

Fig. 12. -Continued.

UGC 6445, contours at 20.0, 24.0, 0.5 R-mag arcsec^{-2}.

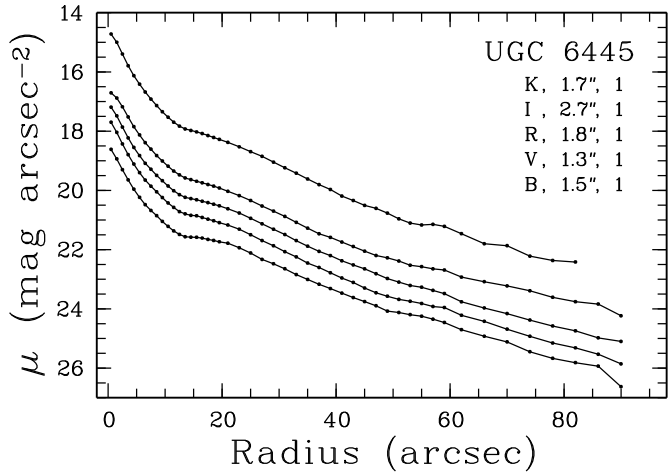

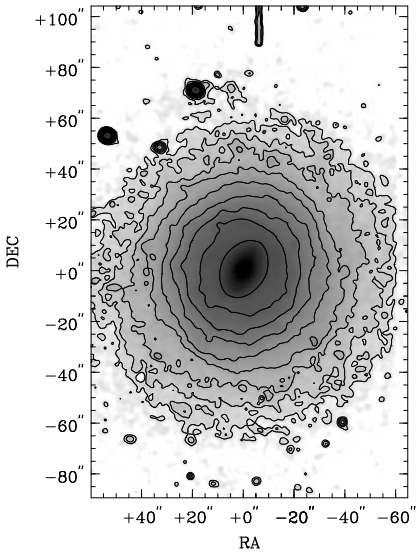

UGC 6453, contours at 19.0, 23.5, 0.5 I-mag arcsec^{-2}.

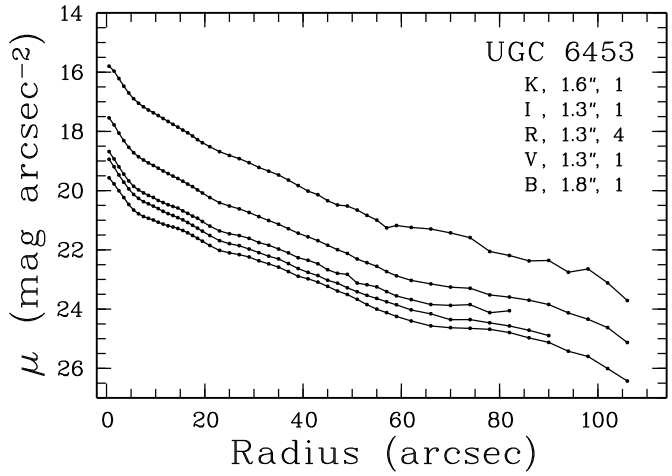

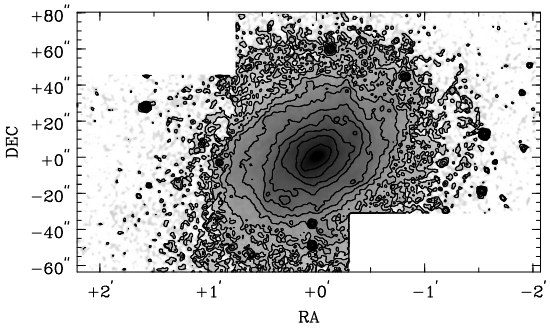

UGC 6460, contours at 19.0, 24.0, 0.5 R-mag arcsec^{-2}.

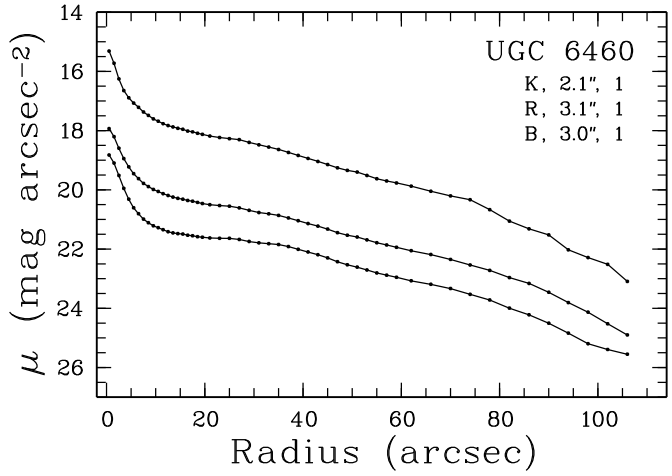

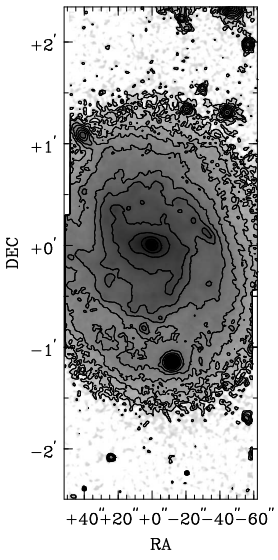

Fig. 12. -Continued.

UGC 6536, contours at 20.0, 25.0, 0.5 R-mag arcsec^{-2}.

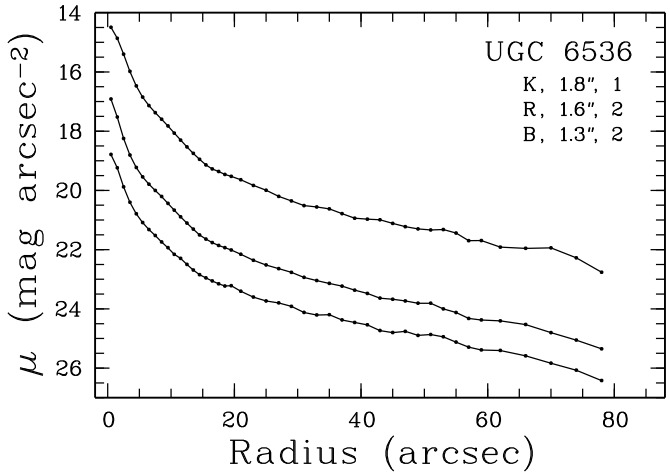

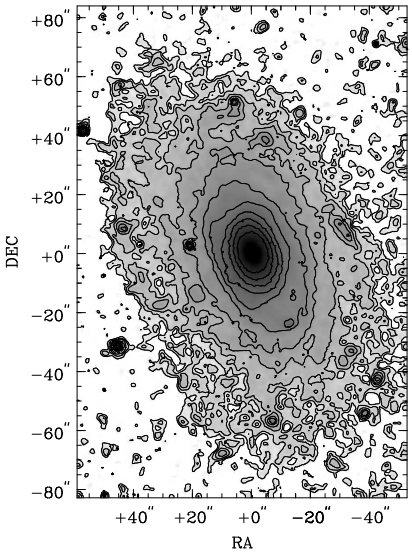

UGC 6693, contours at 20.0, 24.5, 0.5 R-mag arcsec^{-2}.

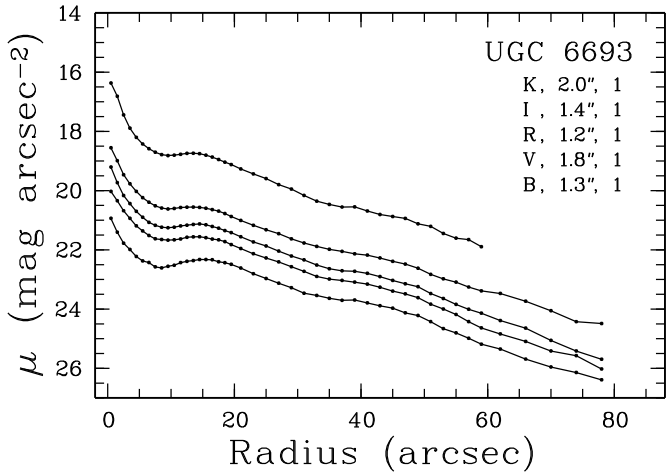

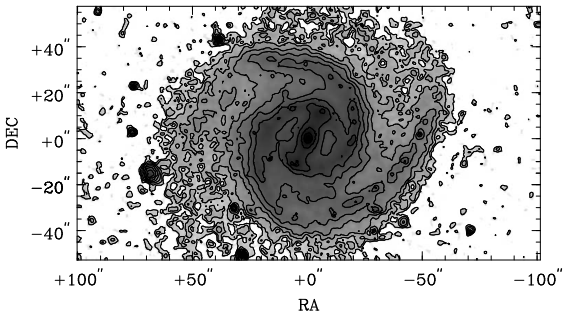

UGC 6746, contours at 20.0, 26.0, 0.5 R-mag arcsec^{-2}.

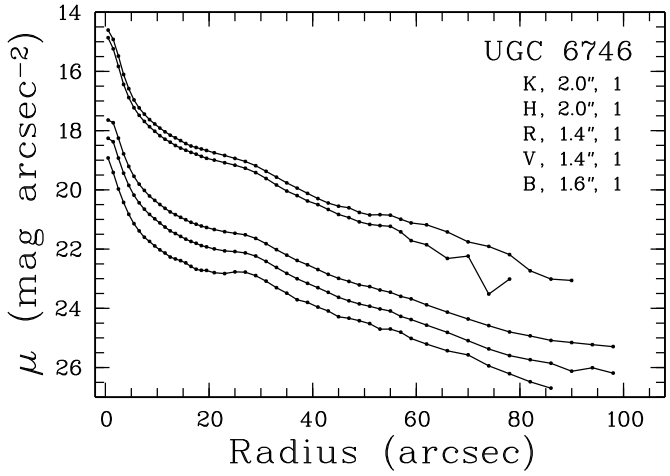

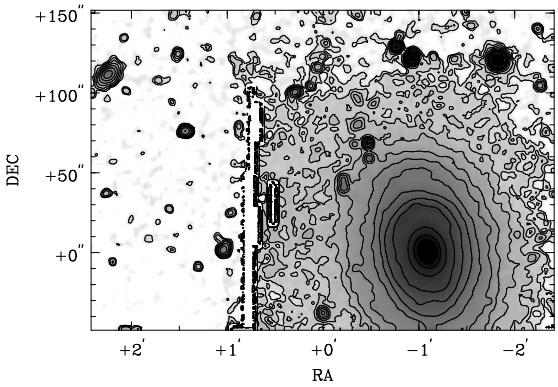

Fig. 12. -Continued.

UGC 6754, contours at 20.0, 24.5, 0.5 R-mag arcsec^{-2}.

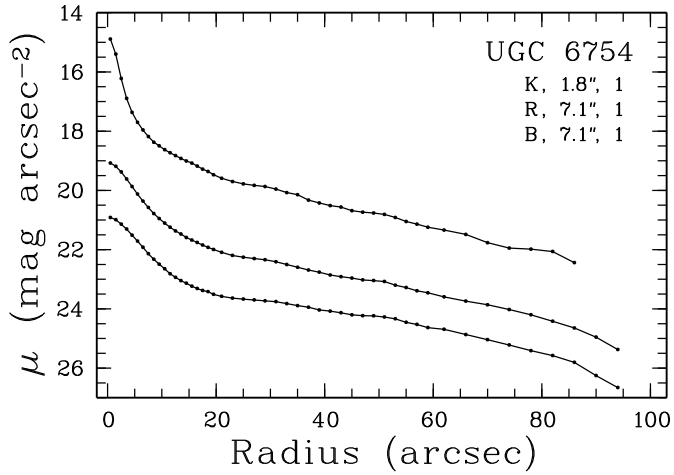

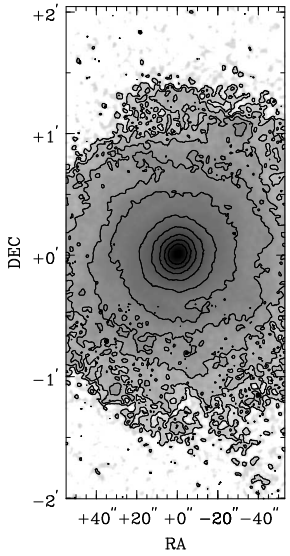

UGC 7169, contours at 19.5, 24.5, 0.5 R-mag arcsec^{-2}.

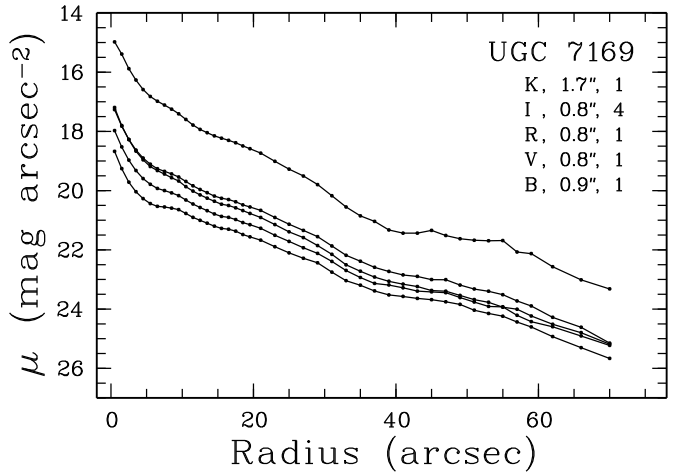

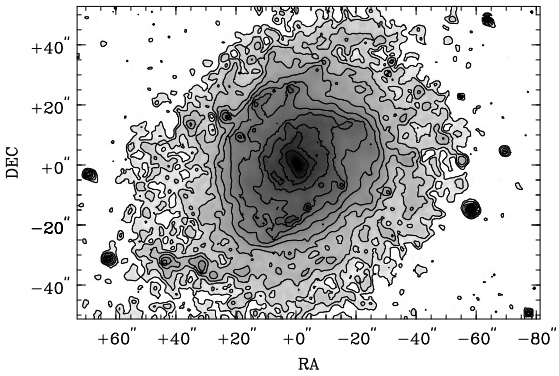

UGC 7315, contours at 19.5, 24.5, 0.5 R-mag arcsec^{-2}.

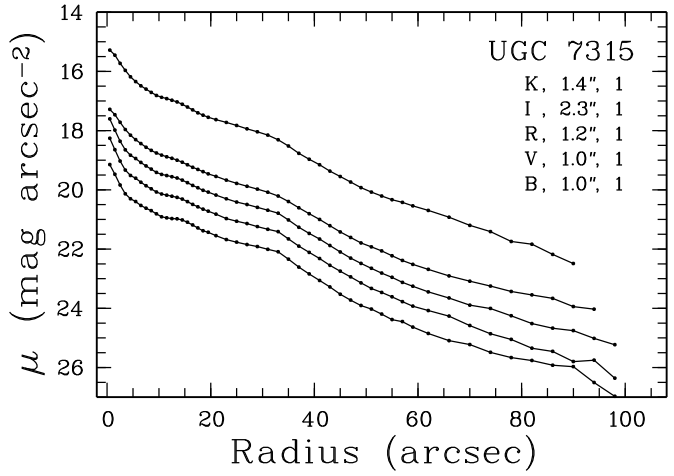

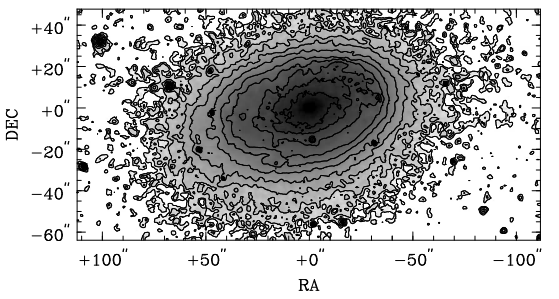

Fig. 12. -Continued.

UGC 7450, contours at 20.0, 24.5, 0.5 R-mag arcsec^{-2}.

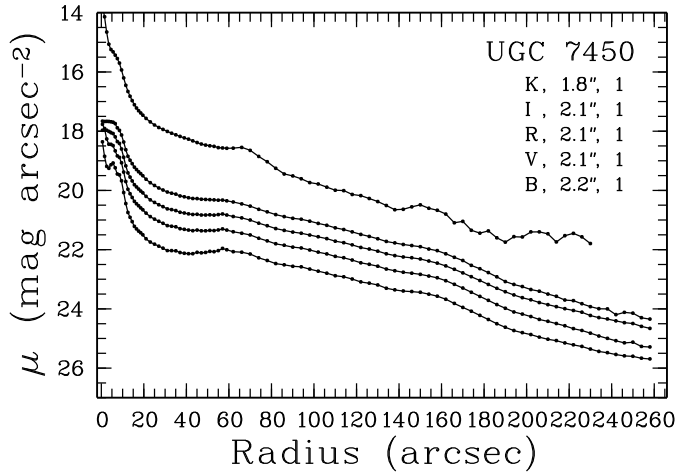

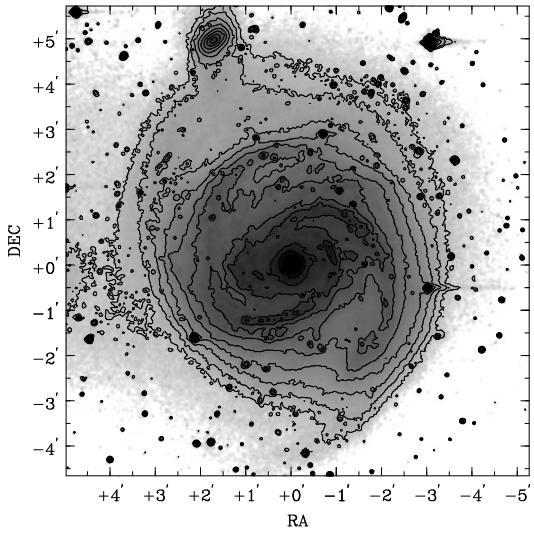

UGC 7523, contours at 18.5, 24.0, 0.5 R-mag arcsec^{-2}.

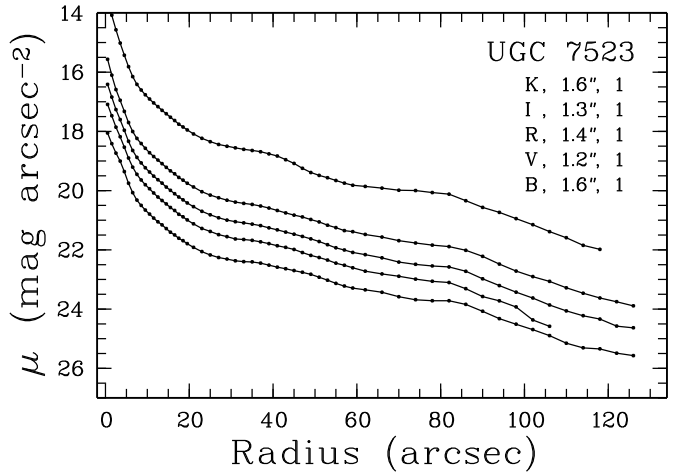

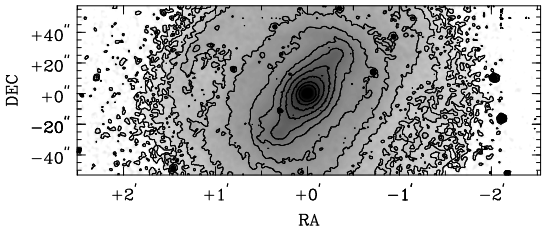

UGC 7594, contours at 19.5, 24.5, 0.5 R-mag arcsec^{-2}.

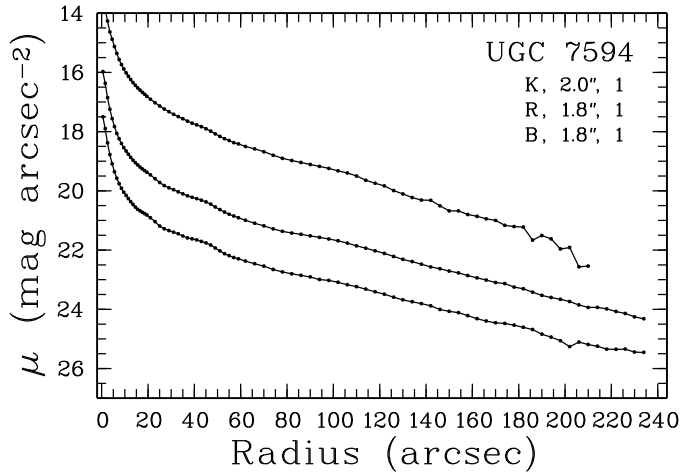

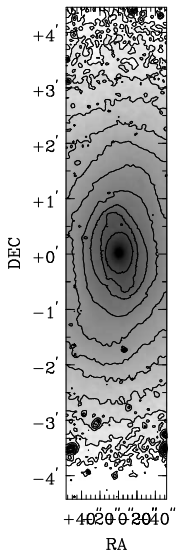

Fig. 12. -Continued.

UGC 7876, contours at 21.0, 25.0, 0.5 R-mag arcsec^{-2}.

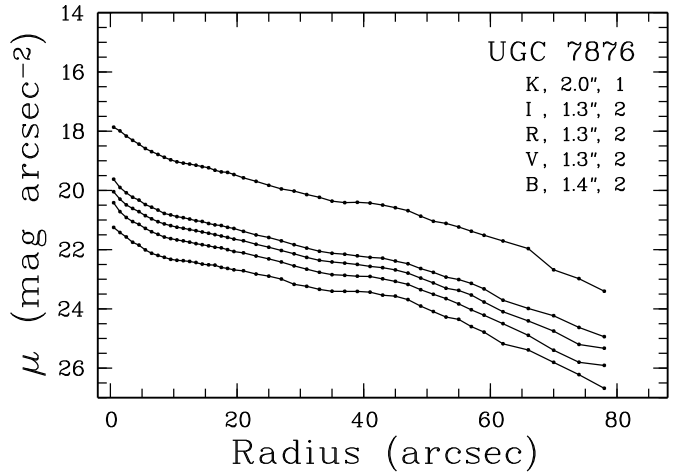

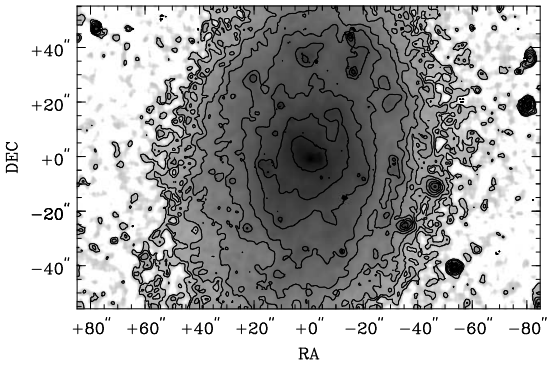

UGC 7901, contours at 19.0, 24.5, 0.5 R-mag arcsec^{-2}.

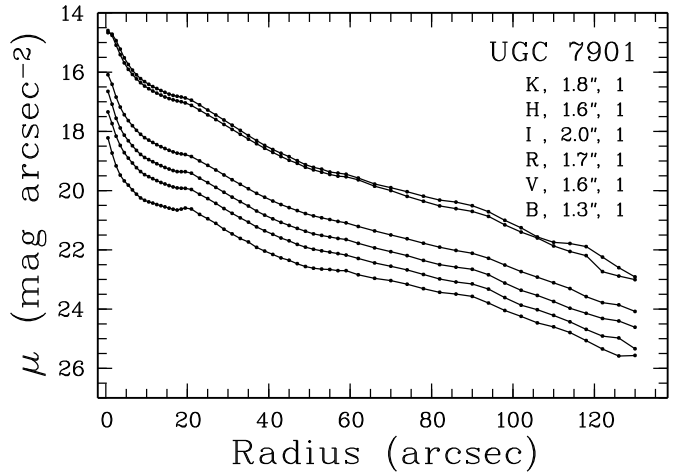

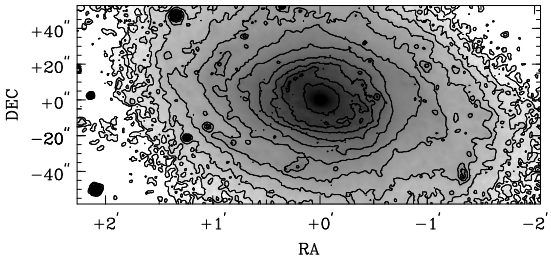

UGC 8279, contours at 19.5, 24.5, 0.5 R-mag arcsec^{-2}.

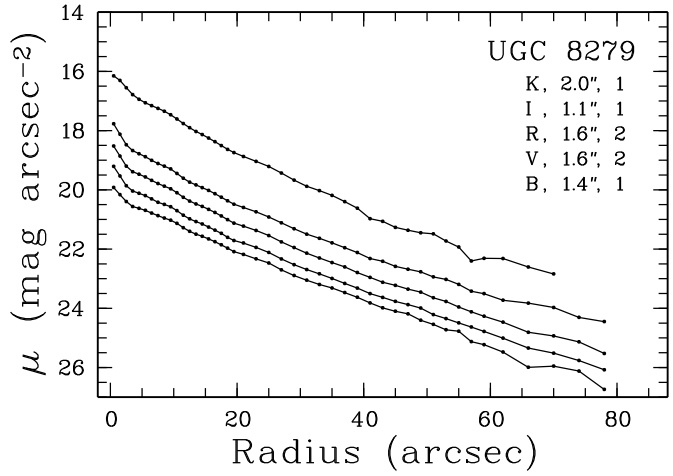

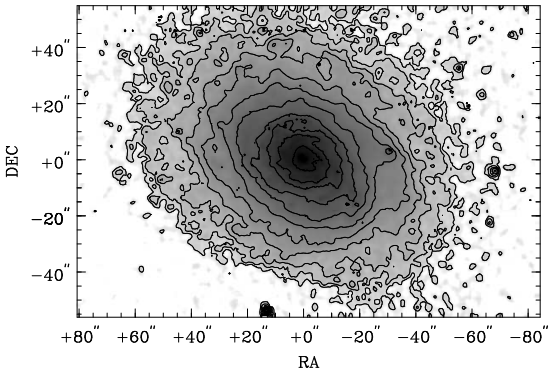

Fig. 12. -Continued.

UGC 8289, contours at 20.5, 24.5, 0.5 R-mag arcsec^{-2}.

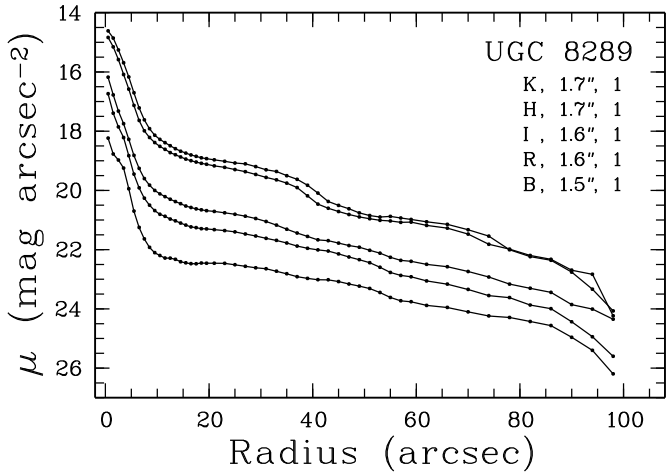

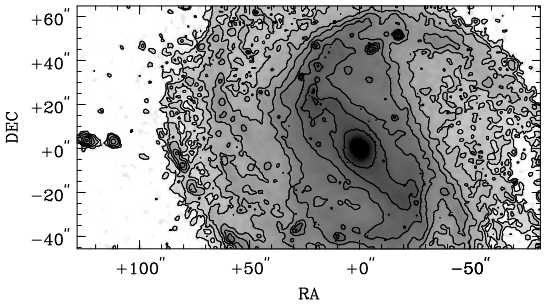

UGC 8865, contours at 19.5, 24.0, 0.5 R-mag arcsec^{-2}.

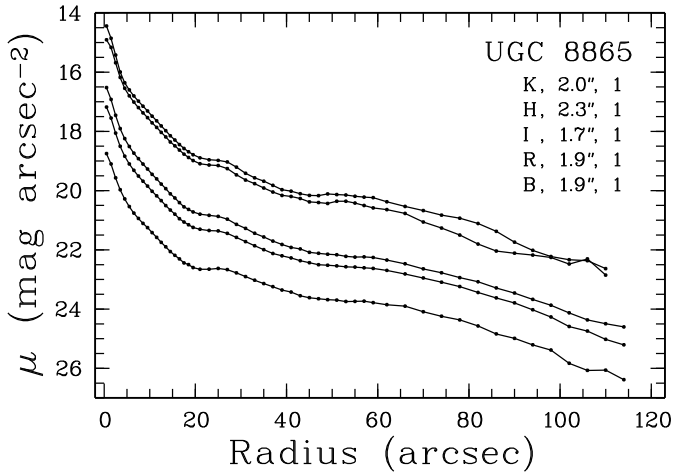

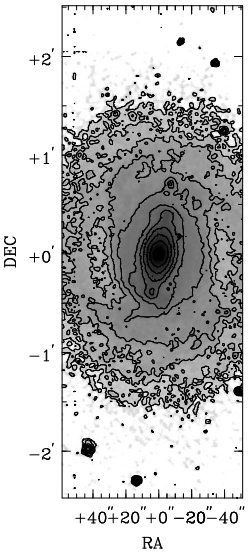

UGC 9024, contours at 21.0, 25.5, 0.5 R-mag arcsec^{-2}.

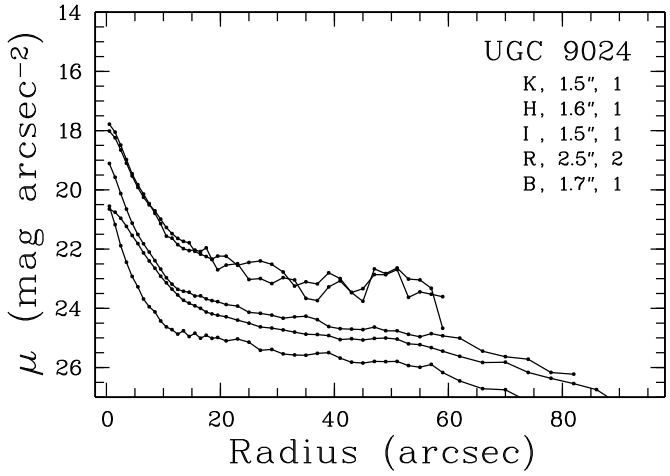

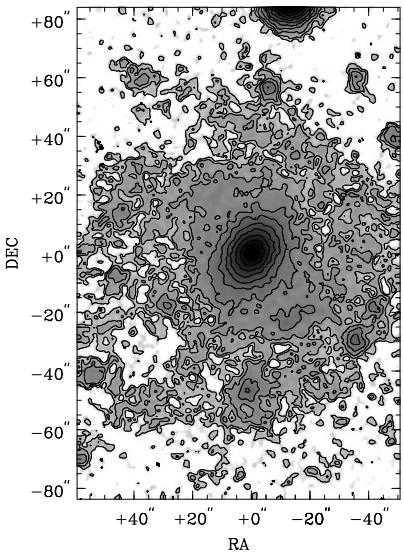

Fig. 12. -Continued.

UGC 9061, contours at 21.5, 24.0, 0.5 R-mag arcsec^{-2}.

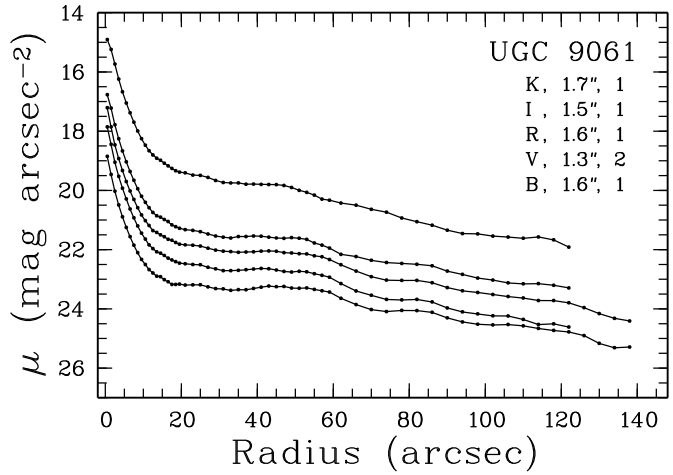

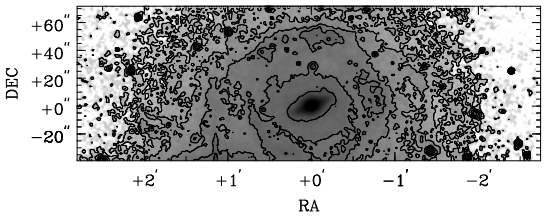

UGC 9481, contours at 20.5, 24.5, 0.5 R-mag arcsec^{-2}.

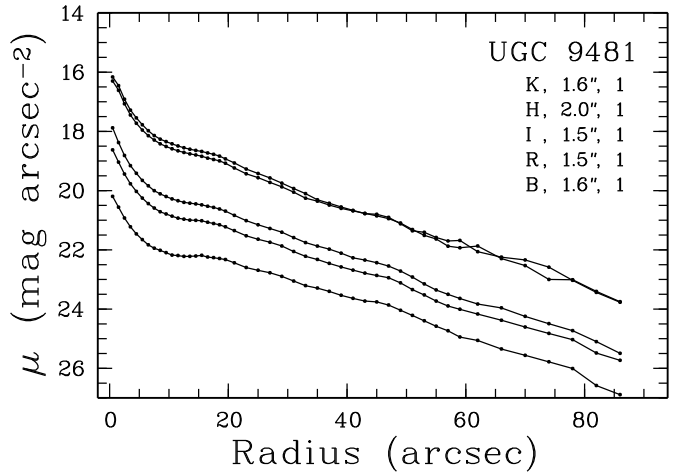

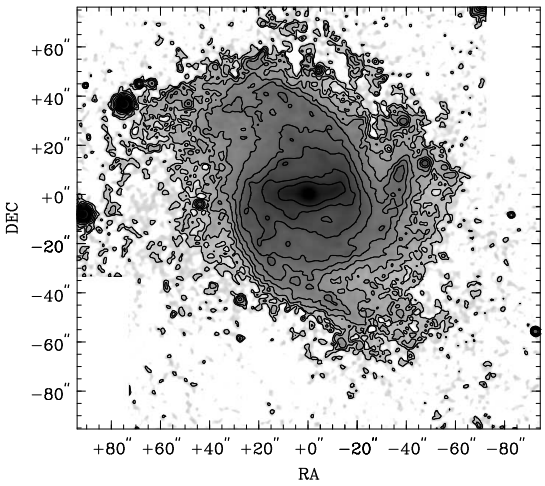

UGC 9915, contours at 20.5, 24.0, 0.5 R-mag arcsec^{-2}.

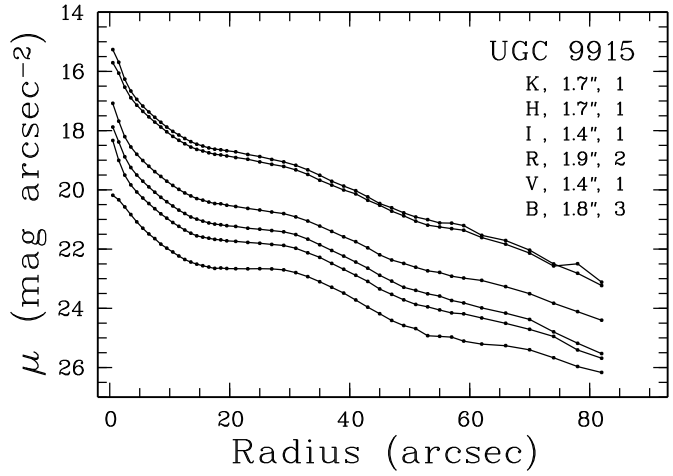

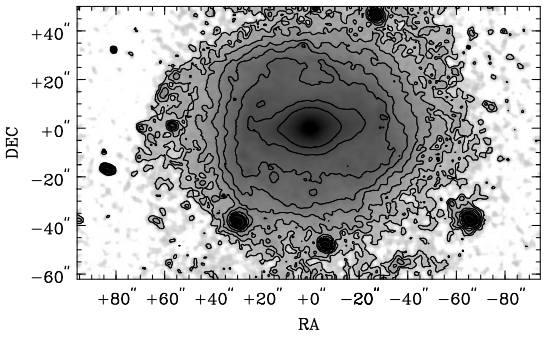

Fig. 12. -Continued.

UGC 9926, contours at 19.0, 24.5, 0.5 R-mag arcsec^{-2}.

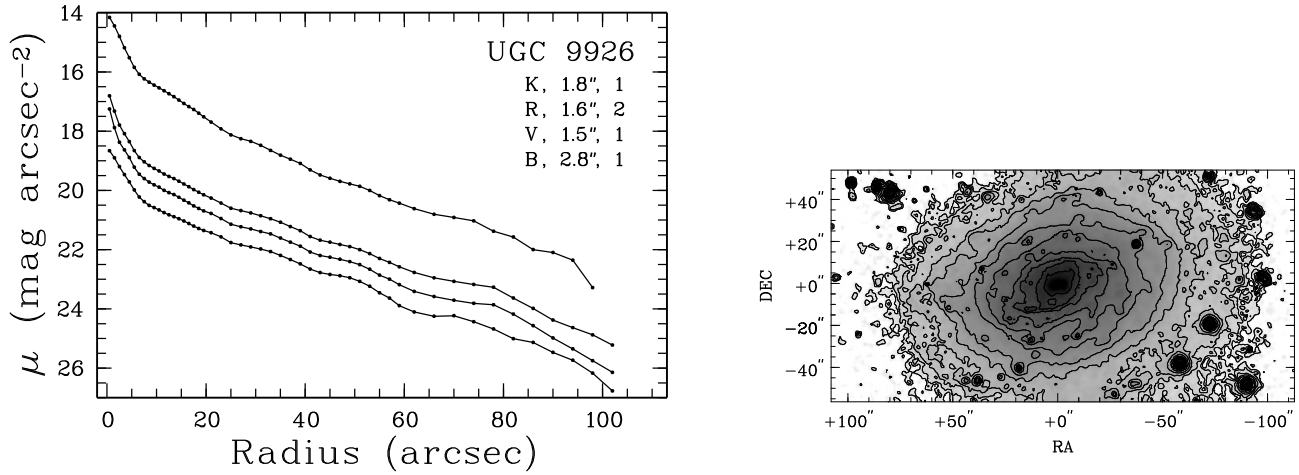

UGC 9943, contours at 19.5, 24.0, 0.5 R-mag arcsec^{-2}.

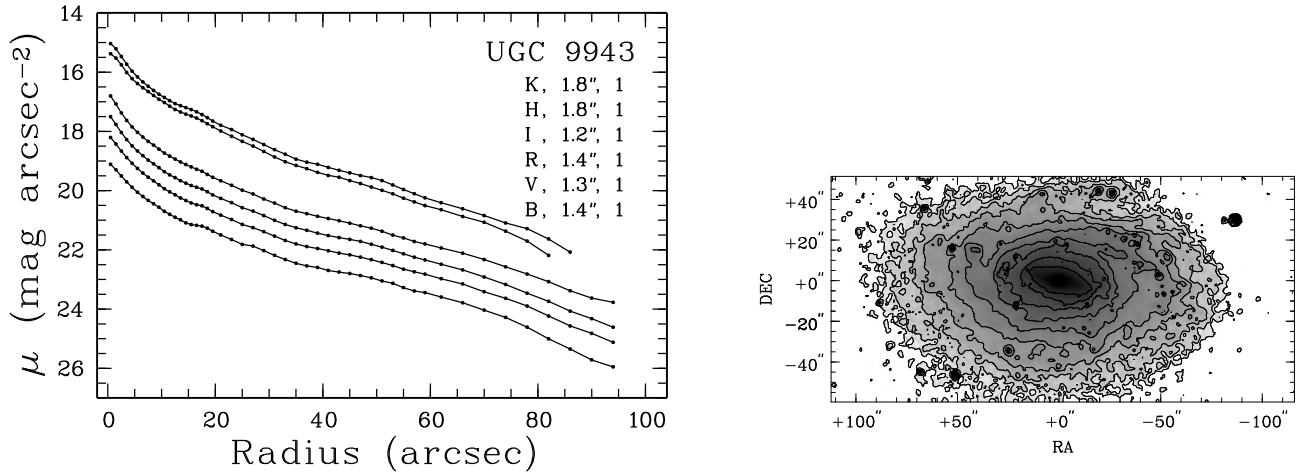

UGC 10083, contours at 19.5, 24.5, 0.5 R-mag arcsec^{-2}.

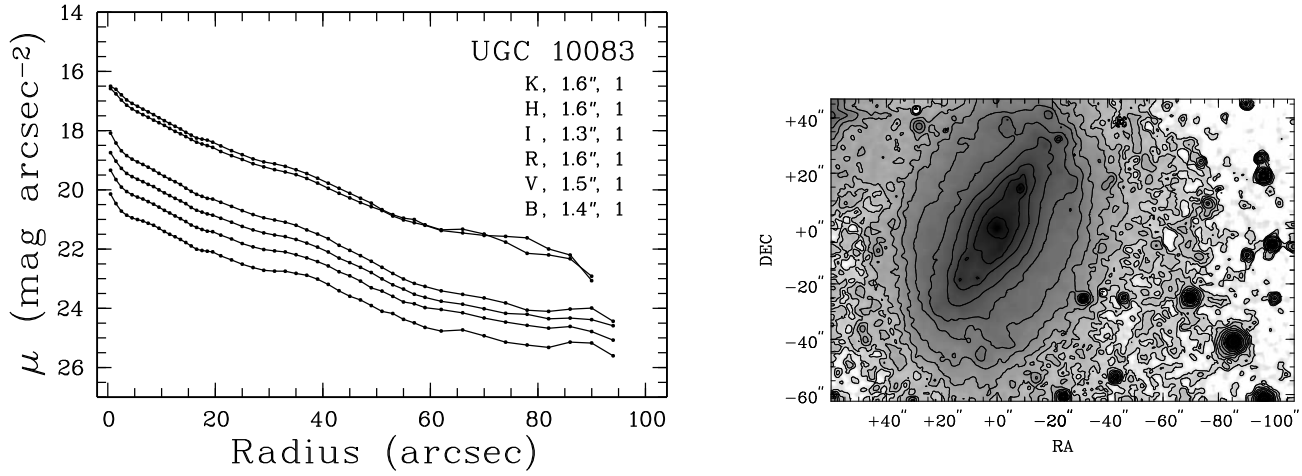

Fig. 12. -Continued.

UGC 10437, contours at 20.0, 24.0, 0.5 I-mag arcsec^{-2}.

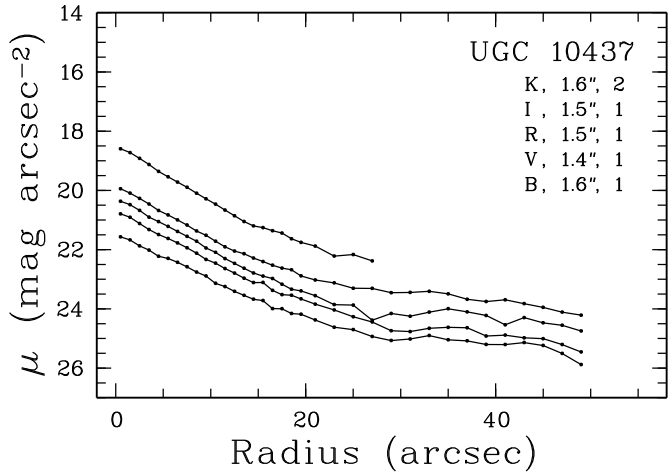

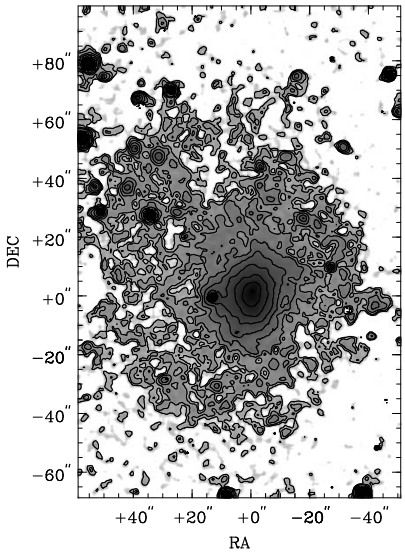

UGC 10445, contours at 21.0, 24.0, 0.5 R-mag arcsec^{-2}.

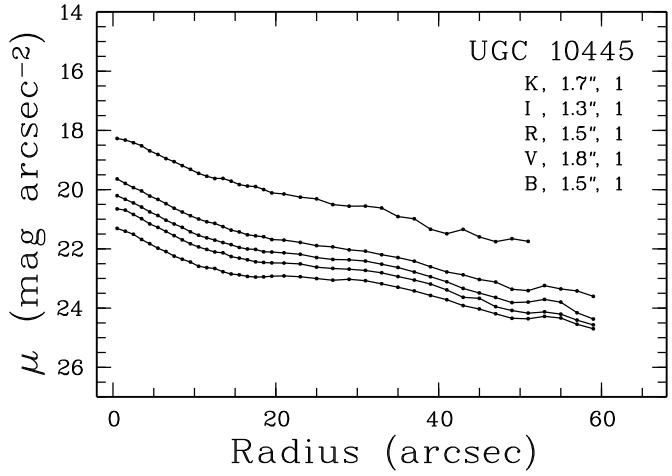

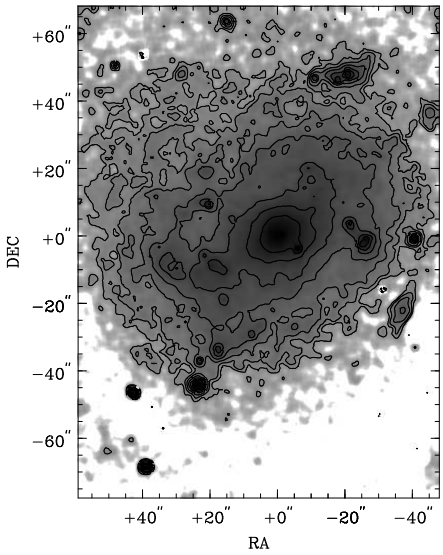

UGC 10445, contours at 21.0, 24.5, 0.5 R-mag arcsec^{-2}.

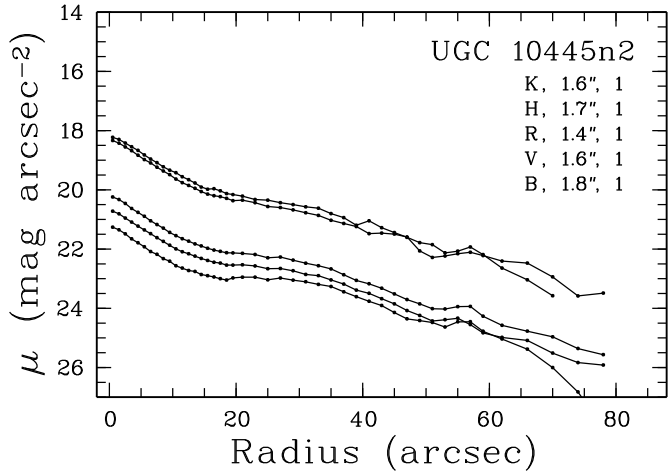

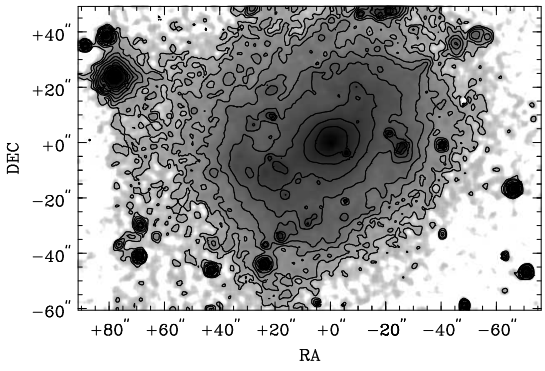

Fig. 12. -Continued.

UGC 10584, contours at 20.0, 24.0, 0.5 R-mag arcsec^{-2}.

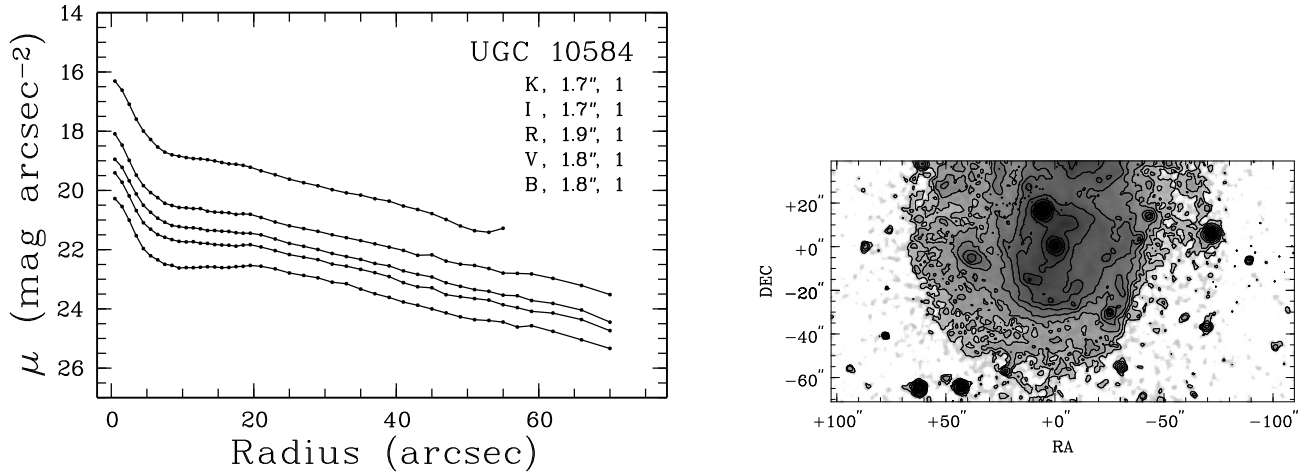

UGC 11628, contours at 19.0, 23.5, 0.5 R-mag arcsec^{-2}.

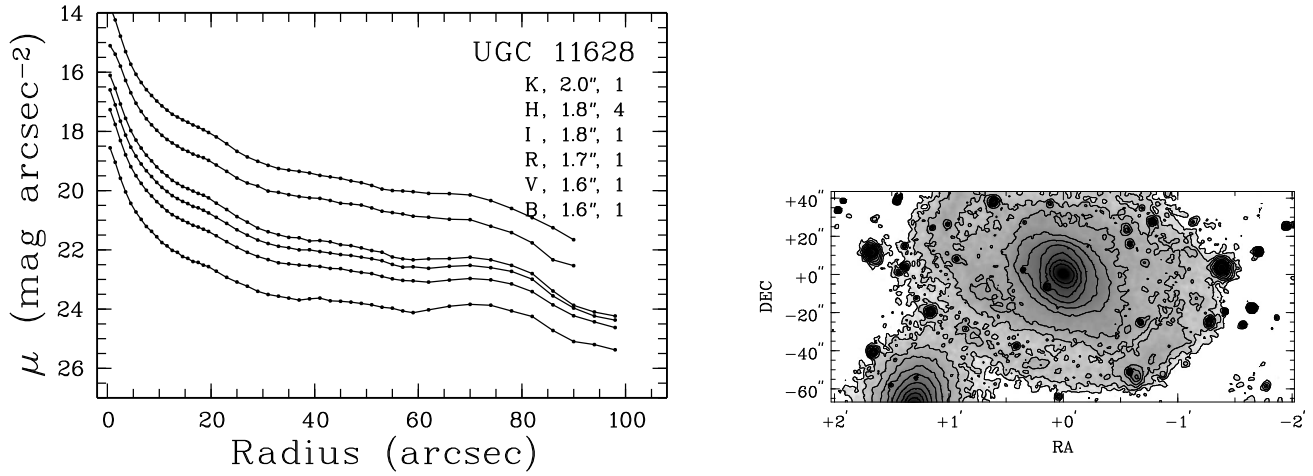

UGC 11708, contours at 20.0, 24.0, 0.5 R-mag arcsec^{-2}.

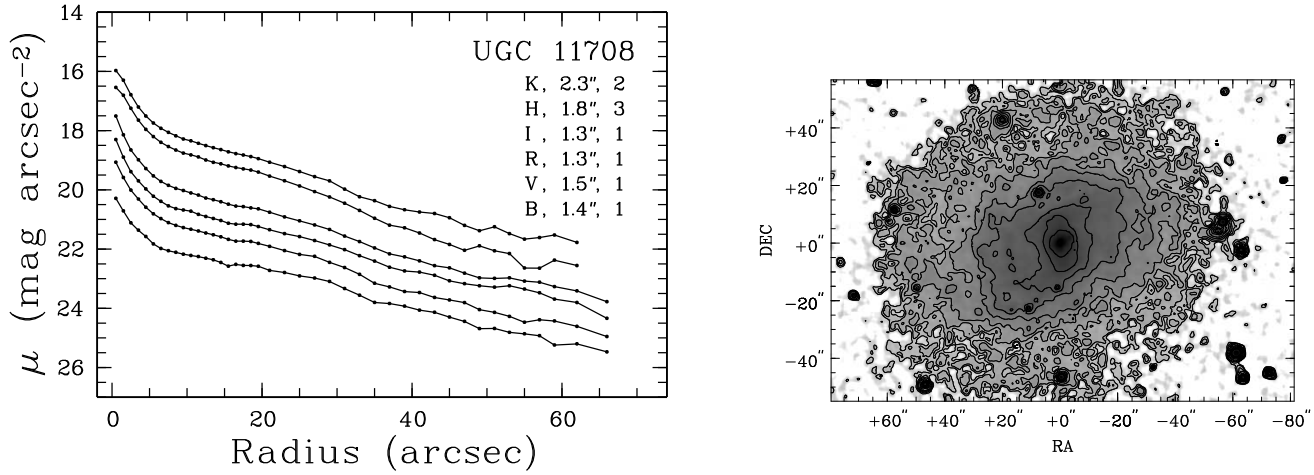

Fig. 12. -Continued.

UGC 11872, contours at 18.0, 24.0, 0.5 R-mag arcsec^{-2}.

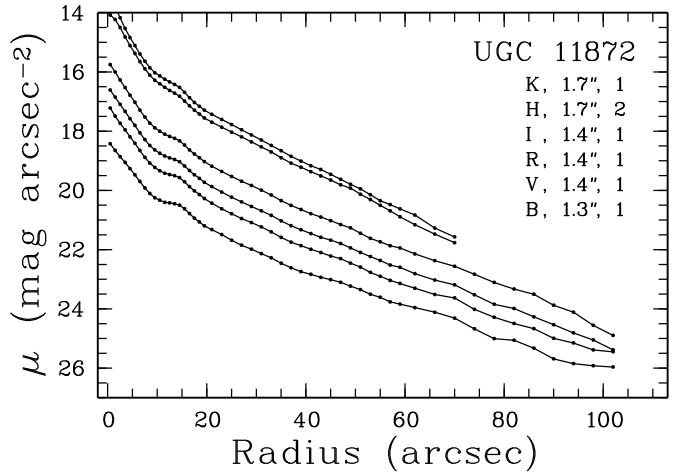

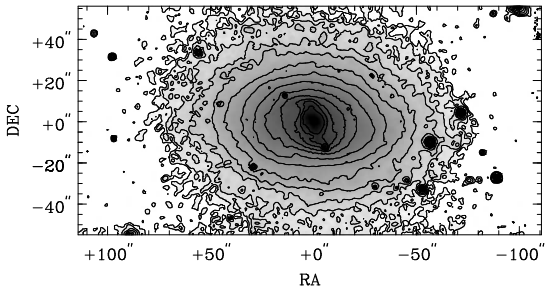

UGC 12151, contours at 21.5, 24.0, 0.5 R-mag arcsec^{-2}.

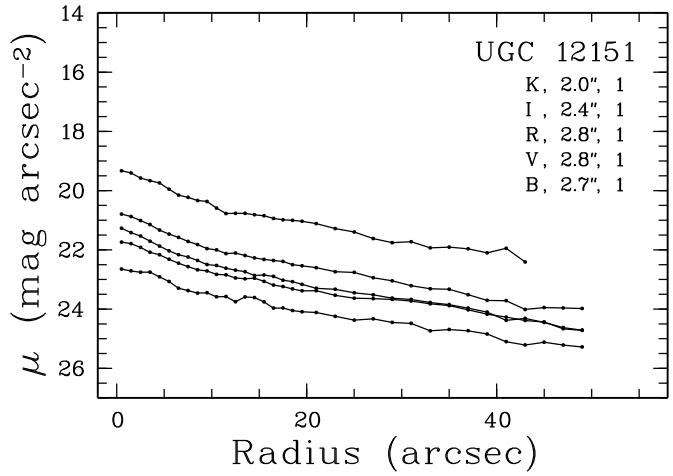

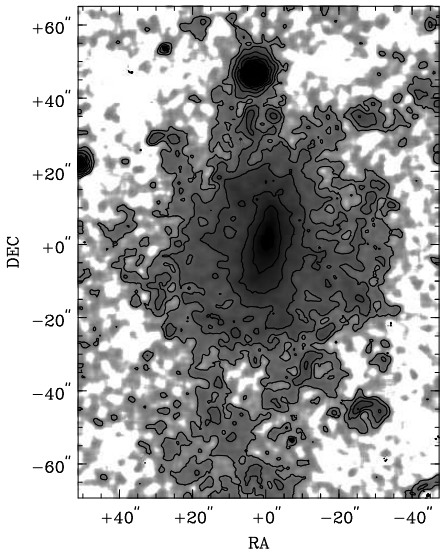

UGC 12343, contours at 18.5, 23.5, 0.5 R-mag arcsec^{-2}.

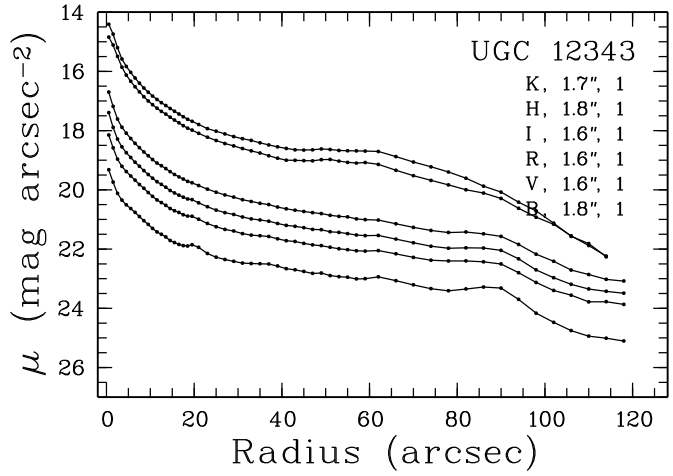

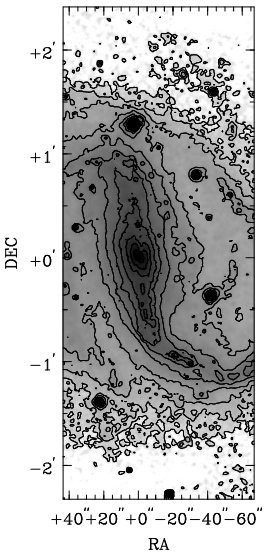

Fig. 12. -Continued.

UGC 12379, contours at 19.0, 24.0, 0.5 R-mag arcsec^{-2}.

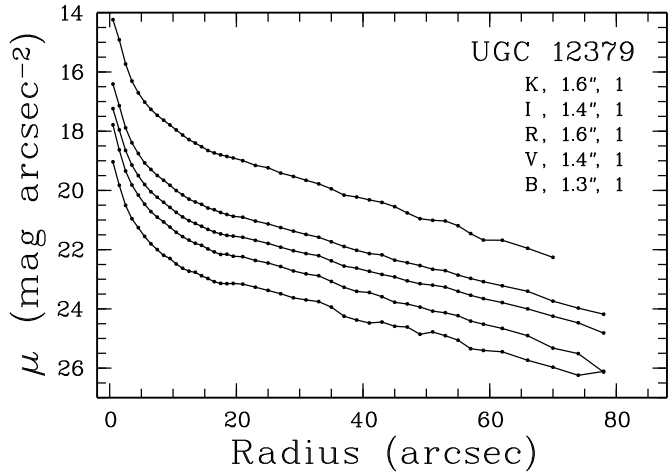

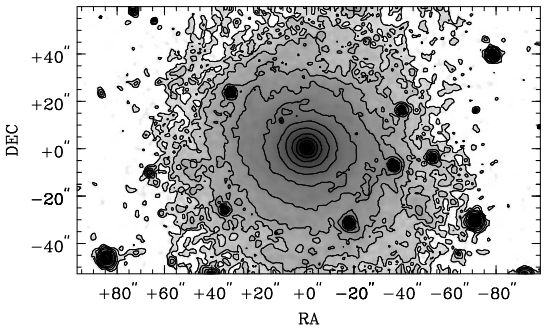

UGC 12391, contours at 20.5, 24.0, 0.5 R-mag arcsec^{-2}.

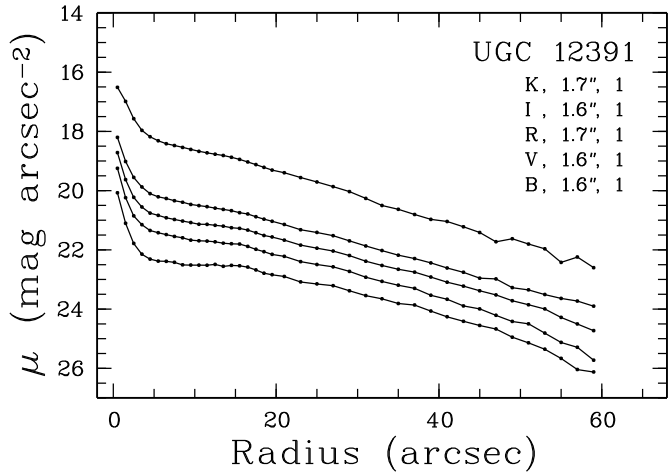

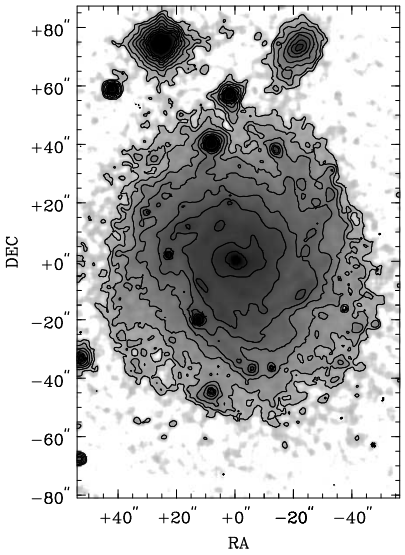

UGC 12511, contours at 20.0, 24.0, 0.5 R-mag arcsec^{-2}.

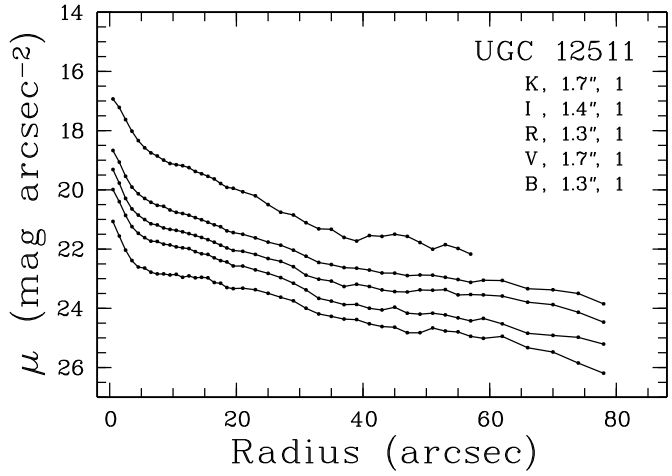

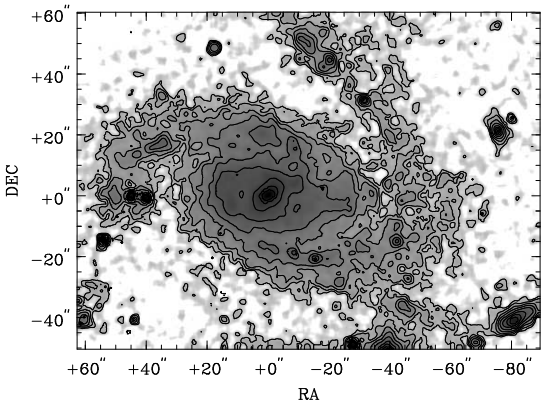

Fig. 12. -Continued.

UGC 12614, contours at 19.0, 24.0, 0.5 R-mag arcsec^{-2}.

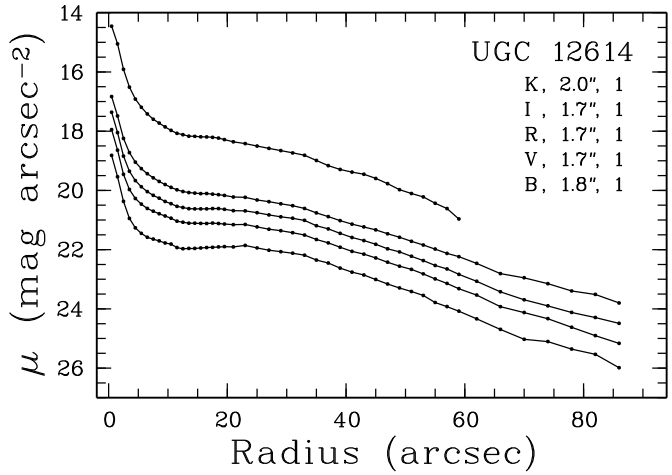

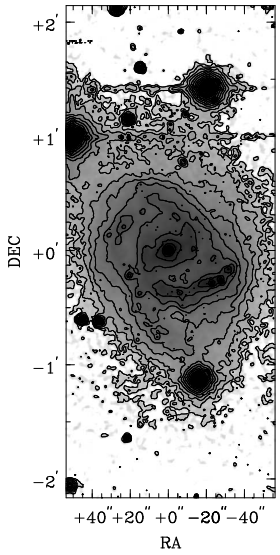

UGC 12638, contours at 21.0, 24.0, 0.5 R-mag arcsec^{-2}.

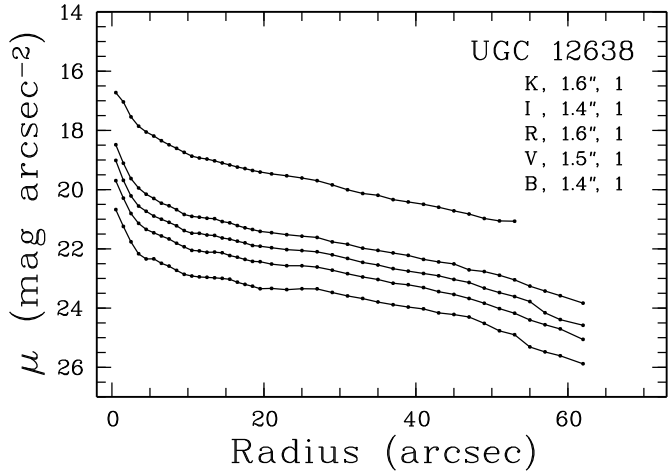

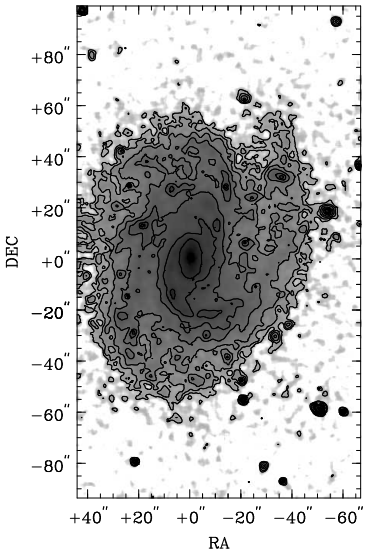

UGC 12654, contours at 20.0, 24.0, 0.5 R-mag arcsec^{-2}.

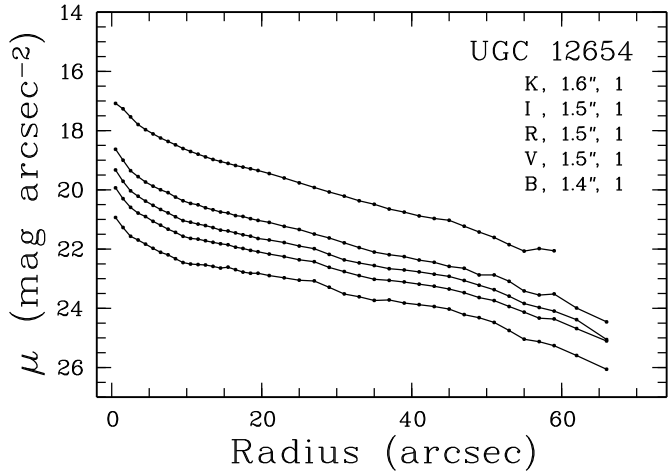

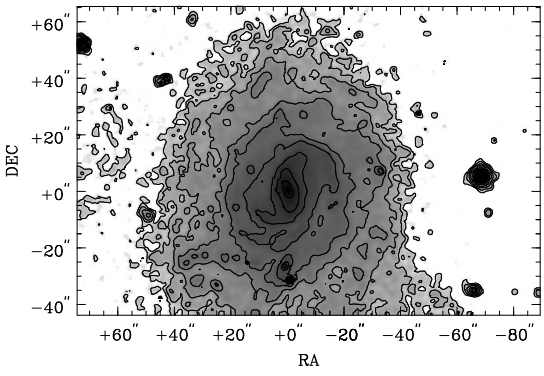

Fig. 12. -Continued.

UGC 12732, contours at 21.0, 24.0, 0.5 I-mag arcsec^{-2}.

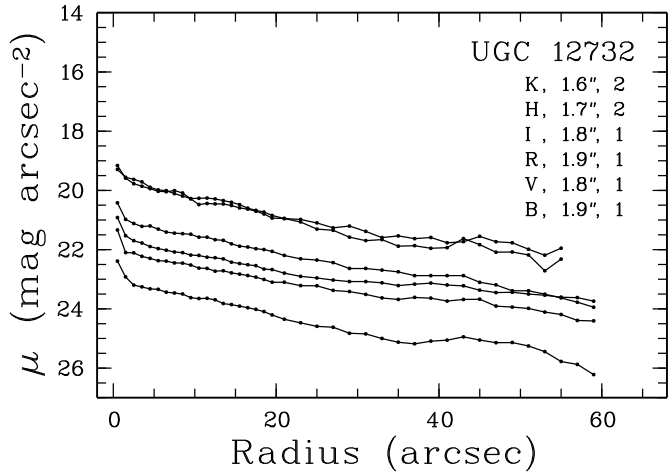

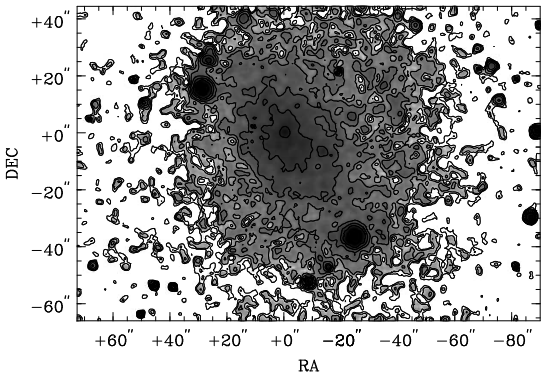

UGC 12754, contours at 20.0, 23.5, 0.5 R-mag arcsec^{-2}.

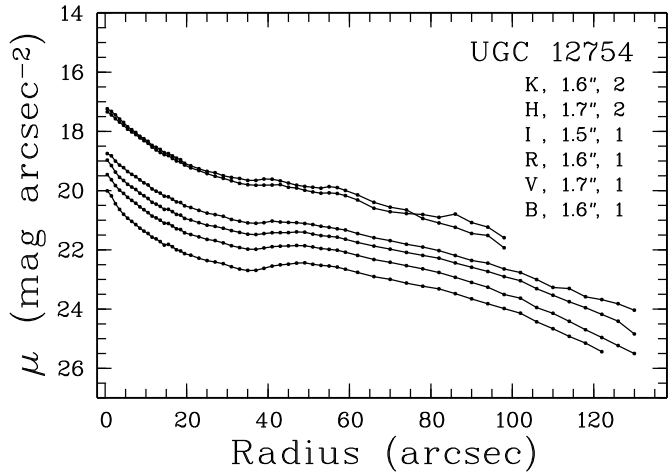

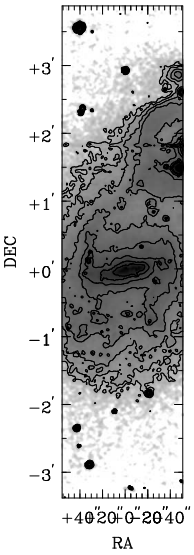

UGC 12776, contours at 20.0, 24.0, 0.5 R-mag arcsec^{-2}.

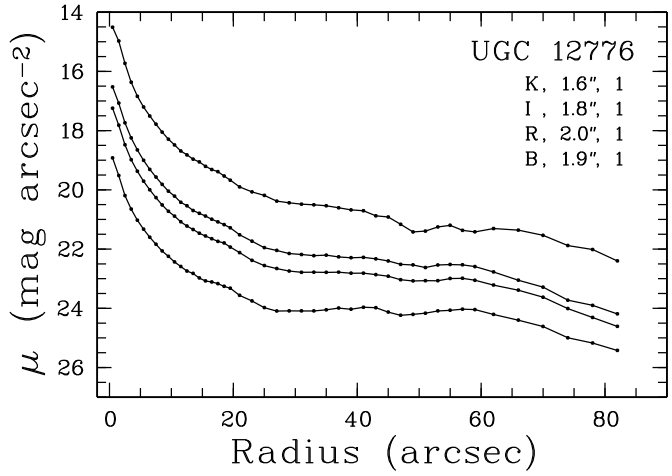

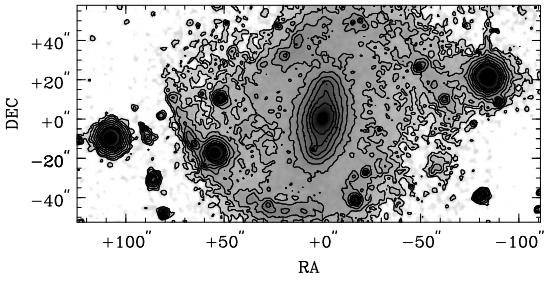

Fig. 12. -Continued.

UGC 12808, contours at 19.0, 24.0, 0.5 R-mag arcsec^{-2}.

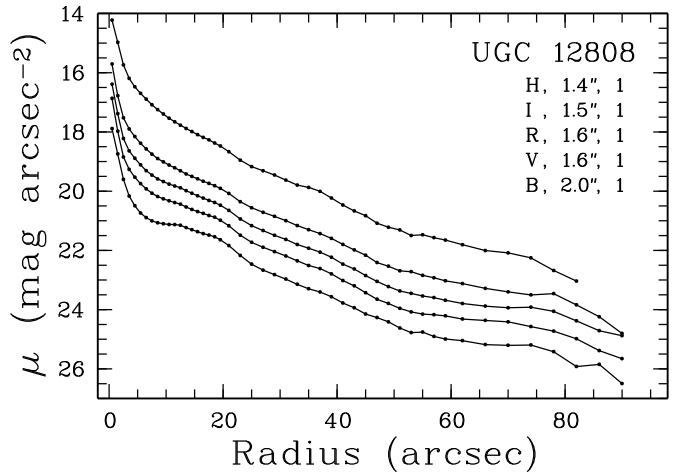

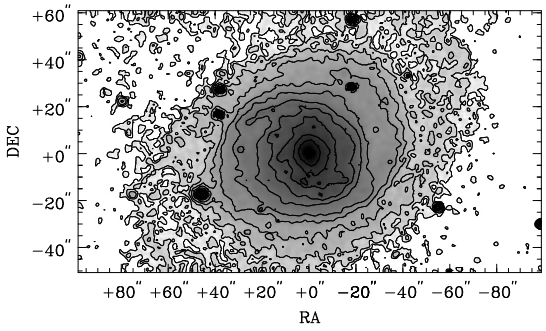

UGC 12845, contours at 21.0, 24.0, 0.5 R-mag arcsec^{-2}.

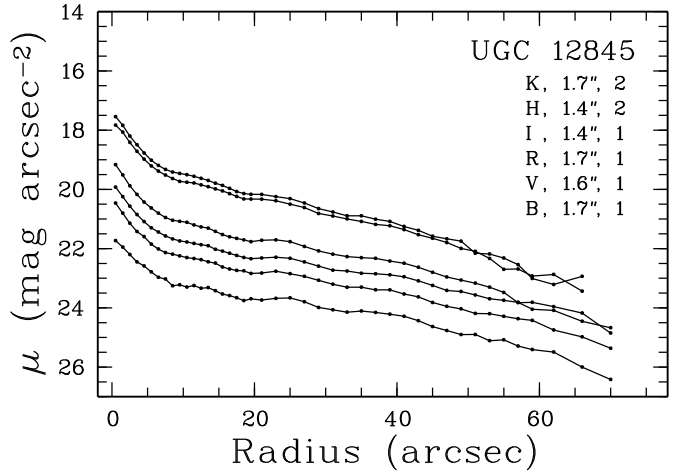

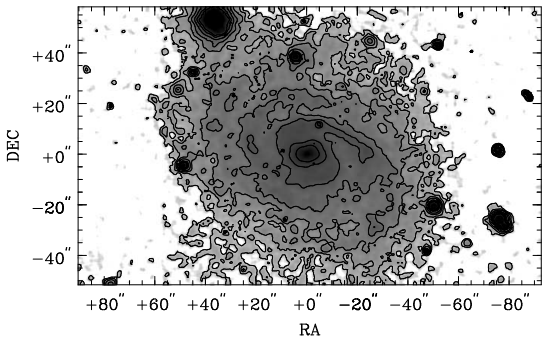

Fig. 12. -Continued.

Chapter 2

A two-dimensional method to determine disk and bulge parameters

Abstract. In this paper I present a new two-dimensional decomposition technique, which models the surface photometry of a galaxy with an exponential light profile for both bulge and disk and, when necessary, with a Freeman bar. The new technique was tested for systematic errors on both artificial and real data and compared with widely used one-dimensional decomposition techniques, where the luminosity profile of the galaxy is used. The comparisons indicate that a decomposition of the two-dimensional image of the galaxy with an exponential light profile for both bulge and disk yields the most reproducible and representative bulge and disk parameters.
An extensive error analysis was made to determine the reliability of the model parameters. If the model with an exponential bulge profile is a reasonable description of a galaxy, the maximum errors in the derived model parameters are of order 20%. The uncertainties in the model parameters will increase, if the exponential bulge function is replaced by other often used bulge functions as the de Vaucouleurs law.
All decomposition methods were applied to the optical and near-infrared data set presented by de Jong & van der Kruit (1994), which comprises 86 galaxies in six passbands.

1 Introduction

The light distribution of disk dominated galaxies is often decomposed into a bulge and a disk component which are assumed to be physically and dynamically distinct. The disk component is flat and governed by rotational dynamics. The spherical bulge component, though mainly rotationally supported against gravity, is dynamically a much hotter system than the disk. Whether this separation is real is hard to say; it is likely that a dynamical interplay exists between the different components in the dense inner regions of galaxies. Seperating both components using only the surface photometry of a galaxy has been a longstanding problem.

When we assume that there are distinct components, the parameters describing the light distribution of these components are of fundamental importance. They reveal the common properties among galaxies and especially in combination with dynamics and (chemical) content they are tracers of galaxy formation and evolution. Two well-known relations with fundamental component parameters are the constancy of central surface brightness among disks of spiral galaxies (Freeman 1970) and the link between bulge-to-disk (B/D) ratio and the Hubble classification sequence.

Many different decomposition techniques can be found in the literature (for reviews see e.g. Simien 1989, Capaccioli & Caon 1992). For most of the methods one postulates some mathematical functions describing the shape of the different components, after which the sum of the components functions is fitted to the observed light distribution. Decomposition techniques differ in both the assumed mathematical functions as well as in the applied fitting algorithms.

The most frequently used function describing the radial surface brightness profile of the disks of spiral galaxies is the exponential function

$$\Sigma_{\rm disk}(r) = \Sigma_0 {\rm e}^{-r/h} \tag{1}$$

or in magnitudes

$$\mu_{\rm disk}(r) = \mu_0 + 1.086 r/h \tag{2}$$

with μ_0 (Σ_0) being the central surface brightness (luminosity) and h the scalelength of the exponential disk. The exponential function is not always a good description of the disk light profile. After the bulge light is subtracted from the luminosity profile, the disk profiles of spiral galaxies sometimes show a deficit of light in their inner regions (Type II profiles, Freeman 1970). An improved disk model in the form of a modified exponential profile (Kormendy 1977) is therefore sometimes fitted to these Type II profiles. Furthermore, it should be noted that the exponential model profile might need a truncation. Especially in edge-on galaxies a sudden decrease in light has often been detected at large radii (van der Kruit 1979).

Compared to the disk profile there is less consensus on the mathematical function to be used for the bulge light profile, because only the central bright part of the bulge can be seen in most spiral galaxies. Away from the center the bulge light is hidden underneath the disk light for a face-on galaxy and therefore only the central region can be used to determine the shape of the bulge luminosity profile. The most widely used bulge function is the $r^{1/4}$ law (de Vaucouleurs 1948). This function generally gives a good description of the light distribution of elliptical galaxies and was first used for spiral bulges, in combination with an exponential disk, by de Vaucouleurs

(1959). The motivation to use the same fitting function for elliptical galaxies and bulges is an assumed evolutionary or at least structural sequence from ellipticals to spirals (or vice versa). Therefore all light profile functions proposed for ellipticals (e.g. Hubble profiles (1930), King profiles (1966), Jaffe profiles (1983) or generalized exponentials (Caon et al. 1993)) can also be used for bulges. Kormendy (1977) showed that the parameters of the Hubble, King and de Vaucouleurs profiles describe the same physical quantities for ellipticals.

One should be careful in making the link between elliptical galaxies and bulges of spiral galaxies. The presence of the disk will influence the dynamics of the bulge, especially for late-type systems with a low B/D ratio. Bulges are for a considerable fraction rotationally supported against gravity and not largely pressure supported as are elliptical galaxies (Kormendy & Illingworth 1978; Kormendy 1993 and references therein). Also deviations from the $r^{1/4}$ law have been observed in bulges of edge-on spirals (Frankston & Schild 1976, Kormendy & Bruzual 1978, Burstein 1979, Jensen & Thuan 1979, Shaw & Gilmore 1989, Wainscoat et al. 1989, Kent et al. 1991). These deviations have motivated Frankston & Schild (1976), Kent et al. (1991) and Andredakis & Sanders (1994) to propose exponential functions for bulge profiles.

Decomposition techniques using the change in ellipticities and position angles of the isophotes (Kent 1986) have the advantage that they do not have to assume fitting functions. They can work perfectly well assuming that spiral galaxies are only made of ellipsoids/tori with changing inclinations. But as real galaxies contain bars, spiral arms and dust lanes these methods will have systematic errors. They only work reasonably well on systems with a high inclination, where the difference in the flattening of the disk and the bulge component is easily measurable.

Decompositions using all the pixels in the full image instead of the one-dimensional (1D) profile of galaxies take little precedence in the literature. The main reason for this being the lack of computer power and an additional reason being the difficulties due to the presence of bars and spiral arms. These are conveniently averaged out in 1D profiles. Two-dimensional (2D) fitting techniques have been applied before on small samples of elliptical galaxies and S0's (Capaccioli et al. 1987; Simien & Michard 1990; Scorza & Bender 1990), but only once before on a large set of spiral galaxies (Byun 1992). Two-dimensional fitting has the same advantage as Kent's method (Kent 1986) in that one uses the difference in projected ellipticities of disk and bulge. The sample used here was selected to be face-on and the differences in ellipticities are expected to be small. Still the 2D fitting technique is applied, because it has the advantage to 1D fitting that non-axisymmetric components can be fitted as well. The method applied here has a non-axisymmetric component in the form of a bar, which will improve the fitting results of the disk and especially the bulge component.

The bulge and disk parameters determined by the 2D method will be used in subsequent papers to determine the relationships among the structural parameters of galaxies. To assess the reliability of these relationships a thorough error analysis is needed. In this paper I will discuss several sources of error, most notably the effects of 1D versus 2D fitting, the uncertainty in the shape of disk and bulge profiles, influences of measurement errors and the effect of different radial weighting functions.

The structure of this paper is as follows. The observational data are briefly described in Section 2. The 2D fitting technique is explained and tested in Section 3. In Section 4 the 2D fitting technique is compared with several 1D fitting techniques. The results of all tests and comparisons are used in the error discussion in Section 5. The main conclusions are summarized in Section 6.

2 The data

In order to examine the parameters describing the global structure of spiral galaxies, 86 systems were observed in the B, V, R, I, H and K passbands. A full description of the observations and data extraction can be found in Paper I (de Jong & van der Kruit 1994). The galaxies in this statistically complete sample of undisturbed spirals were selected from the UGC (Nilson 1973) to have red diameters of at least two minutes of arc and minor over major axis ratios larger than 0.625. The galaxies were imaged along the major axis with the 1m Jacobus Kapteyn Telescope on La Palma in the B, V, R and I passbands and with the United Kingdom Infra-Red Telescope on Hawaii in the H and K passbands. Standard reduction techniques were used to produce calibrated images. The sky brightness was determined outside the galaxy in areas free of stars and its uncertainty constitutes one of the main sources of error in the derived parameters.

The ellipticity and position angle (PA) of each galaxy were determined at an outer isophote. The radial surface brightness profiles were determined by calculating the average surface brightness on elliptical rings of increasing radii using the determined ellipticity and PA. Internal and external comparisons showed that the derived parameters were well within the estimated errors. These estimated errors are included in the analysis discussed here.

3 Two-dimensional decomposition

In this section the 2D fitting technique is described. The motivation for using the 2D method was the large number of galaxies in the sample with a pronounced bar, which can not be fitted in 1D models. The different model components are described and the fitting procedure followed is explained in some detail. The fitting technique was tested on both artificial and real data and is shown to be very accurate in most realistic cases. Finally, the results for the data set are presented for the B and the K passband.

3.1 Advantages of two-dimensional fitting

In the literature one encounters mainly the use of 1D profiles to perform bulge/disk decompositions. The extraction of the profiles improves the signal-to-noise, but the non-axisymmetric

information present in the image is lost. Bars can have considerable influence on profiles (see for example in Paper I UGC 89, UGC 6536, UGC 7523, UGC 7594, UGC 8865 and UGC 12776). These features will make 1D bulge/disk decompositions incorrect, even if the fits seem correct and the χ^2 values are low. One-dimensional models fitted to azimuthally averaged profiles can never include a bar.

A considerable fraction of spiral galaxies are barred. Of the 86 galaxies of our sample only 13 were classified as non-barred according the RC3 (de Vaucouleurs et al. 1991) and 12 galaxies had no bar classification. Therefore fitting bars is desirable, especially if one considers that bars are more pronounced in the near-IR (Block & Wainscoat 1991). This can only be done by fitting the full 2D images. An additional advantage of the 2D technique is that the difference in the flattening of the bulge and the disk is also used for the few systems in the sample with higher inclination.

The technique of fitting models to the full images of spiral galaxies has little precedence in the literature. Shaw & Gilmore (1989) fitted 2D models to two edge-on galaxies, the configuration where disk and bulge are the most distinct. Byun (1992) used a data set of 1355 I passband images of galaxies with inclinations larger than $i > 40^{\rm o}$. From tests on artificial data, Byun showed that the 2D method was better in reproducing the model input parameters than the 1D method. Neither Shaw & Gilmore nor Byun included a bar in their fits.

3.2 The model components

The 2D model consists of two or three components. First of all, a spherically symmetrical bulge with an exponential radial light distribution. The use of an exponential bulge profile instead of the more widely used $r^{1/4}$ law profile (de Vaucouleurs 1948) was motivated by the work of Andredakis & Sanders (1994) and the work presented in Section 4. Bulge parameters are normally expressed in effective parameters which translates the exponential law into

$$\Sigma_{\rm bulge}(r) = \Sigma_{\rm e} {\rm e}^{-1.679(r/r_{\rm e}-1)}, \quad (1)$$

where the effective radius ($r_{\rm e}$) encloses half the total luminosity and $\Sigma_{\rm e}$ is the surface brightness ($\mu_{\rm e}$ in mag) at this radius. In the carthesian coordinate system of the CCD image r schould be read as $\sqrt{x^2+y^2}$, with the center of the coordinate system at the galaxy center.

The second component, the disk, is described by Eq. (1) and has the usual two free parameters of an exponential light distribution (Σ_0 and h). Due to inclination though, the disk has two additional parameters: minor over major axis ratio (b/a) and position angle (PA) and r should be read as $\sqrt{([x\cos({\rm PA})+y\sin({\rm PA})]\frac{b}{a})^2+(-x\sin({\rm PA})+y\cos({\rm PA}))^2}$ in the carthesian coordinate system. Fitting with b/a and PA as free parameters was tried, but it turned out that the the fitting routine often adjusted the b/a and PA in such a way that spiral arms and bars were modeled, instead of the global disk properties. Therefore I decided to keep b/a and PA fixed to the values determined at the outer isophotes (the same values that were used for extracting the radial profiles).

When necessary, a bar was added as a third component to the model. A Freeman bar (1966) was used, which is one of the few available analytic 2D descriptions for the luminosity of a bar

$$\Sigma_{\rm bar}(x,y) = \Sigma_{0,\rm bar}\sqrt{1-(x/a_{\rm bar})^2-(y/b_{\rm bar})^2}, \quad (2)$$

where the free parameters are $\Sigma_{0,\rm bar}$, the bar central surface brightness, and $a_{\rm bar}$ and $b_{\rm bar}$, the semi major and minor axis of the bar respectively. Such a bar has elliptical isophotes and has its position angle ($\rm PA_{bar}$) as additional free parameter. No inclination dependent corrections were applied to the bar profiles, since the studied galaxies are not inclined very much.

Observations of galaxies are distorted by seeing. The model light distributions have to be corrected for this effect. Seeing is only important at the center of the galaxy where the light distribution strongly peaks. The disk and bar light distributions are far less peaked and generally do not dominate the center compared to the bulge, therefore only the bulge model profile was corrected for seeing.

To account for the seeing effects, the model profiles of the bulge were convolved with a Gaussian Point Spread Function (PSF) with the same dispersion (σ) as the Gaussians that were fitted to some field stars in the frame. For a radially symmetric light distribution around the center the seeing convolved profiles are described by

$$\Sigma_{\rm s}(r) = \sigma^{-2}e^{-r^2/2\sigma^2}\int_0^\infty \Sigma(x)I_0(xr/\sigma^2)e^{x^2/2\sigma^2}x\,dx, \quad (3)$$

where $\Sigma(r)$ is the intrinsic surface brightness profile, σ the dispersion of the Gaussian PSF and I_0 the zero-order modified Bessel function of the first kind (Pritchet & Kline 1981).

The total model is simply the sum of the three components

$$\Sigma_{\rm tot}(x,y) = \Sigma_{\rm disk}(x,y) + \Sigma_{\rm bulge}(x,y) + \Sigma_{\rm bar}(x,y). \quad (4)$$

3.3 Fitting procedure

To fit models to the data points a non-linear fitting algorithm capable of accepting different weights for each data point was applied. Non-linear fitting algorithms are particularly sensitive to the initial values provided, when searching for the minimum in the reduced χ^2 of the fit. If the initial values are not "reasonable", the fitting program can end up in a wrong local minimum. The results of the 1D decompositions described in Section 4 were used as initial values. The initial values for the bar were estimated by eye. The routine generally converged to the same result to within the formal errors, independent of the initial values. The formal fit errors were usually much smaller than the errors due to the uncertainties in the measurements and these errors will be discussed in detail in Section 4 and 5.

In decomposing 1D profiles it is common practice to fit in the logarithmic (magnitude) regime. This means that one is effectively trying to minimize the relative errors between model and data. Minimization in the logarithmic regime is not possible in the 2D case; because of the noise some pixels will have negative values (below sky level) in the outer parts of the

Table 1. The test results of the 2D fit using an R passband image of UGC 438. A bulge with μ_e=18.954 R-mag arcsec^{-2} and r_e=2.5$''$ (the parameters resulting from the initial fit) was subtracted. It was replaced by an exponential bulge of the indicated model parameters and fitted by the normal 2D fit routine. The resulting μ_0 and μ_e are in R-mag arcsec^{-2} and the h and r_e are in arcsec. NC indicates that no convergence was reached.

model μ_e		model r_e = 2.5$''$			model r_e = 5.0$''$				model r_e = 1.25$''$			
	fitted μ_0	h	μ_e	r_e	μ_0	h	μ_e	r_e	μ_0	h	μ_e	r_e
16.454	18.891	12.91	16.453	2.502	19.025	13.42	16.457	5.054	18.869	12.81	16.373	1.192
17.207	18.891	12.91	17.205	2.502	19.026	13.42	17.213	5.087	18.869	12.81	17.037	1.125
18.201	18.891	12.91	18.201	2.502	19.026	13.42	18.216	5.205	18.870	12.81	17.719	0.923
18.954	18.891	12.91	18.954	2.502	19.025	13.42	18.977	5.406	18.873	12.83	17.792	0.638
19.707	18.891	12.91	19.703	2.485	19.020	13.40	19.735	5.725	18.882	12.87	17.359	0.353
20.459	18.888	12.90	20.415	2.401	18.997	13.31	20.454	6.011	NC			

galaxy image. To minimize relative errors in the linear regime, a difference between model and data in a low surface brightness region has to be given much more weight during the fitting than the same difference in a high surface brightness area. A weight function of the form $e^{r/h}$ was used, where h is the initial estimate of the disk scalelength and r is the inclination corrected distance of the pixel from the center. To reduce computing time all pixels outside 2.5 initial disk scalelengths were averaged over 5×5 pixels and given proportionally more weight.

The 2D fitting procedure consisted of several steps. First, all images of a galaxy obtained in different passbands were aligned, freed of foreground stars and their center was determined from the R passband image (see Paper I). This center was fixed while fitting the model components to the data. After the fitting routine had converged, the model light distribution was subtracted from the data. The points in the difference image that deviated more than 6 sigma (missed cosmic ray events and faint stars) were flagged and not used in the next iteration. This process was repeated twice, each time taking the initial estimates and the scalelength of the weight function from the results of the previous step. In general, the routine had already converged to a satisfactory result after the second step.

3.4 Tests on artificial data

The 2D fitting routine was extensively tested on artificial images to determine its reliability. Artificial images are not really representative of true galaxies, but can give an indication of the systematic effects due to measurement errors. By varying one by one the observables in the artificial images one can investigate which measurement error influences a model parameter the most.

The artificial images had the characteristics of a typical R passband observation: all artificial galaxies had an exponential disk with a μ_0 equal to 20 mag arcsec^{-2}, a scalelength of 20$''$ and axial ratio of 0.75. Just as with the typical observation the pixel size was set at 0.3$''$, the seeing at 1.5$''$ FWHM and the sky surface brightness at 20 mag arcsec^{-2} in the artificial images. An exponential bulge was added to each image, with the bulge parameters chosen from a range in effective surface brightness and radius . The images were created with photon and read out noise and a few areas were set to undefined values to mimic the removal of foreground stars. The initial fit estimates for the disk and bulge parameters were set at 10-30% off the intrinsic model values to check convergence. The final results showed very little sensitivity to the initial estimates.

The effect of different bulge-to-disk ratios was tested using the artificial images with the different bulge parameter values. The relative differences between artificial image input parameters and the model fit output parameters are listed in Table 2. The fitting routine reproduced the bulge and disk parameters to a very high degree of accuracy. The disk parameters were reproduced with less than 1.5% error. The bulge parameters were less well reproduced, especially for very small effective radii and low effective surface brightnesses. These bulges are so small that they are unresolved with 1.5$''$ seeing in the small region where they are dominating over the disk surface brightness. For these extreme cases it is better to convolve not only the bulge model with the seeing, but also the disk. Increasing the seeing to 2.5$''$ in both the artificial image and the fitting model had no effect on the determination of the disk parameters and slightly decreased the fit performance for the bulge parameters, as can be seen in Table 2.

Some observables measured from the images (seeing, sky background level, b/a and PA) were used as fixed parameters in the fitt models. To estimate their relative effects on the derived parameters, all artificial images were fitted again, but the fixed parameters in the fitting model were given a wrong value with respect to the true values in the artificial image. The typical maximum error was used for each of the fixed parameters. The test results can be found in Table 2. From these tests the largest error in μ_0 is expected to result from a wrong estimation of the sky background. The error will be of order 0.1 mag arcsec^{-2}, increasing, of course, for lower surface brightness galaxies. The errors in the scalelength are dominated by errors in sky brightness and b/a, and both result in errors less than 10% in the typical case. The errors in the bulge parameters are dominated by their brightness and scalelength relative to the disk parameters. The parameters of the brighter bulges are most effected by errors in the seeing. The effective radii of the lower surface brightness bulges are also influenced by sky brightness errors. Except for the extreme low surface brightness bulges and for bulges with effective radii smaller than 1$''$ the errors are never larger than 20%.

Table 2. The relative errors in bulge and disk parameters determined on artificial images of galaxies using the 2D fit method. Tabulated are the results for the standard artificial galaxy as described in the text, as well as the effect of a wrong estimate of one of the observables which were kept fixed while fitting the model. Relative errors are listed, with $\Delta\mu_0 = \mu_{0,\rm in} - \mu_{0,\rm fit}$ and $\Delta\mu_{\rm e}$ in mag arcsec^{-2}, $\Delta h = 2(h_{\rm in} - h_{\rm fit})/(h_{\rm in} + h_{\rm fit})$ and $\Delta r_{\rm e}$ dimensionless.

$\mu_{\rm e}$	$r_{\rm e}$	$\Delta\mu_0$									Δh								
		standard	seeing	seeing error		sky error		b/a error		PA	standard	seeing	seeing error		sky error		b/a error		PA
			2.5″	–0.1″	+0.1″	+1%	–1%	–0.1	+0.1	+20°		2.5″	–0.1″	+0.1″	+1%	–1%	–0.1	+0.1	+20°
(1)	(2)	(3)	(4)	(5)	(6)	(7)	(8)	(9)	(10)	(11)									
17	4.0	-0.012	-0.042	-0.034	0.011	0.088	-0.090	0.034	-0.056	-0.051	-0.005	-0.016	-0.013	0.004	0.083	-0.083	0.094	-0.093	-0.023
18	4.0	-0.005	-0.019	-0.015	0.004	0.094	-0.084	0.041	-0.050	-0.044	-0.001	-0.007	-0.005	0.002	0.086	-0.080	0.096	-0.091	-0.021
19	4.0	-0.002	-0.009	-0.006	0.001	0.096	-0.082	0.043	-0.048	-0.042	-0.001	-0.004	-0.002	0.001	0.086	-0.079	0.097	-0.090	-0.020
20	4.0	-0.002	-0.005	-0.003	0.000	0.095	-0.082	0.043	-0.049	-0.042	-0.000	-0.002	-0.001	0.000	0.086	-0.080	0.097	-0.090	-0.020
21	4.0	-0.001	-0.003	-0.002	-0.001	0.091	-0.085	0.041	-0.052	-0.043	-0.000	-0.001	-0.000	-0.000	0.084	-0.081	0.096	-0.092	-0.021
17	3.0	-0.013	-0.032	-0.029	0.004	0.070	-0.078	0.021	-0.046	-0.043	-0.005	-0.013	-0.011	0.002	0.077	-0.078	0.089	-0.089	-0.020
18	3.0	-0.005	-0.015	-0.013	0.001	0.077	-0.073	0.028	-0.040	-0.036	-0.002	-0.006	-0.005	0.001	0.079	-0.076	0.091	-0.087	-0.018
19	3.0	-0.003	-0.008	-0.006	-0.001	0.079	-0.071	0.029	-0.038	-0.034	-0.001	-0.003	-0.002	0.000	0.080	-0.075	0.092	-0.086	-0.017
20	3.0	-0.002	-0.004	-0.003	-0.001	0.079	-0.071	0.030	-0.038	-0.033	-0.001	-0.002	-0.001	-0.000	0.080	-0.075	0.092	-0.086	-0.017
21	3.0	-0.002	-0.003	-0.002	-0.002	0.077	-0.073	0.030	-0.039	-0.034	-0.000	-0.001	-0.001	-0.000	0.079	-0.076	0.092	-0.086	-0.017
17	2.0	-0.013	-0.006	-0.023	-0.001	0.058	-0.070	0.013	-0.039	-0.037	-0.005	-0.003	-0.009	-0.000	0.072	-0.075	0.086	-0.086	-0.018
18	2.0	-0.006	-0.004	-0.011	-0.002	0.064	-0.064	0.019	-0.034	-0.031	-0.002	-0.001	-0.004	-0.000	0.074	-0.072	0.088	-0.084	-0.016
19	2.0	-0.004	-0.003	-0.005	-0.002	0.066	-0.061	0.022	-0.032	-0.029	-0.001	-0.001	-0.002	-0.000	0.075	-0.071	0.089	-0.083	-0.015
20	2.0	-0.003	-0.003	-0.003	-0.002	0.066	-0.061	0.022	-0.031	-0.028	-0.001	-0.001	-0.001	-0.000	0.075	-0.071	0.089	-0.083	-0.015
21	2.0	-0.002	-0.003	-0.003	-0.002	0.065	-0.063	0.022	-0.031	-0.028	-0.001	-0.001	-0.001	-0.001	0.074	-0.072	0.089	-0.083	-0.015
17	1.0	0.001	0.016	-0.008	0.009	0.063	-0.050	0.023	-0.024	-0.021	0.001	0.007	-0.003	0.004	0.074	-0.066	0.089	-0.080	-0.012
18	1.0	-0.001	0.004	-0.005	0.002	0.061	-0.053	0.020	-0.026	-0.023	-0.000	0.002	-0.002	0.001	0.073	-0.067	0.088	-0.081	-0.013
19	1.0	-0.002	-0.001	-0.004	-0.001	0.059	-0.054	0.019	-0.027	-0.024	-0.001	-0.000	-0.001	-0.000	0.072	-0.068	0.088	-0.081	-0.013
20	1.0	-0.003	-0.003	-0.003	-0.002	0.058	-0.055	0.018	-0.027	-0.025	-0.001	-0.001	-0.001	-0.001	0.072	-0.068	0.088	-0.081	-0.013
21	1.0	-0.003	-0.004	-0.003	-0.003	0.057	-0.056	0.021	-0.028	-0.025	-0.001	-0.001	-0.001	-0.001	0.071	-0.069	0.089	-0.082	-0.013
17	0.5	0.002	-0.001	0.000	0.003	0.061	-0.047	0.023	-0.021	-0.018	0.001	-0.000	0.001	0.001	0.073	-0.065	0.089	-0.079	-0.010
18	0.5	-0.001	-0.003	-0.002	-0.001	0.057	-0.050	0.019	-0.025	-0.022	-0.000	-0.001	-0.000	-0.000	0.071	-0.066	0.088	-0.080	-0.012
19	0.5	-0.003	-0.004	-0.003	-0.003	0.056	-0.051	0.017	-0.026	-0.023	-0.001	-0.002	-0.001	-0.001	0.071	-0.067	0.087	-0.081	-0.013
20	0.5	-0.003	-0.005	-0.003	-0.003	0.055	-0.053	0.017	-0.027	-0.024	-0.001	-0.002	-0.001	-0.001	0.071	-0.068	0.087	-0.081	-0.013
21	0.5	-0.003	-0.005	-0.003	-0.003	0.055	-0.156	0.017	-0.027	-0.264	-0.001	-0.002	-0.001	-0.001	0.071	-0.104	0.087	-0.081	0.017

$\mu_{\rm e}$	$r_{\rm e}$	$\Delta\mu_{\rm e}$									$\Delta r_{\rm e}$								
		standard	seeing	seeing error		sky error		b/a error		PA	standard	seeing	seeing error		sky error		b/a error		PA
			2.5″	–0.1″	+0.1″	+1%	–1%	–0.1	+0.1	+20°		2.5″	–0.1″	+0.1″	+1%	–1%	–0.1	+0.1	+20°
17	4.0	-0.007	-0.021	-0.019	0.004	-0.007	-0.008	-0.006	-0.009	-0.008	-0.010	-0.029	-0.016	-0.004	-0.006	-0.013	-0.007	-0.012	-0.012
18	4.0	-0.007	-0.022	-0.019	0.004	-0.005	-0.009	-0.004	-0.010	-0.010	-0.010	-0.029	-0.016	-0.003	-0.000	-0.017	-0.003	-0.016	-0.014
19	4.0	-0.008	-0.024	-0.019	0.004	-0.002	-0.012	0.001	-0.015	-0.013	-0.009	-0.029	-0.015	-0.003	0.014	-0.027	0.008	-0.025	-0.021
20	4.0	-0.008	-0.029	-0.019	0.003	0.005	-0.021	0.013	-0.029	-0.023	-0.007	-0.029	-0.014	-0.001	0.049	-0.054	0.033	-0.049	-0.038
21	4.0	-0.010	-0.041	-0.021	0.002	0.021	-0.046	0.037	-0.073	-0.050	-0.004	-0.029	-0.011	0.002	0.132	-0.129	0.090	-0.121	-0.087
17	3.0	-0.011	-0.046	-0.028	0.006	-0.010	-0.012	-0.010	-0.012	-0.012	-0.017	-0.050	-0.026	-0.009	-0.014	-0.020	-0.015	-0.019	-0.019
18	3.0	-0.011	-0.046	-0.028	0.007	-0.007	-0.014	-0.007	-0.014	-0.013	-0.017	-0.050	-0.026	-0.008	-0.007	-0.025	-0.011	-0.022	-0.021
19	3.0	-0.010	-0.048	-0.027	0.007	0.000	-0.019	-0.001	-0.019	-0.017	-0.016	-0.050	-0.024	-0.007	0.010	-0.036	-0.001	-0.030	-0.027
20	3.0	-0.010	-0.053	-0.027	0.008	0.014	-0.033	0.012	-0.033	-0.027	-0.014	-0.048	-0.022	-0.005	0.048	-0.067	0.023	-0.051	-0.043
21	3.0	-0.010	-0.068	-0.028	0.008	0.045	-0.078	0.041	-0.078	-0.057	-0.009	-0.046	-0.018	0.000	0.141	-0.155	0.077	-0.115	-0.088
17	2.0	-0.032	-0.105	-0.061	-0.003	-0.030	-0.035	-0.031	-0.034	-0.034	-0.039	-0.087	-0.054	-0.026	-0.034	-0.044	-0.038	-0.042	-0.042
18	2.0	-0.031	-0.105	-0.060	-0.001	-0.024	-0.037	-0.027	-0.035	-0.035	-0.039	-0.087	-0.053	-0.025	-0.026	-0.049	-0.033	-0.044	-0.044
19	2.0	-0.030	-0.105	-0.059	0.000	-0.012	-0.045	-0.020	-0.040	-0.038	-0.036	-0.083	-0.051	-0.022	-0.005	-0.062	-0.022	-0.051	-0.049
20	2.0	-0.027	-0.107	-0.057	0.004	0.015	-0.067	-0.002	-0.054	-0.048	-0.032	-0.077	-0.046	-0.017	0.043	-0.099	0.004	-0.070	-0.063
21	2.0	-0.020	-0.112	-0.052	0.012	0.077	-0.141	0.037	-0.099	-0.079	-0.021	-0.062	-0.038	-0.005	0.157	-0.208	0.062	-0.127	-0.104
17	1.0	-0.121	-0.115	-0.209	-0.022	-0.112	-0.130	-0.118	-0.125	-0.125	-0.096	-0.072	-0.144	-0.045	-0.086	-0.105	-0.093	-0.101	-0.100
18	1.0	-0.121	-0.106	-0.209	-0.022	-0.096	-0.142	-0.112	-0.131	-0.130	-0.096	-0.064	-0.142	-0.043	-0.070	-0.118	-0.086	-0.105	-0.104
19	1.0	-0.120	-0.086	-0.209	-0.021	-0.060	-0.172	-0.097	-0.146	-0.142	-0.095	-0.048	-0.142	-0.042	-0.032	-0.148	-0.072	-0.120	-0.116
20	1.0	-0.120	-0.042	-0.211	-0.019	0.023	-0.250	-0.064	-0.184	-0.172	-0.092	-0.009	-0.140	-0.038	0.058	-0.227	-0.035	-0.157	-0.144
21	1.0	-0.142	0.050	-0.215	-0.016	0.191	-0.501	1.107	-0.282	-0.243	-0.101	0.078	-0.135	-0.031	0.246	-0.469	0.717	-0.249	-0.213
17	0.5	0.001	0.115	-0.368	0.467	0.052	-0.041	0.018	-0.018	-0.014	-0.028	0.037	-0.214	0.198	0.010	-0.053	-0.014	-0.037	-0.037
18	0.5	-0.033	0.125	-0.390	0.417	0.087	-0.139	0.008	-0.082	-0.073	-0.043	0.047	-0.227	0.174	0.037	-0.115	-0.018	-0.075	-0.071
19	0.5	-0.111	0.145	-0.441	0.305	0.169	-0.372	-0.015	-0.229	-0.207	-0.084	0.073	-0.253	0.116	0.105	-0.262	-0.018	-0.163	-0.150
20	0.5	-0.270	0.175	-0.547	0.072	0.340	-0.894	-0.192	-0.536	-0.478	-0.167	0.121	-0.308	0.000	0.257	-0.613	-0.053	-0.357	-0.316
21	0.5	-0.529	0.192	-0.750	-0.304	1.016	-2.653	-0.479	-1.122	-2.505	-0.301	0.227	-0.408	-0.192	0.865	-1.851	-0.167	-0.726	-1.936

Notes:

(1) The bulge effective surface brightness of the artificial galaxy in mag arcsec^{-2}.

(2) The bulge effective radius of the artificial galaxy in arcsec.

(3) Fit results using the standard artificial image (see text) with $\mu_0 = 20$ R-mag arcsec^{-2} and $h = 20''$.

(4) As (3), but artificial image and fitting model have seeing of $2.5''$ instead of $1.5''$.

(5) As (3), but fitting model has $1.4''$ seeing instead of the $1.5''$ of the artificial image.

(6) As (3), but fitting model has $1.6''$ seeing instead of $1.5''$.

(7) As (3), but with sky level of the fitting model 1% too low compared to the real value in the artificial image.

(8) As (3), but with sky level of the fitting model 1% too high compared to the real value in the artificial image.

(9) As (3), but with $b/a = 0.65$ in fitting model and 0.75 in the artificial image.

(10) As (3), but with $b/a = 0.85$ in fitting model and 0.75 in the artificial image.

(11) As (3), with error of 20° in PA between image and model.

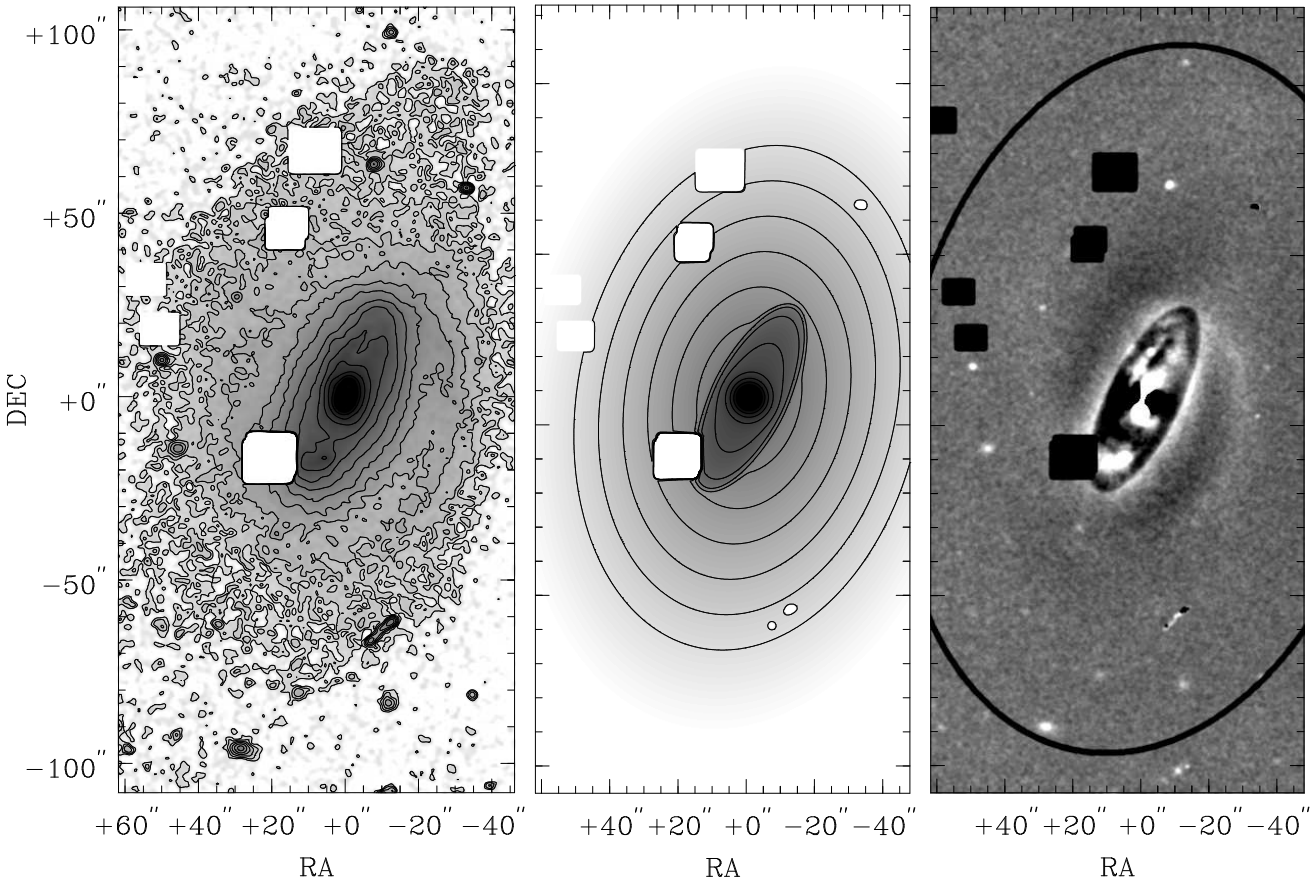

Fig. 1. Left: UGC 89 R passband image, with isophotes overlaid from 18 to 24 R-mag arcsec^{-2} in steps of 0.5 mag arcsec^{-2}. Center: Fitted model on the same grayscale and contour level as the left image. Right: Residual image using the 2D fit model of the center image. The ellipse indicates the area used for the fit and the b/a and PA of the fitted exponential disk. The fitted bar component shows up as the inner ellipse in the residuals. Structure in the bar region and the two arms coming off the ends of the bar are clearly visible and can not be fitted with this simple model.

The fitting routine was also tested on some artificial images with a bar, but with eight free parameters only a limited parameter space could be explored. In general, the routine converged to satisfactory results in just a few iterations.

3.5 Tests on UGC 438

Clearly, artificial images are not a good representation of real galaxies. Therefore, the fitting routine was also tested for different bulge-to-disk ratios on an R passband image of UGC 438. A 2D fitted bulge was subtracted from the original image and replaced by artificial exponential bulges with a range in effective surface brightness and radius. The fit results for the different bulge parameters are listed in Table 1.

The fitting routine generally reproduces the parameters quite well. The disk parameters change little for the different bulges (μ_0 changes at most by 0.04 mag arcsec^{-2} and h by about 4%), but as with the tests on artificial images, the fitting routine breaks down for bulges with a small effective radius and a low surface brightness. Next to the explanations for this effect mentioned earlier for the artificial images, one has another problem when one tests on real images. The model bulge that was originally subtracted to create a bulgeless image might not be perfectly correct. One is then left with some residuals which have the greatest influence when later replaced by a low surface brightness bulge.

3.6 Resulting parameters

The results from the 2D fits for all galaxies in our sample are presented in Table 3 for the B and the K passband. This table contains observed data values. No corrections were applied for inclination and for internal and Galactic extinction. In 23 out of 86 cases it was found that the fits of at least the bulge improved if a bar was also included.

Figure 1 shows an example of an original, a model and a model subtracted image of UGC 89. The relative differences between model and data are quite small and the resulting difference image can be used to study small scale structures in the bulge and bar region and to study spiral arms. UGC 89 is a good example of a galaxy that can only be fitted correctly by a 2D method with a bar, as can be seen more clearly in the resulting 1D profile of Fig. 2.

Table 3. The results from the 2D fit model with μ_0, μ_e and $\mu_{0,bar}$ in mag arcsec^{-2}, h, r_e, a_{bar} and b_{bar} in arcsec and PA_{bar} in degrees. NP means a non-photometric observation, but the scale parameters are still determined.

UGC	B								K							
	μ_0	h	μ_e	r_e	$\mu_{0,bar}$	a_{bar}	b_{bar}	PA_{bar}	μ_0	h	μ_e	r_e	$\mu_{0,bar}$	a_{bar}	b_{bar}	PA_{bar}
89	22.07	28.5	18.87	2.5	21.77	31.6	11.4	152.8	17.46	17.4	14.61	2.5	17.63	29.6	10.3	153.6
93	22.33	21.3	22.02	0.9	—	—	—	—	18.55	15.7	18.82	1.4	—	—	—	—
242	21.26	13.7	18.73	0.2	—	—	—	—	17.28	11.1	17.82	0.9	—	—	—	—
334	23.36	21.5	24.89	2.4	—	—	—	—	20.32	18.1	21.26	3.8	—	—	—	—
438	20.45	14.1	21.22	2.9	—	—	—	—	16.23	11.5	15.84	2.1	—	—	—	—
463	20.76	13.5	20.60	1.3	—	—	—	—	16.80	12.0	16.73	1.9	—	—	—	—
490	21.47	18.5	21.51	2.6	—	—	—	—	17.16	14.9	17.73	3.9	—	—	—	—
508	22.05	30.5	19.81	2.8	22.66	48.1	11.2	93.1	17.74	26.3	15.26	2.9	17.91	40.1	10.5	93.3
628	22.86	14.8	24.61	3.4	—	—	—	—	20.39	18.6	21.46	5.4	—	—	—	—
1305	22.02	33.9	21.24	3.8	—	—	—	—	17.61	26.5	17.00	4.2	—	—	—	—
1455	22.27	24.0	20.47	2.1	22.15	13.2	4.9	19.6	17.64	16.2	15.67	2.0	18.06	16.5	6.2	22.5
1551	22.47	25.8	24.81	2.6	—	—	—	—	18.98	24.4	20.06	2.9	—	—	—	—
1559	22.48	20.0	23.42	3.8	—	—	—	—	20.08	19.6	20.21	5.8	—	—	—	—
1577	22.44	22.1	20.89	2.2	22.80	32.9	10.8	144.5	18.26	17.6	16.01	1.8	18.42	26.8	8.9	145.1
1719	22.45	21.7	20.99	1.6	22.88	13.3	5.2	127.6	17.73	14.3	16.68	1.9	18.45	15.9	5.2	129.3
1792	21.65	17.1	21.31	1.3	—	—	—	—	17.48	14.4	17.21	1.8	—	—	—	—
2064	22.28	20.1	20.78	0.8	—	—	—	—	18.01	17.6	16.25	1.1	—	—	—	—
2081	22.31	19.1	23.46	1.4	—	—	—	—	19.44	19.4	19.83	2.5	—	—	—	—
2124	22.34	23.0	20.07	2.7	21.96	21.4	7.0	100.1	18.11	21.3	15.89	2.7	17.62	21.3	6.1	100.2
2125	23.20	26.8	21.01	1.7	23.47	34.6	6.9	79.5	—	—	—	—	—	—	—	—
2197	22.57	18.2	23.43	2.1	—	—	—	—	17.97	12.3	18.60	2.1	—	—	—	—
2368	23.67	28.3	19.82	1.3	22.50	52.9	14.0	156.9	18.88	18.1	15.19	1.7	18.41	48.0	11.9	156.9
2595	—	—	—	—	—	—	—	—	—	—	—	—	—	—	—	—
3066	22.03	14.6	21.40	0.4	—	—	—	—	17.09	11.2	17.25	1.6	—	—	—	—
3080	21.99	17.2	19.88	0.2	—	—	—	—	18.21	15.1	18.79	1.7	—	—	—	—
3140	20.90	13.1	20.46	2.0	—	—	—	—	16.96	11.3	15.99	2.1	—	—	—	—
4126	21.83	22.6	20.01	1.4	23.34	45.7	9.6	38.1	18.02	18.7	16.09	1.8	19.01	35.2	10.8	48.5
4256	21.18	17.6	19.22	0.7	—	—	—	—	17.27	15.8	16.15	2.1	—	—	—	—
4308	21.34	20.0	19.78	0.8	—	—	—	—	17.66	16.4	17.06	1.9	—	—	—	—
4368	21.52	17.6	22.52	2.0	—	—	—	—	17.81	14.7	18.89	2.2	—	—	—	—
4375	21.31	20.2	22.18	2.1	—	—	—	—	17.21	16.9	18.46	2.5	—	—	—	—
4422	22.04	31.0	20.92	3.5	—	—	—	—	18.38	27.0	16.55	3.4	—	—	—	—
4458	21.72	19.8	19.50	3.0	—	—	—	—	17.75	17.9	15.05	2.5	—	—	—	—
5103	20.50	17.8	19.84	1.3	—	—	—	—	16.56	14.5	16.07	1.9	—	—	—	—
5303	21.32	36.8	21.41	3.0	—	—	—	—	17.89	37.7	17.72	4.3	—	—	—	—
5510	20.66	20.4	19.22	1.3	—	—	—	—	17.37	18.4	16.53	2.2	—	—	—	—
5554	20.98	19.1	19.31	1.5	—	—	—	—	16.94	16.7	15.66	2.1	—	—	—	—
5633	23.13	27.8	23.67	0.9	22.99	23.5	3.0	161.5	20.01	29.4	21.03	1.5	19.88	23.2	3.7	162.5
5842	21.44	30.3	21.01	0.9	—	—	—	—	18.01	27.4	18.52	2.2	—	—	—	—
6028	20.49	15.3	21.57	0.5	—	—	—	—	17.27	13.0	18.66	1.6	—	—	—	—
6077	20.88	18.4	20.17	1.1	—	—	—	—	17.49	18.4	17.22	2.1	—	—	—	—
6123	NP	27.1	NP	2.1	—	—	—	—	17.29	25.0	15.46	2.0	—	—	—	—
6277	20.88	27.9	18.98	1.3	—	—	—	—	17.25	21.5	16.54	2.9	—	—	—	—
6445	20.55	16.1	20.19	2.6	20.94	11.6	4.1	157.6	16.83	14.0	16.17	2.6	17.11	11.4	4.5	154.4
6453	20.91	21.3	22.04	7.9	—	—	—	—	17.16	16.3	17.87	5.6	—	—	—	—
6460	20.66	27.6	19.63	1.8	—	—	—	—	17.15	24.1	16.53	2.1	—	—	—	—
6536	NP	21.7	NP	1.9	NP	13.5	9.3	9.0	18.57	20.3	15.47	1.9	17.80	12.7	8.1	16.5
6693	21.60	18.9	21.72	0.7	—	—	—	—	17.99	16.7	17.13	1.3	—	—	—	—
6746	21.38	17.7	20.18	2.2	—	—	—	—	17.30	16.0	15.64	2.1	—	—	—	—
6754	22.71	32.0	21.58	4.2	—	—	—	—	18.32	21.7	15.77	1.8	—	—	—	—
7169	20.11	13.2	20.20	1.7	—	—	—	—	16.55	10.0	16.38	2.3	—	—	—	—
7315	19.99	14.8	20.75	1.5	—	—	—	—	16.03	14.6	16.96	2.1	—	—	—	—
7450	21.17	64.9	20.14	7.8	—	—	—	—	17.30	48.5	15.72	6.3	—	—	—	—
7523	21.49	36.0	19.61	4.0	22.10	47.2	11.8	144.5	17.70	32.5	15.11	3.1	17.87	44.1	12.9	143.6
7594	21.03	52.4	19.16	3.6	21.72	50.2	21.5	11.8	16.94	44.8	15.21	4.1	17.73	51.2	19.6	8.7
7876	NP	21.2	NP	1.7	—	—	—	—	18.55	22.1	20.06	4.4	—	—	—	—

Table 3. -continued.

UGC	B								K							
	μ_0	h	μ_e	r_e	$\mu_{0,bar}$	a_{bar}	b_{bar}	PA_{bar}	μ_0	h	μ_e	r_e	$\mu_{0,bar}$	a_{bar}	b_{bar}	PA_{bar}
7901	20.07	25.1	20.06	3.0	—	—	—	—	16.06	19.7	16.22	3.8	—	—	—	—
8279	20.52	13.6	22.87	7.0	—	—	—	—	16.90	11.5	18.59	5.9	—	—	—	—
8289	21.80	33.2	19.59	3.2	—	—	—	—	17.90	21.1	15.84	3.2	—	—	—	—
8865	21.89	32.0	20.10	2.7	21.83	19.8	9.4	169.2	18.27	29.3	15.65	2.3	17.84	27.2	9.5	168.4
9024	24.08	28.2	21.64	2.1	—	—	—	—	22.07	45.4	19.15	3.6	—	—	—	—
9061	22.63	62.0	20.08	2.1	21.97	15.0	6.5	111.3	18.75	39.3	16.22	2.8	17.73	16.8	4.0	110.2
9481	21.22	17.6	21.36	1.1	22.87	27.0	4.3	94.2	18.03	17.5	17.26	1.6	18.46	21.5	6.2	98.7
9915	NP	17.7	NP	2.6	—	—	—	—	17.21	15.7	16.58	2.3	—	—	—	—
9926	20.13	17.9	20.16	3.1	—	—	—	—	16.45	16.6	15.96	4.3	—	—	—	—
9943	20.40	20.0	20.92	2.7	21.37	19.8	6.2	73.3	16.60	17.6	16.55	2.3	17.16	19.7	5.9	70.3
10083	21.51	23.3	22.65	4.3	22.08	44.8	8.8	149.2	17.60	18.9	18.64	4.2	18.50	44.2	10.1	149.3
10437	24.03	33.6	23.28	8.9	—	—	—	—	NP	17.0	NP	7.1	—	—	—	—
10445	21.76	20.3	22.99	2.3	—	—	—	—	19.00	19.6	20.08	4.5	—	—	—	—
10584	21.77	23.8	21.22	1.7	—	—	—	—	18.18	19.4	17.47	2.2	—	—	—	—
11628	22.27	38.8	20.10	3.1	—	—	—	—	17.19	21.9	15.09	2.6	—	—	—	—
11708	21.51	17.9	21.77	1.9	—	—	—	—	NP	14.4	NP	2.0	—	—	—	—
11872	20.46	18.3	20.68	7.0	20.61	13.2	3.7	17.6	15.71	12.6	14.94	2.5	16.01	12.8	6.0	13.3
12151	23.27	26.1	24.78	6.4	—	—	—	—	20.14	21.7	21.19	4.8	—	—	—	—
12343	21.95	50.7	21.32	4.3	22.01	66.9	11.0	7.0	17.67	39.7	15.94	3.4	17.67	68.2	12.6	10.7
12379	21.99	19.3	20.40	2.1	—	—	—	—	17.44	15.7	15.33	1.9	—	—	—	—
12391	21.50	15.7	18.03	0.2	—	—	—	—	17.79	13.8	17.36	1.2	—	—	—	—
12511	22.46	24.4	22.38	1.6	—	—	—	—	18.35	13.2	18.09	2.1	—	—	—	—
12614	20.94	21.6	18.76	0.7	—	—	—	—	17.24	20.2	15.00	1.2	—	—	—	—
12638	22.17	21.4	21.74	1.3	—	—	—	—	18.27	19.8	18.24	2.6	—	—	—	—
12654	21.76	19.6	22.73	2.0	—	—	—	—	17.98	15.2	18.82	3.0	—	—	—	—
12732	23.66	29.8	25.30	11.0	—	—	—	—	NP	37.5	NP	10.5	—	—	—	—
12754	21.81	52.7	22.21	5.2	21.83	48.1	6.7	98.0	NP	49.2	NP	7.6	NP	44.6	8.3	100.6
12776	23.39	61.3	20.01	2.0	22.02	22.6	8.9	171.5	19.30	30.2	15.52	2.0	17.90	21.0	7.9	171.6
12808	20.31	13.8	17.50	0.7	—	—	—	—	—	—	—	—	—	—	—	—
12845	22.69	24.6	23.32	2.4	—	—	—	—	NP	18.1	NP	2.5	—	—	—	—

In testing both artificial and real images it appears that the 2D fitting routine has difficulties fitting bulges with a low surface brightness and a small effective radius compared to the disk parameters. There are few galaxies in the sample with a fitted $r_e < 1$. This is only found in the B and V passbands when galaxies have Type II profiles. The routine fits a small bulge to these galaxy images to avoid filling up the "central hole" in the disk. The Type II behavior is always less pronounced at longer wavelengths and indeed in the K passband there are no galaxies with $r_e < 1$. Fortunately, there are no galaxies in the sample with a small effective radius *and* a low effective surface brightness of the bulge relative to the disk central surface brightness. The errors intrinsic to the fitting routine are expected to be less than 10%, the errors caused by other sources will be discussed in the next sections.

4 Comparison of different decomposition methods

The structural parameters derived in the previous section will be used in subsequent papers of this series. In order to assess the reliability of the derived relations in these papers, a good estimate of systematic and random errors in the fitted parameters has to be determined. The 2D fitting results will be compared to various conventional 1D methods to demonstrate the increased accuracy. The 1D methods will also be used to investigate the two most important sources of error in the bulge and disk parameters, namely the sky background error and the uncertainty in the shape of the bulge profile. The 2D method was too time consuming to be used for these tests.

4.1 One-dimensional decompositions

One-dimensional decomposition methods are well known in the literature (Kormendy 1977; Schombert & Bothun 1987; Simien 1989; Capaccioli & Caon 1992; Andredakis & Sanders 1994) and will be described briefly. The resulting parameters are only available in electronic form.

The most elementary way to obtain the disk parameters, the "marking the disk method", was also used by Freeman (1970), when he found the disk central surface brightness to be constant among galaxies. The linear part of the luminosity profile, plotted on a magnitude scale, was marked and a linear least squares fit was made to the data points in the indicated range. To be able to compare the disk parameters of a galaxy in different passbands, I used the same range in radii for all passbands. The resulting parameters can be quite sensitive to the minimum and maximum radius chosen to fit. The difficulties

of the "marking the disk" method have been discussed by Giovanelli et al. (1994) and results obtained by different authors were compared by Knapen & van der Kruit (1991), showing remarkable differences. These differences were mainly caused by a change in scalelength at a lower surface brightness.

The "marking the disk" method yields disk parameters that are intuitively correct for the human eye. However, the luminosity profile is a combination of bulge and disk light and to get correct results both should be fitted simultaneously (Kormendy 1977). The numerical method to decompose the luminosity profiles used here is essentially identical to the method described by Andredakis & Sanders (1994). A non-linear χ^2 minimalization routine was used to fit the model profiles to the data points in the logarithmic regime. Both bulge and disk model profiles were convolved with the seeing PSF using Eq. (3) and the fits were limited by the same maximum radii used for the "marking the disk" fit.

As already indicated in Section 1, several different radial luminosity laws have been proposed for the light of bulges. One of the more general forms for the light profile of the bulge is the generalized exponential law, originally proposed by Sérsic (1968):

$$\Sigma(r) = \Sigma_0 \mathrm{e}^{-(r/h)^{1/n}}. \quad (1)$$

This generalized exponential law has been applied to fit elliptical and S0 galaxies by Caon et al. (1993) and to dwarf ellipticals by Young & Currie (1994).

As a first step, the fitting of an exponential disk and a generalized exponential bulge profile was tried. A wide variety of initial values for the five free parameters were tried, but for most of the galaxies the fits did not converge to physically acceptable values (negative Σ_0, Σ_e, h or r_e). The value of n in Eq. (1) was of order 0.5–5 in the cases where the fit did converge, that is for the galaxies with pronounced bulges. For most galaxies the bulge light dominates over the disk light at only a few data points and these few points do not carry enough information to limit the shape parameter n.

To reach more stable results the same fits were made again with n fixed to values 1, 2 and 4. With $n = 4$ and after redefining Σ_0 and h into effective parameters, Eq. (1) translates in the most commonly used bulge fitting function, the de Vaucouleurs (1948) or $r^{1/4}$ law:

$$\Sigma(r) = \Sigma_\mathrm{e} \mathrm{e}^{-7.67\left(r/{r_\mathrm{e}}^{1/4}-1\right)}. \quad (2)$$

Setting $n = 2$ in Eq. (1) gives an "$r^{1/2}$ law" profile:

$$\Sigma(r) = \Sigma_\mathrm{e} \mathrm{e}^{-3.672\left(r/{r_\mathrm{e}}^{1/2}-1\right)}. \quad (3)$$

In the case of $n = 1$ in Eq. (1) one has the exponential law normally used for disk profiles, which translates into Eq. (1) when rewritten to effective parameters and which was also used for the 2D fit.

More stable results were reached than with the general exponential law, but the intrinsic properties of the $r^{1/4}$ law still made it impossible to reach convergence in many cases. With $n = 2$ the situation improved considerably and using an exponential profile for the bulge, the fitting converged for all galaxies except for UGC 6028. This galaxy has a very small bulge in a Type II profile (Freeman 1970) and therefore the fitting routine tends to make the bulge negative in order to create a hole in the disk profile. The fits with the exponential bulge are the most stable; convergence is reached more often and the fit results are less sensitive to initial values with the exponential bulge than with the other tested profiles.

The tests on the artificial images in Section 3.4 showed that one of the main sources of error in the bulge and disk parameters was the uncertainty in the sky background level. The maximum errors in the fit parameters due to this uncertainty were calculated for each galaxy using the sky errors determined in Paper I. All 1D fits were repeated with the maximum sky error estimate added to and subtracted from the luminosity profile. These error estimates will be used in the next sections.

4.2 Profile comparison

The different decompositions of eight galaxies are discussed in more detail as it will give some insight in the problems dealing with bulge/disk decompositions. Figure 2 shows some typical best and worst cases of four different decomposition models on B passband profiles/images. Images of these galaxies can be found in Paper I.

UGC 89 is probably the clearest example in the sample of a galaxy with three distinct components, which can only be fitted correctly using a 2D fitting technique. In Fig. 2 we see that in the $r^{1/4}$ law fit the bulge fills up the bar region, but also replaces part of the disk. The central surface brightness of the disk is probably too faint and the scalelength too large in this fit. When we use an $r^{1/2}$ or an exponential bulge, the disk tries to fill up the bar region, making the fit to the outer exponential part of the profile worse. The disk parameters are obviously incorrect for these fits, but now the surface brightness is too faint and the scalelength too small. Only including a bar yields a satisfying result, also displayed in Fig. 1.

UGC 438 is a galaxy with a small bulge and a distinct exponential disk with some enhanced star formation in the spiral arms near the center. All fitting methods seem to be equally justified, but notice the very extended bulge in the case of the $r^{1/4}$ bulge profile, while the bulge is only evident in the very center.

UGC 1455 is a symmetrical galaxy with a small bar/oval component in the center. All fits seem equally justifiable as long as we assume that the oval component is part of the bulge. The μ_0 becomes gradually fainter going from $r^{1/4}$ to the exponential bulge. If we assume that the bar is part of the disk, which is likely as some spiral arms start at the ends of the bar, the 2D fit is the best fit.

UGC 1551 has a low surface brightness disk with some flocculent star formation and a very small bulge. The $r^{1/4}$ profile did not converge for the B passband (though it did for the other passbands). Even though convergence was reached with the other fitting functions, the bulge results can hardly be called reliable; the small bulge is very hard to fit.

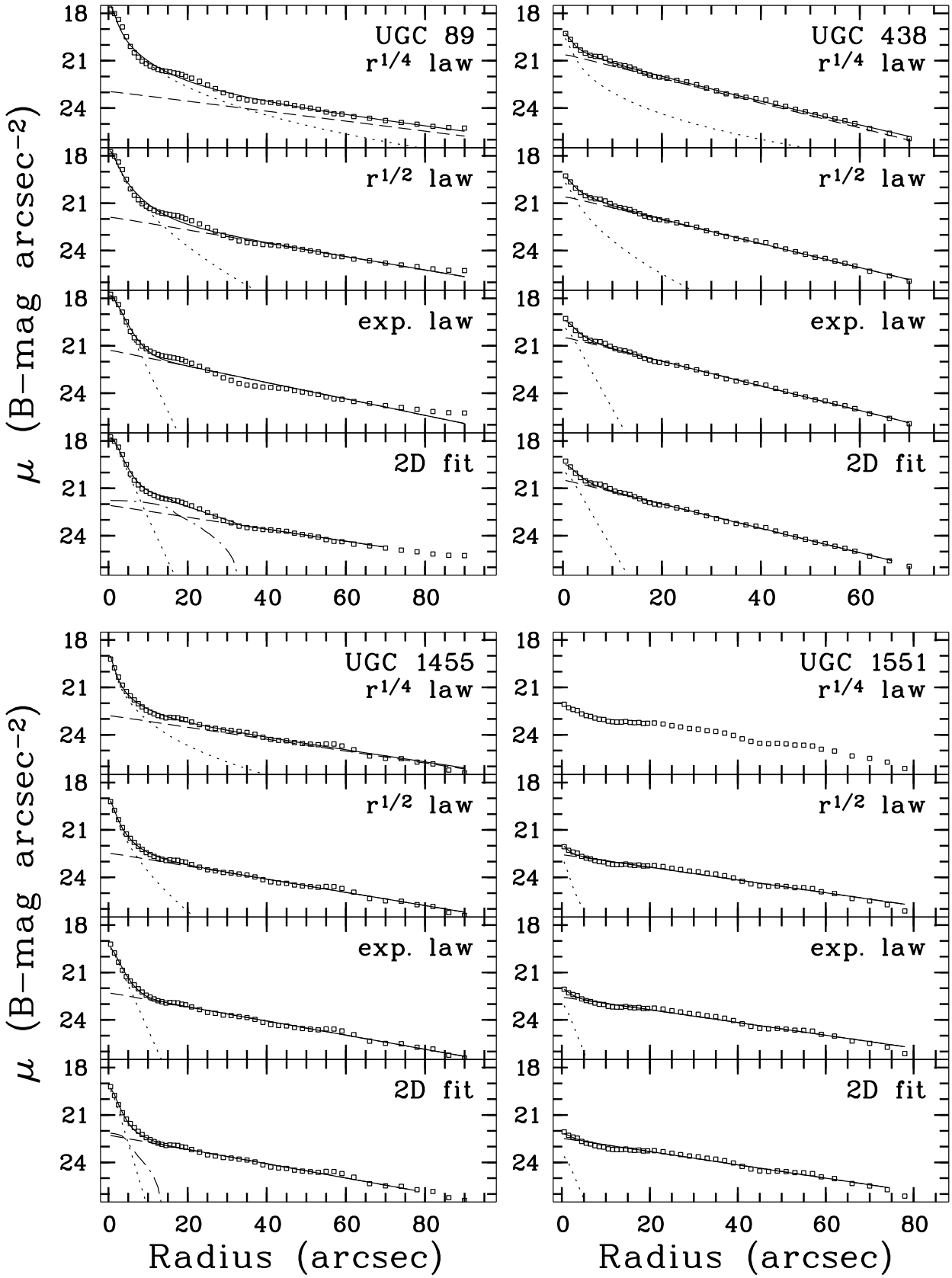

Fig. 2. Some examples of the fits made to the B passband surface brightness profiles. The squares indicate the measured profile, the dashed line represents the fitted disk, the dotted line the fitted bulge and the dashed-dotted line the bar. The full line is the sum of the different model components. The method to extract the model luminosity profiles from the 2D model images was the same as used on the real data.

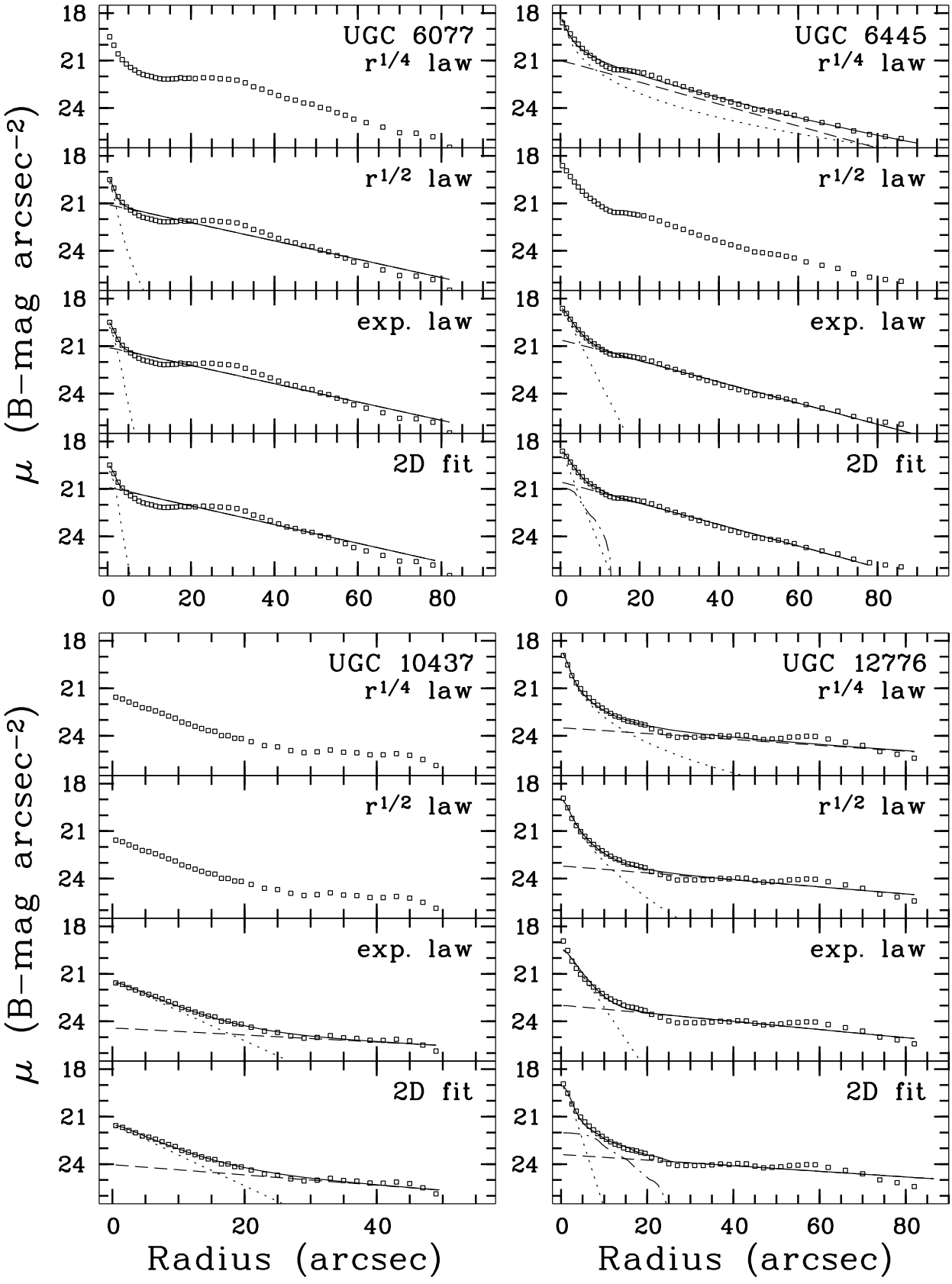

Fig. 2. -continued.

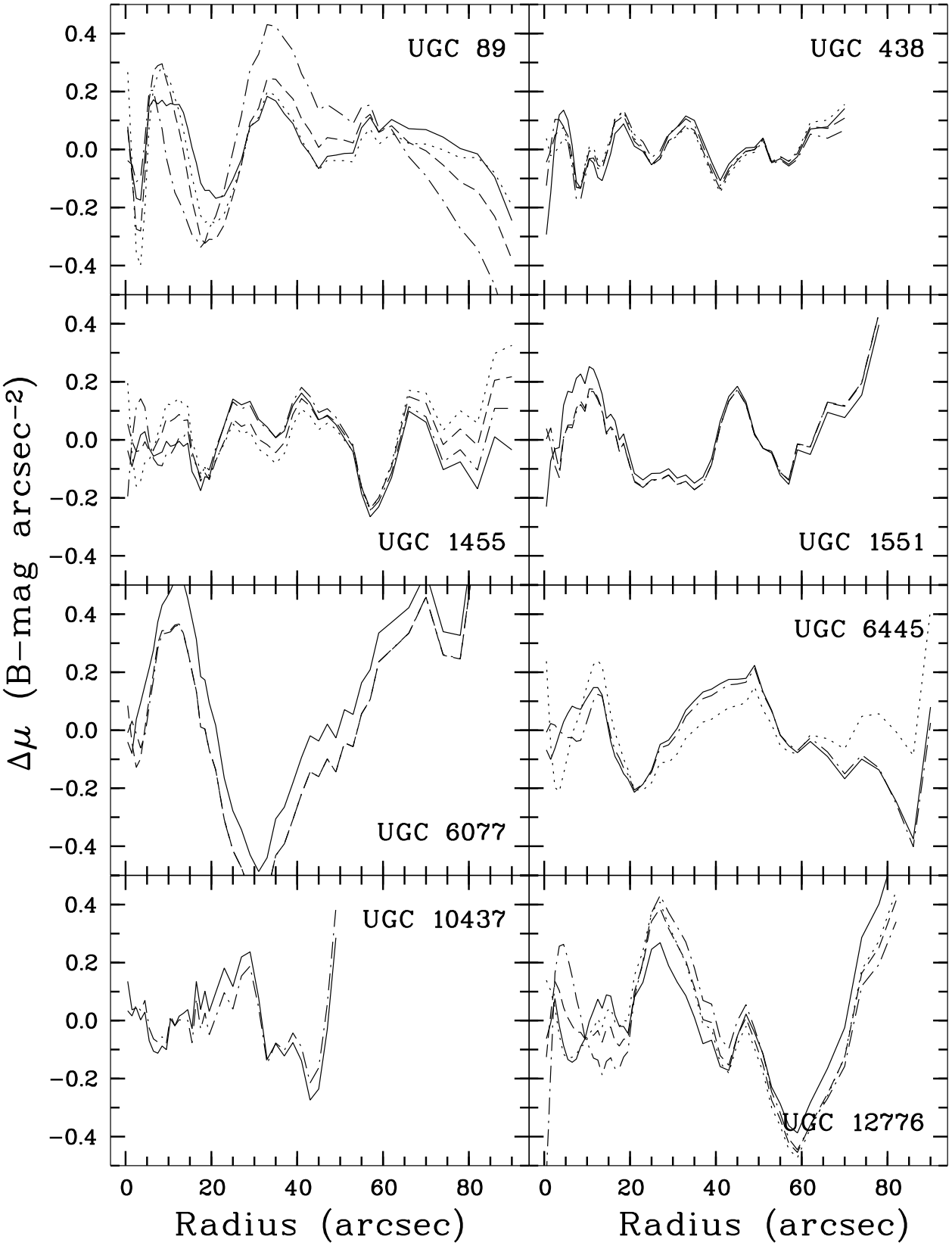

Fig. 3. The residuals $\Delta\mu$ between data and model for the galaxies plotted in Fig. 2. The dotted line indicates the model with the $r^{1/4}$ law bulge, the dashed line the $r^{1/2}$ law bulge fit, the dashed dotted line the exponential bulge fit and the full drawn line the 2D fit method. Note that generally the 2D fit method results in smaller residuals, but that the difference between the models is small compared to the intrinsic fluctuations in the luminosity profile.

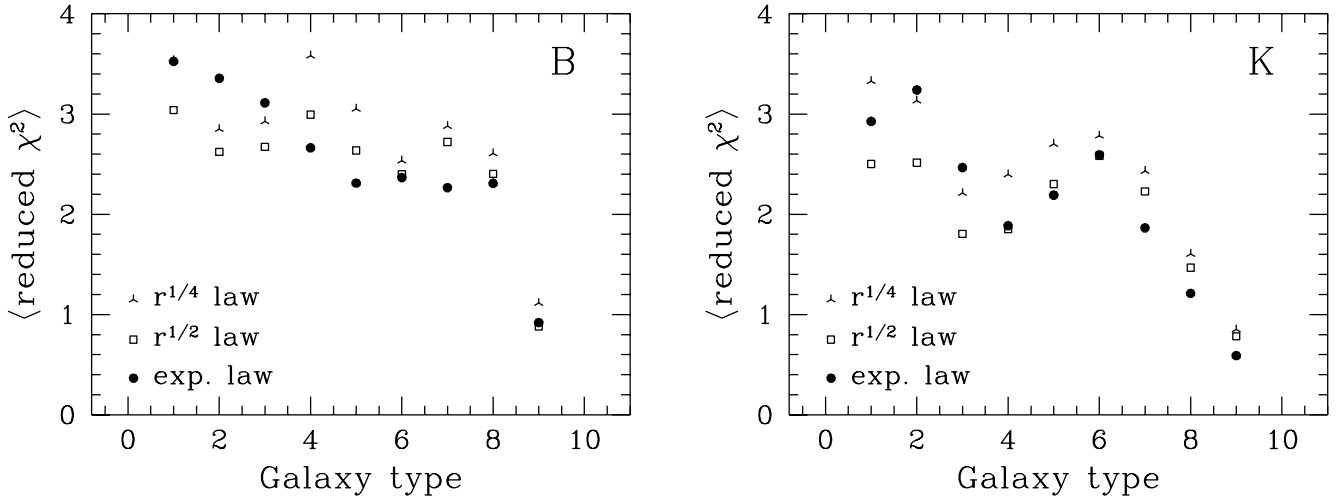

Fig. 4. The average reduced χ^2 values per morphological type for the 1D fit with different bulge models.

UGC 6077 is a typical case of a Type II profile, where the exponential outer profile does not continue all the way inward before the bulge takes over the luminosity in the central part of the galaxy. Morphologically these galaxies are in general barred with strong spiral arms forming at the end which are tightly wound to form a ring. Sometimes the bar is less pronounced. Moving to longer wavelengths the bump becomes less pronounced as the enhanced star formation doesn't show up so clearly at those wavelengths. None of the tested fitting models is able to decompose this type of galaxies well. One has to adjust the exponential law of the disk to contain an inner hole or one has to model spiral arms in the disk. None of the fitting techniques are correct (the $r^{1/4}$ law fit did not even converge for this galaxy) and the central surface brightnesses and scalelengths found are just an indication of the extent and surface brightness of the disk.

UGC 6445 , a galaxy with a small oval component, has a less pronounced Type II profile. Because of a slight shift in steepness of the luminosity profile in the outer region of the galaxy, the $r^{1/4}$ fit will tend to dominate in the central and outer region. Consequently bulge and disk are equally important over the whole extent of the galaxy in such a fit. Inclusion of a bar or oval component immediately diminishes the bulge contribution at large radii, even if one would fit an $r^{1/4}$ bulge profile. Clearly the 2D fit is the best option for this galaxy.

UGC 10437 is an example of one of the galaxies in the sample with a very low surface brightness disk. The fits made to this kind of galaxy are in general very unstable as the disk disappears rapidly in the sky noise. This means that the profile that can be fitted only extends over a few scalelengths. The H and K passband observations especially could pose some problems as these showed hardly anything else other than the bulge above the sky noise (see also UGC 334, UGC 628 and UGC 9024). The fits with $r^{1/4}$ and $r^{1/2}$ bulge profiles only converged to unphysical values for this galaxy, the exponential 1D bulge and the 2D fit yield nearly the same result, as might be expected for a nearly face-on galaxy.

UGC 12776 is a galaxy that consists mainly of a bar, with two arms originating at the ends. Similar galaxies are UGC 2368 and UGC 10083. Obviously a bar should be included in the models to fit these galaxies, but we have to keep in mind that in these cases the bar really seems to belong to the disk. The central surface brightness of such a galaxy is probably best described by the sum of the contributions of the disk and the bar.

Figure 3 shows the residuals between models and data. This figure shows that including a bar in the fitting routine can indeed improve the overall fit, but also shows that the residuals are dominated by fluctuations in the profiles. These fluctuations are not due to signal-to-noise problems, but are intrinsic to the light distribution of the galaxy. This makes it difficult to decide which bulge model is best, as the change in reduced χ^2 is small compared to the reduced χ^2 value itself. One would need additional components to fit the fluctuations, but this is beyond the scope of this work.

4.3 Comparison of χ^2 values

An exponential bulge was used in the 2D fitting technique, which was motivated by the 1D test results. One such test is the comparison of the reduced χ^2 values for the different bulge models. Figure 4 shows the different reduced χ^2 values as function of morphological type. Note that the χ^2 values are smaller in the K passband than in the B passband and that the differences between the χ^2 values of the different bulge models are small compared to these χ^2 values themselfs.

For galaxies with types later than Sb, the fits with the exponential bulge give the smallest residuals. For galaxies in the range from Sa-Sb, the $r^{1/2}$ law bulge fits give the best results. In this range, the $r^{1/4}$ law and exponential law bulge give comparable results in reduced χ^2 values. Therefore one could propose an intermediate transition type bulge for early spirals between the $r^{1/4}$ law ellipticals and the exponential bulges of late-type spirals. This could be analogous to the

Table 4. The median of the error estimates of the fit parameters for the different fit methods. The maximum error in the sky background subtraction was used to calculate the errors in the fit parameters. The errors in μ_0 and μ_e are in mag arcsec^{-2}, the relative errors in h and r_e were defined by $\Delta h/h$ and $\Delta r_e/r_e$.

Band	median error in μ_0				median error in h				median error in μ_e			median error in r_e		
	marking	$r^{1/4}$	$r^{1/2}$	exp.	marking	$r^{1/4}$	$r^{1/2}$	exp.	$r^{1/4}$	$r^{1/2}$	exp.	$r^{1/4}$	$r^{1/2}$	exp.
B	0.02	0.07	0.06	0.05	0.037	0.044	0.033	0.029	0.15	0.06	0.02	0.50	0.26	0.14
V	0.03	0.08	0.07	0.05	0.033	0.035	0.030	0.025	0.18	0.06	0.02	0.33	0.21	0.12
R	0.02	0.07	0.06	0.04	0.027	0.034	0.026	0.023	0.11	0.05	0.02	0.40	0.18	0.09
I	0.03	0.11	0.10	0.07	0.042	0.030	0.026	0.021	0.18	0.08	0.03	0.43	0.15	0.08
H	0.04	0.16	0.20	0.12	0.041	0.039	0.028	0.023	0.28	0.12	0.04	0.43	0.15	0.09
K	0.04	0.17	0.14	0.11	0.049	0.032	0.025	0.021	0.27	0.09	0.04	0.39	0.16	0.09

Table 5. The relative change in disk parameters due to different techniques for the galaxies where the fit routine converged to physical values for all techniques. All average changes are relative to the "marking the disk" method, with $\Delta\mu_0$ in mag arcsec^{-2}, $d = 2(h_{\rm mark} - h_{\rm other})/(h_{\rm mark} + h_{\rm other})$ dimensionless. The errors are standard deviations.

Band		$\langle\Delta\mu_0\rangle$				$\langle d\rangle$			
	#	$r^{1/4}$ law	$r^{1/2}$ law	exp. law	2D fit	$r^{1/4}$ law	$r^{1/2}$ law	exp. law	2D fit
B	71	–0.21 ± 0.31	–0.06 ± 0.20	0.06 ± 0.20	0.07 ± 0.24	–0.01 ± 0.14	0.02 ± 0.10	0.06 ± 0.11	0.06 ± 0.14
V	64	–0.21 ± 0.28	–0.16 ± 0.53	0.03 ± 0.18	0.02 ± 0.31	0.02 ± 0.12	–0.00 ± 0.09	0.04 ± 0.09	0.03 ± 0.13
R	72	–0.25 ± 0.37	–0.13 ± 0.38	0.05 ± 0.21	0.02 ± 0.30	–0.01 ± 0.15	–0.01 ± 0.12	0.04 ± 0.11	0.03 ± 0.12
I	68	–0.28 ± 0.39	–0.21 ± 0.50	0.04 ± 0.19	0.03 ± 0.29	0.01 ± 0.15	–0.03 ± 0.15	0.03 ± 0.10	0.03 ± 0.12
H	34	–0.19 ± 0.47	–0.17 ± 0.35	–0.00 ± 0.43	–0.04 ± 0.56	0.05 ± 0.22	0.00 ± 0.15	0.00 ± 0.09	-0.02 ± 0.13
K	65	–0.22 ± 0.40	–0.15 ± 0.45	0.08 ± 0.19	0.02 ± 0.28	0.02 ± 0.18	0.00 ± 0.09	0.05 ± 0.09	0.02 ± 0.10

pure elliptical systems, where low luminosity systems are less centrally concentrated than high luminosity systems (Young & Curie 1994).

The results of the study by Andredakis & Sanders (1994) are confirmed using this sample. Exponential bulges are statistically at least as justified as $r^{1/4}$ law bulges. When the galaxy image does not contain enough information to determine the shape of the bulge, the exponential bulge is preferred for galaxies with classification later than Sb. For early-type spiral galaxies an $r^{1/2}$ law bulge is a good alternative. For consistency reasons, only the results obtained with the exponential bulge will be used in subsequent papers when analyzing this large sample of galaxies.

4.4 Comparisons of errors due to sky uncertainties

The tests on artificial images discussed in Section 3 indicated that the uncertainty in the sky background level is, once a bulge model has been chosen, the largest source of error. As explained before, the maximum errors due to incorrect sky background subtraction were only calculated for the 1D methods. The median relative errors for each parameter and each method are listed in Table 4. Two trends can be seen in this table:
1) the median errors in the surface brightness parameters increase going from the B to the K passband, while the uncertainties in the scale parameters decrease and
2) the median errors in *all* parameters decrease moving from the fits with the more centrally peaked $r^{1/4}$ law bulge profile to the fits with the shallower exponential bulge profile.

A change in sky background level affects mostly the faint outer regions of the galaxy profiles. The $r^{1/4}$ law profile offers often a greater contribution to the outer parts of galaxies than the exponential bulge profile and will be more affected by a sky level change. The parameters resulting from the fit with the exponential bulge are the most stable and reproducible according to the results in Table 4 which is independent of the conclusion whether this bulge model is correct or not.

4.5 Comparison of the resulting disk parameters

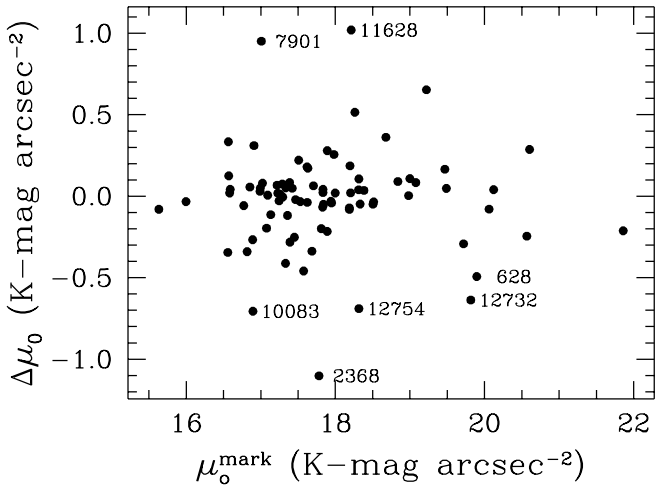

Fig. 5. The difference between the central surface brightnesses obtained with the "marking the disk" method and the 2D fit method ($\Delta\mu_0 = \mu_0^{\rm mark} - \mu_0^{\rm 2D}$) as function of μ_0 in the K passband. The UGC numbers of the most deviant galaxies are indicated.

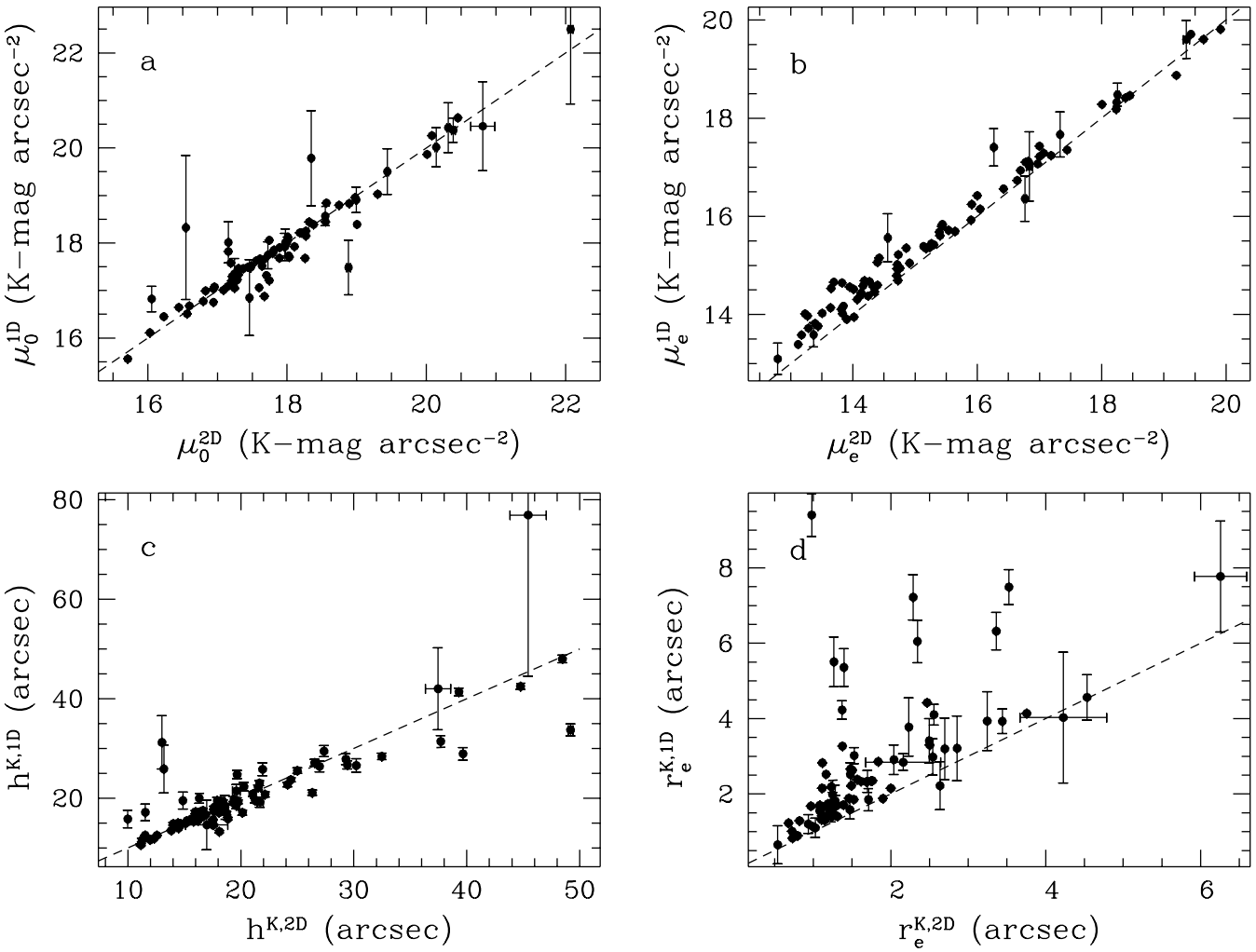

Fig. 6. A comparison between the K passband parameters obtained with the 1D and the 2D methods. An exponential bulge profile was used for both the 1D and the 2D method. **a)** Central surface brightness of the disk, **b)** effective surface brightness of the bulge, **c)** scalelength of the disk and **d)** effective radius of the bulge. The errors in the 2D parameters are the formal fit errors of the fit routine, the errors in the 1D parameters are the maximum errors due to the uncertainty in the sky background subtraction.

As a final point in the comparison of the different bulge models and fitting methods the resulting parameters are compared. Table 5 lists the average differences in the disk parameters using the different methods. The disk parameters of all different models are compared to those of the "marking the disk" method. The change in central surface brightness $\Delta\mu_0 = \mu_{0,\mathrm{mark}} - \mu_{0,\mathrm{other}}$ is on average the largest for the $r^{1/4}$ law bulge and small for the exponential bulge in both the 1D and 2D case. The central surface brightness of the disk is lower for the $r^{1/2}$ and $r^{1/4}$ law bulges as part of the disk light is replaced by the light of these more extended bulges. The average relative change in scalelength ($d = 2(h_{\mathrm{mark}} - h_{\mathrm{other}})/(h_{\mathrm{mark}} + h_{\mathrm{other}})$) is a few percent at most for all models. The scalelengths become on average a little bit smaller. The standard deviations of the differences in μ_0 are much larger for the $r^{1/2}$ and $r^{1/4}$ law bulges than for the exponential bulges. Apparently the methods using exponential bulges yield more often disk parameters that are in accordance with the "marking the disk" results, which represent the human intuition.

A comparison the results from the "marking the disk" fit with the 2D fit (Fig. 5), shows that the central surface brightnesses agree for most galaxies to within 0.5 mag arcsec^{-2}. The few exceptions to this can be easily explained. On the one hand, the surface brightness is fainter in the 2D case for UGC 2368, UGC 10083 and UGC 12754, as a bar is making up a large fraction of the disk and for some low surface brightness galaxies (UGC 628 and UGC 12732), because the distinction between the nearly absent bulge and the disk is hard to make. On the other hand, UGC 7901 and UGC 11628 have a gradual change in slope of their luminosity profile, which is interpreted differently by the 2D fitting program than by the human eye. The 2D fit central surface brightnesses are much brighter.

Figure 6 shows a comparison between the 1D and 2D bulge and disk parameters, both obtained with the exponential bulge profile. The errorbars on the 2D results indicate the formal fitting errors of the fitting routine, thus the uncertainty in the χ^2 minimum found by the routine. The errors in the 1D parameters result from recalculations of the fit with the sky background uncertainties added and subtracted.

Two points can readily be made from these errors: 1) the errors due to sky uncertainties are almost always much larger than the formal fitting errors and 2) the data points which are the most deviant from the equality line have in general also the largest uncertainty due to the sky errors. The errors due to sky uncertainty are apparently also indicaters of the differences between both fitting methods.

The 1D and 2D disk parameters in Fig. 6 agree quite well without any systematic deviations. The effective surface brightness of the bulge shows a small but systematic deviation, the surface brightnesses determined with the 1D method are most of the times a little fainter. The comparison of the effective radii shows the largest deviations. The 2D effective radii are smaller, especially for the galaxies where a bar was fitted. The profile comparisons of Fig. 2 showed that these smaller effective radii are more realistic.

4.6 The exponential bulge versus other bulge models

The exponential bulge profile was used in the 2D fitting technique instead of the more widely used $r^{1/4}$ law profile. The previous tests have shown that this is justified. The profile decompositions look at least as good as with other bulge models, which is reflected in the reduced χ^2 results. Table 4 shows that the exponential bulge results are least effected by the uncertainty in the sky level and Table 5 shows that the exponential bulge fit reflects the "marking the disk" results the most. The choise for the exponential bulge is obvious if one further realizes that the exponential bulge fit, contrary to the other models, almost always converges without fine tuning the initial parameters. One could propose to use $r^{1/2}$ law bulges for early-type spiral galaxies, but for consistency reasons I will use only the exponential bulge law results in subsequent papers.

5 Error discussion

Good error estimates of the fit parameters are important to determine the reliability of the derived relations in the next papers of this series. All sources of error and the typical percentage of error they cause in the different bulge and disk parameters are discussed.

In the decomposition methods discussed in this article one is confronted with three kinds of uncertainties: 1) uncertainties in the component profiles, 2) the uncertainties due to the fitting method and 3) measurement errors. The first two items give systematic effects in the derived parameters, but make comparisons within such a framework still possible. The last item has no systematic effect, assuming measurement errors are randomly distributed. Each of these points will be addressed separately, indicating the order of magnitude uncertainty in the resulting parameters.

1) Errors due to uncertainties in component profiles

- The best choice for the description of the bulge light is probably the generalized exponential (Eq. (1)), as it includes both the $r^{1/4}$ and the exponential law. Its mathematical peculiarities make it less useful in combination with an exponential disk profile. Therefore the exponential function for the bulge is preferred, as it gives a first moment analysis of the part of the bulge that is seen above the disk luminosity. In this way, a surface brightness and a scale size of the central region of the bulge can be determined. These quantities must have some physical meaning, even though they show only a weak relation to the ones obtained with $r^{1/2}$ and $r^{1/4}$ law bulges. The average value of μ_0 of the disk will be 0.2 mag arcsec^{-2} fainter using these bulges and the rms differences will increase to 0.4 mag arcsec^{-2} with respect to the "marking the disk" fit. The scalelengths of the disks are about the same for all bulge models used. A comparison of Tables 4 and 5 shows that the bulge profile uncertainty is more important than the uncertainty due to the sky background measurement errors.
- The use of exponential light profiles for disks of spiral galaxies is well established, but Type II profiles introduce an uncertainty. Are we dealing with a hole in the light distribution (intrinsic or due to dust) or do we have an extra stellar component at intermediate radii in the form of a ring of spiral arms? Morphology and color considerations favor the second option. Therefore one has to include the inner region in the fit as this is also part of the disk and observe at wavelengths which are least affected by young stellar populations. In the B passband, the Type II profiles can give uncertainties of order 20% in the disk parameters and up to 50% in the bulge parameters. In the K passband the effect is strongly reduced to order 10% for all parameters.

2) Uncertainties induced by different fitting methods

- The uncertainties in the "marking the disk" method have been discussed by Giovanelli et al. (1994) and by Knapen & van der Kruit (1991). They showed that the uncertainties using this method are of order 15%. It has been argued that this method gives *systematically* wrong results (Kormendy 1977, Phillipps & Disney 1983, Davies 1990) which will be discussed in Paper III (de Jong 1995b).
- The decomposition of the 1D profile in a bulge and a disk component should in principle be better than the previous method, but when performed with an exponential bulge profile the disk parameters hardly change compared to the "marking the disk" results. Byun (1992) showed that this method gives systematically wrong results for inclined galaxies.
- The 2D fitting method is intrinsically the best method tested here. It includes the effect of inclination and makes it possible to introduce a non-axisymmetric component in the form of a bar. With respect to the double exponential 1D fit it has little effect on the disk parameters and on μ_e of the bulge. The estimate of r_e of the bulge improves. The tests on artificial images showed that the errors in the parameters are at most a few percent for bulges with r_e larger than $1''$.
- One source of error that has never been investigated in detail is the choice of weighting function for the fitting routine. I have only used weighting schemes which reduce relative errors between model and data, but one could argue that the inner part of galaxies should get more weight as the signal-

to-noise is better in these regions. Likewise one could also argue that the outer part of the luminosity profile should get more weight as many more points are sampled (this is what happens automatically in the 2D fitting technique). Therefore even a single model for bulge and disk luminosity distribution has an intrinsic uncertainty depending on where one puts the most weight for the fitting accuracy. It is hard to define an acceptable range of weighting functions, but the uncertainty in the disk parameters induced in this way is estimated to be at most 5% for most galaxies. It will be of order 10% for the bulge parameters.

3) Uncertainties caused by measurement errors

- The dominant source of error in both bulge and disk parameters is the uncertainty in the sky background subtraction. As a second order effect b/a is also important for the estimate of μ_0. The seeing estimate influences the determination of the parameters of relatively small bulges. Each of these errors has at most order 10% effect on the disk parameters and a 20% effect on the bulge parameters. The errors will be slightly larger for low surface brightness galaxies, due to the relatively larger contribution of the sky background error.
- Another source of error, independent of the fitting method employed, stems from the determination of the zero-point of the magnitude scale. In Paper I, we calculated that this was for our sample in the range from 0.03 to 0.12 mag arcsec^{-2}, resulting in this contribution being of the same order of or less than the above mentioned measurement errors.

6 Conclusions

The bulge, disk and bar parameters of the 86 spiral galaxies presented in Paper I were calculated. In the different decomposition methods that were explored, we were confronted with three kinds of uncertainties: 1) the uncertainties in the component profiles, 2) the uncertainties due to the fitting method and 3) measurement errors. The first two items will give systematic effects in the derived parameters, but comparisons within such a framework are still possible. The last item has no systematic effect, assuming measurement errors are randomly distributed.

In conclusion, the use of the 2D fitting technique with exponential light profiles for both bulge and disk yields the most reproducible and representative component parameters. Assuming that the 2D model with exponential profiles for both bulge and disk is a reasonable correct description of the global structure of a galaxy, the estimated maximum errors of the structural parameters are of order 20%. These errors are dominated by the uncertainty in the sky background level. The errors in the disk parameters will double if the model for the bulge is better represented by an $r^{1/4}$ law profile. The errors on the bulge parameters will then be very uncertain. The determined parameters will be used in the subsequent articles in these series.

The two dimensional decomposition technique exploited here has many advantages above other often used decomposition techniques. Still we are far away from full scale 3D models which link complete self-consistent dynamics of the different components to a 2D morphological projection.

Acknowledgements. I would like to thank Yanis Andredakis, Piet van der Kruit, Reynier Peletier and David Sprayberry for the fruitful discussions. Erwin de Blok, Joyce Majewski, René Oudmaijer and Arpad Szomoru are acknowledged for their many useful suggestions on the manuscript. This research was supported under grant no. 782-373-044 from the Netherlands Foundation for Research in Astronomy (ASTRON), which receives its funds from the Netherlands Foundation for Scientific Research (NWO).

References

Andredakis Y.C., Sanders R.H. 1994, MNRAS 267, 283
Block D.L., Wainscoat R.J. 1991, Nature 353, 48
Burstein D. 1979, ApJ 234, 829
Byun Y.-I. 1992, Ph.D. Thesis, The Australian National University
Capaccioli M., Caon N. 1992, In: Longo G., Capaccioli M., Busarello G. (eds.) Morphological and Physical Classification of Galaxies (Kluwer, Dordrecht), p.99
Capaccioli M., Held E.V., Nieto J.-L. 1987, AJ 94, 1519
Caon N., Capaccioli M., D'Onofrio M. 1993, MNRAS 265, 1013
Davies J.I. 1990, MNRAS 244, 8
de Jong R.S. 1995, A&A, to be submitted to A&A **(Chapter 3)**
de Jong R.S., van der Kruit P.C. 1994, A&AS 106, 451 **(Chapter 1)**
de Vaucouleurs G. 1948, Ann. d'Astrophys. 11, 247
de Vaucouleurs G. 1959, Hdb. d. Physik 53, 311
de Vaucouleurs G., de Vaucouleurs A., Corwin H.G., Buta R.J. et al. 1991, Third Reference Catalog of Bright Galaxies (Springer-Verlag, New York) (RC3)
Frankston M., Schild R. 1976, AJ 81, 500
Freeman K.C. 1966, MNRAS 133, 47
Freeman K.C. 1970, ApJ 160, 811
Giovanelli R., Haynes M.P., Salzer J.J., Wegner G., Da Costa L.N., Freudling W. 1994, AJ 107, 2036
Hubble E.P. 1930, ApJ 71, 231
Jaffe W. 1983, MNRAS 202, 995
Jensen E.B., Thuan T.X. 1979, In: Photometry, Kinematics and Dynamics of Galaxies (Univ. of Texas, Austin)
Kent S.M. 1986, ApS 91, 1301
Kent S.M., Dame T., Fazio G. 1991, ApJ 378, 131
King I.R. 1966, AJ 71, 64
Knapen J.H., Kruit P.C., van der 1991, A&A 248, 57
Kormendy J. 1977, ApJ 217, 406
Kormendy J. 1993, In: Dejonghe H., Habing H.J. (eds.) IAU Symp. 153, Galactic Bulges (Kluwer, Dordrecht), p.209
Kormendy J., Bruzual A. 1978, ApJ 223, L63
Kormendy J., Illingworth, G. 1982, ApJ 256, 460
Nilson P. 1973, Uppsala General Catalog of Galaxies (Roy. Soc. Sci., Uppsala) (UGC)
Phillipps S., Disney M.J. 1983, MNRAS 203, 55
Pritchet C., Kline M.I. 1981, AJ 86, 1859
Schombert J.M., Bothun G.D. 1987, AJ 93, 60
Scorza C., Bender R. 1990, A&A 235, 49
Sérsic J.-L. 1968, Atlas de galaxias australes (Observatorio Astronomica, Cordoba)
Shaw M.A., Gilmore G. 1989, MNRAS 237, 903
Simien F. 1989, In: Corwin H.G., Bottinelli L. (eds.) The World of Galaxies (Springer-Verlag, New York), 293
Simien F., Michard R. 1990, A&A 227, 11

van der Kruit P.C. 1979, A&AS 38, 15
Wainscoat R.J., Freeman K.C., Hyland A.R. 1989, ApJ 337, 163
Young C.K., Currie M.J. 1994, MNRAS 268, L11

Chapter 3

The statistics of disk and bulge parameters

Abstract. The statistics of the fundamental bulge and disk parameters of galaxies and their relation to the Hubble sequence were investigated by an analysis of optical and near-infrared observations of 86 face-on spiral galaxies. The availability of near-infrared K passband data made it possible for the first time to trace fundamental parameters related to the luminous mass while hardly being hampered by the effects of dust and stellar populations. The observed number frequency of galaxies was corrected for selection effects to calculate volume number densities of galaxies with respect to their fundamental parameters. The main conclusions of this investigation are:
1) Freeman's law has to be redefined. There is no single preferred value for the central surface brightnesses of disks in galaxies. There is only an upper limit to the central surface brightnesses of disks, while for lower central surface brightnesses the number of galaxies per volume element decreases only slowly as function of the central surface brightness.
2) The Hubble sequence type index correlates strongly with the effective surface brightness of the bulge, much better than with the bulge-to-disk ratio.
3) The disk and bulge scalelengths are correlated.
4) These scalelengths are not correlated with Hubble type. Hubble type is a lengthscale-free parameter and each type therefore comes in a range of magnitudes (and presumably a range of total masses).
5) Low surface brightness spiral galaxies are not a separate class of galaxies. In a number of aspects they are a continuation of a trend defined by the high surface brightness galaxies. Low surface brightness galaxies are in general of late Hubble type.

1 Introduction

The light of a spiral galaxy is dominated by two components, the disk and the bulge. The basic difference between these components lies in their support against gravitational collapse. The disk is almost completely rotationally supported, while the bulge is for some fraction also pressure supported. At least two parameters are needed to describe the light distribution of each of these components: a surface brightness term and a spatial scaling factor. The fundamental parameters of the disk are usually expressed in central surface brightness (μ_0) and scalelength (h), while the bulge parameters are expressed in effective surface brightness ($\mu_{\rm e}$) and effective radius ($r_{\rm e}$). These fundamental parameters were determined for a large statistically complete sample of galaxies by de Jong (1995a, Paper II). The distributions of the fundamental parameters are still poorly known and their statistics are investigated in this paper with some emphasis on three relationships: 1) "Freeman's law", the empirical relation found by Freeman (1970) indicating the constancy of disk central surface brightness among galaxies, 2) the number density of galaxies as a function of their fundamental parameters and 3) the relation between the fundamental parameters and Hubble classification.

1.1 Freeman's law

One of the most remarkable results presented in the classical paper of Freeman (1970) was the apparent constancy of the B passband μ_0 of spiral galaxies. For a subsample of 28 (out of 36) galaxies he found $\langle \mu_0 \rangle = 21.65 \pm 0.3$ B-mag arcsec^{-2}. If the central M/L is approximately constant among galaxies, this translates directly into a constant central surface density of matter associated with the luminous material.

Several authors have tried to explain this result. It has been argued that ignoring the contribution of the bulge to the light profile could produce the effect (Kormendy 1977; Phillipps & Disney 1983; Davies 1990). Freeman (1970) did not decompose the luminosity profiles in a bulge and disk, but fitted a line to the linear part of the luminosity profile plotted on a magnitude scale. This linear part of the profile could be contaminated by bulge light. With their models Kormendy (1977) and Davies (1990) show that the central surface brightness of low surface brightness disks will be overestimated by this procedure because of the extra bulge light near the center. The central surface brightnesses of high surface brightness disks with a short scalelength are underestimated; because of the small disk scalelength the bulge light dominates the luminosity profile again in the outer region, but with a longer scalelength and a lower surface brightness than the disk. Several arguments can be raised against this interpretation (see also Freeman 1978): 1) even with bulge light included the result is still important, 2) many later type galaxies hardly have a bulge, but the effect is still present (van der Kruit 1987), 3) in samples where proper decomposition techniques are used the effect is still found, although with a larger dispersion (Boroson 1981), 4) a limited range in bulge parameter space was explored in the models mentioned above, which might not be representative of the bulges in spiral galaxies.

Dust extinction has also been proposed as an explanation for the constancy of μ_0 (Jura 1980; Valentijn 1990). If galaxies are optically thick in the B passband, one is only looking one optical depth into the galaxies and always observes the same outer layer. This removes the inclination dependence from the Freeman relation, but leaves the unsolved problem of why all galaxies should have the same surface brightness at optical depth equal to one.

Freeman established his relation in the B passband where the light of galaxies is dominated by a very young population of stars, which make up only a few percent of the stellar mass. Of all commonly used passbands the light of the massive old stellar population is relatively the most important in the near-infrared (near-IR) K passband used here. The K passband has the additional advantage that the extinction by dust is strongly reduced. The K passband is therefore best suited to trace the fundamental parameters of the luminous mass. However, other passbands have been used as well in this study to investigate the wavelength dependence of the bulge and disk parameters due to dust and population effects.

De Vaucouleurs (1974) was one of the first to suggest that the constancy of μ_0 might result from a selection effect. This was later quantified by Disney (1976) and Allen & Shu (1979). Catalogs of galaxies have usually been selected by eye from photographic plates using some kind of diameter limit. One might therefore select against very compact galaxies with a high central surface brightness, because these have small isophotal diameters. Likewise, galaxies with a very low surface brightness might have been missed due to the lack of contrast with the sky background. Disney & Phillipps (1983; see also Davies 1990) define a visibility for a galaxy, which enables one to correct a sample for these selection effects if one has made a careful initial sample selection.

1.2 Bivariate distributions

Correcting for selection effects is in fact trying to determine from the observed statistics how many galaxies there are per unit volume with a certain property. More than one property can be used in determining such a distribution per volume. One needs at least two parameters to characterize the exponential light profile of a disk dominated galaxy and a bivariate distribution function of both disk parameters is a more general statistical description of galaxy properties than a one parameter function. The diameter, the central surface brightness and the luminosity distribution functions of galaxies are integrations of this bivariate distribution in a certain direction. In this process information is lost and the bivariate distribution function is therefore more useful in studies of deep galaxy counts and provides more constraints on theories of galaxy formation and evolution than its one dimensional counterparts.

Bivariate distribution functions of galaxies have been determined only a few times before (Choloniewski 1985; Phillips & Disney 1986; van der Kruit 1987, 1989; Saunders et al. 1990; Sodré & Lahav 1993). Even though different fundamental parameters are used, almost all (except Saunders et al.) of these distributions describe fundamentally the same thing in different ways. These studies were performed in the B or comparable passbands, which is, as mentioned before, not the wavelength most suited to study global fundamental properties of galaxies.

1.3 Morphological classification

For classification of spiral galaxies on the Hubble sequence three principal discriminators are used: 1) the pitch-angle of the spiral arms, 2) the degree of resolution of the arms (into H II regions, dust lanes and resolved stars) and 3) the bulge-to-disk (B/D) ratio. In his detailed description of the Hubble sequence, Sandage (1961) indicates that the B/D ratio is the weakest discriminator unless galaxies are seen edge-on. He finds clear mismatches in type between classifications using items 1) and 2) and classifications using item 3). Another factor hampers the use of B/D ratio for classification of early spirals. On the photographs used for classification the central region of an early spiral galaxy is normally overexposed in order to show clearly the faint spiral structure.

Still, the B/D ratio is often assumed to be the principle underlying the Hubble sequence, even though a tight correlation between classification and measured B/D ratios was never found. The measurements indicate at best a trend (e.g. Simien & de Vaucouleurs 1986; Andredakis & Sanders 1994) and the discrepancies between B/D ratio and Hubble type have been attributed to two sources of error. First there is the uncertainty in classification. Comparisons of Hubble types given by different classifiers show an rms uncertainty in type index of order 2 T-units (Lahav et al. 1995). The second source of error is the uncertainty in the bulge/disk decomposition, due to, among other things, the mathematical peculiarities of the widely used $r^{1/4}$ bulge law (de Vaucouleurs 1948).

1.4 Outline

The main goal of this investigation is to determine the nature of the Freeman law. In order to address the problems concerning the Freeman law, a large sample of face-on spiral galaxies was carefully selected and surface photometry was obtained in the K passband as well as in several other passbands. A large number of other global and structural parameters of the galaxies were determined in this investigation and their nature is also explored in this paper.

The remainder of this article is organized as follows. The data set and the extraction of the observed bulge and disk parameters are briefly described in Section 2. The corrections to the observations in order to calculate number distributions are described in Section 3 and these distributions are presented for the B and the K passband in Section 4. The relations found are discussed within the context of the three main points of interest (Freeman's law, bivariate distributions and Hubble sequence) in Section 5. The conclusions are summarized in Section 6.

2 The data

In order to examine the parameters describing the global structure of spiral galaxies, 86 systems were observed in the

B, V, R, I, H and K passbands. A full description of the selection, observations and data extraction can be found in de Jong & van der Kruit (1994, Paper I). The galaxies in this statistically complete sample of undisturbed spirals were selected from the UGC (Nilson 1973) to have red diameters of at least two arcmin and minor over major axis ratios larger than 0.625. The survey was limited to 12.5% of the sky globe. Standard reduction techniques were used to produce calibrated images.

In Paper II the extraction of the bulge and disk parameters from the calibrated images is described. An extensive error analysis was performed using different fit techniques. The best results were obtained with a model galaxy with an exponential radial light profile for both bulge and disk, that was two-dimensionally (2D) fitted to the full calibrated image. This 2D fit technique made it also possible to fit an additional Freeman bar (Freeman 1966) component, which improved the fit for 23 of the 86 galaxies. The error analysis revealed the two dominant sources of error in the derived component parameters to be: 1) the assumed luminosity profile of the bulge and 2) the uncertainty in the sky background subtraction.

Assuming that the exponential profile is a reasonable description of the bulge light distribution, the dominant source of error in the parameters is caused by the uncertainty in the sky background level. This uncertainty was not taken into account using the 2D fit technique, but the 1D errors can be used, because the 2D fit results are generally comparable to the double exponential 1D fit results (see Paper II, Fig.6). The 1D errors do include the uncertainty of sky background subtraction and are always larger than the formal 2D fit errors. The 1D errors are only shown in the graphs presented here if they are significantly larger than the symbol size.

In this paper the RC3 (de Vaucouleurs et al. 1991) morphological type index T is used (see also Paper I). Because a few galaxies had no RC3 classification, I classified them as UGC 1551–(8), UGC 1577–(4), UGC 9024–(8) and UGC 10437–(7). The mean error in type index in the RC3 is stated to be 0.89. This number seems to be very low. Lahav et al. (1995) showed that the dispersion between the RC3 T-index and the T-values of six expert classifiers was on average 2.2 T-units for a sample of 831 galaxies. The dispersion between any two classifiers ranged between 1.3 and 2.3 T-units, with 1.8 on average. It is safe to say that the uncertainty in classification in the RC3 is at least 1.5 T-units.

The data set comprises 86 galaxies in six passbands. To keep a clear view on the obtained results I will concentrate on the two most extreme cases, the B and the K passband data. The results for the other passbands are available in electronic form. The B and K passband results are displayed in the graphs with the same dynamic range (but often with different zero-points) and therefore they can be compared directly.

3 Corrections

The observed bulge and disk parameters determined in Paper II have to be corrected for all kinds of systematic effects. These corrections are often uncertain but necessary. One can only expect that they are at least in a statistical sense correct.

3.1 Galactic foreground extinction

The measurements of brightness and surface brightness were corrected (unless stated otherwise) for Galactic foreground extinction according to the precepts of Burstein & Heiles (1984) and the actual B passband extinction values were adopted from the RC3. The Galactic extinction curve of Rieke & Lebofsky (1985) was used to convert these B passband extinction values to other passbands. The sample galaxies were selected to have a Galactic latitude larger than 25°; the extinction correction is in general small and gets smaller for the longer wavelength passbands. The average correction is 0.14 B-mag and the largest correction is 0.68 B-mag, which translates into 0.06 K-mag.

3.2 Inclination corrections

Since Valentijn (1990) reopened the debate of optically thin versus optically thick spiral galaxies, inclination corrections for surface brightness have become less trivial. A simple equation for correcting surface brightnesses for inclination effects, taking internal extinction into account, has the form

$$\mu^i = \mu - 2.5C\log(a/b), \tag{1}$$

where a/b is the major over minor axis ratio of the galaxy and C the internal extinction parameter, which takes values $0 \leq C \leq 1$. Fully transparent galaxies are described by $C = 1$, while the case $C = 0$ describes the optically thick ones.

It is unlikely that the inclination correction indeed takes such a form in the optical passbands, as extinction in the optical passbands is for a considerable fraction caused by scattering and not just by absorption alone. Light will be scattered preferably from edge-on directions to face-on directions, which means that extinctions will seem to be higher for edge-on than for face-on galaxies. On top of that, certain configurations of dust and stars can behave optically thin in an inclination test, while they may in fact be completely opaque. A clear example of this is a very thin layer of optically thick dust between a thicker slab of stars. It is not trivial to produce a better description as there are too many unknowns and C itself may be a function of galactic radius (see e.g. Giovanelli et al. 1994; Byun et al. 1994). Therefore Eq. (1) is used as a working hypothesis. However, for a face-on selected sample such corrections are small. The average correction for the sample examined here is 0.26 mag arcsec^{-2} when $C = 1$, with a maximum of 0.60 mag arcsec^{-2} if $b/a = 0.58$.

3.3 Distances

The distances to the observed galaxies were calculated using a Hubble flow with an H_0 of 100 km s^{-1} Mpc^{-1}, corrected for infall into the Virgo cluster using the 220 model of Kraan-Korteweg (1986). This model assumes that the Local Group has an infall velocity of 220 km/s towards the Virgo cluster and describes the motions of the galaxies around the cluster by a non-linear flow model. The $V_{\rm hel}$ velocities needed for this model were calculated from the $V_{\rm GSR}$ velocities listed in the

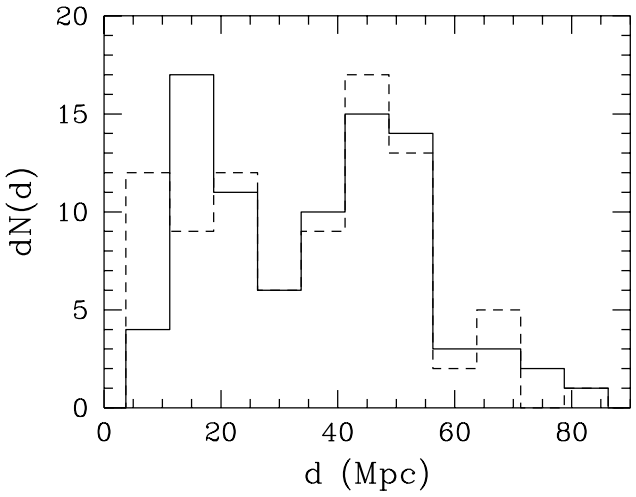

Fig. 1. The distance distribution of the sample galaxies. For the dashed line the $V_{\rm GSR}$ velocities from the RC3 were used, the full line indicates the distance distribution when the velocities are corrected for Virgocentric infall.

RC3, which are also tabulated in Paper I. The nearest galaxy is at 6.2 Mpc, the most distant galaxy is at 82.5 Mpc. The peculiar velocities of galaxies were assumed to be on average 200 km/s in the line of sight, which introduces an error (σ_d) of 2 Mpc in the distance estimates. The distribution of distances is displayed in Fig. 1, which shows a small excess of galaxies at ∼45 Mpc because of an extension of the Pisces-Perseus supercluster. The relationships presented in this study are very little affected when other infall and flow models are used to calculate distances.

3.4 Selection correction

The physically relevant quantities are not the observed numbers of galaxies with a certain property, but the frequency of galaxies with a certain property in a volume. Therefore, the fact that a galaxy is included in the sample has to be linked to the statistical probability of finding such a galaxy in a certain volume. The galaxies in the sample were selected to have UGC red major axis diameter ($D^{\rm lim}_{\rm maj}$) of at least 2 arcmin. This creates a selection bias against galaxies with low surface brightness and/or small scalelengths, as they appear smaller on photographic plates. The distances (d) to the observed galaxies and their angular diameters ($D_{\rm maj}$) are known and the maximum distance at which galaxy can be placed, while still obeying the selection criteria, can be calculated ($d_{\rm max} = dD_{\rm maj}/D^{\rm lim}_{\rm maj}$). A galaxy can only enter the sample if it lies in a spherical volume which has this maximum observable distance as radius. Turning this argument around, one can expect on statistical grounds that a selected galaxy samples a spherical volume with a radius equal to its maximum observable distance (a more formal discussion can be found in Felten 1976). The volume sampled by a galaxy in a diameter limited sample is thus

$$V_{\rm max} = \frac{4\pi}{3}(d_{\rm max})^3 = \frac{4\pi}{3}(dD_{\rm maj}/D^{\rm lim}_{\rm maj})^3. \quad (2)$$

Following the previous line of reasoning, an estimate for the average number of galaxies in a unit volume obeying a certain specification (S) *for a complete sample of* N *galaxies* is

$$\Phi(S) = \sum_i^N S^i/V^i_{\rm max}, \quad (3)$$

where i is summed over all N galaxies in the sample and $S^i = 1$ if the specification is true for galaxy i and $S^i = 0$ if false. The error in $\Phi(S)$, assuming Poison statistics in a homogeneous universe and considering the uncertainties in the distances, can be calculated by

$$\sigma^2_{\Phi(S)} = \sum_i^N (S^i/V^i_{\rm max})^2 + \sigma_d^2 \sum_i^N (3S^i/dV^i_{\rm max})^2. \quad (4)$$

There is always a chance that a member of a peculiar class of galaxy happens to be nearby and gets a lot weight in Eq.(3) and this volume correction can therefore only be applied to large samples. One must ensure that a large enough volume of space is sampled so that galaxies are randomly distributed in space. Figure 1 shows that the sample mainly traces the local density enhancement, as large scale structures in the universe have scales of order 50 Mpc. Equation 3 should therefore be used with care, because the number of galaxies with small intrinsic diameters will be overestimated relative to the larger ones due to the local density enhancement. The average number of galaxies per Mpc^3 calculated with Eq. (3) might be more representative of the local environment than of the mean cosmological values. Still it is a useful equation to observe general trends in bivariate distributions and to compare results obtained from different passbands.

Other methods to correct distributions for selection effects have been advocated, because they take spatial density fluctuations into account (for an overview see Efstathiou et al. 1988). These methods assume that the intrinsic distribution function is independent of position (**x**) in space, so that we can write $\Phi(S) = \phi(S)\rho(\mathbf{x})$, thereby losing the absolute calibration of the number density. These methods all assume a clear relation between the distribution parameter(s) and the limiting selection parameter(s). This is not the case for the current investigation. A diameter limit is not trivially linked to the central surface brightness distribution, certainly not when a different passband is used for the selection and the distribution.

The correction of Eq. (3) is only valid if a particular galaxy would have been measured at the same intrinsic (as opposed to angular) diameter, had it been at a different distance. In Paper I it was shown that this is probably the case for the UGC galaxies with type index T≤6. For later types the situation is less clear, there is a too short a range in diameters to check and it must be assumed that for late-type systems the same type of galaxy is measured at the same intrinsic diameter at different distances. Under this assumption it is *not* important that the UGC eye estimated diameters of late-type galaxies correspond to lower average surface brightness than that of early types (see Paper I, Fig. 11). This effect just means that there are more late-type galaxies in the sample than expected based on their isophotal

diameter, but their average distance will be larger so that the number of galaxies per sampled volume stays the same.

The volume correction of Eq. (3) can be used to calculate number density distributions for all passbands, as long as the red UGC diameters are used to calculate the $V_{\rm max}$. The distribution of any galaxy parameter S^i can be determined in any passband; the use of the red UGC diameters in Eq. (3) ensures the correction for the intrinsic selection effects of the whole sample.

Next to the diameter limit, there are two more selection criteria defining the sample. The selection was limited to 12.5% of the sky and only galaxies with $b/a > 0.625$ were used, which is only 37.5% of all possible random orientations. Equation 3 was corrected for these selection criteria. A correction was also applied for the fraction of galaxies for which no (photometric) data was available in a certain passband. All these corrections were made under the assumption that the incompleteness had no correlation with the investigated parameters.

Equation (3) can only be applied when the sample is complete. The statistical completeness of the sample can be tested with the $V/V_{\rm max}$-test (Paper I). The $V/V_{\rm max}$ of a galaxy is the spherical volume associated with the distance of a galaxy divided by $V_{\rm max}$ as defined in Eq.(3), thus for a galaxy in this diameter limited sample $V/V_{\rm max} = (D^{\rm lim}_{\rm maj}/D_{\rm maj})^3$. For objects distributed randomly in space the average value of $V/V_{\rm max}$ should be $0.5 \pm 1/\sqrt{12 \times N}$, where N is the number of objects in the test. For the current sample $\langle V/V_{\rm max}\rangle = 0.57 \pm 0.03$ and therefore there are slightly too many galaxies with a small angular diameter in the sample. The original sample of 368 galaxies from which the current subsample was selected had a $\langle V/V_{\rm max}\rangle = 0.496 \pm 0.015$ (Paper I). Subsequent selection depended only on the position on the sky and therefore the excess of small diameter galaxies is probably caused by the density enhancement of the Pisces-Perseus supercluster, which gives some extra galaxies at the diameter selection limit. This might give some extra high surface brightness and/or large scalelength galaxies in the sample above the cosmological mean, because galaxies have to be intrinsically large to be included in the sample being at the distance of the Pisces-Perseus supercluster.

In a recent paper Davies et al. (1994) argued that the sample used by van der Kruit (1987) was incomplete in a magnitude $V/V_{\rm max}$-test. They argued that a hidden magnitude limit had influenced the selection, so that an extra selection correction should be applied. I will follow up on this argument as the sample used here has been selected using similar criteria as van der Kruit used for his sample. [1]

There is nothing hidden about a magnitude selection effect for a diameter limited sample. On the contrary, it is expected. For galaxies with a certain absolute magnitude M there exists a range of possible (μ_0,h) combinations, satisfying $M \propto \mu_0 - 5\log(h)$, but only a limited range of them will satisfy the diameter selection criterion $D_{\rm maj} \propto (\mu_{\rm lim} - \mu_0)h > D^{\rm lim}_{\rm maj}$. Thus for galaxies of the same apparent magnitude we will miss some of the small scalelength, bright μ_0 and some of the large scalelength, faint μ_0 galaxies, while still having selected a complete sample in diameter. The complication arises because apparent diameters and magnitudes are not independent parameters for galaxies and their $V/V_{\rm max}$-tests cannot be applied independently. Similar to Eq. (2), a $V_{\rm max}$ corresponding to a magnitude limit can be constructed. The smallest of the magnitude $V_{\rm max}$ and the diameter $V_{\rm max}$ values should be used for each galaxy in a combined $V/V_{\rm max}$-test. These tests cannot be performed separately. The fundamental premisse of a diameter limited sample is that the diameter $V_{\rm max}$ is always smaller than the magnitude $V_{\rm max}$, and therefore a "hidden" magnitude limit does not have to be taken into account and Eq. (3) is sufficient.

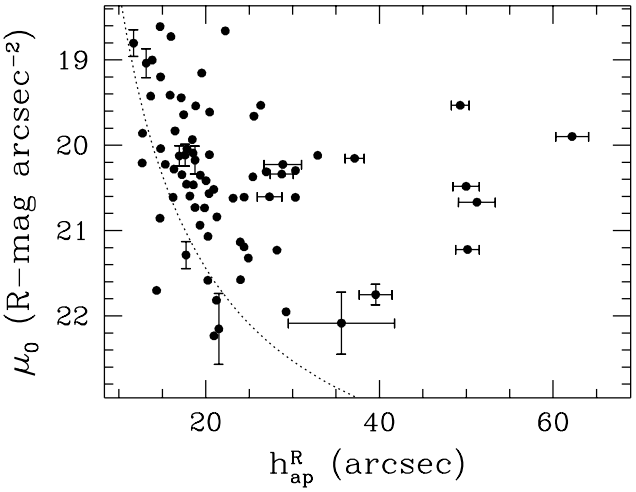

Fig. 2. The apparent scalelength versus observed central surface brightness of the disks. The dashed line indicates the selection limit of $D_{\rm maj} \geq 2'$ at the 24.7 R-mag arcsec^{-2} isophote for galaxies with perfect exponential disks. The indicated error estimates are the errors from the 1D profile fitting with exponential bulge taking the uncertainty in the sky background level into acount The errors are only plotted if they are significantly larger than the symbol size.

4 The distribution of disk, bulge and bar parameters

In this section I investigate the distributions of the structural parameters of the different galaxy components as a function of morphological type and of each other. First the structural parameters of the disk and bulge are examined independently. In the final subsection, the relationships between disk and bulge parameters are investigated. The distributions of bulge and disk parameters are corrected for selection effects to yield volume number densities.

4.1 The disk parameters

Figure 2 indicates some aspects of the completeness and selection effects of the sample. It shows the distribution of the observed central surface brightnesses versus scalelength as

[1] Davies et al. (1994) also indicate that van der Kruit's sample becomes incomplete for low surface brightnesses at $\mu_0 > 22.3$ as $\langle V/V_{\rm max}\rangle = 0.35 \pm 0.08$. I would like to note that this might just be a statistical fluctuation of low number statistics, as $\langle V/V_{\rm max}\rangle = 0.41 \pm 0.10$ for $\mu_0 > 22.5$ and $\langle V/V_{\rm max}\rangle = 0.46 \pm 0.13$ for $\mu_0 > 22.7$, and thus for even lower surface brightnesses the sample is in the statistically complete range of $\langle V/V_{\rm max}\rangle = 0.5$.

obtained from the 2D fits of Paper II. The R passband values are plotted, because these values are most closely related to the (red UGC diameter) selection criteria. The dotted line indicates the selection limit for a diameter cutoff at 2 arcmin at a surface brightness of 24.7 R-mag arcsec^{-2} for a perfect exponential disk. The 24.7 R-mag arcsec^{-2} is the average surface brightness at which the UGC red diameters were determined (see Paper I). As mentioned in Paper I, not all UGC galaxies had their diameters estimated at the same isophote level. This explains why there are some galaxies to the left of the selection line in Fig. 2. If all galaxies have the same scalelength, the number of galaxies expected in the sample will decrease as $h_{\rm ap}^3$ and therefore it is not surprising that there are hardly any galaxies in the sample below 22 R-mag arcsec^{-2}. Obviously no galaxies can enter the sample with μ_0 fainter than $\sim$24.7 R-mag arcsec^{-2}.

Let us now look at the central surface brightness as function of morphological type (Fig. 3). Apparently the galaxies from type T$=1$ to 6 have on average the same μ_0, but with a large scatter. The later types have on average a significantly lower central surface brightnesses and they might be classified as late types just because they are low surface brightness (LSB) systems. It can be readily seen that this difference between early and late-type galaxies increases when going from the B to the K passband. This indicates that disks of the later type spirals are bluer than the disks of the early ones, but the discussion on the colors of these galaxies is postponed to Paper IV in this series (de Jong 1995b). The average μ_0 values were calculated for three morphological type bins indicated by the horizontal bars in Fig. 3 as well as for the total sample. The values with their standard deviations are tabulated in Table 1.

The average μ_0 values were also calculated with an inclination correction according to Eq. (1) with values for $C=0.5$ and $C=1$ (semi transparent and completely transparent behavior). The results can also be found in Table 1. The standard deviations on the average μ_0 values are slightly smaller for $C=1$, and even though it is a small effect, it is persistent for all subgroups and all passbands. The main result is of course a shift in the mean central surface brightness of the disks. For all remaining plots an inclination correction with $C=1$ will be used.

The distribution of the other disk parameter, the scalelength (h), as function of type is shown in Fig. 4. There is no trend of h with type and there is a large range in scalelengths. There might be a lack of late-type galaxies with small scalelengths, but this can probably be attributed to a selection effect: the selection criteria are heavily biased against LSB galaxies with small scalelengths. The scalelengths are smaller in the B passband than in the K passband (discussion in Paper IV).

The information of Figs 3 and 4 are combined in Fig. 5. This figure shows that there is an upper limit in the (μ_0,h)-plane, as there are no galaxies with large scalelengths and high central surface brightnesses. This cannot be caused by selection effects, large bright galaxies just cannot be missed in a diameter selected sample. This upper limit has been noted before by Grosbøl (1985). The upper limit partly follows the line of constant total disk luminosity, as indicated by the dashed line in Fig. 5. Note that the Tully-Fisher relation (1977, hereafter TF-relation) implies that this is also a line of constant maximum rotation speed of the disk. There is also an upper limit to the central surface brightness at about 20 B-mag arcsec^{-2} (16 K-mag arcsec^{-2}). Again galaxies brighter than these limits are hard to miss because of selection effects.

Late-type galaxies have lower central surface brightnesses in Fig. 5, but the early and intermediate types show no segregation. The scalelengths also gives no segregation according to type. Very few late-type galaxies with very short scalelengths were selected, but as shown before, late-type galaxies have lower surface brightnesses and the selection biases against galaxies with low surface brightness and short scalelengths are large. These biases are indicated by the dotted lines in Fig. 5. To the right of these lines the sample should be complete to the indicated distance. The lines are calculated under the assumption that all galaxies have perfect exponential disks with the same color at the selection radius (B–$R=1.3$, R–$K=2.5$) and that the selection limit is at $2'$ diameter at the 24.7 R-mag arcsec^{-2} isophote (as in Fig. 2). Although these assumptions are not valid for an individual galaxy, the dotted lines help to estimate the selection effects; the galaxies near the 50 Mpc line had about 125 times more chance of being included in the sample than the galaxies near the 10 Mpc line! The fact that the number density of objects does not decrease by 125 from one line to the other already indicates that there are many more "small" galaxies per volume element than "large" galaxies.

The distribution of the absolute magnitude of the disk ($M_{\rm disk}$) against type (Fig.6) can also be deduced from Figs 3 and 4 ($M_{\rm disk} \propto \mu_0 - 2.5\log(2\pi h^2)$, no inclination dependent extinction correction was applied). As scalelengths show little correlation with type, the distribution of disk magnitudes reflects the distribution of the central surface brightness against type. There was no apparent segregation according to bar classification in Figs 3, 4, 5 and 6.

So far, only the observed distributions were presented, but the distributions per volume are of more importance. Therefore the volume correction as described in Section 3 was applied. The correction transforms Fig. 5 into the bivariate distribution in the (μ_0,h)-plane presented in Fig. 7. This is a representation of the true number distribution of spiral galaxies per volume element of one Mpc^3 with respect to both disk parameters. The magnitude and μ_0 upper limits noticed in Fig. 5 are also present here. We are dealing with low number statistics now, which is reflected in the erratic behavior of the distribution. The uncertainty increases in the direction of small scalelength and low surface brightness. These galaxies have so small isophotal diameters that they really have to be nearby to be included in the sample and such a small volume is sampled that statistics are working against us. For example if the true volume densities in the (17 K-mag arcsec^{-2}, 1 kpc) and (21 K-mag arcsec^{-2}, 1 kpc)-bins are equal, the chance of observing a galaxy in the last bin would be 0.5. If there had been such a galaxy in the sample, a lot of weight would have been given to it. In short, the distributions are not well sampled in the low surface

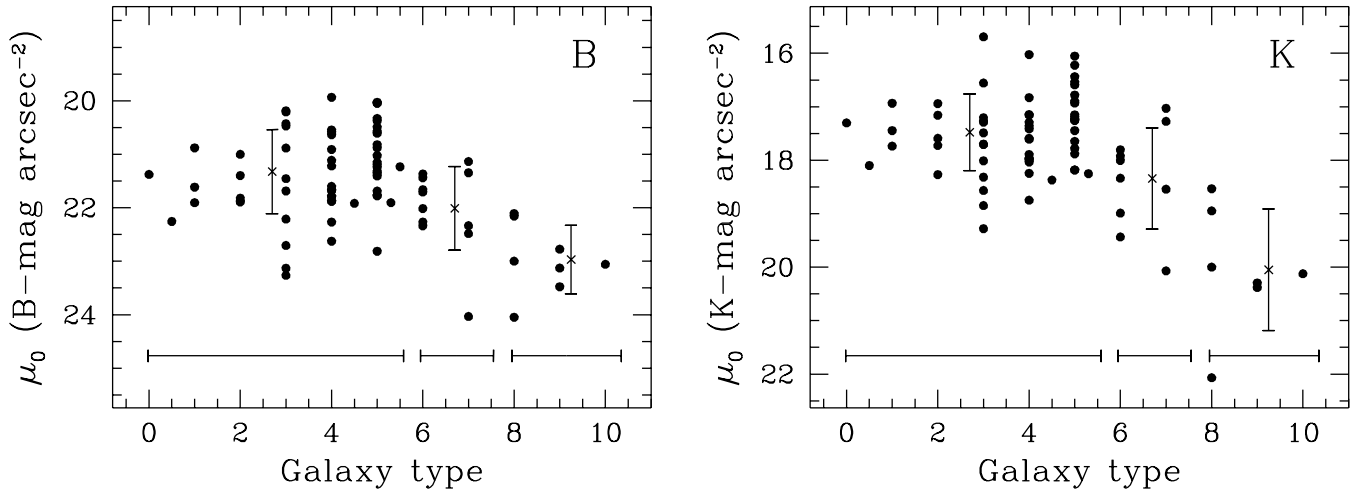

Fig. 3. The Galactic extinction corrected central surface brightness of the disks as function of morphological RC3 type. The crosses show the values averaged over the bins indicated by the horizontal bars. The vertical bars indicate the standard deviations of the mean values.

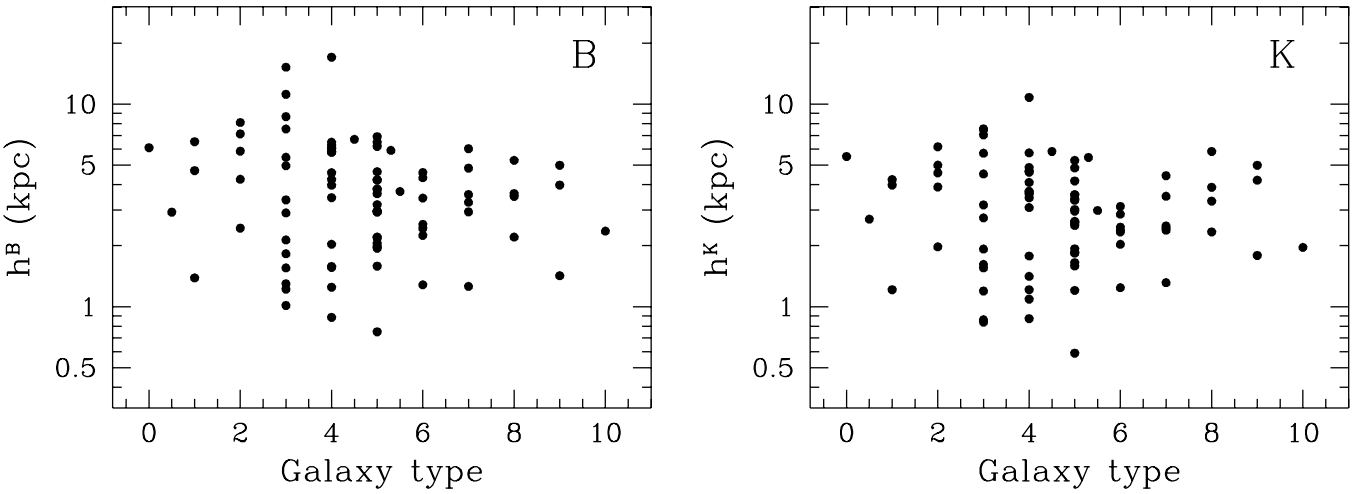

Fig. 4. The scalelength of the disk as function of morphological type.

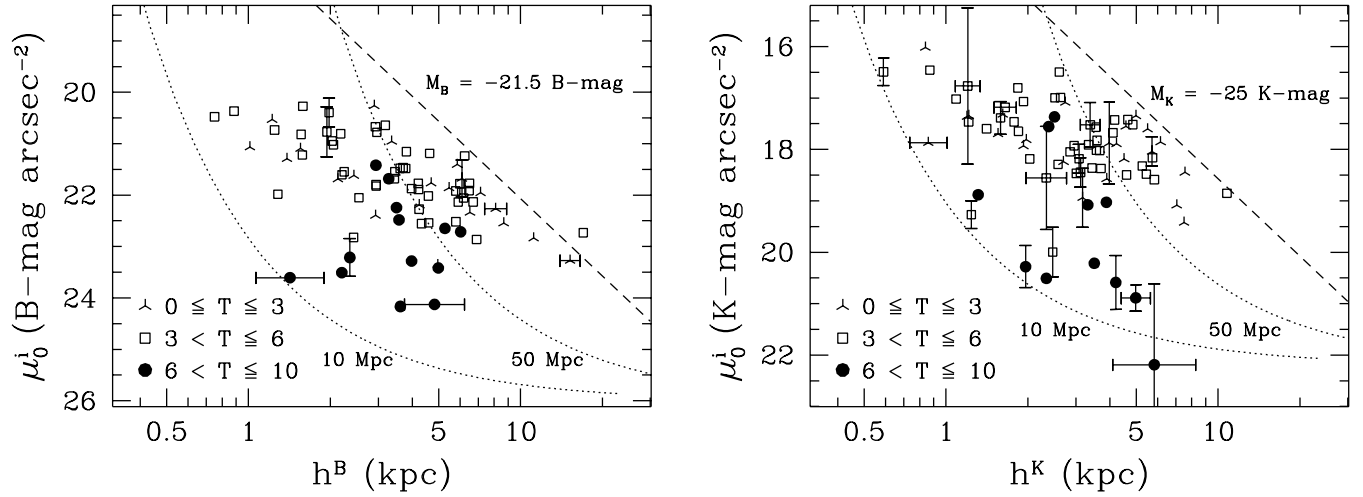

Fig. 5. The scalelength of the disks versus the central surface brightness. Different symbols are used to denote the indicated morphological type ranges. Exponential disks with equal absolute luminosity of indicated magnitude are found on the dashed line. Equality lines of other magnitudes lie parallel to the dashed line. The dotted lines indicate the selection limits for all exponential disk galaxies closer than 10 and 50 Mpc respectively, under the assumptions made in the text.

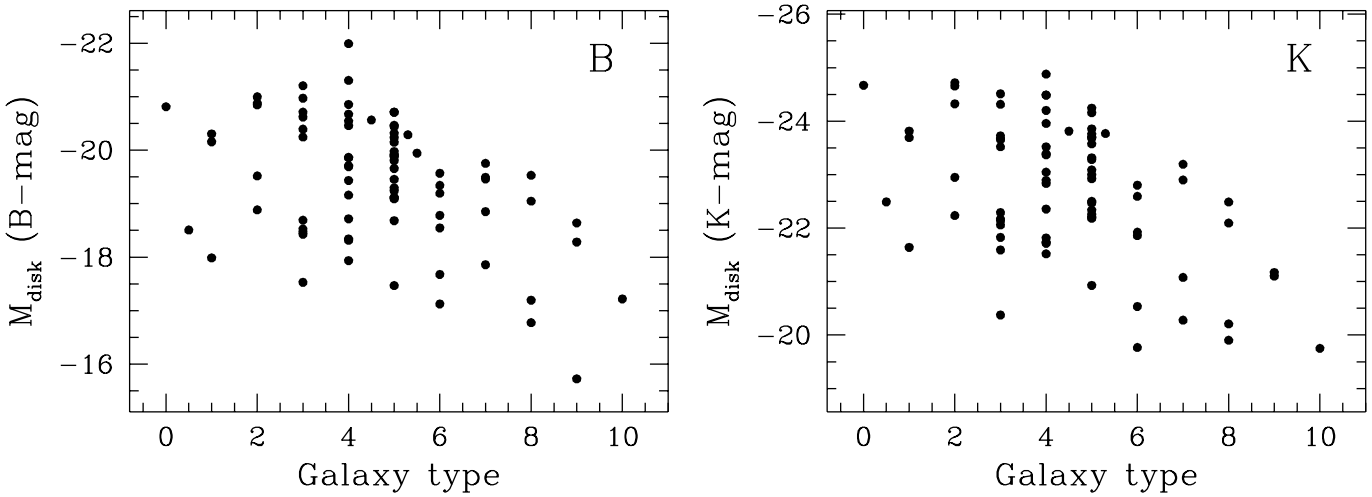

Fig. 6. The distribution of absolute disk magnitudes as function of type index.

Table 1. The average Galactic extinction corrected central surface brightnesses for different inclination corrections (Eq. (1)) and type index bins. $C = 0$ corresponds to an optically thick disk, $C = 0.5$ to a semi transparent disk and $C = 1$ to a fully transparent disk. The values are in mag arcsec^{-2} with their standard deviations.

		$\langle\mu_0\rangle$ (B-mag arcsec^{-2})				$\langle\mu_0\rangle$ (K-mag arcsec^{-2})		
RC3 type	nr.	$C = 0$	$C = 0.5$	$C = 1$	nr.	$C = 0$	$C = 0.5$	$C = 1$
$0 \leq T < 6$	61	21.32 ± 0.78	21.45 ± 0.76	21.58 ± 0.74	60	17.48 ± 0.71	17.61 ± 0.69	17.75 ± 0.67
$6 \leq T < 8$	12	22.01 ± 0.75	22.16 ± 0.73	22.30 ± 0.72	10	18.34 ± 0.90	18.50 ± 0.90	18.65 ± 0.90
$8 \leq T \leq 10$	8	22.97 ± 0.60	23.12 ± 0.57	23.26 ± 0.55	7	20.05 ± 1.05	20.21 ± 1.03	20.37 ± 1.01
all	81	21.59 ± 0.92	21.72 ± 0.90	21.86 ± 0.89	77	17.82 ± 1.08	17.96 ± 1.08	18.10 ± 1.08

brightness, small scalelength region. No galaxies were selected in this region, but the traced volume is also very small. The dominant type of spiral galaxy has a scalelength of about 1 kpc and a central surface brightness of 21 B-mag arcsec^{-2} (17 K-mag arcsec^{-2}).

By summing all bins in one direction, the bivariate distributions of Fig. 7 can be used to calculate the distributions of μ_0 and h separately. This figure indicates therefore where one can expect problems in the determinations of the μ_0 and h distributions due to the undersampling in the low surface brightness, small scalelength region. The μ_0 distributions will get incomplete for central surface brightnesses fainter than 21.5 B-mag arcsec^{-2} (19 K-mag arcsec^{-2}) and the h distributions should not be trusted for scalelengths smaller than 1 kpc. The undersampling in the μ_0 distribution is considerably reduced when only the galaxies with scalelength larger than 1 kpc are used. The undersampling problem of this sample could also be circumvented by imposing absolute magnitude or intrinsic diameter limits. To speak of *the* μ_0 distribution is incorrect and one should indicate to what type of galaxies the sample is restricted.

The distributions of central surface brightnesses of galaxies with scalelength larger than 1 kpc are displayed in Fig. 8. The distributions are remarkably flat for the total sample. The number density density decreases by about a factor of 4 from ${\mu_0}^i \simeq 21$ to 24 B-mag arcsec^{-2} and by a factor $\sim$10 from 17.5 to 22 K-mag arcsec^{-2}. The distributions are narrower when only types earlier than T=6 are used. Disks of late-type galaxies are bluer, which makes the overall distribution narrower in B than in K. The distributions are not limited by selection effects at the bright end, even if one assumes there is an upper limit to the total luminosity of a galaxy (see Fig. 5). The number density of galaxies decreases sharply with μ_0^i brighter than 20 B-mag arcsec^{-2} ($\sim$16 K-mag arcsec^{-2}). At the faint end a limited volume is sampled, and Fig. 5 indicates that the sample is biased against galaxies with a μ_0^i fainter than 23 B-mag arcsec^{-2} even for galaxies with scalelength larger than 1 kpc. Obviously galaxies with central surface brightness fainter than 26 B-mag arcsec^{-2} could never enter the sample. The distributions of μ_0 in Fig. 8 could be slightly higher at the faint end and should probably be extended to much lower surface brightnesses.

The volume corrected distributions of the logarithm of the scalelengths (Fig. 9) show first a small increase of galaxies to scalelengths of about 1 kpc. This is probably caused by the undersampling effect at low surface brightnesses and small scalelengths. For scalelengths larger than 1 kpc we notice a steady decline of about a factor 100 in one dex. There is no segregation with morphological type.

The most important results obtained in this subsection are as follows. There is a large range in disk central surface brightnesses among galaxies, mainly due to the lower surface brightnesses of late-type galaxies. The range decreases slightly when a transparent inclination correction is used. Selection effects are very significant in determining number density distributions and after correcting for these effects there is no

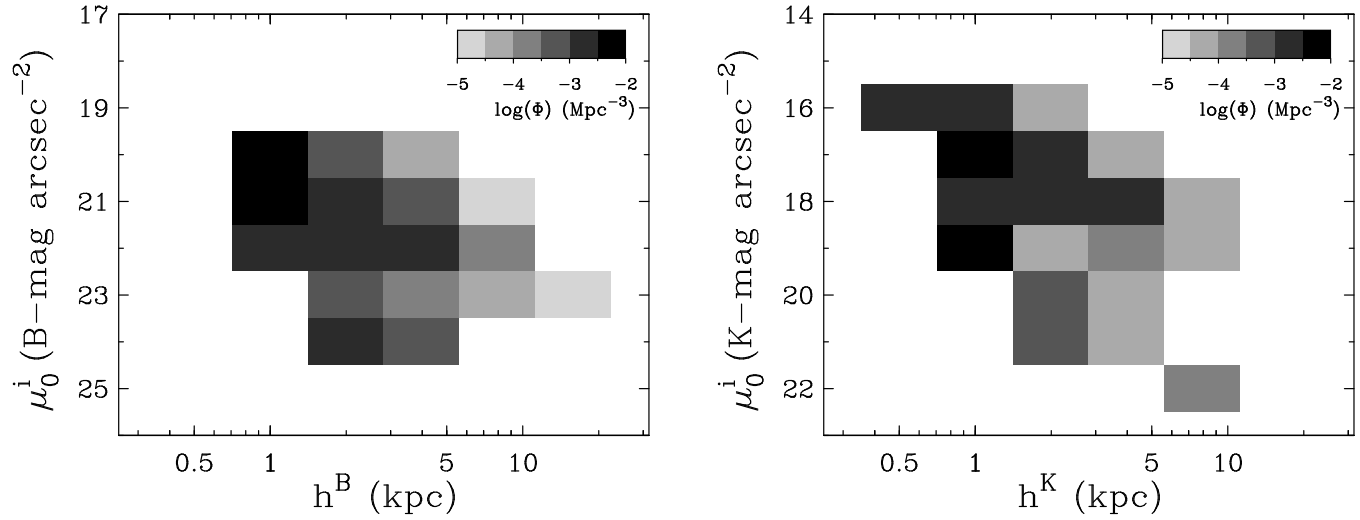

Fig. 7. The volume corrected bivariate distribution of galaxies in the (μ_0,h)-plane. The number density $\Phi(\mu_0^i,h)$ is per bin size, which is in steps of 0.3 in log(h) and 1 mag arcsec^{-2} in μ_0^i.

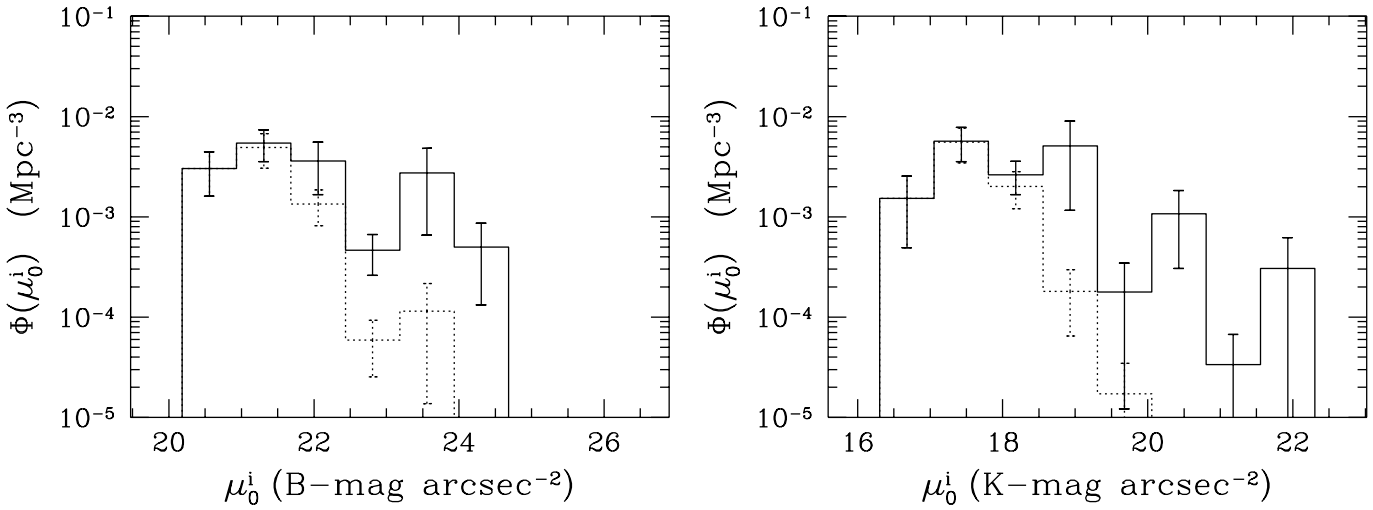

Fig. 8. The volume corrected distribution of the central surface brightness. The dashed line indicates the distribution for types earlier than type T=6. The number density is per bin size, which is in steps of 0.75 mag arcsec^{-2} in μ_0.

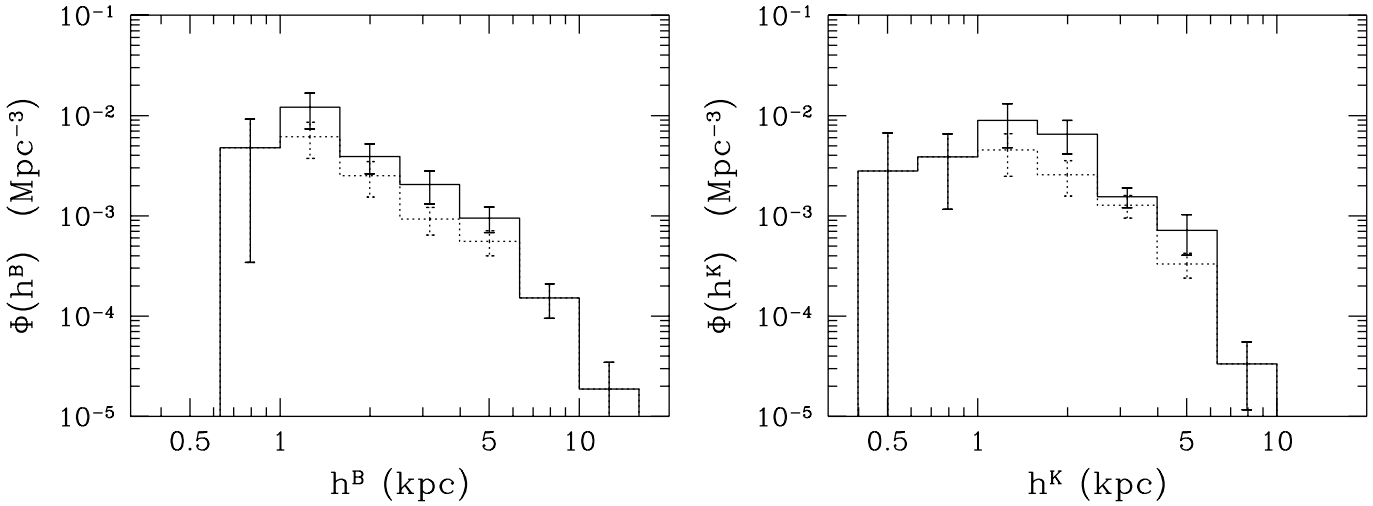

Fig. 9. The volume corrected distribution of the disk scalelengths. The dashed line indicates the distribution for type earlier than T=6. The number density is per bin size, which is in steps of 0.2 in log(h).

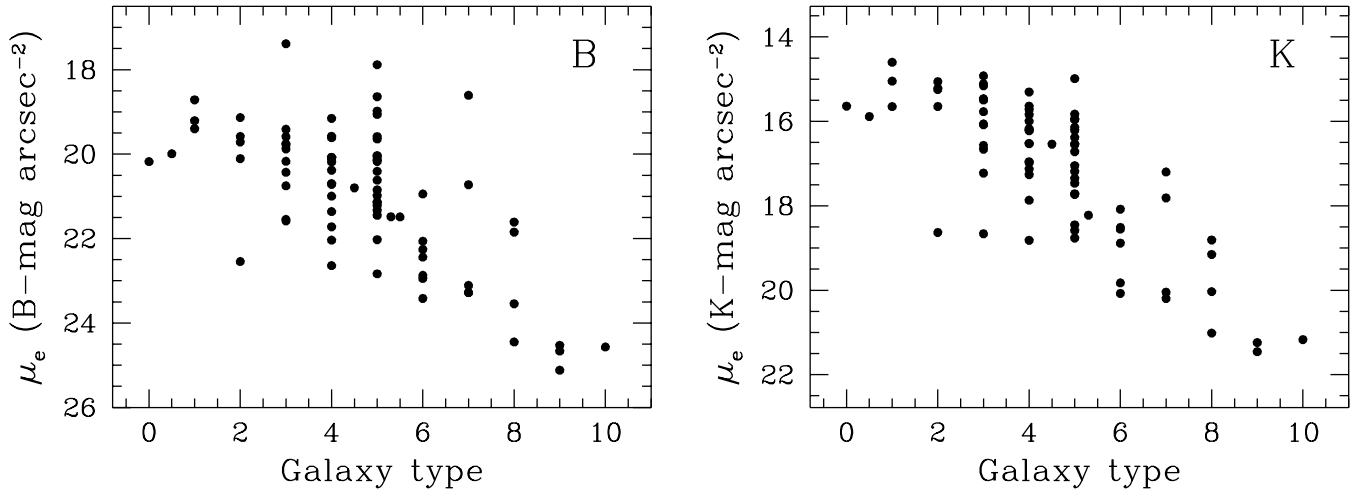

Fig. 10. The Galactic extinction corrected effective surface brightness of the bulge as function of morphological RC3 type.

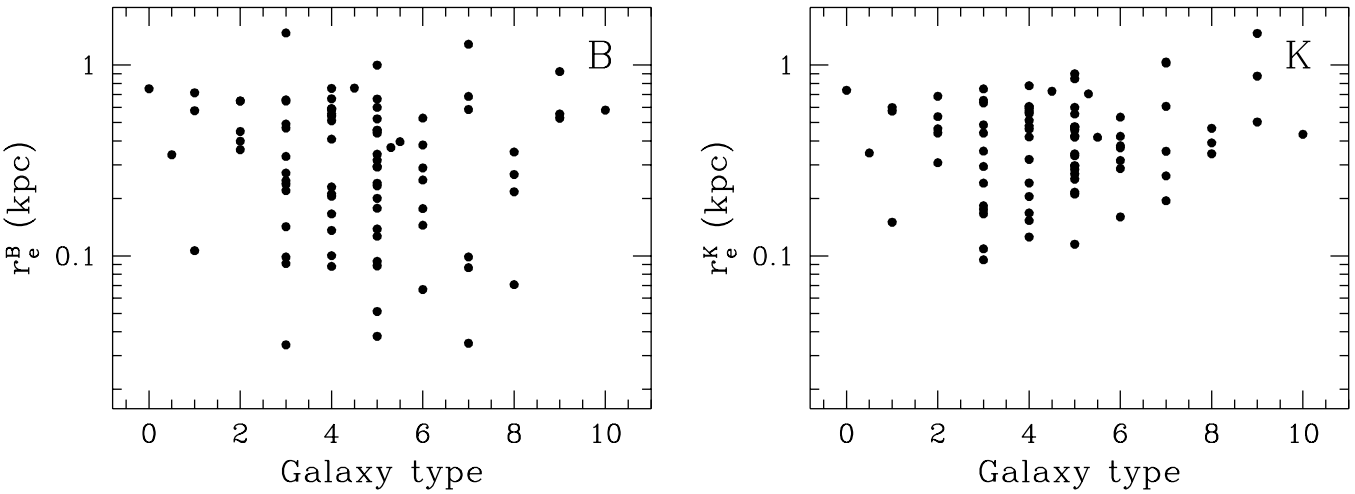

Fig. 11. The effective radius of the bulge as function of morphological type.

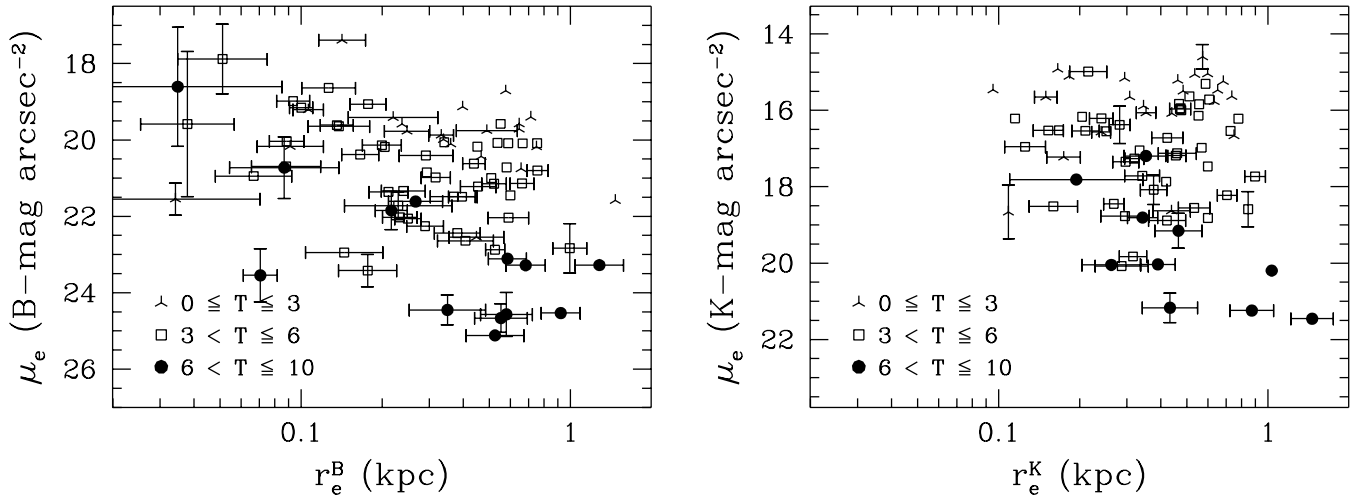

Fig. 12. The effective radius of the bulge versus the effective surface brightness at this radius. Different symbols are used to denote the indicated type ranges.

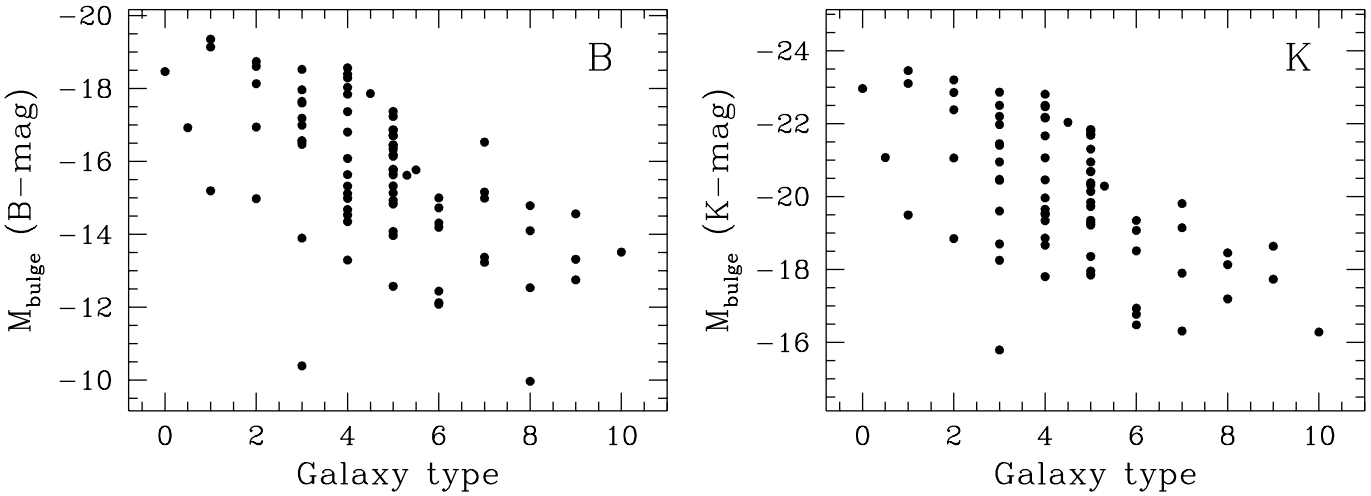

Fig. 13. The Galactic extinction corrected absolute magnitude of the bulge as function of morphological RC3 type.

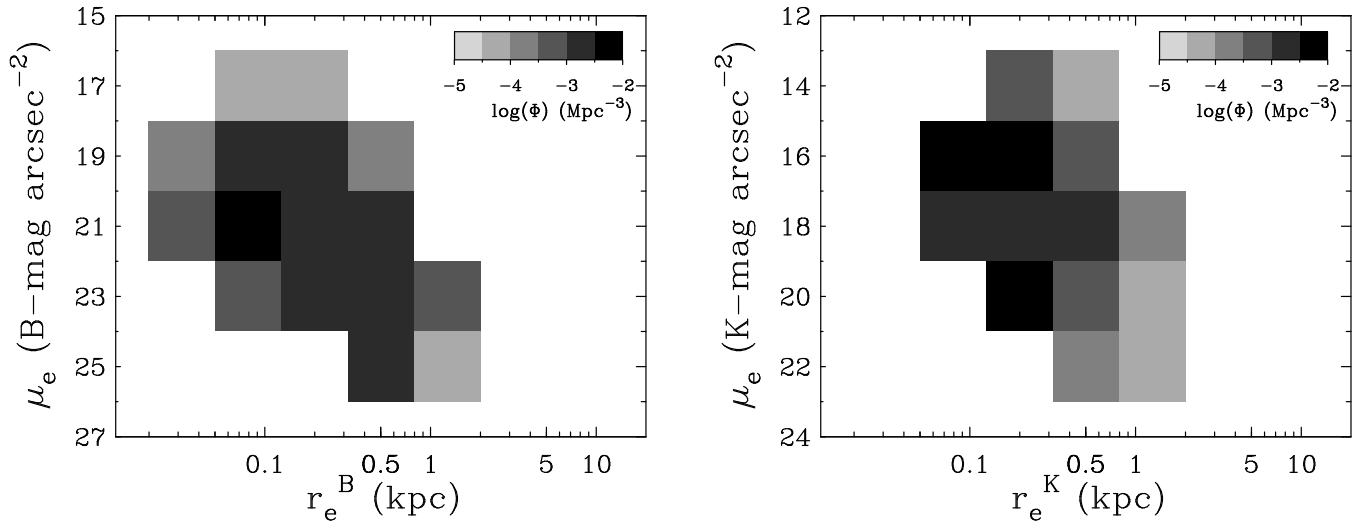

Fig. 14. The volume corrected bivariate distribution of galaxies in the (μ_e,r_e)-plane. The number density $\Phi(\mu_e,r_e)$ is per bin size, which is in steps of 0.3 in log(r_e) and 2 mag arcsec^{-2} in μ_e.

single preferred value for the central surface brightnesses of disks. There is an upper limit to μ_0, but the number density distribution decreases only slowly at the faint end.

4.2 The bulge parameters

The same diagrams used to describe the disk parameters are now used to present the bulge parameters. The distributions of effective surface brightness are presented in Fig. 10. The effective surface brightness shows a tight correlation with type index, especially considering the uncertainty of at least 1.5 T-units (1 sigma) in type index (Lahav 1995). Almost all of the scatter can be explained by this uncertainty. This relation also holds for the μ_e parameters obtained with the other fitting methods presented in Paper II, although with a slightly larger scatter. There is no apparent correlation of effective radius with galaxy type (Fig. 11). The relations in Figs 10 and 11 are tighter in K than in B. There are several explanations for this effect. Bulges are relatively brighter with respect to the disks in K compared to B, which will make the fit routine work better. Furthermore, circumnuclear star formation and dust lanes will affect the B passband more than the K passband and make the quality of the decomposition worse. There are some galaxies in the sample with clear circumnuclear star formation and with dust lanes right down to the center. Finally, there is the effect of the Freeman Type II profiles (Freeman 1970) which is reduced in K, thus making fitting easier (see Paper II). The distribution of points in the (μ_e,r_e)-plane (Fig. 12) shows no correlation. The absence of a correlation between r_e and morphological type makes the trend in the distribution of the absolute bulge magnitude ($M_{bulge} \propto \mu_e - 2.5\log(r_e^2)$) versus type (Fig. 13) dominated by the μ_e. rather large though.

The bivariate distribution of μ_e and r_e (Fig. 14) shows no trends. The dominant type of galaxy in our local universe has a bulge with effective radius in the range of 0.1-0.3 kpc and effective surface brightness of order 21 B-mag arcsec^{-2} (∼16 K-mag arcsec^{-2}). The relation between the bulge parameters and the diameter selection criterion is not very obvious and

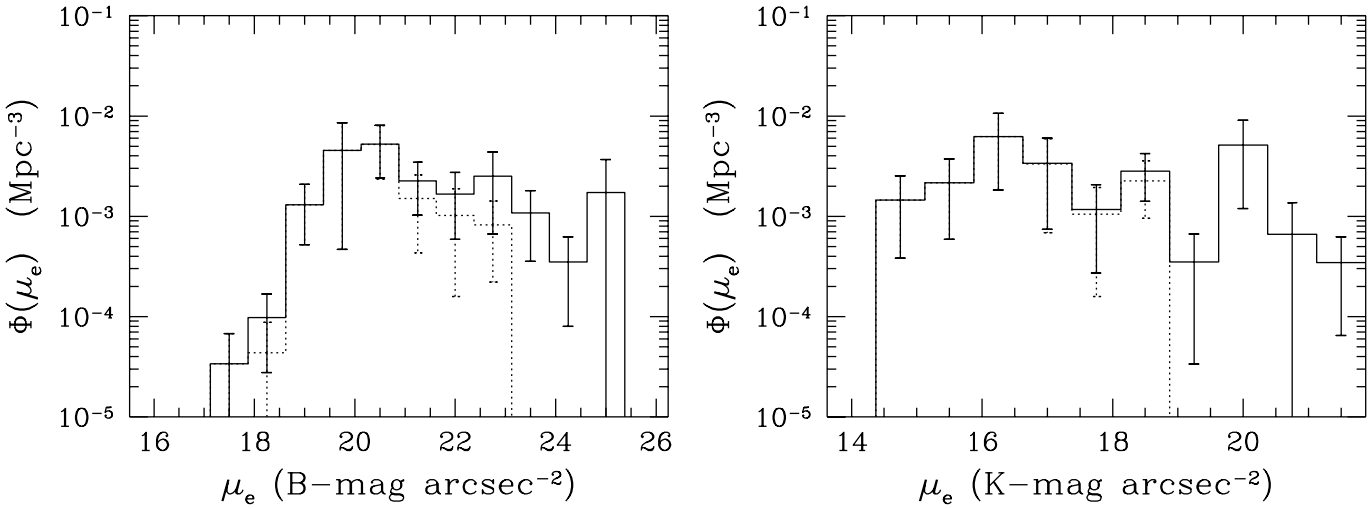

Fig. 15. The volume corrected distribution of the effective surface brightnesses of the bulge. The dashed line indicates the distribution for types with T<6. The Φ distribution is per bin size, which is in steps of 0.75 mag arcsec^{-2} in μ_e.

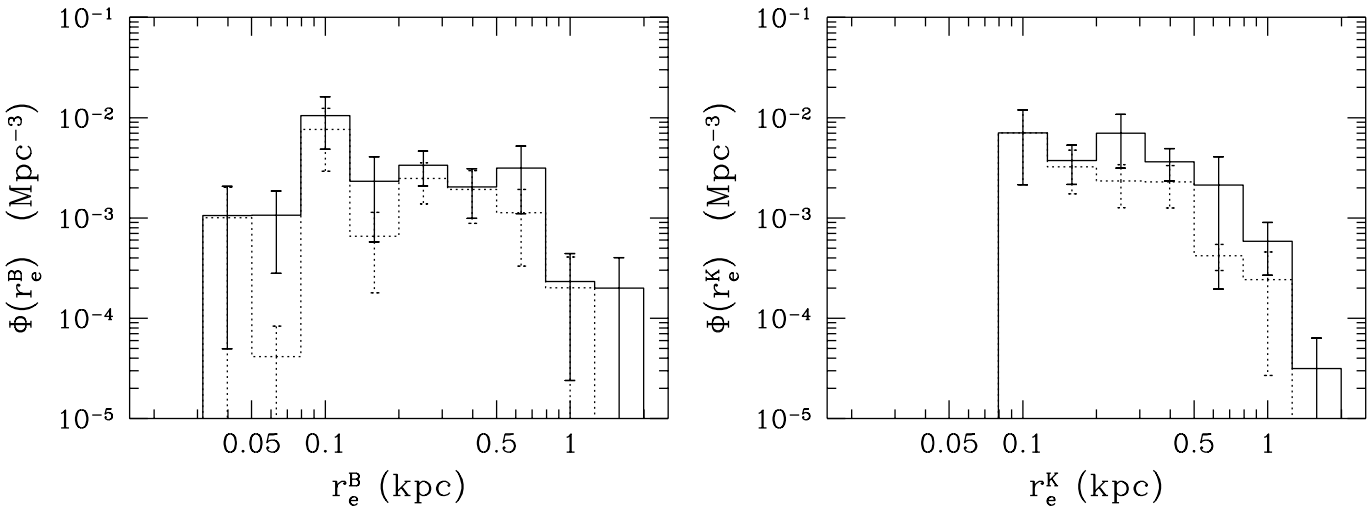

Fig. 16. The volume corrected distribution of the bulge effective radii. The dashed line indicates the distribution for types with T<6. The Φ distribution is per bin size, which is in steps of 0.2 in log(r_e).

therefore all galaxies are used in the calculations of the separate bulge parameter distributions. The volume corrected distributions of the bulge μ_e and r_e (Figs 15 and 16) show the same behavior as the disk parameters, i.e. constant distribution of the effective surface brightness and a steady decline of a factor of 50-100 per dex of the effective radius in the K passband.

4.3 The bulge/disk relation

The chronology of the bulge and disk formation is a major issue and the relationships between bulge and disk parameters might give some insight in this matter. A strong correlation between bulge and disk parameters is expected if the bulge formed from the disk by secular evolution. A correlation might be expected in the hierarchical infall and small merger models producing bulges, because both bulge and disk originate from the same smaller components. In models where the bulge forms first and the disk forms later, there is no obvious reason for a bulge-disk correlation.

Comparing the μ_0^i with μ_e (Fig. 17) we see no correlation, except that the late-type spirals clearly stand out. This is most obvious in the K passband. The correlation between h and r_e (Fig. 18) is only tight in the K passband and not in the B passband. Actually the correlation is becoming steadily tighter from the B to the K passband with correlation coefficients increasing from 0.6 in B and V to $\sim$ 0.75 in R and I and $\sim$ 0.8 in H and K passbands. The equation for the least squares fitted line is in the K passband

$$\log(r_e^K) = 0.95 \log(h^K) - 0.86 \quad (1)$$

with a standard deviation of 0.17. The scalelength difference between bulge and disk thus is of order 10. The relation also holds for all the 1D fit techniques presented in Paper II (but less strongly) except for the case of an $r^{1/4}$ law bulge. In the case of 1D $r^{1/4}$ law bulge there is at best a weak trend (correlation coefficient 0.15). This relation could partly be produced by the fitting routine if the errors in both parameters are intrinsically correlated. The facts that this relation holds in the K but not

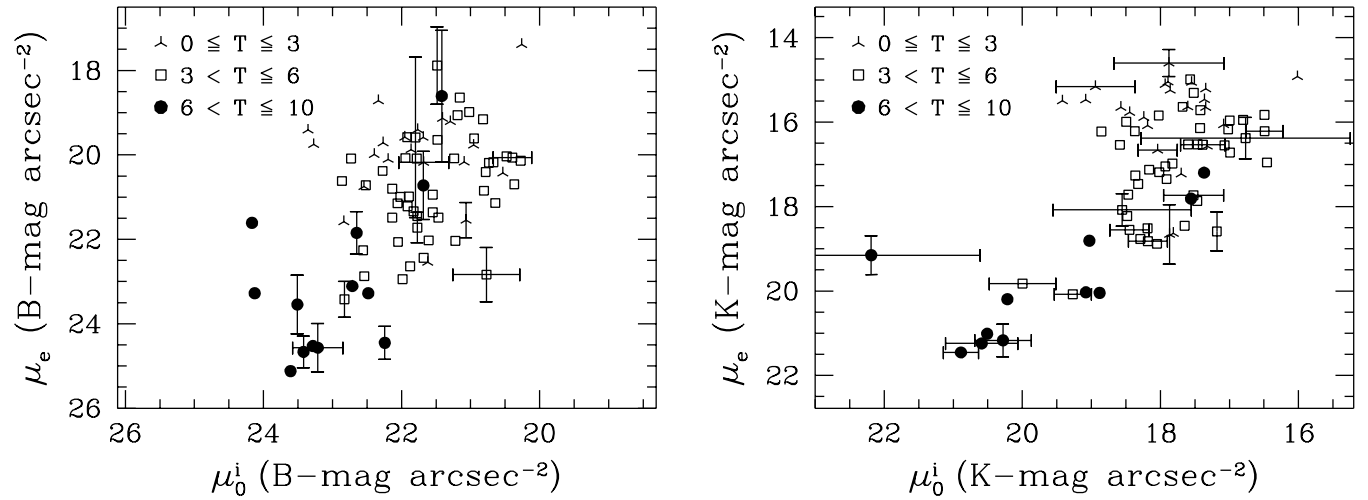

Fig. 17. The central surface brightness of the disk versus the effective surface brightness of the bulge. Different symbols are used to denote the indicated morphological type ranges.

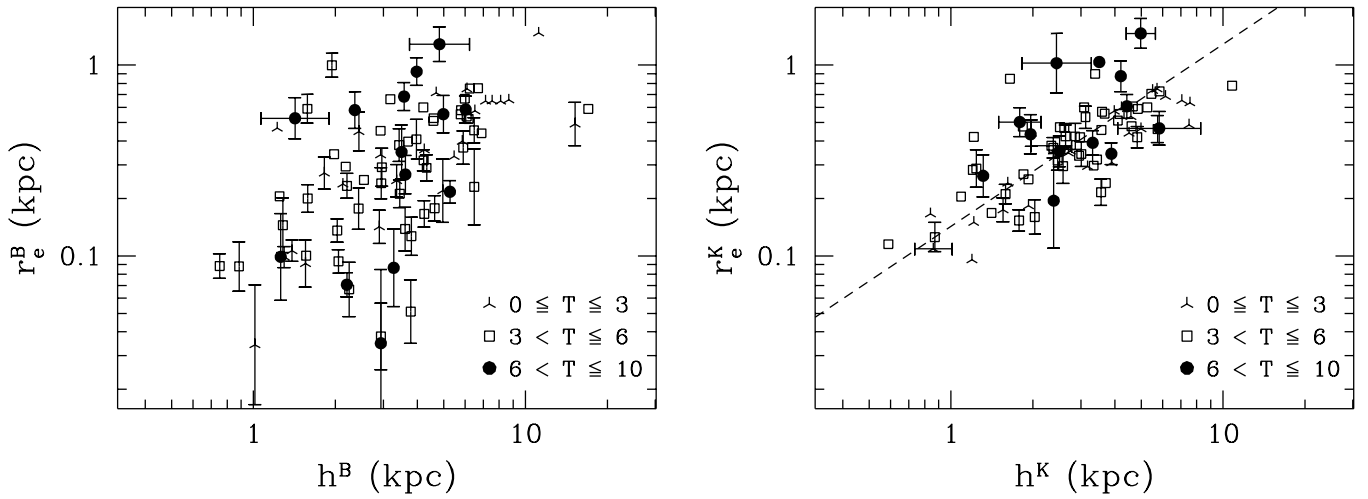

Fig. 18. The scalelength of the disks versus the effective radius of the bulge. Different symbols are used to denote the indicated morphological type ranges. The dashed line in the K passband diagram gives the least squares fit relationship between both parameters.

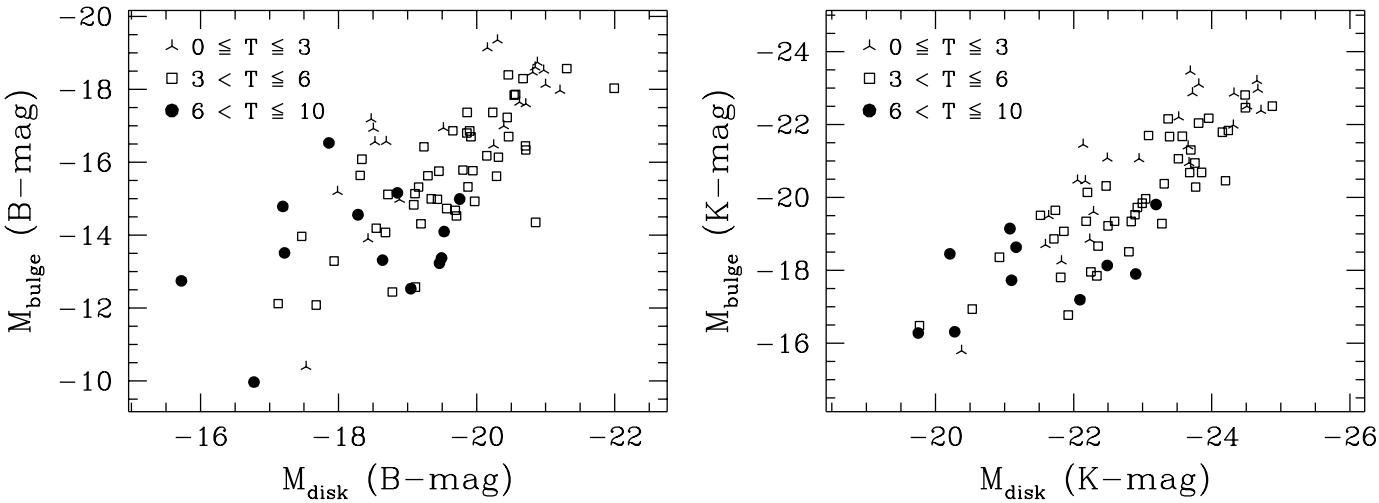

Fig. 19. The galactic absorption corrected absolute magnitude of the disk versus that of bulge. Morphological types ranges are denoted by the indicated symbols.

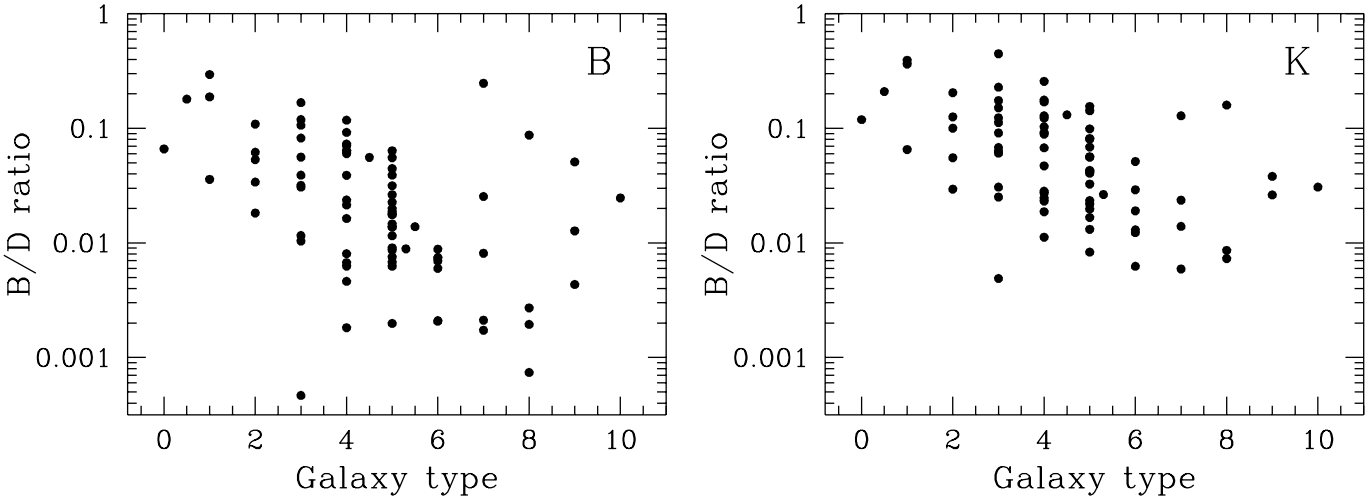

Fig. 20. The bulge to disk ratio as function of morphological type, using the results from the 2D fit of Paper II.

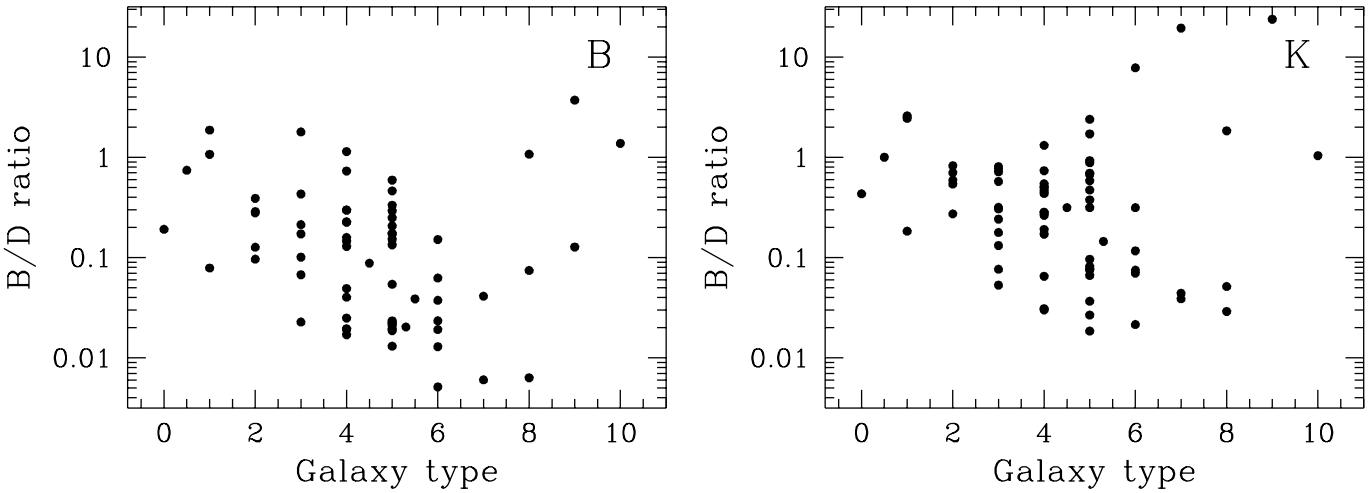

Fig. 21. The bulge to disk ratio as function of morphological type using an $r^{1/4}$ law bulge in the bulge/disk decomposition.

in the B passband and for both of the totally different 1D and 2D fitting techniques indicate that the correlation is intrinsic and not an artifact of the fit routines. The χ^2 distribution around the solutions found by the fit routine also showed no correlation with the relationship between disk scalelength and bulge effective radius.

The absolute magnitudes of bulge and disk correlate well (Fig. 19). This is probably an example that large galaxies have more of everything, more bulge, more disk. The combined effect of good correlation between $r_{\rm e}$ and h and weak correlation between μ_0 and $\mu_{\rm e}$ ensures the correlation between $M_{\rm d}$ and $M_{\rm b}$. Looking at the bulge-to-disk ratio as function of morphological type (Fig. 20), one sees that there is a correlation, but this correlation is less strong than for instance the one of $\mu_{\rm e}$ with type (Fig. 10). The B/D ratio is on average higher in K than in B; bulges are redder than disks. This partly explains why the correlations which involve bulge parameters are tighter in K. The bulge/disk decomposition is more easily performed when the bulge is relatively brighter.

Fig. 20 shows also that the selected galaxies are indeed disk dominated systems. The B/D ratios plotted here are much smaller than the ratios normally found in the literature. This is mainly due to the use of an exponential bulge. In Fig. 21 the results with an $r^{1/4}$ law bulge (Paper II) are shown. The B/D ratios are higher, but the scatter has increased and there still is no tight correlation with morphological type.

5 Discussion

In this section I will place the previously described relations in the context of the three topics of main interest: 1) Freeman's law, 2) bivariate distributions and 3) the relation between Hubble classification and the structural parameters. I will conclude this section by confronting some galaxy formation and evolution theories with the newly found and some well known relationships. A combination of several models is probably needed to explain all aspects discussed here.

5.1 Freeman's law

Since Freeman 1970 found disk central surface brightnesses to be constant among spiral galaxies, a number of explanations have been brought forward. In the introduction three expla-

nations were mentioned: 1) optically thick dust, 2) erroneous measuring of the disk parameters from the light profiles and 3) selection effects. For each of these possibilities I check if they are of importance for the current sample and whether they can explain Freeman's result.

5.1.1 Optically thick dust

It has been suggested that optically thick dust could be the cause of Freeman's law (Jura 1980; Valentijn 1990; Peletier et al. 1994). This is only a partial explanation, because it removes the inclination dependence from the law. To produce Freeman's law in this way, galaxies must have the same surface brightness at $\tau = 1$ (where the typical surface brightness is produced in an optically thick system), which means the problem is only shifted from one part of the galaxy to another. One now has to explain why all galaxies have the same surface brightness at $\tau = 1$. Taking a constant dust-to-stellar light ratio will not produce a constant surface brightness. This is only the case if all dust is in front of the star light, but dust and stars are mixed in a galaxy and a fraction of stars to the near side is less obscured. The amount of extinction in a galaxy is not linearly dependent on the amount of dust present (see also Paper IV). Coupling the amount of dust and stars in galaxies can only reduce the scatter in μ_0, but can never produce a constant μ_0.

I have shown that applying the inclination correction of Eq. (1) reduces the scatter in the μ_0 of the disk going from $C = 0$ to $C = 1$ (Table 1, indicating transparent behavior. The effect is small and the scatter is still dominated by the intrinsic differences in the brightnesses of the disks. One should realize that the disk parameters are largely determined by the outer regions of the galaxy. They probably do not reflect the optical thickness of the central regions. I note again that galaxies can behave optically thin in an inclination test, while in fact being optically thick.

The K passband data should hardly be affected by dust extinction. Looking at Table 1 one can see that the standard deviation of μ_0 is for the early-type galaxies smaller in the K passband than in the B passband, contrary to what is expected for optically thick dust. The increase in standard deviations for the later types can be explained by stellar population differences (Paper IV). I conclude that dust extinction is not a major effect in Freeman's law, certainly not in the K passband data used here.

5.1.2 Erroneous profile fitting

Kormendy (1977), Phillipps & Disney (1983) and Davies (1990) have argued that Freeman's law results from fitting the exponential disks to light profiles without taking the bulge contribution to the profiles into account. To prove their point, they created model profiles with $r^{1/4}$ law bulges and exponential disks with a range of properties, to which exponential disks were fitted in a specified range. These models were able to reproduce Freeman's "universal" central surface brightness value of 21.65 B-mag arcsec^{-2} with just a small scatter.

The parameter space explored in the models is not very physical according to current insights. Kormendy 1977 used B/D ratios of 1–120 for the low surface brightness systems and Phillipps & Disney 1983 assumed that bulges were so extended that they dominated the light profiles again at the 24.5 B-mag arcsec^{-2}. Davies (1990) used a range of properties for the bulge parameters which are typical in samples of galaxies, which suffer from severe selection effects. He used a *constant* central surface brightness of the *bulge* to show that the central surface brightnesses of disks need not be constant. A change in r_e/h ratio was used to produce a range in bulge-to-total light ratios (BT). I have shown that μ_e is not constant (Fig. 10) and that the r_e/h ratio is nearly constant (Fig. 18). Even though these results where obtained with a exponential rather then a $r^{1/4}$ law bulge, a constant central brightness for bulges is excluded and a relationship between r_e and h might be expected.

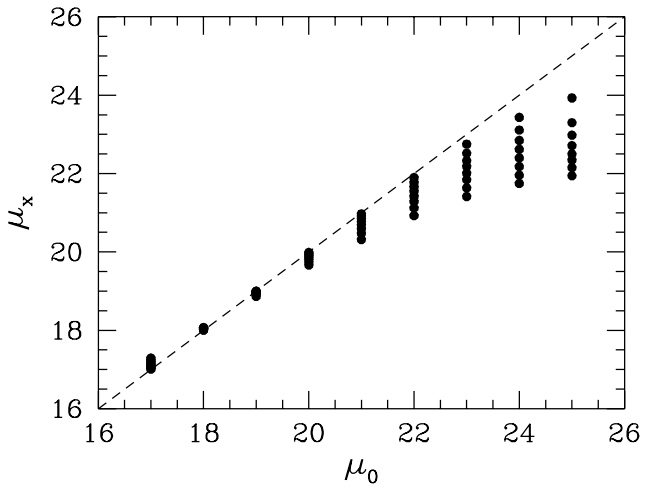

Fig. 22. The variation of the measured extrapolated central surface brightness (μ_x) with bulge-to-total light ratio (BT) ranging from 0.05 to 0.75, at a given model central surface brightness μ_0 (see text).

I use the parameterization of Davies 1990 to show that erroneous bulge/disk decomposition is not a major factor in the Freeman law. Figure 22 was produced in the same way as Davies' Fig. 6 by fitting exponential profiles in the range of 22 to 25.5 mag arcsec^{-2} to model profiles, which were a combination of an $r^{1/4}$ law bulge and an exponential disk. In this figure the intrinsic μ_0 of the model profile is compared with the central surface brightness of the fitted disk (μ_x). The r_e/h ratio was taken fixed to 0.4 and μ_e was adjusted to produce BT ratios in the range from 0.05 to 0.75 in steps of 0.1 (contrary to Davies, who used a fixed μ_e and varied the r_e/h ratio). The tendency to shift intrinsic bright disks to the observed value of 21.65 mag arcsec^{-2} has disappeared. The low surface brightness disks have too bright μ_x values for their μ_0, but these were clearly fitted in the curved part of the profile at the brighter end. From Fig. 22 one can conclude that it is unlikely that the high surface brightness disks were underestimated (even with using the "marking the disk" fit of Paper II). The situation for LSB systems is not as bad as it seems, because the B/D ratios are low for LSB galaxies and the curvature of the profiles can be readily seen. Choosing values for r_e/h in the range from 0.1 to 1 hardly changes these results.

The central surface brightnesses of the galaxies were determined in Paper II with a full 2D decomposition technique, but also with the "marking the disk" technique and a few 1D decomposition techniques. If Freeman's result was caused by his use of the "marking the disk" method, the central surface brightnesses obtained with this method should show large and systematic differences with the results of the other methods. In Paper II it was shown that making a proper decomposition of the profiles in a $r^{1/4}$ law bulge and an exponential disk adds a scatter of at most 0.4 mag arcsec^{-2} to μ_0 with respect to the "marking the disk" results. Assuming that about the same value would hold for Freeman's sample, this would still result in a rather small range in μ_0 for his sample. In Paper II it is furthermore argued that the 2D decomposition technique, using exponential light profiles for both disk and bulge, is more accurate and reduces the rms difference between the "marking the disk" method and the 2D fit to 0.3 mag arcsec^{-2}. Both the model decompositions using Davies' method and the comparisons between different decomposition methods of real galaxies indicate that it is unlikely that Freeman's results were caused by improper decompositions.

5.1.3 Selection effects

After taking selection effects into account, Fig. 8 shows that there is no such thing as a simple Freeman's law for galaxies with scalelengths larger than 1 kpc. There seems to be a clear upper limit to the central surface brightness, which cannot be explained by selection effects. Even taking the apparent upper limit in absolute luminosity in Fig. 5 into account, there still should have been galaxies with μ_0 brighter than 20 B-mag arcsec^{-2} (16 K-mag arcsec^{-2}) in the sample according to this figure. Figure 8 shows further that there is no strong decrease in the number of galaxies with lower surface brightness. The distribution becomes narrower if we exclude late-type spirals, but this exclusion can hardly be justified. Late-type spirals are in many respects no separate class of galaxies, but just a continuation of the trends set by the earlier type spirals. A clear example of such a trend is seen in Fig. 10.

In Paper II it was shown that there is at most ∼0.30 mag arcsec^{-2} rms uncertainty in the central surface brightnesses. The uncertainties also showed no correlation with the surface brightness itself (Paper II, Fig. 4) and the results presented here can therefore not be the results of measurement errors. The central surface brightness distribution of Fig. 8 changes in some details if one of the other fit techniques of Paper II is used, but the general trend remains unchanged. The same holds true when the distances of the galaxies are calculated with other flow models.

Sample selections are influenced by both μ_0 and h and therefore the most important distribution for disk dominated galaxies is the bivariate distribution in the (μ_0,h)-plane (Fig. 7). These two parameters describe a large fraction of the light of disk dominated galaxies and to derive this distribution one needs distances. To derive the distribution of μ_0 of sample of galaxies without knowing the distance to the galaxies, one must assume that the distribution of μ_0 is not correlated to for instance h or M (Davies et al. 1994; McGaugh et al. 1995). The total μ_0 distribution can only be calculated in this statistical way if the μ_0 distribution at each h or at each M has the same shape. Figure 7 shows that this is probably not the case for h and Figure 23 shows the same for M. The statistical methods can at best only be used to get an impression of the μ_0 distribution.

5.2 Bivariate distributions

The reason for our limited knowledge of low surface brightness galaxies is clearly indicated by the selection lines in Fig. 5. The use of catalogs like the UGC prevents galaxies with central surface brightness fainter than ∼25 B-mag arcsec^{-2} from being included in a sample, independent whether the sample is diameter or magnitude selected. Only the use of deeper photographic plates enabling a selection at fainter isophotes (Schombert et al. 1992) or deep CCD surveys will result in samples with a larger number of low surface brightness galaxies. A galaxy like Malin I (Impey & Bothun 1989), with $\mu_0 \simeq 26.5$ B-mag arcsec^{-2} and $h \simeq 55$ kpc, is not found in conventional catalogs, even though it has an integrated magnitude comparable to M 101 and a ∼10 times as a large scalelength as M 101. Figure 7 indicates that galaxies like Malin I are probably not very numerous in the local universe, but this cannot be said of galaxies with $\mu_0 > 24$ B-mag arcsec^{-2} and $h \approx 1$ kpc. There is a clear need for deeper local surveys, especially in the near-IR.

Few bivariate distributions have appeared in the literature which can be used in comparisons with the current results. Van der Kruit (1987) calculated a bivariate distribution of spiral galaxies in the (μ_0-h)-plane. His distribution shows similar features as the distribution presented here. The distribution has an upper limit in central surface brightness at about 21 J-mag arcsec^{-2}(photographic J passband, which is similar to the Johnson B passband) and an exponentially declining density distribution with scalelength.

Another comparison can be made with the bivariate distribution of van der Kruit (1989). This distribution was constructed in exactly the same way as Fig. 7, with only a modification to Eq. (3) to include the effects of an additional magnitude selection limit. The central surface brightnesses were convolved with a Gaussian of 0.3 mag arcsec^{-2} to incorporate the effects of calibration uncertainty. This explains the smoothness of the distribution. The galaxies of type later than T = 5 were excluded and a Hubble constant of 75 km s^{-1} Mpc^{-1} was used. The same upper limits in absolute magnitude and central surface brightness can be seen as in Fig. 5. There is only one galaxy with μ_0 brighter than 18 R-mag arcsec^{-2} at 0.7(100/75) kpc. The general trend in the bivariate distribution of van der Kruit agrees quite well with Fig. 7, with equal probabilities along lines of equal absolute luminosity.

The luminosity function of galaxies is a tool often used to investigate galaxy evolution on cosmological time scales. This makes sense as the total luminosity of a galaxy seems, also by use of the TF-relation, related to the total mass of a galaxy. In determining the local LF one has sometimes failed to notice that galaxies are extended and that for selection correction

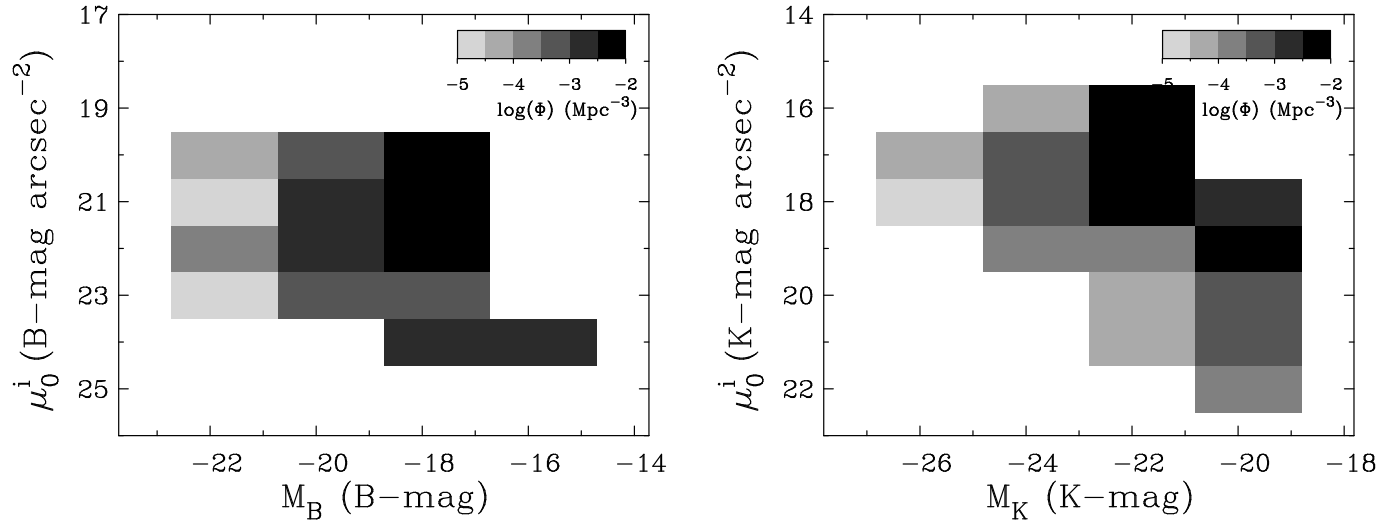

Fig. 23. The volume corrected bivariate distribution of galaxies in the (μ_0,M)-plane. The number density $\Phi(\mu_0^i,M)$ is per bin size, which is in steps of 1 mag in M and 1 mag arcsec^{-2} in μ_0^i.

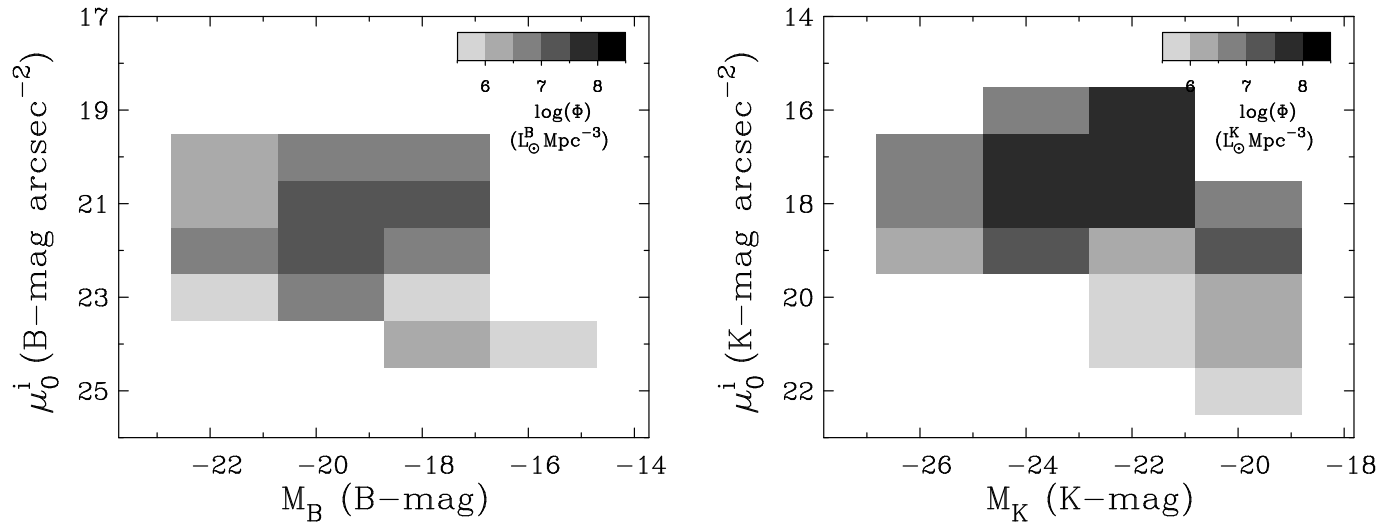

Fig. 24. The volume corrected luminosity distribution of galaxies in the (μ_0,M)-plane. Each galaxy in Fig. 23 was given an additional weight according to its absolute luminosity. The luminosity density $\Phi(\mu_0^i,M)$ is per bin size, which is in steps of 1 mag in M and 1 mag arcsec^{-2} in μ_0^i.

one should not treat them as point sources. This can lead to a change in the slope of the LF as function of redshift and results in the faint blue galaxy problem (McGaugh 1994). Another disadvantage of the one-dimensional LF is that each luminosity bin contains galaxies with totally different surface brightnesses and scalelengths (Fig. 5). The physical processes in disk galaxies seem to be more related to surface brightness than to total mass (see also Paper IV). Therefore, to investigate the distributions related to both the total mass and the surface brightness, the luminosity function has been divided in several central surface brightness bins in Fig. 23. The absolute magnitudes were calculated from the values given in Paper I. Figure 23 shows the bivariate distribution of a local sample of galaxies and can be useful as a reference for high redshift samples observed with the Hubble Space Telescope.

Figure 23 shows that the LF is more or less the same for all central surface brightness bins in the B passband. In the K passband something becomes apparent which was already hinted at in the B passband. The LF for fainter central surface brightnesses is lower and/or shifted to lower absolute luminosities. Figure 23 is somewhere in between both options presented in Fig. 3 of McGaugh (1994), which means that both the shape of the LF and its normalization depend on the bivariate distribution of M and μ_0. Unfortunately, this data is too scarce to make a firm quantitative statement, but it is clear that further attention should be given to "the LF".

It is also interesting to know what type of galaxies provides most of the total luminosity in the local universe. In order to calculate this, the number density value of each galaxy used in Fig. 23 was given an additional weight depending on its absolute luminosity, which results in Fig. 24. This figure shows

the total luminosity one expects to find in a random Mpc^3 from galaxies in the indicated bins of (μ_0,M). The luminosities are expressed in solar luminosities per passband, calibrated using the absolute solar luminosity values of Worthey (1994).

The distribution in the B passband is remarkably flat, almost all bins that contain galaxies are equal to within 1.5 order of magnitude. In the K passband distribution there is more structure, as most of the K passband light in the local universe comes from higher surface brightness galaxies. Due to the scarceness of the data, this figure is again more of qualitative than of quantitative interest.

5.3 Hubble classification

The Hubble sequence is one of the basic ingredients of galaxy formation and evolution schemes, even though the underlying physical processes are only partly understood. In this section I describe the consequences of some of the relations between the structural parameters and Hubble type as presented here.

Figure 20 showed that B/D ratio cannot be used to determine the Hubble type of face-on systems, which means that the classification of edge-on systems is different from that of face-on systems. Furthermore, the B/D ratios seem to be quite small (< 0.5), even in the K passband where the differences in color (and M/L) due to stellar population effects between disk and bulge are minimized. The B/D ratios are larger when $r^{1/4}$ law bulges are used. The difference between exponential and $r^{1/4}$ law bulges in terms of generalized exponential profiles is extensively discussed in Paper II. Young & Curry (1994) showed that for ellipticals and dwarf ellipticals there is a trend in profile shape with luminosity. The brighter ellipticals have $r^{1/4}$ like profiles, while fainter (dwarf) ellipticals have more exponential like profiles. If this is also true for bulges, we might expect early-type spirals to have more centrally peaked bulge profiles than later type spirals. In Paper II it was found that $r^{1/2}$ law bulges gave smaller χ^2 residuals for T$<$3 than exponential bulges. This picture conflicts with the scale independence of Hubble type as seen in the K passband data of Fig. 18. Within one Hubble type, a range in integrated bulge luminosities exists, which should result in different profiles when the model of Young & Curry (1994) is applied to bulges. There is a weak indication for this trend, because the galaxies with the brightest bulges are slightly better fitted by the $r^{1/2}$ law bulges than by the exponential bulges. The $r^{1/4}$ law bulges never give the smallest residuals, not even for the most luminous bulges.

Using an exponential bulge, an important relation is found, which is not apparent if an $r^{1/4}$ law bulge is used: h correlates with $r_{\rm e}$, but these parameters do not correlate with Hubble type (Fig. 18). This is an important relation as it makes the Hubble sequence scale free. Each Hubble type comes in a range of different sizes, both in terms of diameter and total luminosity It is an example of larger (in the sense of scale size, not mass) galaxies having more of everything, larger disk, larger bulge. Due to this correlation the scale parameters cancel each other out in calculating B/D ratios, which means that a plot of $\mu_{\rm e}$–μ_0 ($\propto \Sigma_{\rm e}/\Sigma_0$, important in density wave models) versus type looks like Fig. 20 with a different scaling. Consequently $\mu_{\rm e}$–μ_0 is also a bad diagnostic for Hubble type.

The relationship between Hubble type and $\mu_{\rm e}$ (Fig. 10) holds, independent of bulge profile function used. In fact the relation holds if one just fits a line to the central region of the profile and uses the true central surface brightnesses, because the bulge generally dominates the luminosity in this central region. One might wonder if in classifying galaxies one has mainly looked at the surface brightness of the bulge and not at the B/D ratio. For the earlier systems this is harder to accept; the central regions are in general overexposed on photographic plates used for classifying. It is instructive to know that S0 galaxies do not fit in this relation. The central surface brightnesses of S0 galaxies range from $\sim$17.7 to $\sim$19 B-mag arcsec^{-2}, estimated from the data of Kormendy (1977) and Peletier et al. (1990). This translates to effective surface brightnesses in the range of 19.5-21 B-mag arcsec^{-2}, in accordance with the two S0 galaxies in the current sample, but significantly below the trend of the rest of the spiral galaxies (Fig. 10).

If B/D ratio is such a bad diagnostic for Hubble type, we are left according to Sandage (1961) with only two other classification discriminators: 1) the spiral arm structure, 2) the pitch angle of the arms. The two remaining criteria indicate that the Hubble sequence should be explained in terms of spiral arm appearance, even though the second criterion might also be in doubt, as measurements by Kennicutt (1981) showed that pitch angle has no tight correlation with morphological type.

The main theory on spiral structure is the spiral density wave theory (Lin & Shu 1964; Roberts et al. 1975). The fact that Hubble type is a scale free quantity fits into this theory. When the bulge and the disk scale with the same amount, the shape of the rotation curve stays the same, only its amplitude changes. This means that the shape of the resonances also scale along with the scalelength changes. If bulge and disk scalelengths are correlated, the shape of the rotation curve is fully determined by the relative brightness of the bulge and disk component. Therefore it is harder to understand in the density wave theory why Hubble type does not correlate tightly with B/D ratio (Fig. 20), or to be more precise $\mu_{\rm e}$–μ_0. The strength and the pitch angle of the density wave gets modified by the ratio of mass that participates in the density wave to the mass that does not. If B/D ratios are so small that they hardly could affect the density wave (Fig. 20) and if on top of that the B/D ratios and $\mu_{\rm e}$–μ_0 values are only weakly correlated with Hubble type, it seems that some modifications to the standard density wave model are needed. Maybe a connection between the $\mu_{\rm e}$ of the bulge and the distribution of dark matter can solve this problem.

5.4 Galaxy formation and evolution models

A number of new observations and relations have been presented here, which can be compared with the predictions of existing galaxy formation and evolution models, e.g.:

1) the upper limit to disk central surface brightness.
2) the nearly constant $\Phi(\mu_0^i)$.
3) the correlation of the bulge central surface brightness with

Hubble type.

4) the scale independence of Hubble type.

Most formation and evolution models were designed to explain other observations. One can think of the exponential radial light distribution of disk galaxies, the TF-relation, the density-morphology relation (Dressler 1980; Postman & Geller 1984) and the fact that disk scaleheight is constant as function of radius (Shaw & Gilmore 1990). Also the relative fractions of different Hubble types needs to be explained.

The models in the literature are in general scale free. This means that physical limits in surface brightness or total luminosity as presented here are often not discussed. As a consequence the following discussion will be qualitative, not quantitative. The Freeman value of 21.65 B-mag arcsec^{-2} is often assumed for the central surface brightness in these evolution models, but as shown here this is an invalid simplification.

The chronology of bulge and disk formation is still a major issue. The disk galaxy evolution models can to first order be divided into three categories: those that form the disk first, those that form the bulge first, and hierarchical clustering models in which both are formed together by accreting smaller clumps of proto-galaxies. These models can partly be mixed at the different stages of galaxy evolution. Figure 18 shows that bulge and disk scalelengths are correlated. In models where the bulge forms first and then the disk, it is hard to understand how a small dynamically hot bulge can influence the disk scalelength. In models where the bulge forms from the disk, a natural correlation between their scalelengths is expected. The situation is reversed for S0 galaxies, because in these galaxies the bulge is much larger than the disk.

In recent years theories on galaxy formation start making use of the developments in the study of large-scale structure within the framework of the standard cosmological models, such as Cold Dark Matter (CDM) models (Blumenthal et al. 1984). In the standard cosmological models a galaxy principally forms when its matter dynamically decouples from the main Hubble flow. The observations presented here concern the stellar component of galaxies and the main obstacle to translate the predictions of the CDM models into these observations are the poorly known star formation mechanisms. There are some qualitative scenarios relating initial conditions to morphological type (e.g. Lake & Carlberg 1988; Zaritsky 1993) and therefore to the stellar component. In these scenarios the large potential well, which will form the final galaxy, contains smaller density fluctuations. In some of these subclumps enhanced star formation may occur, triggered by neighboring clumps or galaxies. The clumps with enhanced star formation violently relax in the main potential well to become the bulge and the halo, while the other clumps dissipate and form the disk. Such scenarios can hardly be compared with the quantitative descriptions of the bivariate distribution (most notably the upper limit in μ_0) and the correlation between bulge and disk scalelength presented here as long as there are no quantitative descriptions of the star formation processes involved.

The secular evolution models in which the bulge is formed from the disk have more predictive power. In these models the disk is formed first by a dissipational collapse of the initial gas cloud after getting its angular momentum from tidal torques from neighboring galaxies. In the following some secular evolution models are described. All of them could play a role after an initial collapse as described by the CDM models has occurred.

One of the models that has successfully explained the nature of exponential disks is the viscous evolution model (Lin & Pringle 1987; Yoshii & Sommer-Larsen 1989). In this model the angular momentum in the disk is redistributed by the viscosity of the gas, while star formation occurs on the same time scale. Saio & Yoshii (1990) showed that such a model automatically develops, next to the exponential disk, a bulge with properties only depending on the time scale of star formation relative to the time scale of viscosity and on the total angular momentum. This model could produce galaxies with correlated bulge and disk scalelengths. There is no obvious reason why there should be an upper limit to the surface brightness in these models.

The secular evolution model (Kormendy 1993 and references therein), in which small bulges form from the bar instability, can explain a number of the observations described here. In this model disk gas is transported to the center by a bar or oval distortion. The disk stars in the central region are heated in vertical direction by resonant scattering off of the bar instability to become a "bulge-like" component (Combes & Sanders 1981; Pfenniger & Friedli 1991). This model will naturally develop a *exponential* bulge, where only a limited range in bulge-to-disk scalelengths is possible. Furthermore, the bar forms when the disk surface density is too high for its velocity dispersion (see e.g. Binney & Tremaine 1987), which might explain the upper limit observed for surface brightnesses. The density-morphology relation is in this model partly explained by the higher chance of dynamical interaction in denser environments, which triggers the bar formation (Elmegreen et al. 1990).

A model to explain the Hubble sequence is the model of bulge formation by a central starburst, by Sofue & Habe (1992). This model has links with the previous two models. Instead of a bar, galactic winds driven by starbursts are used to produce the dynamical hotter bulge component from the disk component. Tidal interactions are known to produce starbursts, therefore more interactions give rise to larger bulges, thus explaining the density-morphology relation. This model might explain the upper limit in central surface brightness observed for the sample galaxies. When a critical gas density is reached, a burst of star formation will occur and all remaining gas will be expelled or put in orbits with a much higher vertical component. The "chimneys" of ionized gas observed in some edge-on galaxies (Rand et al. 1990) indicate that large amounts of gas can be driven out off the disk plane.

6 Conclusions

The statistics of the fundamental parameters of 86 spiral galaxies have been studied in the optical and the near-IR. The use of the near-IR K passband enabled for the first time determination of these parameters without being hampered by the effects of dust and differences in stellar populations.

Volume density distributions with respect to the fundamental parameters were made, which was possible due to the careful selection of the sample. The main conclusions are as follows:

- Freeman's law of a preferred disk central surface brightness value needs a modification. Although there seems to be a clear upper limit to the central surface brightnesses of galaxies, there is no clear limit at the faint end of the μ_0 distribution. The number of galaxies in a volume with a certain μ_0 is only slowly declining function of μ_0.
- The bulge and disk scalelengths are correlated, parameterized by $\log(r_e^K) = 0.95\log(h^K) - 0.86$. This correlation suggests that the formation of the bulge and the disk is coupled.
- The Hubble classification is related to the surface brightness properties of spiral galaxies. However, the relations are in general not very tight and can therefore not be turned around to give morphological classification. The B/D ratio is not a good indication of Hubble type (Fig. 20 and 21). The best relation with Hubble type found in this study is the one with μ_e (Fig. 10). The physical interpretation is difficult, because cause and effect are hard to separate.
- Hubble type is a scale size independent parameter, but not a total luminosity independent parameter of a galaxy. Therefore, it would be better to divide by scale size instead of luminosity to derive scale independent parameters of galaxies in comparisons. The suggestion that Hubble type is mainly driven by total mass (Zaritsky 1993) seems an oversimplification. To carry this point a bit further, it is probably better to separate the determination of the LF of galaxies into bins which are related to the effective surface brightness (like Fig. 23) than into bins which are related to Hubble type.

Larger samples are needed to enable the parameterization of the bivariate distributions. There is especially need for accurate surface photometry of a large sample of galaxies, selected from deep photographic plates providing isophotal diameters at very faint levels.

Acknowledgements. I thank Renée Kraan-Korteweg for providing her Virgocentric inflow computer model. Piet van der Kruit and Reynier Peletier are thanked for the many fruitful discussions. Erwin de Blok, René Oudmaijer, David Sprayberry and Arpad Szomoru are acknowledged for their many useful suggestions on the manuscript. This research was supported under grant no. 782-373-044 from the Netherlands Foundation for Research in Astronomy (ASTRON), which receives its funds from the Netherlands Foundation for Scientific Research (NWO).

References

Andredakis Y.C., Sanders R.H. 1994, MNRAS 267, 283
Allen R.J., Shu F.H 1979, ApJ 227, 67
Binney J., Tremaine S. 1987, Galactic Dynamics (Princeton University Press, Princeton)
Block D.L., Wainscoat R.J. 1991, Nature 353, 48
Blumenthal G.R., Faber S.M., Primack J.R., Rees M.J. 1984, Nature 311, 517
Boroson T.A. 1981, ApJS 46, 177
Burstein D., Heiles C. 1984, ApJS 54, 33
Byun Y.I., Freeman K.C., Kylafis N.D. 1994, ApJ 432, 114
Choloniewski J. 1985, MNRAS 214, 197
Combes F., Sanders R.H. 1981, A&A 96, 164
Davies J.I. 1990, MNRAS 244, 8
Davies J., Phillipps S., Disney M., Boyce P., Evans Rh. 1994, MNRAS 268, 984
de Jong R.S. 1995a, to be submitted to A&A **(Chapter 2)**
de Jong R.S. 1995b, to be submitted to A&A **(Chapter 4)**
de Jong R.S., van der Kruit P.C. 1994, A&AS 106, 451 **(Chapter 1)**
de Vaucouleurs G. 1948, Ann. d'Astrophys. 11, 247
de Vaucouleurs G. 1974, in The Formation and Dynamics of Galaxies, IAU Symp. 58, ed. J.R. Shakeshaft (Reidel, Dordrecht), p. 1
de Vaucouleurs G., de Vaucouleurs A., Corwin H.G., Buta R.J. et al. 1991, Third Reference Catalog of Bright Galaxies (Springer-Verlag, New York) (RC3)
Disney M.J. 1976, Nature 263, 573
Disney M.J., Phillipps S. 1983, MNRAS 205, 1253
Dressler A. 1980, ApJ 236, 351
Efstathiou G., Ellis R.S., Peterson B.A. 1988, MNRAS 232, 431
Elmegreen D.M., Bellin A.D., Elmegreen B.G. 1990, ApJ 364, 415
Felten, J.E., 1976, ApJ 207, 700
Freeman K.C. 1966, MNRAS 133, 47
Freeman K.C. 1970, ApJ 160, 811
Freeman K.C. 1978, in Structure and Properties of Nearby Galaxies, IAU Symp. 77, eds: E. Berkhuysen and R. Wielebinski (Reidel, Dordrecht), p. 3
Giovanelli R., Haynes M.P., Salzer J.J., Wegner G., Da Costa L.N., Freudling W. 1994, AJ 107, 2036
Grosbøl P.J. 1985, A&AS 60, 261
Impey C; Bothun G. 1989, ApJ 341, 89
Jura M. 1980, ApJ 238, 499
Kennicutt Jr. R.C. 1981, AJ 86, 1847
Kormendy J. 1977, ApJ 217, 406
Kormendy J. 1993, in Galactic Bulges, IAU Symp. 153, eds: H. Dejonghe and H.J. Habing (Kluwer, Dordrecht), p. 209
Kraan-Korteweg R.C. 1986, A&AS 66, 255
Lahav O., Naim A., Buta R.J, Corwin H.G., de Vaucouleurs G. et al. 1995, Science, in press
Lake G., Carlberg R.G. 1988, AJ 96, 1587
Lin C.C., Shu F.H. 1964, ApJ 140, 646
Lin D.N.C., Pringle J.E. 1987, ApJ 320, L87
McGaugh, S.S. 1994, Nat 367, 538
McGaugh, S.S., Bothun D.B., Schombert J.M. 1995, in preparation
Nilson P. 1973, Uppsala General Catalog of Galaxies (Roy. Soc. Sci., Uppsala) (UGC)
Peletier R.F., Davies R.L., Davis L.E., Illingworth G.D., Cawson M. 1990, AJ 100, 1091
Peletier R.F., Valentijn E.A., Moorwood A.F.M., Freudling W. 1994, A&AS 108, 621
Pfenniger D., Friedli D. 1991, A&A 252, 75
Phillipps S., Disney M.J. 1983, MNRAS 203, 55
Phillipps S., Disney M.J. 1986, MNRAS 221, 1039
Phillipps S., Evans Rh., Davies J.I., Disney M.J. 1991, MNRAS 253, 496
Postman M., Geller M.J. 1984, ApJ 281, 95
Rand R.J., Kulkarni S.R., Hester J.J. 1990, ApJ 352, L1
Rieke G.H., Lebofsky M.J. 1985, ApJ 288, 618
Roberts Jr. W.W., Roberts M.S., Shu F.H. 1975, ApJ 196, 381
Saio H., Yoshii Y. 1990, ApJ 363, 40

Sandage A. 1961, The Hubble Atlas of Galaxies (Carnegie Inst. of Washington, Washington DC)
Saunders W., Rowan-Robinson M., Lawrence A., Efstathiou G., Kaiser N., Ellis R.S., Frenk C.S. 1990, MNRAS 242, 318
Schombert J.M., Bothun G.D., Schneider S.E., McGaugh S.S. 1992, AJ 103, 1107
Shaw M.A., Gilmore G. 1990, MNRAS 242, 59
Simien F., de Vaucouleurs G. 1986, ApJ 302, 564
Sodré L.Jr., Lahav O. 1993, MNRAS 260, 285
Sofue Y., Habe A. 1992, PASJ 44, 325
Tully R.B., Fisher J.R. 1977, A&A 54, 661
Valentijn E.A. 1990, Nat 346, 153
van der Kruit P.C. 1987, A&A 173, 59
van der Kruit P.C. 1989, The distribution of properties of galaxies. In: Gilmore, G., King, I., van der Kruit, P.C., The Milky Way as a Galaxy (Geneva Observatory, Sauverny-Versoix, Switzerland), p.263
Worthey, G. 1994, ApJS 95, 107
Yoshii Y., Sommer-Larsen J. 1989, MNRAS 236, 779
Young C.K., Currie M.J. 1994, MNRAS 268, L11
Zaritsky D. 1993, PASP 105, 1006

Chapter 4

Colors and color gradients of spiral galaxies

Abstract. The stellar and dust content of spiral galaxies as function of radius has been investigated using near-infrared and optical broadband surface photometry of 86 face-on spiral galaxies. Colors of galaxies correlate with the local surface brightness both within and among galaxies, with the lower surface brightness regions being bluer. The colors formed from different passband combinations correlate strongly indicating that they probably arise from the same physical process.
A realistic 3D radiative transfer model was developed to calculate the effect of dust absorption and scattering on the luminosity and color profiles of galaxies. Stellar synthesis models were used to investigate the effects of the star formation history and the metallicity on the broadband color profiles. Combining all optical and near-infrared data shows that the color gradients in this sample of face-on galaxies are best explained by a combined stellar age and metallicity gradient across the disk, with the outer regions being younger and of lower metallicity. Dust reddening probably plays only a minor role, as the dust models cannot produce reddening profiles that are compatible with the observations.
The observed color differences implicate substantial M/L_λ differences, both within galaxies and among galaxies. The variations are such that the "missing mass" problem derived from rotation fitting becomes even worse. Late-type galaxies (T>6) have lower metallicities and are often of younger average age than earlier types and have therefore an entirely different M/L_λ in most passbands. Late-type galaxies should be used with caution in the Tully-Fisher relation. The near-infrared passbands are recommended for studies where the M/L_λ ratios should not vary too much.

1 Introduction

For many years broadband colors have been used to obtain a basic insight into the contents of galaxies. Broadband photometry is relatively easy to obtain and gives an immediate impression of the spectral energy distribution (SED) of an object. Broadband colors are particularly efficient when used for statistical investigations such as this one. Colors have been used to estimate the stellar populations of galaxies (e.g. Searle et al. 1973; Tinsley 1980; Frogel 1985; Peletier 1989; Silva & Elston 1994) and it has been suggested that colors can give information about the dust content of galaxies (Evans 1994; Peletier et al. 1994). In this paper I use radial color profiles to investigate the stellar and dust content of galaxies.

The problem of determining the stellar content of galaxies from integrated SEDs has been approached from two sides, which are called the empirical and the evolutionary approaches (for a review, see O'Connell 1987). In the first method, stellar SEDs are fitted to the observed galaxy SEDs (Pickles 1985; Peletier 1989). This method works only if one has spectral (line) information. Generally, the broadband colors of a galaxy can be explained by a combination of the SEDs of two or three types of stars (Aaronson 1978; Bershady 1993). In the second, more theoretical approach, stellar SEDs are combined, using some knowledge of initial conditions and evolutionary time scales of different stellar populations, to produce evolutionary stellar population synthesis models (for reviews Tinsley 1980; Renzini & Buzzoni 1986; more recent models are e.g. Buzoni 1989; Bruzual & Charlot 1993; Worthey 1994).

The papers of Disney et al. (1989) and Valentijn (1990) have renewed the debate on whether spiral galaxies are optically thick or thin. Broadband colors of galaxies can be used to examine this problem, because the dependence of dust extinction on wavelength causes reddening. This can be used to measure extinction at a certain point through the disk using a galaxy or another object behind it (Andredakis & van der Kruit 1992) or to measure extinction within a galaxy, for instance across a spiral arm (Rix & Rieke 1993; Block et al. 1994). To measure the global dust properties of a galaxy by reddening one can use the color profile. If one assumes that dust is more concentrated towards the center (just like the stars), the higher extinction in the center produces a color gradient that makes galaxies redder inwards (Evans 1994; Byun et al. 1994).

Integrated broadband colors of galaxies have been used in most previous studies investigating stellar population and dust properties of galaxies. The use of surface photometry colors is less common, as it is easier to compare integrated photometry than surface photometry for large samples of galaxies. Integrated photometry samples the bulk properties of galaxies, but because the light distribution of galaxies is strongly concentrated, one effectively measures the colors of the inner regions of galaxies. The half total light radius of an exponential disk is $\sim$1.7 scalelengths, while luminosity profiles are easily traced out to 4-6 scalelengths. Therefore, half of the light in integrated colors comes from an area that is less than $1/5$ of the area commonly observed in galaxies (say within D_{25}).

Our knowledge of the star formation history (SFH) and the dust content of galaxies improves when we start looking at local colors instead of integrated colors. A first improvement is obtained by using the radial color distribution (i.e. the color profile) of a galaxy. This has been common practice for elliptical galaxies (e.g. Peletier et al. 1990a; Goudfrooij et

al. 1994), but not for spiral galaxies, because elliptical galaxies are assumed to have a simple SFH and low dust content (but see Goudfrooij 1994) opposed to spirals. Even more detailed information about galaxies can be obtained by the use of azimuthal profiles (Schweizer 1976; Wevers et al. 1986) and color maps, but these techniques require high resolution, high signal-to-noise observations and are hard to parameterize, which means that they cannot be used in statistical studies.

Due to the large variety of galaxies, statistical studies of galaxies require large samples. The introduction of CCDs into astronomy made it possible to obtain for large samples of galaxies accurate optical surface photometry in reasonable observing times (Kent 1984). Very large data sets of CCD surface photometry have recently become available (Cornell 1987; Han 1992; Mathewson et al. 1992; Giovanelli et al. 1994). Unfortunately, most of these samples are observed in only one or two passbands. Furthermore, the surface photometry is often reduced to integrated magnitudes and isophotal diameters to study extinction effects with an inclination test or to study the Tully-Fisher relation (Tully & Fisher 1977, hereafter TF-relation). Fast plate measuring machines have also produced surface photometry of large sets of galaxies (e.g. Lauberts & Valentijn 1989, hereafter ESO-LV), but again only in one or two passbands.

Since near-infrared (near-IR) arrays have become available only in the late eighties, near-IR surface photometry in the J, H or K passbands is available for only a few small samples of galaxies. Most of the work has been concentrated on starburst galaxies (e.g. Bushouse & Stanford 1992) or elliptical galaxies (e.g. Peletier et al. 1990b; Silva & Elston 1994). Near-IR surface photometry of somewhat larger sets of spiral galaxies are presented by Terndrup et al. (1994) and by Peletier et al. (1994). The data of Terndrup et al. was complemented with r passband photometry of Kent (1984, 1986, 1987); they explained the observed colors mainly by population synthesis and invoked dust only for the reddest galaxies. Peletier et al. combined their data with the photometry of the ESO-LV catalog and explained their surface photometry predominantly in terms of dust distributions. They concluded that spiral galaxies are optically thick in the center in the B passband, under the assumption that there are no population gradients across the disk.

Near-IR photometry has two advantages compared to the optical. 1) The light in the optical passbands is dominated by light of young stellar populations, but a larger fraction of old stars contribute to the near-IR light. This old population contains most of the stellar mass of a galaxy and therefore the mass distribution is better traced in the near-IR than in the optical. 2) The dust extinction is about ten times less in the K passband than in the B passband. This again enables a better estimate of the true luminous mass distribution of galaxies.

There are two sets of observations that allow a direct physical interpretation of color gradients in spiral galaxies: 1) The current star formation rate (SFR) as measured by the Hα flux has a larger scalelength than the underlying older stellar population (Ryder & Dopita 1994). There are relatively more young stars in the outer regions of spiral galaxies than in the central regions. This will be reflected in broadband colors of spiral galaxies. 2) From metallicity measurements of H II regions it is known that there are clear metallicity differences in the gas among different galaxies and that there are metallicity gradients as function of radius within galaxies (Villa-Costas & Edmunds 1992; Zaritsky et al. 1994). If the metallicity gradients in the gas are also (partly) present in the stellar components, the effects might be observable in the broadband colors.

Broadband photometry is often assumed to trace baryonic mass, and the transformation from light to mass is performed by postulating a mass-to-light ratio (M/L_λ). Both dust extinction and differences in stellar populations will influence M/L_λ ratios, most notably in the bluer optical passbands. Young massive stars contribute a lot of blue light for relatively little mass, and dust extinction hides a fraction of the light while the mass stays the same. Color differences, among galaxies and locally within galaxies, will translate in different M/L_λ values; one can expect that this will influence studies involving rotation curve fitting and the TF-relation.

In this paper I concentrate on the use of color profiles as a diagnostic tool to investigate dust and stellar content of spiral galaxies. Other processes that may contribute to the broadband colors (e.g. emission from hot dust in the K passband) are ignored. The structure of this paper is as follows. In Section 2 the data set is described and the color profiles of the 86 spiral galaxies using the B, V, R, I and K passband data are presented. Section 3 describes the extinction models and the stellar population models used in this paper and then compares these models to the data. In Section 4, I investigate the relation between the color properties of the galaxies and the structural galaxy parameters derived in the previous papers of this series. Implications of the current measurements are discussed in Section 5 and the paper is summarized in Section 6.

2 The data

In order to examine the parameters describing the global structure of spiral galaxies, 86 face-on systems were observed in the B, V, R, I, H and K passbands. A full description of the observations and data extraction can be found in Paper I (de Jong & van der Kruit 1994). The galaxies in this statistically complete sample of undisturbed spirals were selected from the UGC (Nilson 1973) to have red diameters of at least $2'$ and axis ratios larger than 0.625. The galaxies were imaged along the major axis with a GEC CCD on the 1m Jacobus Kapteyn Telescope at La Palma in the B, V, R and I passbands and with a near-IR array on the United Kingdom Infra-Red Telescope at Hawaii in the H and K passbands. Standard reduction techniques were used to produce the images, which were calibrated using globular cluster standard star fields. The sky brightness was determined outside the galaxy in areas free of stars and its uncertainty constitutes one of the main sources of error in the derived parameters.

The ellipticity and position angle (PA) of each galaxy were determined at an outer isophote. The radial surface brightness profiles were determined by calculating the average surface

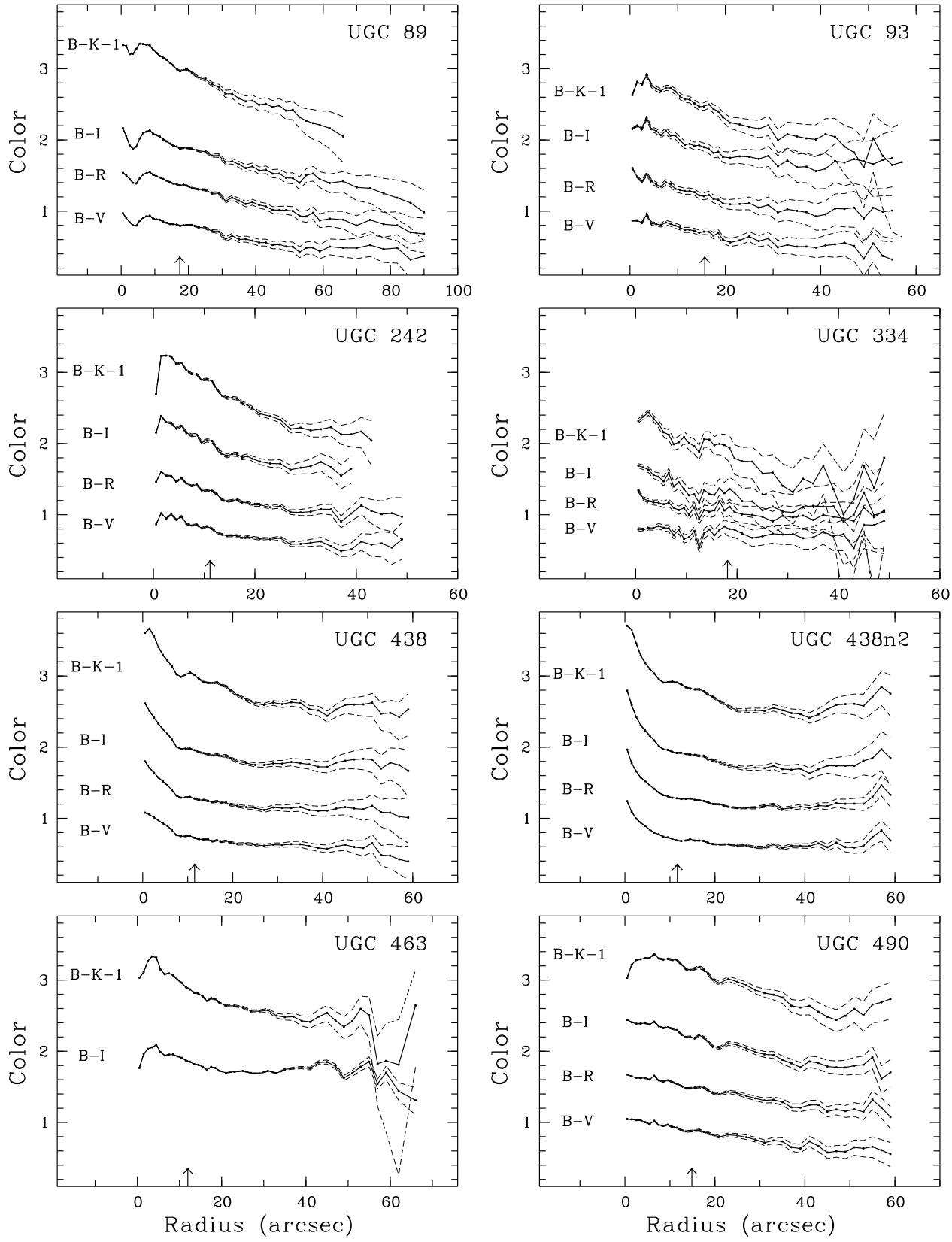

Fig. 1. Observed color profiles of all galaxies. Non-photometric observations are indicated with an italic font. The dashed lines indicate the maximum error because of wrong sky background subtraction and the arrow indicates one disk scalelength in the K passband.

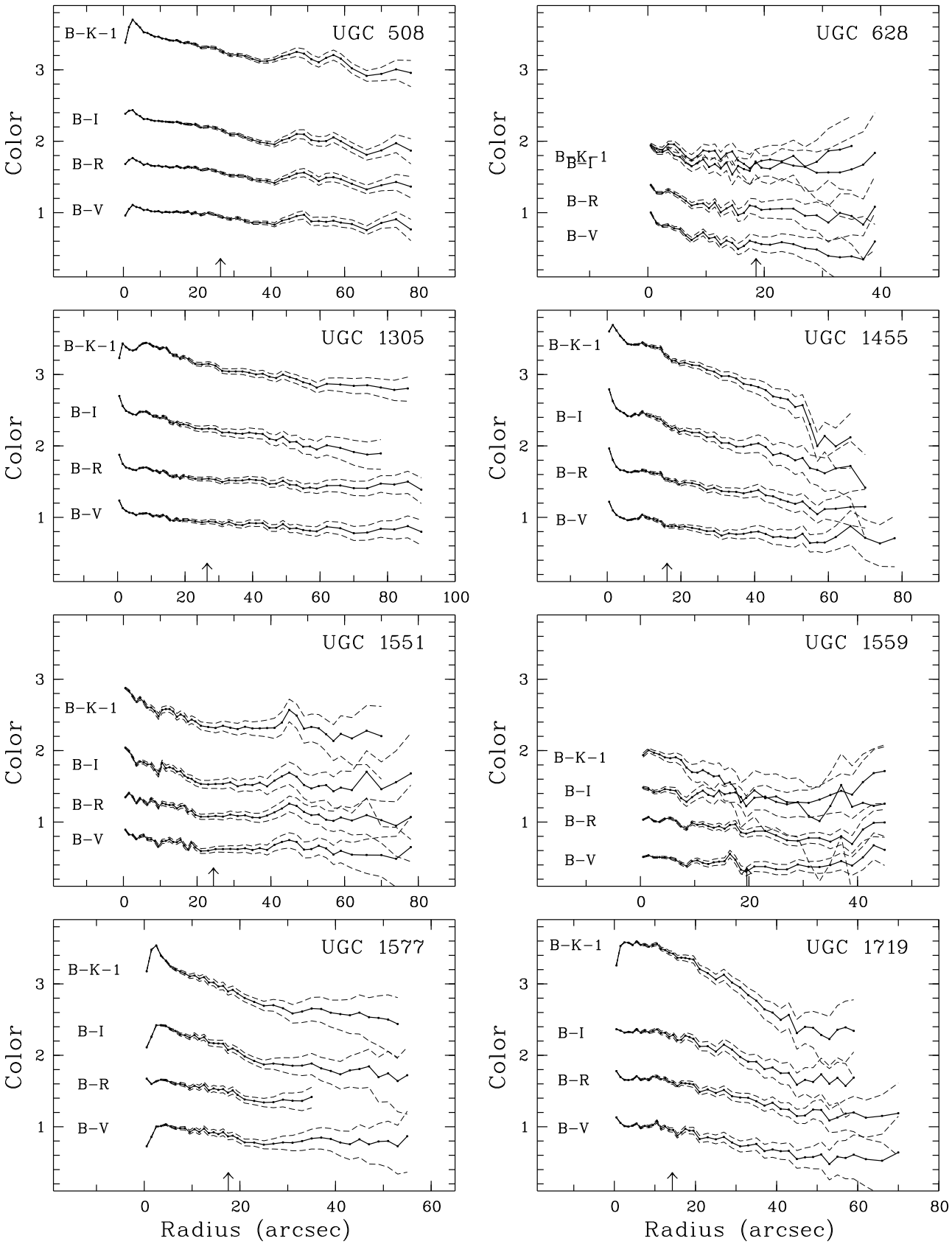

Fig. 1. -Continued.

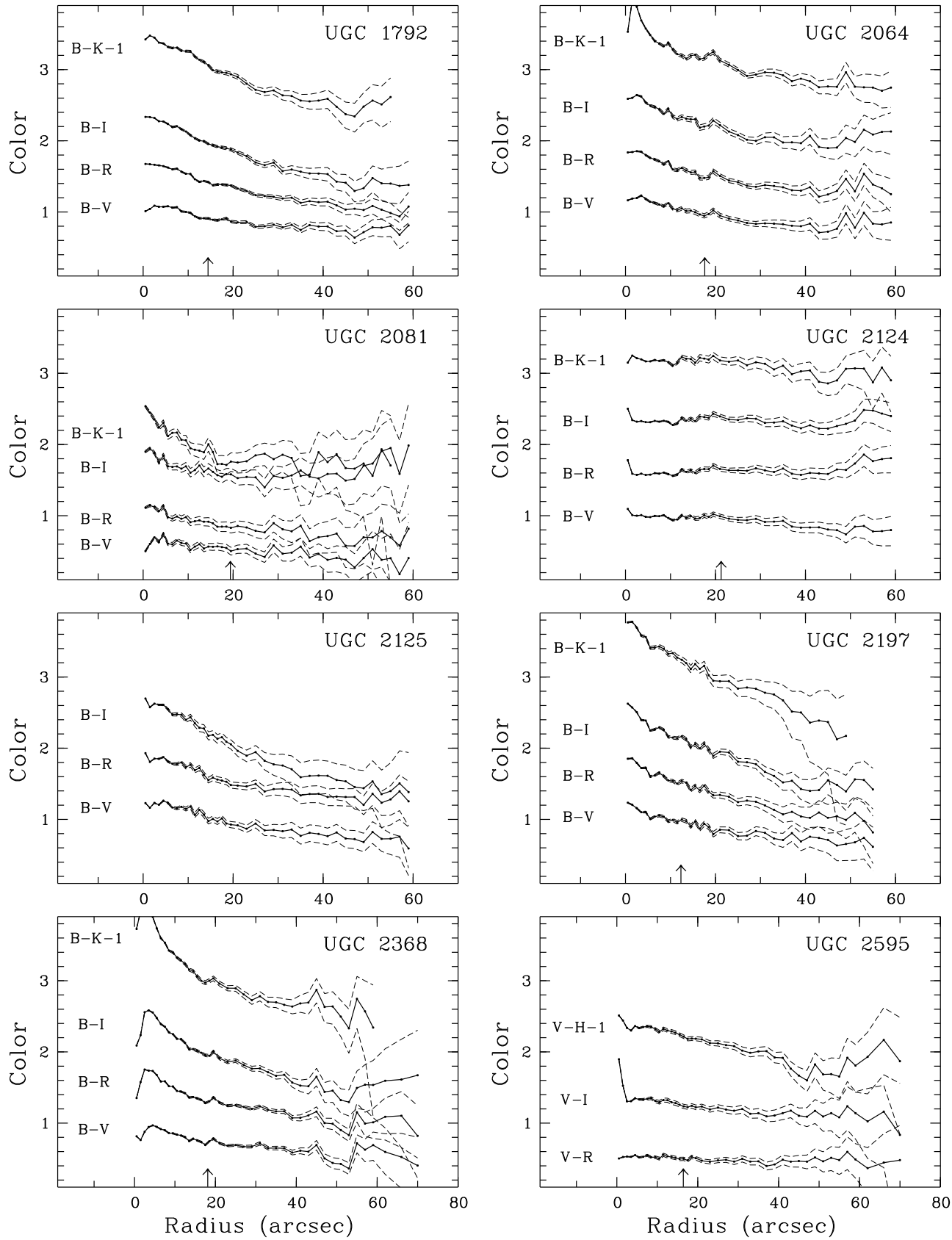

Fig. 1. -Continued.

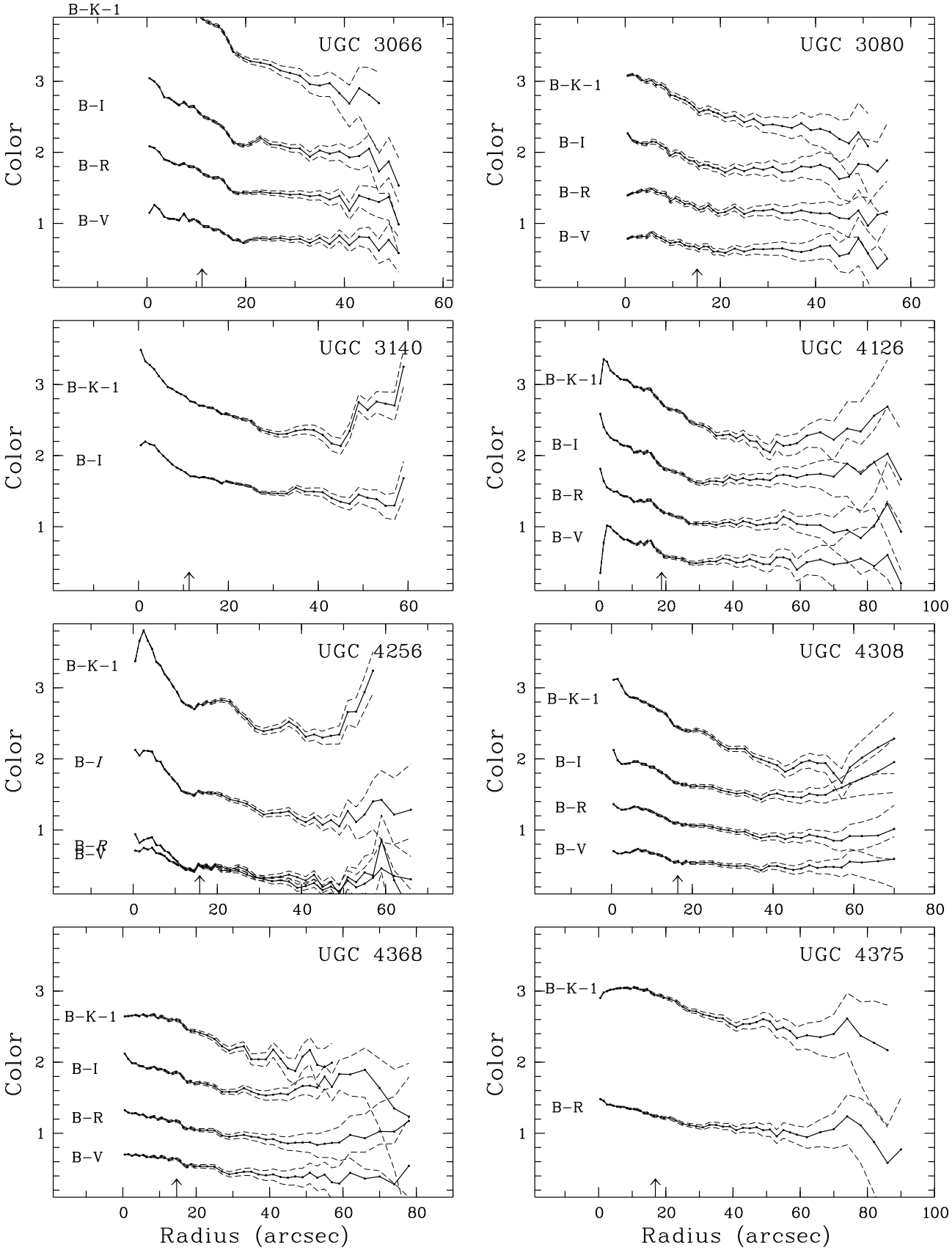

Fig. 1. -Continued.

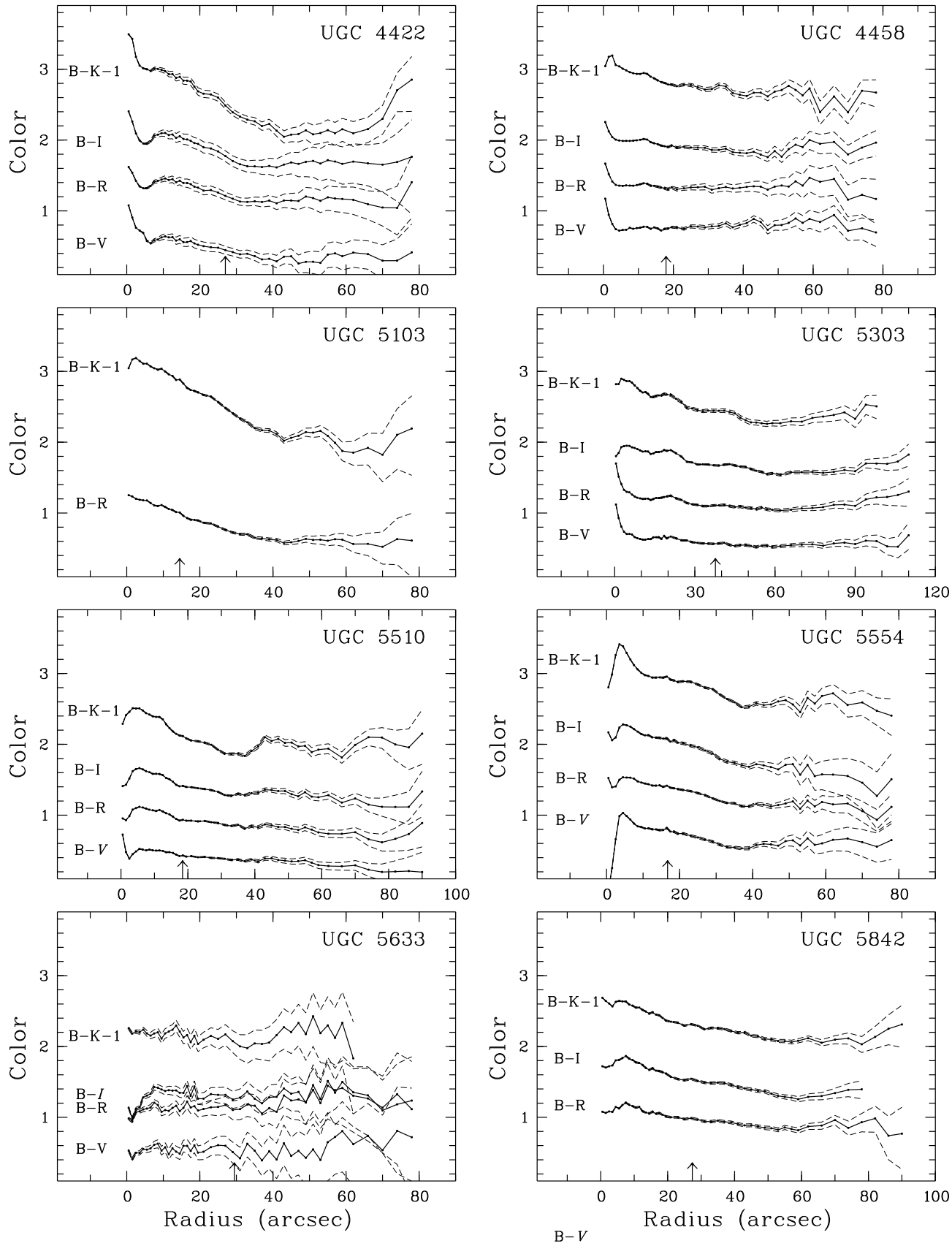

Fig. 1. -Continued.

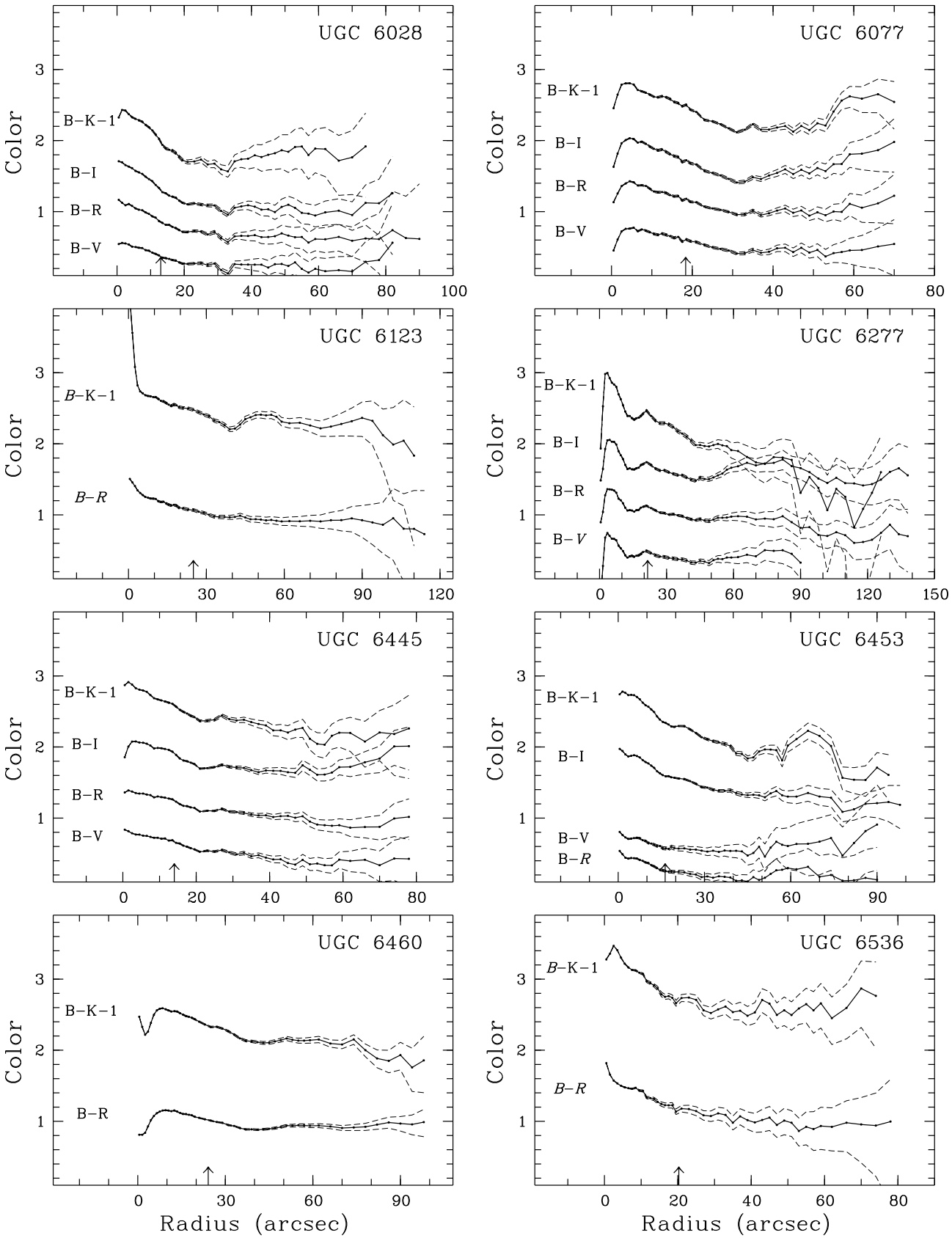

Fig. 1. -Continued.

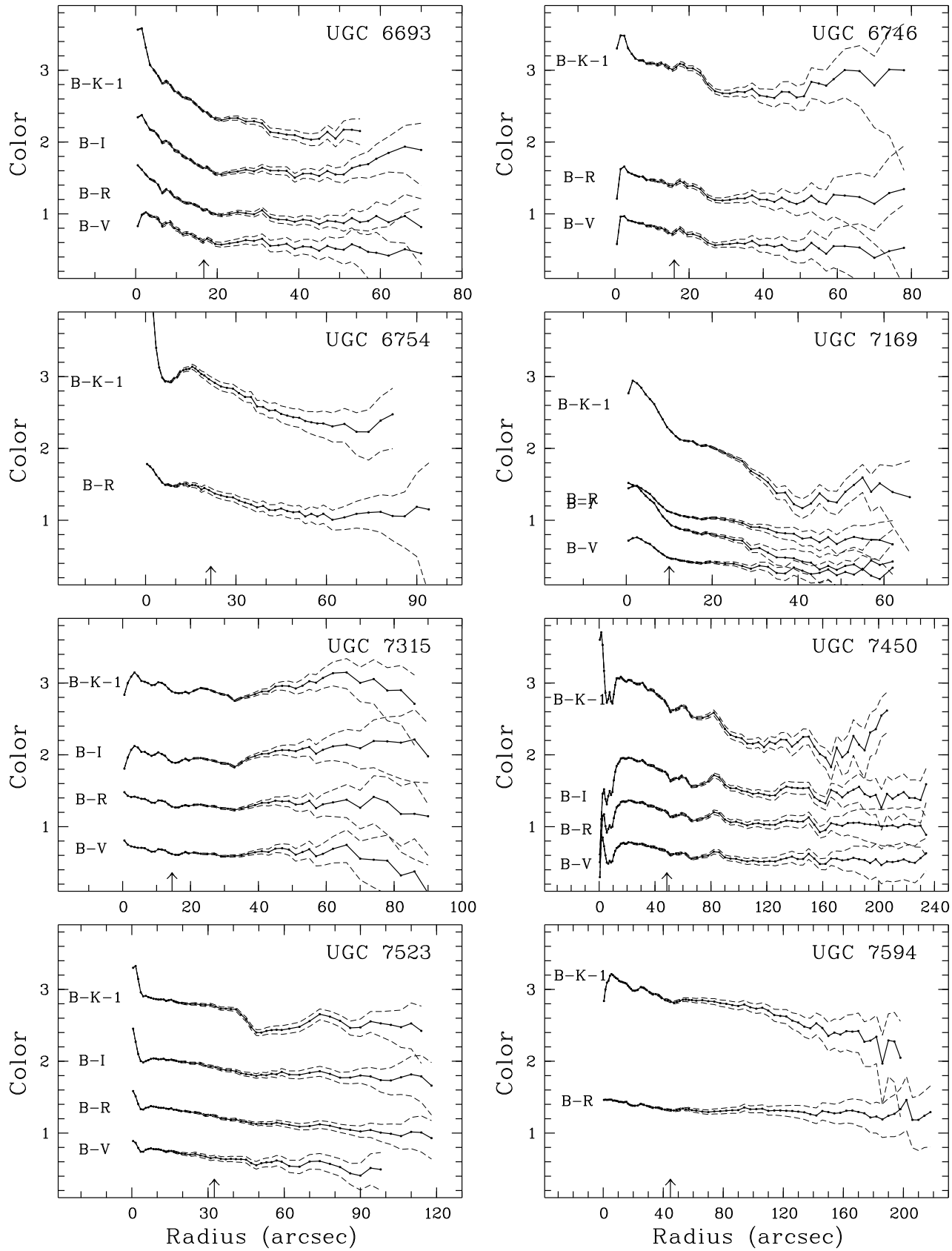

Fig. 1. -Continued.

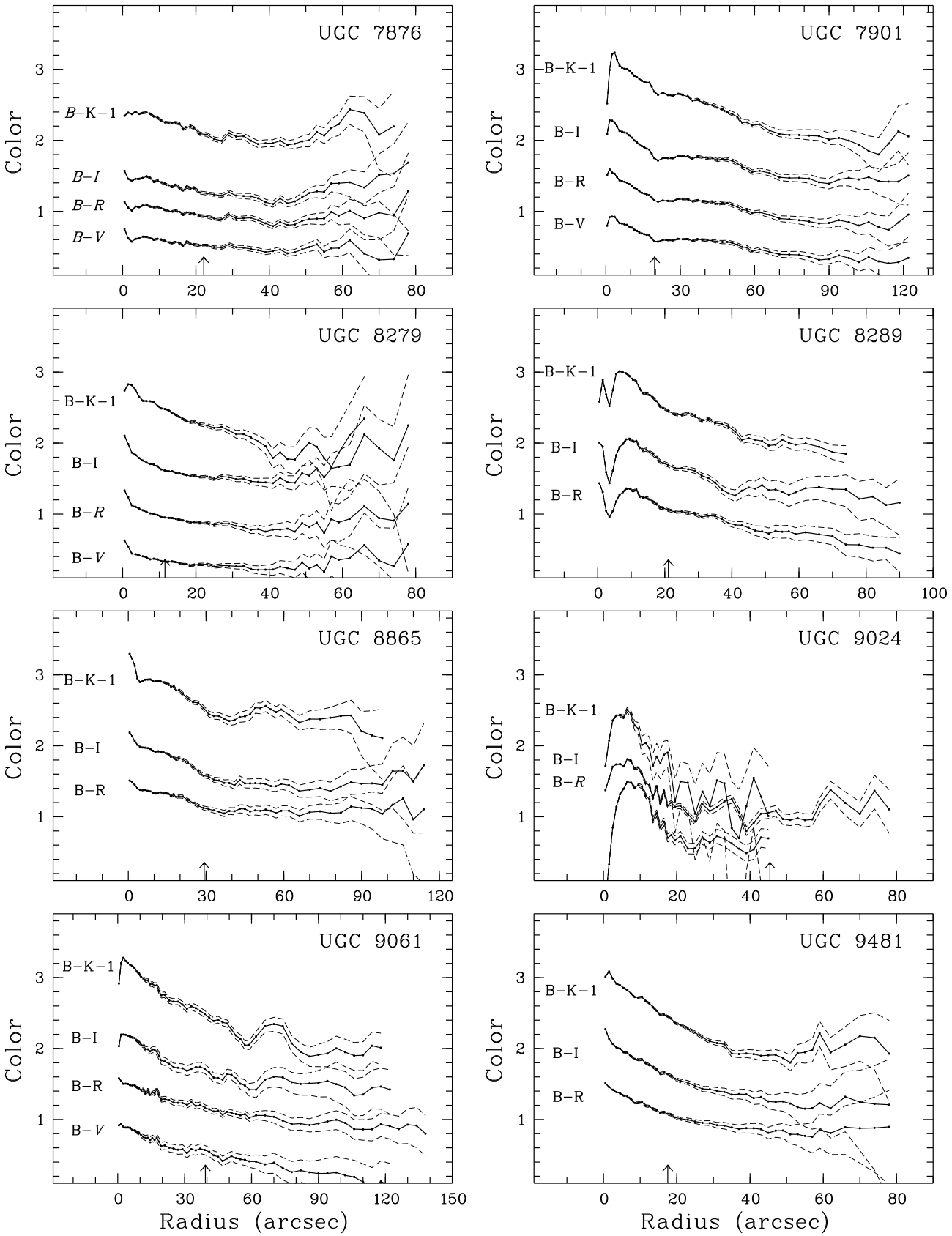

Fig. 1. -Continued.

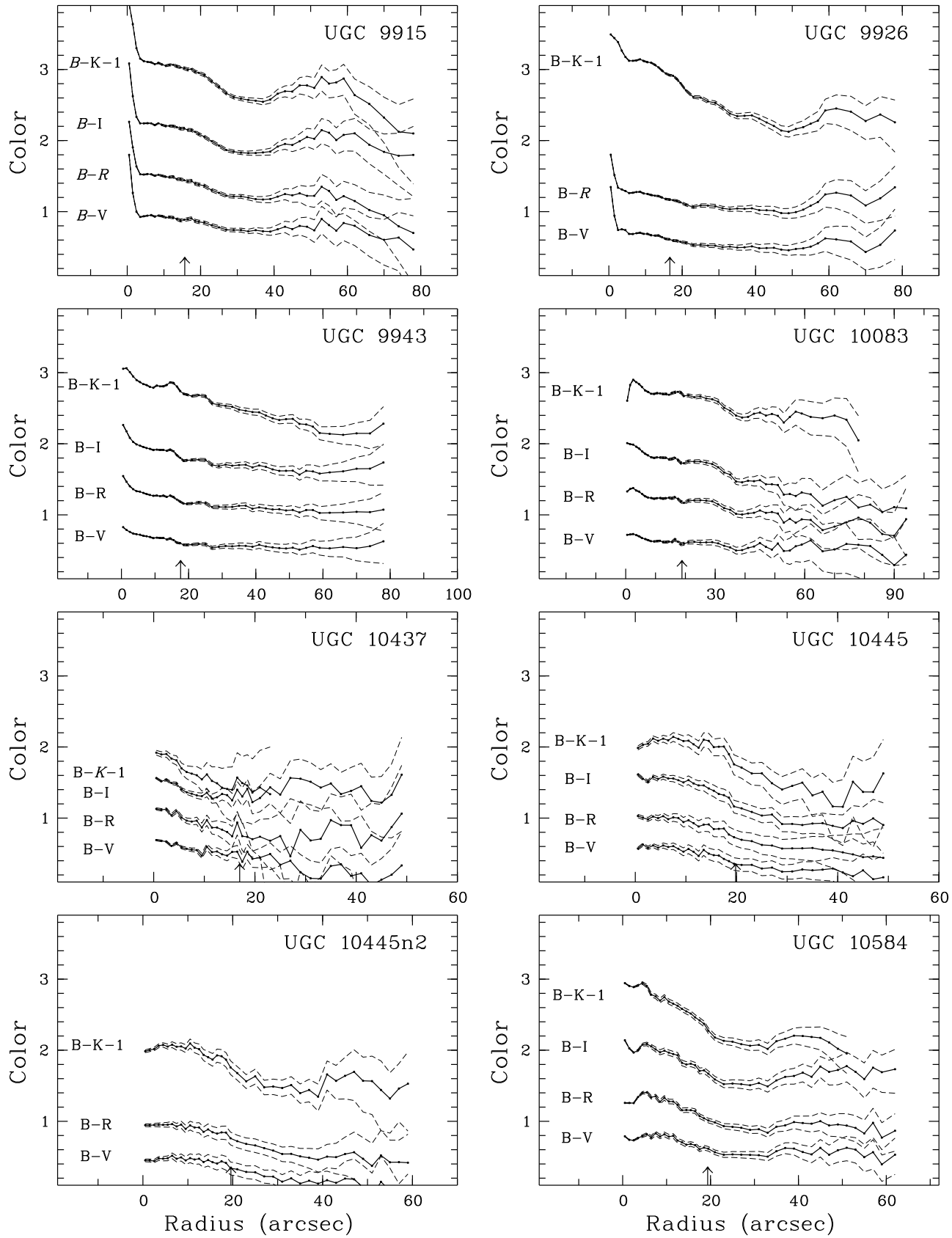

Fig. 1. -Continued.

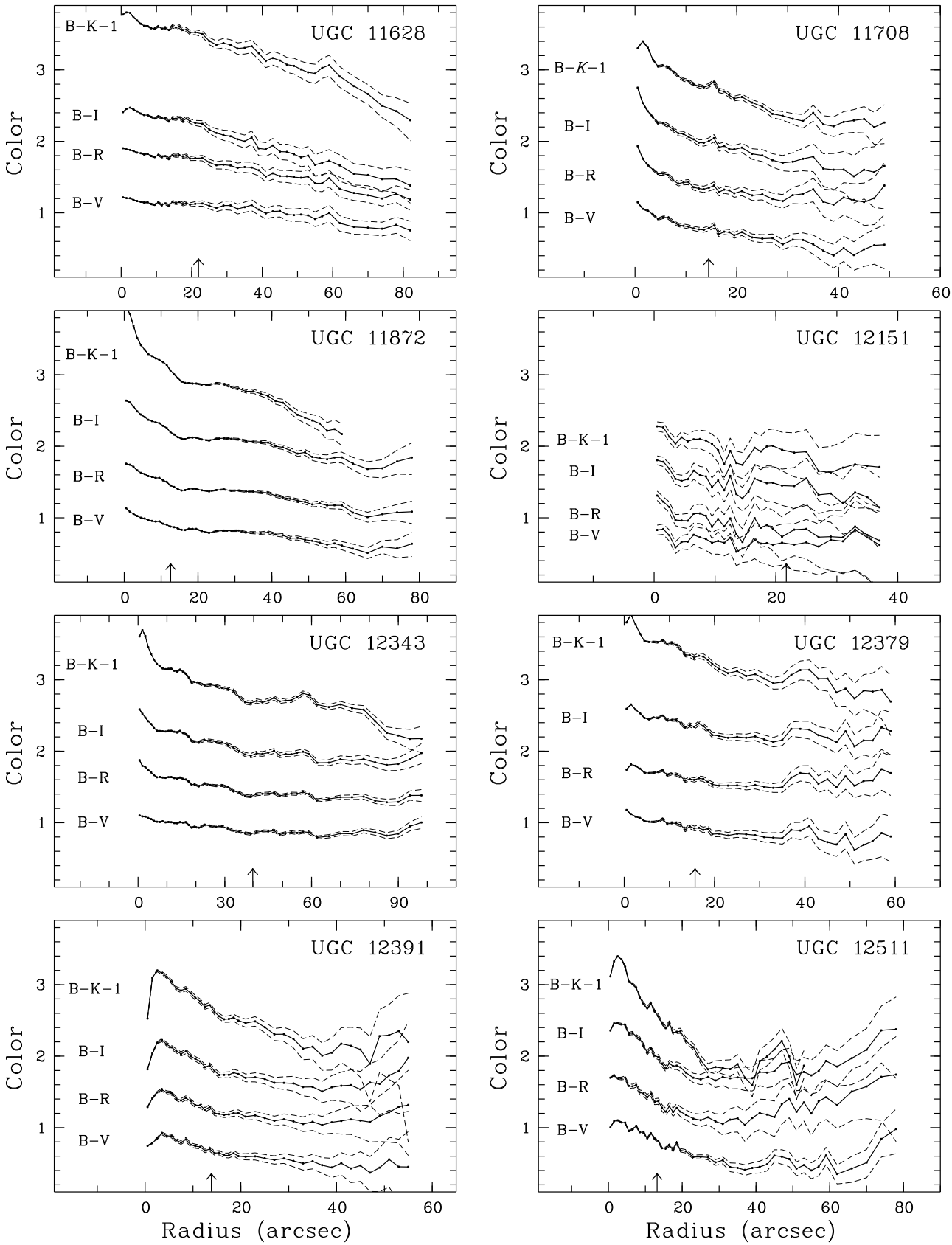

Fig. 1. -Continued.

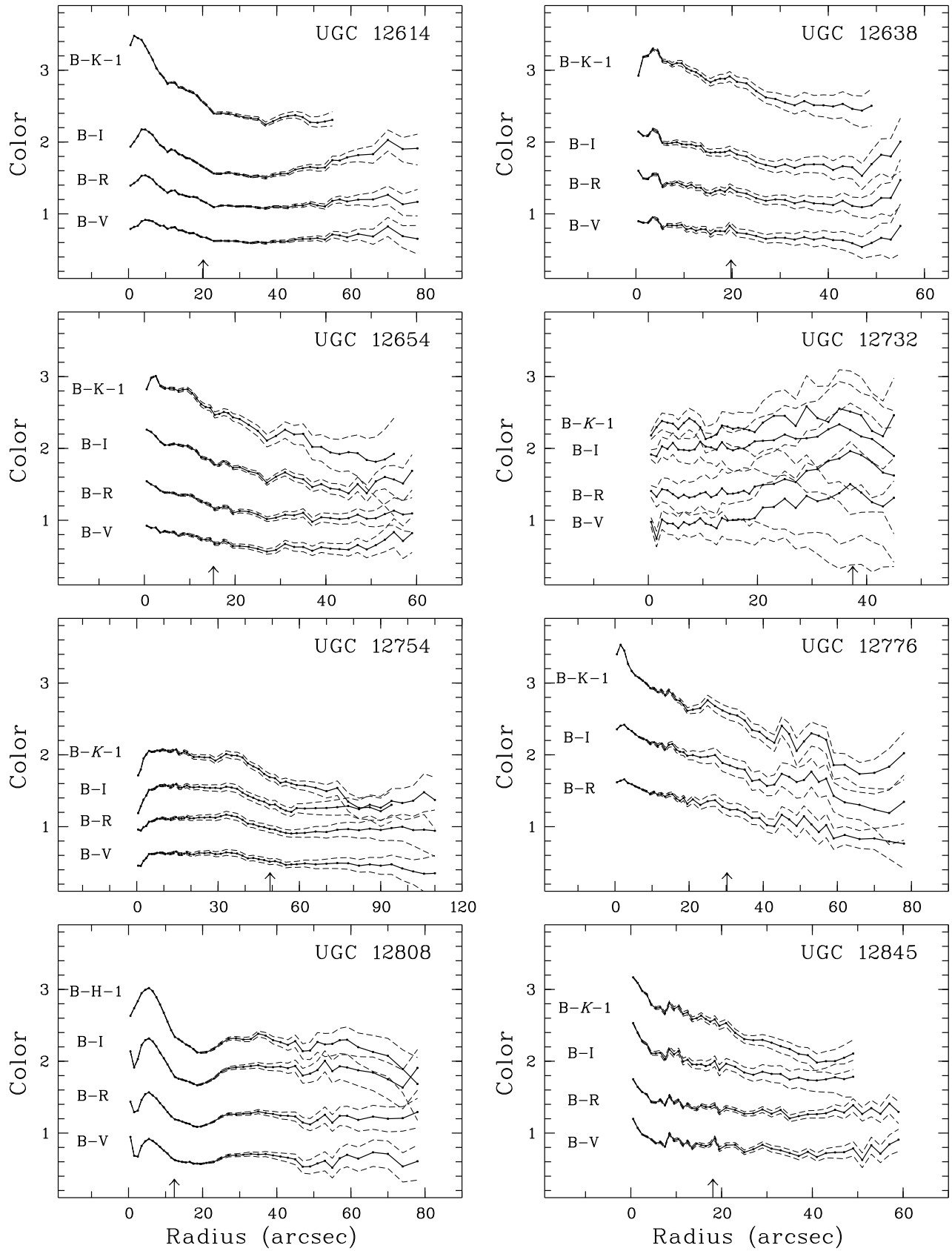

Fig. 1. -Continued.

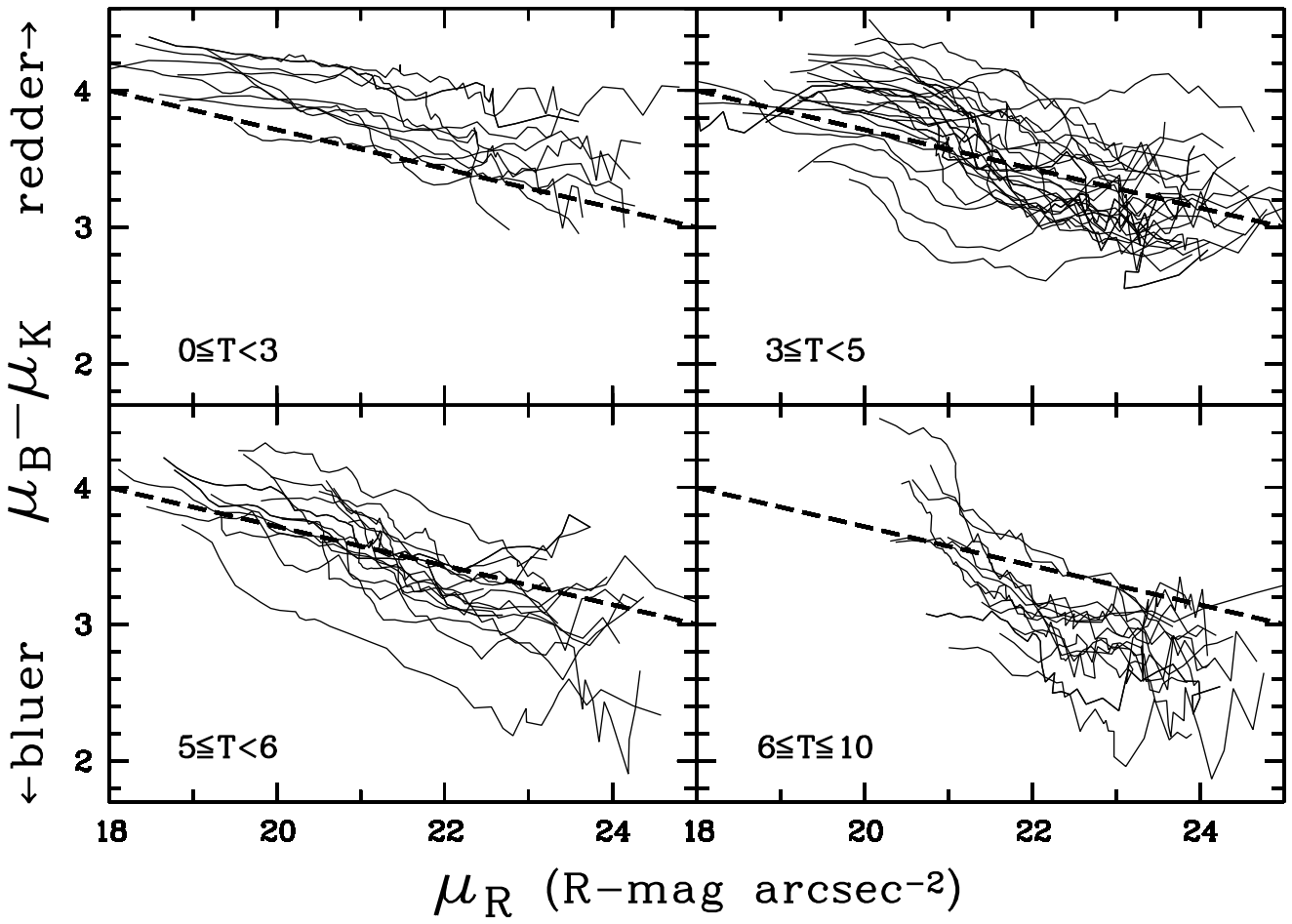

Fig. 2. The local $B-K$ colors of all galaxies as function of R passband surface brightness measured at different radii. The galaxies are divided into the four indicated RC3 morphological type index (T) bins. The dashed lines give a common reference in all four bins, but have no physical meaning. The lines have a B–K color gradient of 1/7 mag per R-mag arcsec^{-2}.

brightness on elliptical rings of increasing radius using the previously determined ellipticity and PA. The surface brightness profiles were used to calculate the integrated luminosity of the galaxies. Internal and external comparisons showed that the derived parameters are well within the estimated errors.

The decomposition of the light of the galaxies into its fundamental components (bulge, disk and sometimes a bar) is described by de Jong (1995a, hereafter Paper II). An exponential light distribution was assumed for both the bulge and the disk and these were fitted to the full 2D image. An extensive error analysis of the determination of the fundamental galaxy parameters was performed and this revealed that the dominant source of error is the uncertainty in the sky background.

The color profiles of the galaxies were calculated by subtracting the radial surface brightness profiles of the different passbands from one another. The profiles are presented in Fig. 1, where the dashed lines indicate the maximum errors due to the uncertainty in the sky surface brightness. Non-photometric observations are also shown, because the slope of the color profile is correct for non-photometric observations, even if the zero-point is incorrect. One should be cautious in interpreting the colors in the inner few seconds of arc, because the profiles were not corrected for the differences in seeing (Paper I) between the different passbands.

It can be readily seen that almost all galaxies show color gradients. They become bluer going radially outward, even when taking the sky background subtraction uncertainties into account. The color gradients extend over several disk scale-lengths. Note that bulges leave no clear signature in the color profiles. From the color profiles alone one can not tell which part is bulge dominated and which part is disk dominated.

The profiles in Fig. 1 are the observed profiles. The corrections needed to translate observed quantities into more physical quantities are discussed by de Jong (1995b, Paper III). In the remainder of this paper, only the photometric observations are used, corrected for Galactic extinction using the precepts of Burstein and Heiles (1984) and the extinction curve of Rieke and Lebofsky (1985).

3 Color gradients

The color gradients of Fig. 1 have been put on a common scale in Fig. 2, where the B–K colors of the galaxies are plotted as function of the local R passband surface brightness. The

galaxies are divided in four bins based on their morphological type, using the RC3 (de Vaucouleurs et al. 1991) type indices T (see also Papers I and III). There is a clear correlation between surface brightness and color; the lower surface brightness regions are bluer. This indicates the relation between Hubble type, surface brightness and integrated color: since late-type galaxies have on average a lower central surface brightness (Paper III), they are bluer. This is not the whole story, since for each morphological type at each surface brightness there is considerable scatter. Furthermore, even at the same surface brightness, late-type galaxies are on the average bluer than early-type galaxies.

The two most straightforward explanations for the color gradients are 1) radial changes in stellar populations and 2) radial variations in reddening due to dust extinction. For both possibilities, I investigate a range of models to limit the acceptable parameters. The extinction models have a range in relative distributions of dust and stars. The colors of the stellar synthesis population models depend on the star formation history (SFH) and the metallicity of the stars.

The colors and color gradients of the galaxies formed from the different passbands combinations are correlated and the models should be fitted in a six-dimensional "passband space". Predicting the right color gradient in one combination of passbands, but a wrong one in an other combination makes a model at best incomplete and therefore undesirable. Six dimensional plots do not exist and therefore color–color plots will be used to combine as much information as possible in one plot. The H passband colors are not shown, as the differences between H and K predicted by the models (both the population and the extinction models) are smaller than the measurement errors. In the remainder of this section I first discuss the extinction models and the stellar population synthesis models used in this paper and then compare the models with the data.

3.1 Extinction models

Since Valentijn (1990) suggested that spiral galaxies were optically thick over a large fraction of their disk, dust in galaxies has gained renewed attention. Dust has been used to explain "Freeman's law" (Freeman 1970), i.e. the constancy of central surface brightness of disks (Valentijn 1990), and the color gradients in disk galaxies (Peletier et al. 1994). In this section, I present my dust models, show the predicted luminosity profiles, color profiles and color–color diagrams, and compare the results with existing dust models.

3.1.1 Modeling dust effects

Numerous researches have investigated the effects of dust extinction on the observed light distributions of galaxies. The primary goal of most of the studies is to investigate the inclination dependent effects of the total magnitude of galaxies (e.g. Huizinga 1994). In some studies the extinction effects on the observed (exponential) light profile of galaxies is studied. The most detailed are the Triplex models by Disney, Davies & Phillipps (1989 DDP hereafter, see also Huizinga 1994; Evans 1994).

The effects of reddening on the observed colors and color profiles has been examine in a number of studies. The simplest model to predict the reddening of a galaxy is to use directly the standard (Galactic) extinction law, but this is of course a gross oversimplification. DDP have named this the Screen model, which has all dust placed between us and the galaxy. In reality the dust is mixed between the stars, so that on the near side of the galaxy a considerable fraction of stars will be only slightly obscured. For the same amount of dust, the observed reddening is considerably less than predicted by the Screen model, especially since the most reddened stars are also the most obscured stars and therefore the ones that contribute less to the overall color of the system.

As soon as the dust is mixed with the stars one has to take both absorption and scattering into account. Intuitively one expects that for face-on galaxies at least as much light gets scattered into the line of sight as out of it, especially since there are more photons traveling in the plane of a galaxy which can be scattered into face-on directions than the other way around. As only the absorbed photons really disappear, it is better to use relative absorption rather than relative extinction between different passbands to estimate reddening effects in face-on galaxies. It is essential to incorporate both absorption and scattering into extinction models to make accurate predictions of the effects of dust on colors and color gradients of galaxies.

A number of studies have investigated the effect of reddening on integrated colors of galaxies (Bruzual et al. 1988; Witt et al. 1992 and references therein). In these studies scattering is included and stellar and dust distributions are used that allow approximations to reduce computing time; e.g. Bruzual et al. use plane parallel distributions and Witt et al. use spherically symmetric distributions. Color profiles produced by dust models are not often presented. Evans (1994) investigates the effects of extinction as function of radius in face-on galaxies for a non-scattering medium. Byun et al. (1994) also investigate the effects of dust on luminosity and color profiles, using the method of Kylafis & Bahcall (1987). Their method includes first order scattering and approximates multiple scattering. The results of Byun et al. 1994 are compared with the results presented here in Section 3.1.2.

To estimate to what extent the color gradients can be attributed to reddening by dust extinction, Monte Carlo simulations were made of light rays traveling through a dusty medium. The models are described in full detail in Appendix A.

The distributions of stellar light and dust in these models were described by exponential laws in both the radial and vertical directions. In the radial direction these distributions were parameterized by the scalelength of the stars ($h_{\rm s}$) and the dust ($h_{\rm d}$), and in vertical direction by the scaleheight of stars ($z_{\rm s}$) and dust ($z_{\rm d}$). In all models $h_{\rm s}/z_{\rm s} = 10$ was used and for simplicity no bulge component was added to the stellar light distribution.

Since the effects of dust on the color profiles is the main interest of this study, absolute calibration of the amount of starlight is arbitrary. Only the relative effect of dust from one passband to the other is important. The amount of dust in the models is parameterized by *the* optical depth of a system $\tau_{0,V}$,

defined as the optical thickness due to dust absorption and scattering in the V passband through the disk from one pole to the other along the symmetry axis (Eq. (A16)).

Three dust properties were incorporated into the dust model to describe the wavelength dependent effects of dust extinction: the relative extinction (τ_λ/τ_V), the albedo (a_λ), and the scattering asymmetry parameter (g_λ). The relative extinction was adopted from Rieke and Lebofsky (1985); the other two parameters were drawn from Bruzual et al. (1988). These values are listed in Table 3.

Before presenting the model results, a few words of caution are in order. First, extragalactic dust properties are poorly known. There are only a few measurements of extinction laws in extragalactic systems (e.g. Knapen et al. 1991; Jansen et al. 1994) other than for the Magellanic Clouds (see Mathis 1992 for references). All measurements seem to be consistent with the Galactic extinction law, except for a few measurements in the Small Magellanic Cloud. It is well known that the Galactic extinction curve is not the same in all directions, but the one adopted here is appropriate for the diffuse interstellar medium (for discussion see Mathis 1990). The parameters a_λ and g_λ have never been measured in extragalactic systems and are poorly known even for our own Galaxy. The adopted values for these parameters stem, especially for the longer wavelengths, from model calculations. Still, no large variations are expected in the extinction properties, unless the dust in other galaxies is made of totally different material (see also the discussion in Bruzual et al. 1988).

As a second word of caution, the models presented here describe only smooth diffuse dust. The effects of non-homogeneous dust distributions should be considered. A large ensemble of optically thick clouds has only a reddening effect if the clouds have a large filling factor, but such a configuration becomes comparable to the presented models with high $\tau_{0,V}$. The reddening effect of a clumpy medium will be smaller than the effect predicted by the diffuse dust models for the same amount of dust, but the direction of the reddening vectors will be the same as long as the dust properties in the clouds are more or less the same. If clouds are optically thick at all wavelengths one has the case of gray dust and no color gradients at all. Model calculations using a clumpy dust medium in the absence of scattering are presented in Huizinga (1994, Chapter 5).

As a final word of caution, a young population of stars probably has a smaller scaleheight than an old population of stars. It might be more appropriate to use a smaller stellar scaleheight in the blue than in the near-IR. The relative contributions from young and old populations are difficult to estimate however, and for simplicity one stellar scaleheight is used for all passbands. These models do not include the dust shells around the extremely luminous stars in the final stages of their life. Even though such shells will make these stars redder, they will not produce a radial effect (unless the shell properties depend on galactic radius). Effectively these shells will only make the total underlying population redder at all radii and they are of no further concern here.

3.1.2 Resulting profiles

Figure 3 shows luminosity and color profiles resulting from the Monte Carlo simulations. The luminosity profiles for the different passbands have been given an arbitrary offset and the dust free cases of the B and the K passbands are indicated by the dashed lines. The color profiles have been plotted under the arbitrary assumption that the underlying stellar populations have color indices of zero in all passband combinations. The noise in the color profiles is due to the statistical processes inherent to Monte Carlo simulations.

The luminosity profiles of the $h_\mathrm{d}/h_\mathrm{s}=1$ models presented on page 115 show only deviations from the unobscured profiles at the inner two scalelengths. These deviations are quite small except for the highest $\tau_{0,V}$ values. The differences between the different $z_\mathrm{d}/z_\mathrm{s}$ models are also quite small and are only apparent for the high $\tau_{0,V}$ values. The luminosity profiles for the $h_\mathrm{d}/h_\mathrm{s}=$ 2-3 models on page 116 are affected over several scalelengths by dust extinction. In fact, the $h_\mathrm{d}/h_\mathrm{s}=3$, $\tau_{0,V}=$ 10-20 models are optically thick over almost the entire disk. The result is that the profiles stay exponential, but with a lower surface brightness and a slightly different scalelength from the unobscured case.

The color profiles of the $h_\mathrm{d}/h_\mathrm{s}=1$ models of Fig. 3 show color gradients over the first two scalelengths. The gradients can be large in B–H and B–K, but are in general smaller than 0.3 mag in the other color combinations. The gradients are small in the wavelength range from the U to the R passband, because the absorption properties do not differ very much among these passbands. The change in scattering properties causes the differences in extinction in this wavelength range. The optically thick behavior of the $h_\mathrm{d}/h_\mathrm{s}=3$, $\tau_{0,V}=$ 10-20 models is reflected in the color profiles of the optical color indices; there are no color gradients, only color offsets. The typical surface brightness is produced at $\tau_\lambda=1$ over the entire disk, and the color offsets reflect that different wavelengths probe different depths into the galaxy.

To my knowledge, the models of Byun et al. 1994 are the only models in the literature that have exponential light and dust distributions, and include scattering to calculate luminosity and color profiles. These models can be compared to the models presented, but only indirect, because Byun et al. defined the optical depth of a system differently. They parameterize the optical depth of a system as the *absorption* in the V passband through the whole disk of a face-on galaxy along the symmetry axis, while here the *extinction* is used (Eq.(A16)). Furthermore, they use the Galactic *extinction* law to translate the *absorption* coefficient from one passband to another. Using Table 3 one can calculate that their $\tau_V(0)$ models corresponds to my $\tau_{0,V}=\tau_V(0)/(1-a_\lambda)$ models, which is $2.9\tau_V(0)$ for the B passband and $1.8\tau_V(0)$ for the I passband. It is probably most meaningful to compare the $\tau_{0,V}=20$, $z_\mathrm{d}/z_\mathrm{s}=0.3$, $h_\mathrm{d}/h_\mathrm{s}=1$ B passband profile of Fig. 3 with the bulgeless (BT0.0), face-on $\tau(0)=5.0$ profile of their Fig. 7. The central extinction of slightly more than 1 mag and the general shape of the luminosity profile (which is unaffected by extinction for radii larger than 2-3 scalelengths) are comparable. Their B–I

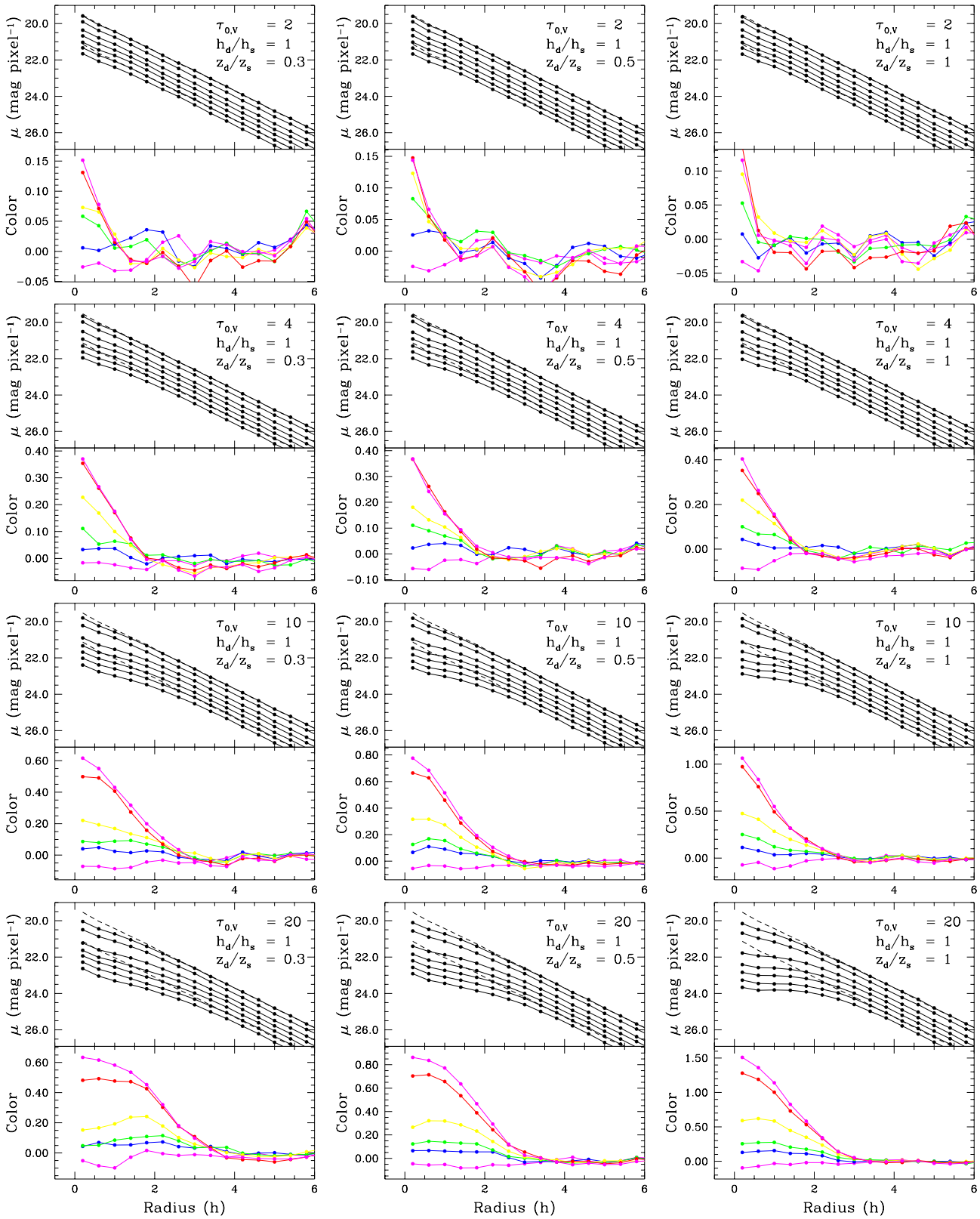

Fig. 3. The surface brightness (top) and color (bottom) as function of radius resulting from the Monte Carlo dust simulations of face-on galaxies. The radius is units of disk scalelength. The central optical depth and dust to stellar scalelength and scaleheight ratios are indicated top right. The dotted lines indicate unobscured B and K passband profiles. The luminosity profiles have an arbitrary offset and are from top to bottom the K, H, I, R, V, B and U passband profiles. The color profiles are plotted under the assumption that the underlying color indices are zero, and are from top to bottom (B–K), (B–H), (B–I), (B–R), (B–V) and (B–U).

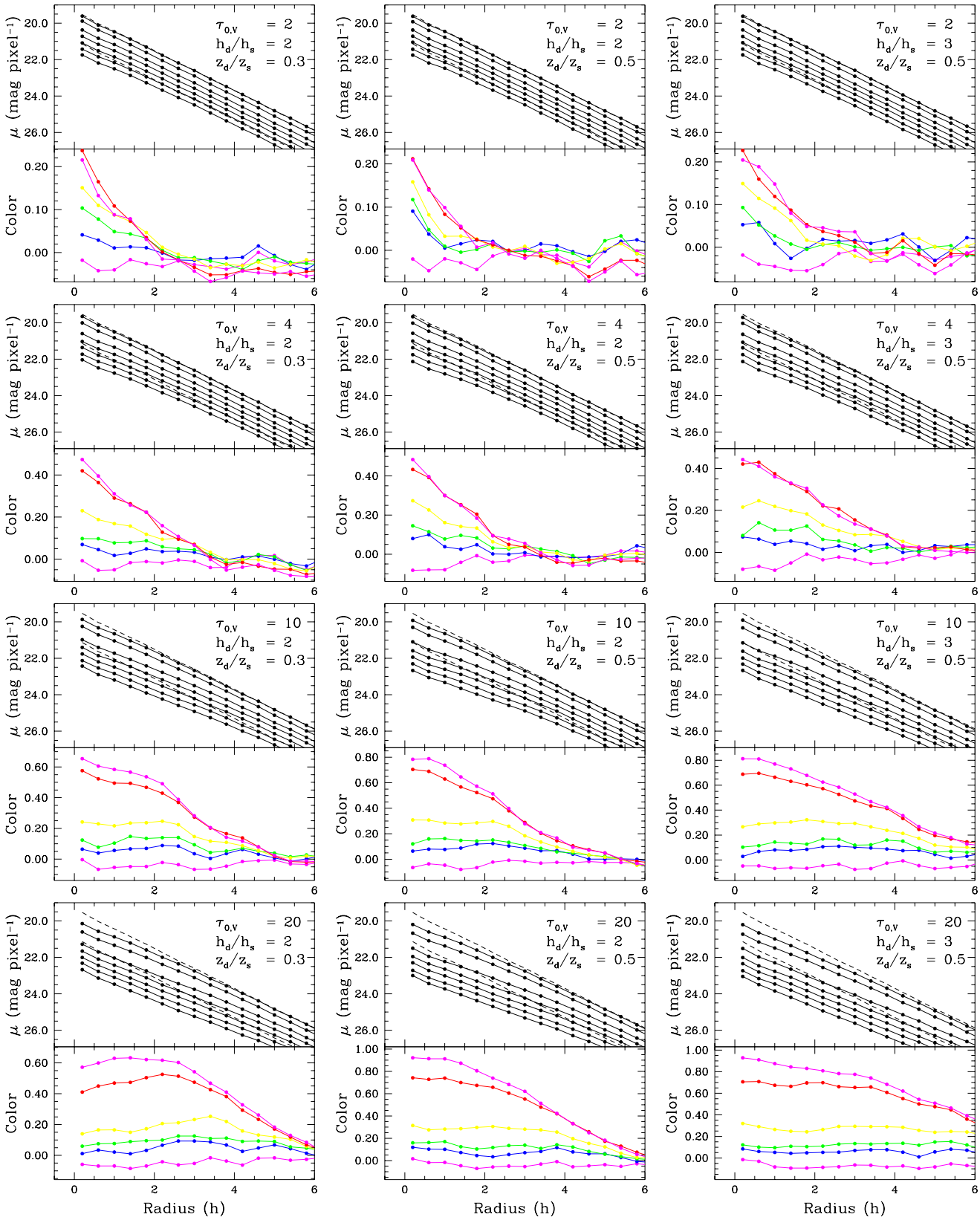

Fig. 3. -continued.

color profiles are physically not very plausible, because they use the Galactic extinction curve instead of an absorption curve to translate their absorption coefficients from one passband to another. A comparison of the color profiles is therefore not meaningful. Their luminosity profiles can be used, but note that their $\tau_V(0)$ should be divided by $(1–a_V)$ to get the extinction suffered by a point source behind the galaxy, as done here.

What is the range of plausible model parameter values? Quite high $\tau_{0,V}$ and/or $h_\mathrm{d}/h_\mathrm{s}$ values are needed to explain the observed $B–K$ color gradients of one magnitude over five scalelengths (Fig. 1) by dust reddening alone. On the other hand, models with equal scaleheight for dust and stars need an additional dust component, because these models do not produce a clear dust lane in edge-on galaxies. It is also unlikely on dynamical grounds that the dissipational dust and the dissipationless stars have the same scaleheight. Kylafis & Bahcall (1987) find a dust-to-star scaleheight ratio of 0.4 in their best fitting model of edge-on galaxy NGC 891 and the dominant dust component is expected to have a $z_\mathrm{d}/z_\mathrm{s}$ ratio between 0.3 and 0.5.

The high $h_\mathrm{d}/h_\mathrm{s}$ models are favored by Valentijn (1990, 1994), who concluded from inclination tests that Sb-Sc galaxies have a $\tau_B \sim 1$ through the disk at D_{25}. This extinction at about 3-4 stellar scalelengths translates to $\tau_{0,V} \sim 20$ models, if the dust density is distributed exponentially with $h_\mathrm{d}/h_\mathrm{s} = 1$. The edge-on extinction from the center out to 3-4 stellar scalelengths gives at least $\tau_V \approx 50$ in such a model, which is in conflict with observations of edge-on galaxies. A few edge-on galaxies have been imaged in the near-IR indicating $A_V \approx$ 8-10 (Wainscoat et al. 1989; Aoki et al. 1991), and the Galactic center can be seen in the K passband (Rieke & Lebofsky 1985, $A_V \approx 30$ and $A_K \approx 3$). Thus $\tau_{0,V} = 20$ models represent extremely dusty galaxies, and certainly no galaxies with $\tau_{0,V} \geq 20$ are expected. If one increases $h_\mathrm{d}/h_\mathrm{s}$ to 3, $\tau_{0,V}$ has to be 2-4 to get $\tau_V = 1$ through the disk at 3 stellar scalelengths. This then gives an edge-on $\tau_V =$ 20-40 from the center out to 3 stellar scalelengths when using large $z_\mathrm{d}/z_\mathrm{s}$ values, which are the most favorable for these models. Therefore, the edge-on extinction values of the $\tau =$ 2-4, $h_\mathrm{d}/h_\mathrm{s} = 3$ models are marginally consistent with the observations, but these models do not produce very large color gradients.

3.1.3 Resulting color–color diagrams

Four color–color plots of dust models are presented in Fig. 4. Because extinction is a relative measurement, the zero-point can be chosen freely in these plots; only the shapes of the profiles are fixed. The solid lines show the results from the Monte Carlo simulations. The dotted lines are the result of the Triplex models of Disney, Davies & Phillipps (1989, DDP models hereafter). To calculate the τ_0 for the DDP models in the different passbands, the indicated $\tau_{0,V}$ values were multiplied by $(\tau_V/\tau_\lambda)(1 - a_\lambda)/2$ (Table 3). This is equivalent to using an absorption law rather than an extinction law between the different passbands. The factor 2 arises because the DDP models are characterized by the optical depth from the galaxy center to the pole and not by the optical depth through the whole disk.

Comparing the results from the Monte Carlo simulations with the DDP models, one can see that the models agree remarkably well for high optical depths. The intuitive idea that just as many photons are scattered out of the line of sight as are scattered in seems correct for face-on galaxies. Photons are only lost due to absorption. For low optical depths the reddening almost completely disappears. Once a photon gets scattered into the line of sight, the chances of it getting absorbed or scattered again are minimal; even bluing instead of reddening can occur. Even though the amount of reddening is a strong function of the dust configuration, it seems that the direction of the reddening vector is largely dependent on the dust properties. Obviously the reddening produced by these models is different from the reddening produced by a Screen model with the Galactic *extinction* law (also indicated in Fig. 4).

In conclusion, dust can produce color gradients in face-on galaxies, but this requires quite high central optical depths and preferably long dust scalelengths. The reddening vectors of realistic dust models that include both absorption and scattering are completely different from the often-used Screen model extinction models.

3.2 Evolutionary stellar population synthesis models

Ever since the invention of the concept of stellar populations in galaxies (Baade 1944), numerous models have been made to predict the integrated light properties of such populations and thus of galaxies as a whole. In the beginning the empirical approach was often followed, in which the different contributions of the stellar populations are added to match the observed galaxy SED. Later, knowledge about initial conditions and stellar evolution were added to make evolutionary synthesis models. This section contains a brief description of population synthesis models, concentrating on the synthesis models used here, followed by a description of the effects that star formation history (SFH) and metallicity have on the colors produced by synthesis models.

3.2.1 Modeling stellar populations

In recent years a large number of synthesis methods have appeared in the literature, all of which require many input parameters (Tinsley 1980; Renzini & Buzzoni 1986; Worthey 1994 and references therein). The simplest models use a initial mass function (IMF) to create a single burst of stars, whose evolution in time is then followed. Slightly more complicated models describe the star formation rate (SFR) in time. In the most complicated models, the gas, stellar, and chemical evolution are linked and described in a self-consistent way. This last type of model has not been used here, since to date only a small range of SFHs have been investigated with these models. The description of the evolution alone does not produce an SED and therefore the models are linked to a stellar library to calculate the evolution in time of the integrated passband fluxes or of the integrated spectrum.

The results from the models in the literature are not all in agreement. The disagreements arise mainly from differences in the treatment of the late stages of stellar evolution. The models

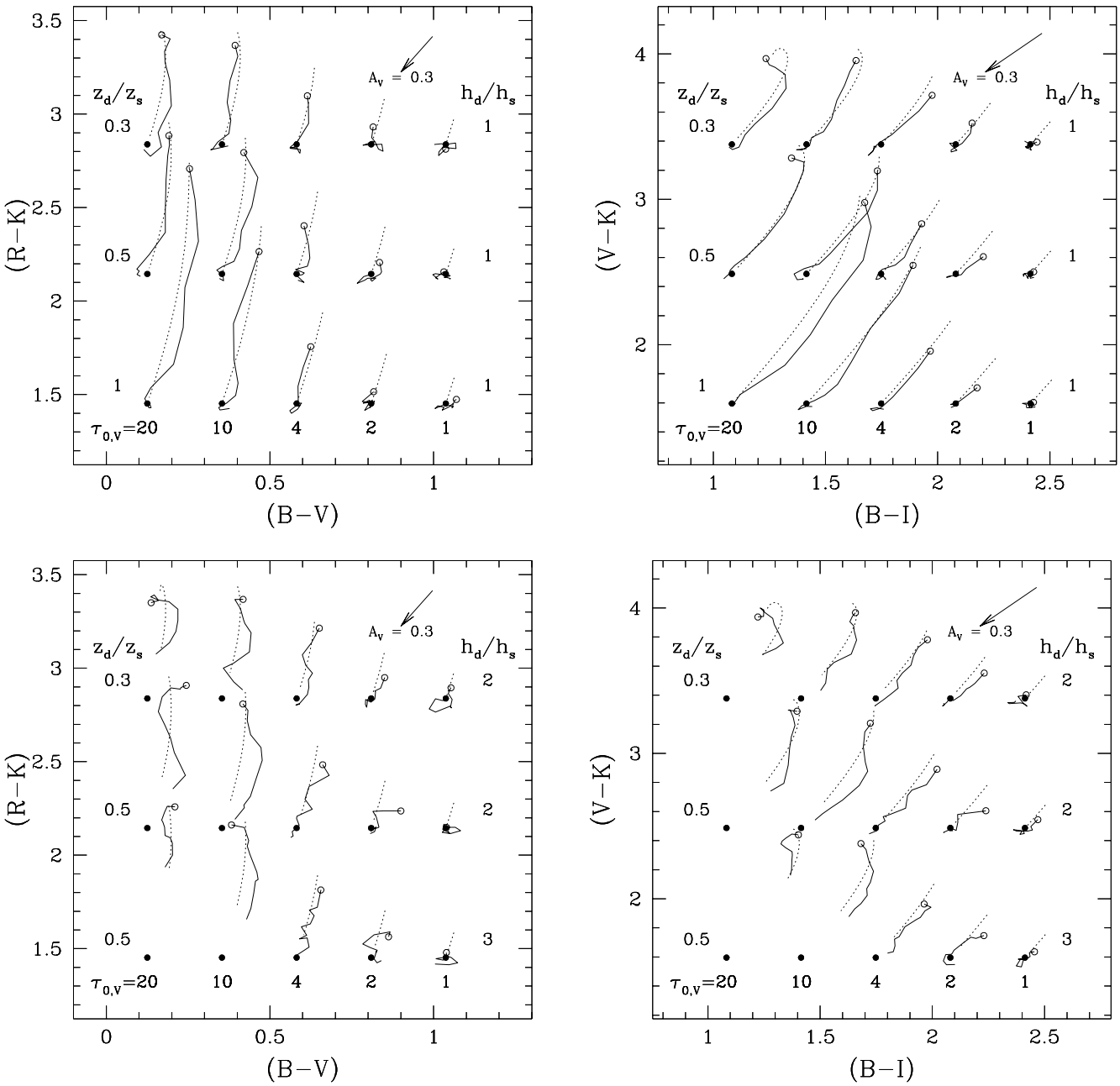

Fig. 4. Color–color plots resulting from dust models of face-on galaxies. The color zero-points are arbitrary (depending on the color of the underlying stellar population) and are indicated by the filled circles. The centers of the model galaxies are indicated by the open circles and the colors are followed in radial direction for four and a half scale lengths. The solid lines are the results from the Monte Carlo simulations, described in Appendix A. The dotted lines are the results from the DDP models, using the Galactic absorption law rather than the extinction law between the different passbands. The reddening vectors in the top right corners indicate the Galactic extinction law (ie. Screen model).

do agree on the two main parameters determining the integrated colors of a synthesized galaxy. First of all the colors are strongly determined by the colors of the youngest population, thus by the SFH, and secondly the colors are considerably affected by the metallicities of the populations. In Section 1 it was noted that both these SFH and metallicity changes have been observed on a radial scale in spiral galaxies. Furthermore, the radial age and metallicity gradients in our own Galaxy are well known and have been extensively studied (Gilmore et al. 1989; Matteucci 1989, 1992 and references therein). Synthesis models incorporating both age and metallicity effects are needed in the comparisons with spiral galaxy data.

The population synthesis models of Bruzual & Charlot (1993, BC models hereafter, see also Charlot & Bruzual 1991) and of Worthey (1994, W94 models hereafter) are used in the remainder of this paper; they are shown in the color–color diagram of Fig. 5. The BC models are based on the isochrone tracks of the Maeder & Meynet group (1991; Schaerer et al. 1993 and references therein) and on an empirical stellar flux library. The BC isochrone synthesis approach makes calculation of the very early stages of evolution of a population

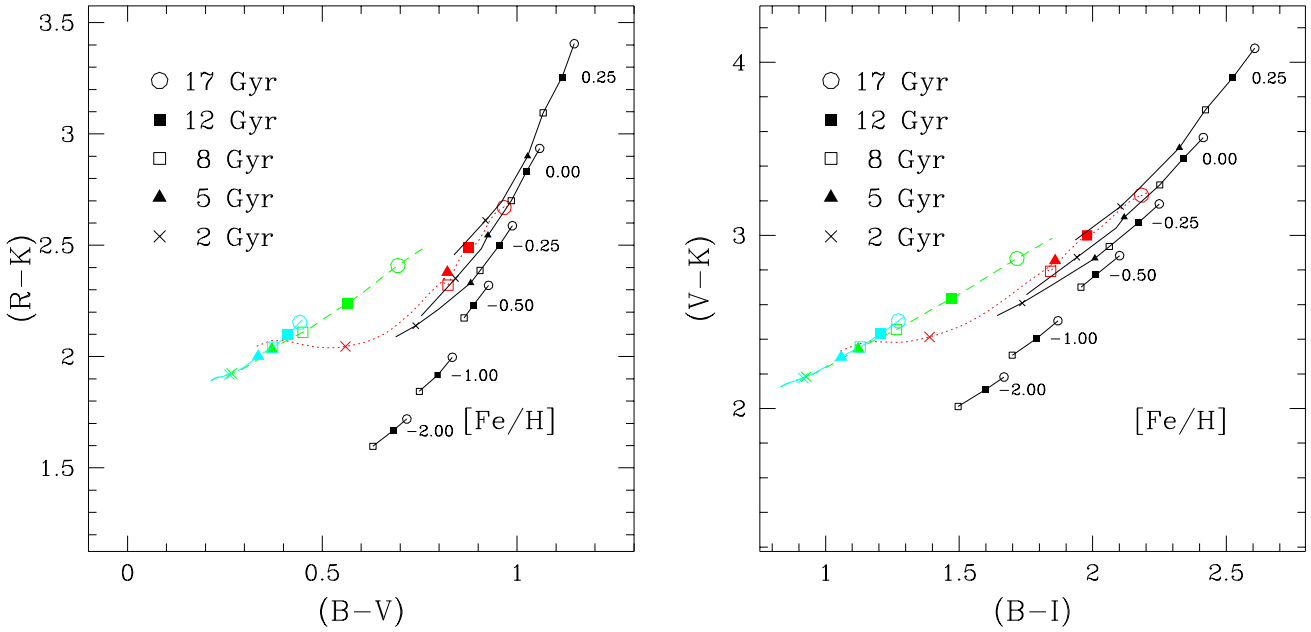

Fig. 5. Evolutionairy color–color plots of stellar synthesis models. The symbols indicate the number of years after creation of this population. To the right in each panel, connected by full drawn lines, are the single burst models of Worthey (1994) for different metallicities. The corresponding [Fe/H] values are indicated next to them. To the left in each panel are the solar metallicity models of Bruzual & Charlot (1993). The dotted line indicates the single burst evolution. The dashed line is a model with an exponentialy declining star formation rate. The leftmost dot-dashed line indicates a model with constant star formation. Bruzual & Charlot used the Johnson R and I passbands which were here converted to Kron-Cousins R and I passbands using the equations of Bessell (1979).

possible. The W94 models are constructed from the isochrones of VandenBerg (1985) and the Revised Yale Isochrones (Green et al. 1987) and use a theoretical stellar flux library. A different approach was followed in the BC and W94 models to calculate the integrated spectra of an evolving stellar population, but the main difference of interest here is the regions of age-metallicty parameter space that were investigated. The BC models were only calculated for solar metallicity, but give colors of populations as young as 1.26×10^5yr. The W94 models span a wide range in metallicity, but the youngest population is 1.5 Gyr.

3.2.2 SFH in color–color diagrams

Three evolutionary tracks of the BC models are shown in Fig. 5. The simplest is the single burst model, in which the color evolution of one initial starburst is followed in time. In the other two tracks this single burst model has been convolved in time to yield color evolution for different star formation histories. In one model an exponentially declining SFR with a time scale of 5 Gyr was used, in the other model the SFR was held constant. These models show the importance of the very early stages of stellar evolution. The constant SFR model at 17 Gyr is as blue in B–V and B–I as the exponentially declining model at 8 Gyr and the single burst model at 1.5 Gyr! The early stages of stellar populations are extremely luminous and a small percentage of young stars can give the total population a much younger appearance. Still, a solar metallicity starburst cannot produce colors to the right of the indicated single burst line in Fig. 5, because the colors of very young populations (age $<$1.5 Gyr, not shown) all lie to the left of (or in the direction of) the single burst trend.

The BC models used here have a Salpeter IMF (Salpeter 1955) with lower and upper mass cutoffs at 0.1 $M_\odot$ and 65 $M_\odot$ respectively. The use of a different IMF or other cutoffs has only a small effect compared to the main factors determining the colors of a synthesized population, namely age (or SFH) and metallicity. A discussion of the effects on color produced by the other parameters used in these models can be found in W94.

3.2.3 Age and metallicity in color–color diagrams

Of the W94 models, only the single burst models of different metallicities are shown in Fig. 5. The synthesis method of W94 prevents calculation of the very early evolution stages of a stellar population. Young populations are especially hard to synthesize for the lower metallicities, simply because there are no young, low metallicity stars in the solar neighborhood that can be used as input stars for the models.

The lower metallicity populations of the W94 models are clearly bluer in all color combinations. Age and metallicity are not complete degenerate. The offset in optical–near-IR colors is slightly larger than the offset in optical–optical colors. A low metallicity system can be recognized by its blue V–K or R–K color with respect to its B–V and B–I colors. When mixing populations of different age and metallicity the model grid points can be more or less added as vectors and then age and metallicity are degenerate. An individual galaxy can never be pinpointed to a certain age and metallicity using broadband colors.

The single burst BC and W94 models are clearly offset from each other. The solar metallicity BC model is probably

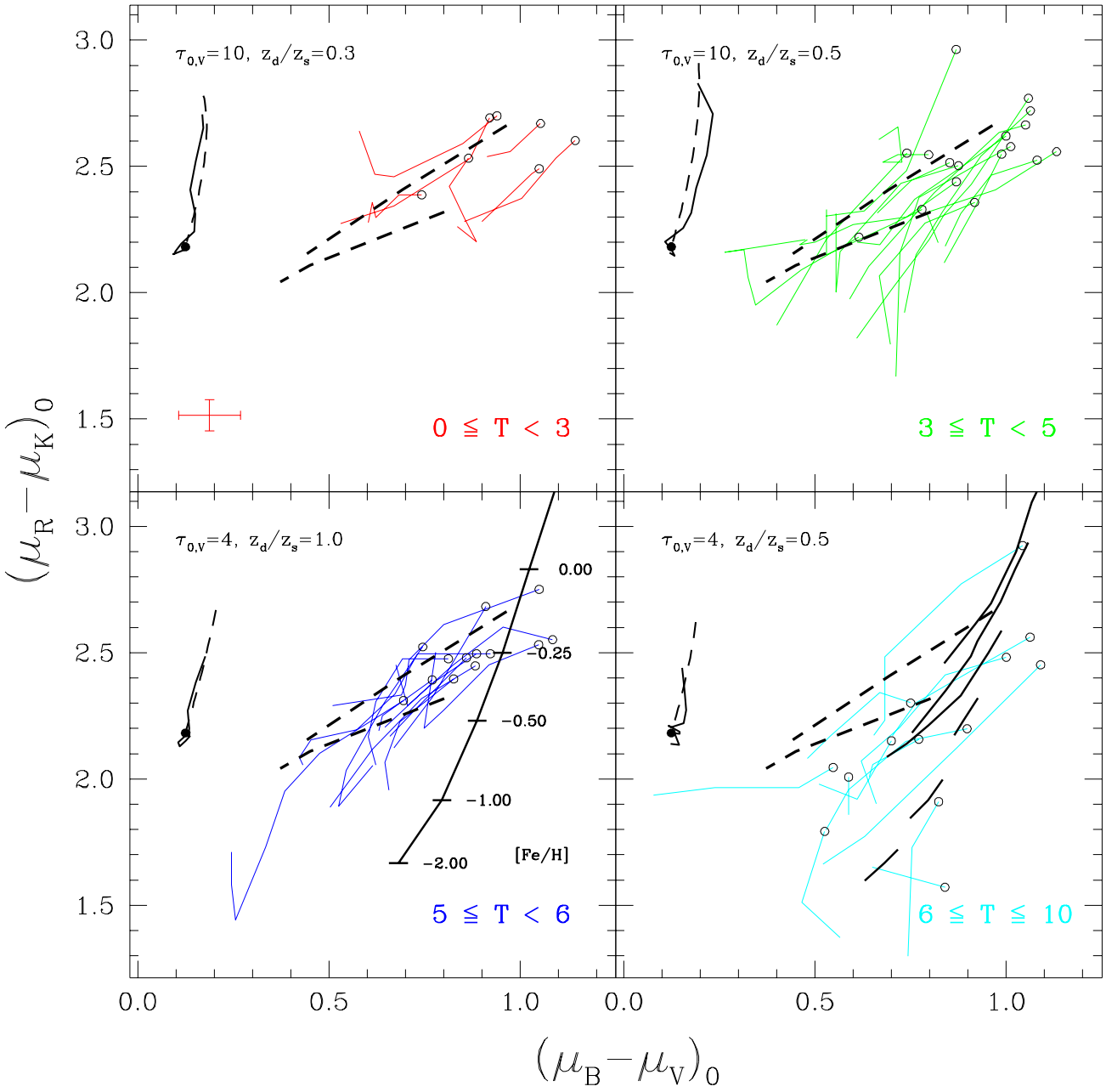

Fig. 6. The B–V versus R–K color–color plots of the program galaxies divided into the four morphological type bins indicated at the bottom-right of the panels. The centers of the galaxies are indicated by the open circles; the thin lines follow the color profiles in radial direction in steps of 1 K passband scalelength. At the bottom-left of the $0 \leq T \leq 3$ panel, the typical rms error in the zero-point calibration is indicated. Some of the dust models of Sect. 3.1 are plotted in the top-left of the panels. The thick dashed lines in the center of the panels connect the 17 Gyr and the 8 Gyr points of the BC models presented in Sect. 3.2. In the $5 < T \leq 6$ panel the 12 Gyr single burst W94 models for different metallicities are connected, the marks indicate the [Fe/H] values. The thick solid lines in the $6 < T \leq 10$ panels represent the W94 models. Points of equal metallicity, but different age are connected.

best matched by the [Fe/H] $= -0.25$ W94 model. These kinds of differences between different models have been noticed (Charlot & Bruzual 1991; W94) and are generally attributed to differences in treatment of late stages of stellar evolution. It is therefore better not to look at the absolute values of the different models, but only at the relative trends in color space. The BC models will be mainly used to investigate trends in SFH, because contrary to the W94 models, they incorporate the very early stages of stellar evolution. To compare with the data, I will connect the 8 Gyr points of the different SFH BC models and do the same for the 17 Gyr points. These connected data points will indicate the color trends for equally old populations with different SFHs. The W94 models have to be used to look at the effects caused by metallicity, because different metallicities are not available in the BC models.

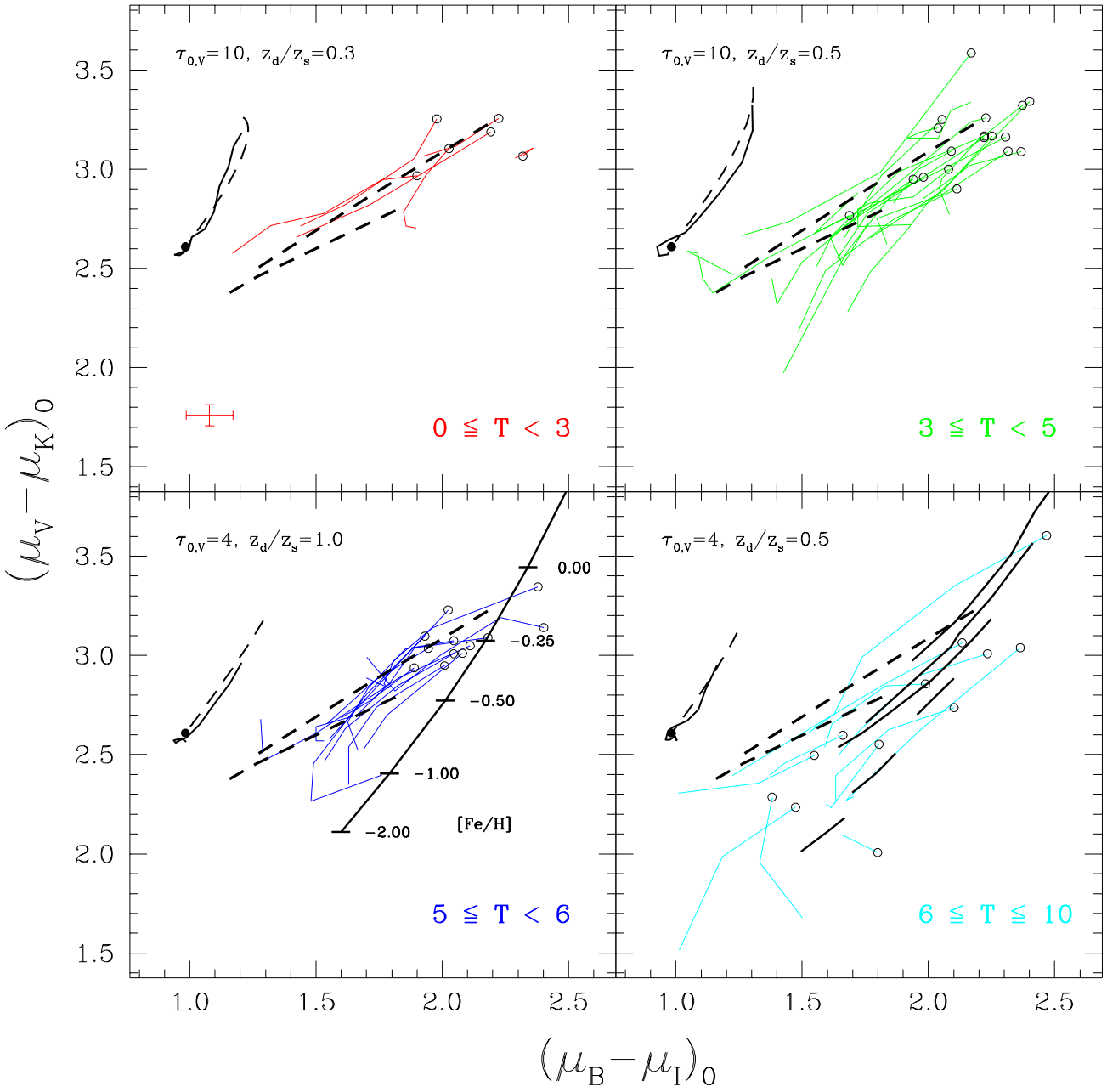

Fig. 7. Same as Fig. 6, but for B–I versus V–K.

3.3 Color gradients; measurements versus models

In this section I first use color–color diagrams to display the observations. I then try to explain the observed color gradients by comparing these measurements with the dust models, the different SFH synthesis models, and finally the full population synthesis models, that incorporate both age and metallicity effects.

3.3.1 The measurements in color–color diagrams

The color–color profiles of the galaxies are presented in Figs 6 and 7. The data were smoothed to reduce the noise in the profiles. The first data point (at the open circle) is the average over the inner half scalelength (in the K passband) of the luminosity profiles, the other points are averages moving outward in steps of one K scalelength. The uncertainty of the inner point is dominated by the zero-point uncertainty of the calibration and is indicated at the bottom of the top-left panels of Figs 6 and 7. In the blue direction of the color–color profiles, lower surface brightnesses are traced (see Fig. 2) and errors are dominated by sky background uncertainties. Strange kinks at the blue ends of the profiles should thus not be trusted.

The profiles of galaxies with T≤6 are confined to a small region in the color–color plots. The colors of a galaxy as function of radius are strongly correlated. The scatter is slightly larger than the average zero-point error. The central colors of the galaxies become on average a little bit bluer going from T=0 to T=6, but they follow the main trend.

The galaxies with morphological classification T>6 clearly deviate from the main trend. Their central colors range from the normal red to extreme blue, even bluer than the bluest outer parts of the earlier type galaxies. The spread in the color–color diagram is also significantly larger. Some of the late-type galaxies have very blue V–K and R–K colors for their B–V and B–I colors, especially when compared to the earlier types.

When comparing models with the data one should realize that as soon as a model for a galaxy has been chosen, it should be applied to all color combinations. In particular, the same model should be used in both Figs 6 *and* 7. It is tempting to propose one single model for *all* galaxies, because the profiles are confined to a small region in the diagrams. We only need to explain the offsets from the main trends with additional parameters.

3.3.2 Measurements versus dust models

The reddening profiles produced by the dust models are indicated on the left in the panels of Figs 6 and 7. The color of the underlying stellar population is arbitrary and thus the dust profile can be placed anywhere in the diagram. The dust models have a distinct direction in the color-color diagrams independent of the dust configuration, as explained in Sect. 3.1. This direction is clearly different from the general trend of the data and therefore the whole gradient cannot be produced entirely by the dust reddening. A small fraction of the color gradients could be due to dust reddening, but an additional component is needed to explain the full gradient. This does not mean that there could not be large amounts of dust, but rather that the color gradients are not mainly caused by dust reddening. If the dust is not diffuse, but strongly clumped into clouds the amount of reddening is strongly reduced. It could be that a large fraction of the most luminous stars is embedded in dust clouds. This will not induce a color gradient or an inclination dependent extinction effect, but will give the total color profile an offset in the general direction of the calculated dust models. The "dusty nucleus" models of Witt et al. (1992) give an even better indication of the expected offset vector if the luminous stars are embedded in dust clouds.

3.3.3 Measurements versus metallicity effects

To what extent can metallicity differences in the stellar populations account for the color gradients? The 12-Gyr-old W94 single burst models for different metallicities are connected in the 5<T≤6 panels of Figs 6 and7. Models at other ages follow the same direction in color space. The single-age, different-metallicity model does not match the data for most of the galaxies. Again another component is needed to explain the color gradients; the radial metallicity differences alone are not sufficient. It is important to note that population models cannot be arbitrarily shifted, they predict fixed colors for a given SFH and metallicity.

3.3.4 Measurements versus SFH

The BC models are indicated by dashed lines in Figs 6 and 7. The 8 Gyr points of the models have been connected as well as the 17 Gyr points. The reddest ends of these lines indicate single burst models, the bluest ends represent constant SFR models. In between is a model with an exponentially decreasing SFR with a time scale of 5 Gyr. The galaxy data for T≤6 systems seem to be reasonably well matched by the 17 Gyr models. Still most galaxies are slightly offset to the blue in the V–K and R–K colors. This could be remedied by taking a 12 Gyr model (somewhere in between the 8 and 17 Gyr models), but then most of the galaxy centers are even redder than predicted by the single burst model. Because we know that galaxies still have star formation in their centers, this is an unlikely situation. The conclusion has to be that although SFH variations as function of radius seem a good driving force for radial color gradients, alone they cannot explain the full gradients. This is especially true for the galaxies with T>6, which have V–K and R–K colors too blue to be explained by the solar metallicity BC models.

3.3.5 Measurements versus both age and metallicity effects

The W94 models in the 6<T≤10 panel indicate that the very blue galaxies in this panel can be described very well by low-metallicity stellar synthesis models. As with the earlier type galaxies, the radial color trends are reasonably well described by age differences, but at all radii lower metallicities are needed for most of the galaxies. A number of them are so blue in all color combinations that their stellar components must be young and of low metallicity.

Galaxies are known to have radial metallicity gradients in their current gas content (Villa-Costas & Edmunds 1992, hereafter VE; Zaritsky et al. 1994, hereafter ZKH), and have radial SFRs that are not linearly correlated with their radial stellar surface brightness, which means they do not have one SFH as function of radius (Ryder & Dopita 1994). As long as there are no consistent stellar population synthesis models that incorporate very young stellar evolutionary stages at all metallicities, it is difficult to make quantitative statements about the observed colors and color gradients of the galaxies.

Limits can be set on the models using the metallicity measurements collected by VE and ZKH. Recall that metallicity measurements yield the current gas metallicities in H II regions, so that the underlying stellar component could have completely different metallicity values. For galaxies T<6 the 12+log(O/H) values run from ∼9.3 in the center to ∼8.6 at R_{25}. The O/H indices of later type galaxies are a few tenths lower, from about 8.9 to 8.2, but with more or less the same gradient across the disk. Using $\log(\mathrm{O/H})_\odot \simeq -3.08$ (Grevesse & Anders 1989) and [O/Fe]$\simeq 0.1\sim0.5$ (e.g. Wyse & Gilmore 1994) the O/H values can be transformed to [Fe/H] values and used with the W94 models. The [Fe/H] values run from about a central 0.2 to –0.6 in the outer regions in galaxies with T<6, and from approximately –0.1 to –1.1 in the later type galaxies.

The mettalicities just calculated should not be taken too literallyly in the comparison of the W94 models with the data in Figs 6 and 7. As noted before, models should be used to indicate trends in color–color space but cannot be expected to give absolute colors in an individual galaxy. Still, the B–V and B–I colors are far too red at each radius using the 12 Gyr W94 models using [Fe/H] = 0.2 to -0.6, the metallicity range

determined from the H II regions. This must mean that either the underlying stellar populations have a much lower average metallicity than the surrounding gas or that at each radius a much younger stellar population is present, making the average age lower than 12 Gyr. In the center, the contribution of the young stars cannot be very large, because the color vector of SFH (indicated for solar metallicity by the BC models) is in the wrong direction. Therefore the center probably contains a mix of populations of different metallicities, with an average metallicity far lower than the current metallicity of the surrounding gas. In the outer parts of galaxies, the SFH color vector gives an excellent description of the observed colors. It is unlikely that the metallicity of the stars in the outer regions of all galaxies is much higher than that of the gas, thus the color gradients are probably driven by a combination of SFH and metallicity differences as function of radius. The outer parts of galaxies are clearly younger on average than the central regions. If part of the color gradients is also caused by reddening, the age effect must even be larger, because this is the only effect that has a color vector that can compensate the dust color vector.

In conclusion, the centers of spiral galaxies with T≤6 contain probably a relatively old population of stars, with a range in metallicities. The populations in the outer regions are on average much younger and their metallicity is probably lower, as the gas metallicity is much lower than the metallicity needed to explain the central colors. Overall, later type galaxies have lower metallicity, and a number of them are dominated by very young, low-metallicity populations. The observed color gradients cannot be caused by reddening alone, if the dust properties used in the models are more or less correct. Age gradients across the disk have to be even larger if reddening is important. It should be noted that the population models can predict *both* the right colors and the right color gradients within one system of models, while the dust models can at best explain only the color gradients.

4 Colors and the structural galaxy parameters

Most of the information that can be extracted from the galaxy colors of this data set is contained in the previous sections, but for most data sets such detailed radial color information is not available. In order to allow comparisons with these other data sets, a number of relationships between colors and fundamental galaxy parameters are shown in this section.

In the previous section I argued that color gradients derived from different passband combinations are correlated in such a way that stellar population differences seem to be the most reasonable explanation of the phenomenon. Figure 2 suggests that the slope of the color gradient has a universal value for all galaxies, but this is an oversimplification.

The change in scalelength (h_λ) as function of passband can be used to parameterize color gradients in the disk. The bulge/disk decomposition technique and the method used to determine the central surface brightnesses and scalelengths for the current data set were described in Paper II. A trivial recalculation shows that each axis of Fig. 8 indicates approximately the color change per scalelength in the relevant passband combinations. This figure illustrates again that color gradients are correlated, but also that there is no universal value for the gradient for all galaxies. The values range from about 0.1 to –0.8 mag per scalelength in B–K.

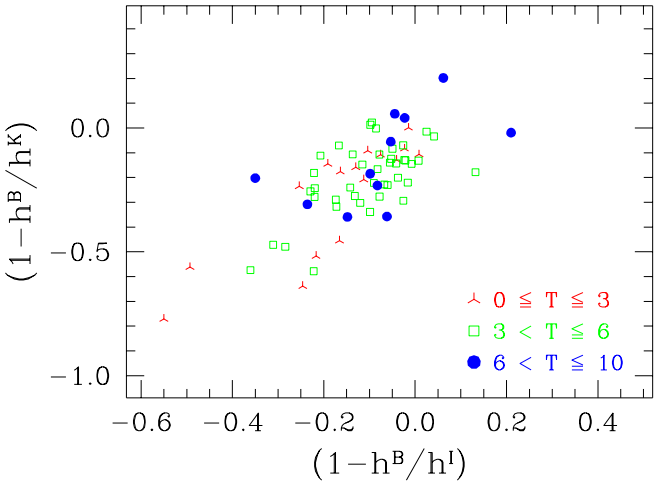

Fig. 8. The difference in scalelength between the different passbands. Only points with errors smaller than 0.15 are plotted. Different symbols are used to denote the indicated morphological types.

The changes in scalelength were used to find correlations between the steepness of the color gradient and other structural galaxy parameters. A large number of structural parameters were investigated, but none of them showed a correlation with color gradient. The parameters investigated include: inclination, morphological type, central surface brightness, scalelength, bulge-to-disk ratio, integrated magnitude, integrated colors, bulge color, bar versus non-bar, H I and CO fluxes, far-infrared IRAS fluxes and colors, group membership and rotation velocity. Fluxes at the different wavelengths normalized by area or integrated K passband flux were also used in the correlations, but with a negative result. A weak correlation was found only between the steepness of the color gradient and the central surface brightness color of the disk.

In the literature integrated colors of galaxies are usually used to determine galaxy properties. The integrated colors as function of type are presented in Fig. 9 and Table 1 for this galaxy sample. There is a clear correlation between type and color, but the scatter is large. The integrated color of a galaxy is dominated by the color of the central region and even though color correlates with (central) surface brightnesses (Fig. 2), one should note that each morphological type comes in a range of central surface brightnesses (Paper III) which then explains the large scatter in the integrated colors. It is better to determine and compare the colors of galaxies at a fixed isophote when looking for correlations.

In Fig. 10, the central bulge and disk colors of the galaxies are compared. The colors of bulge and disk are clearly correlated. This could be expected, as most color profiles show no clear changes in color gradient in the bulge region. Excluding the three deviant points with bulge B–K colors bluer than 2 mag, the bulge is on average 0.14±0.55 mag redder in

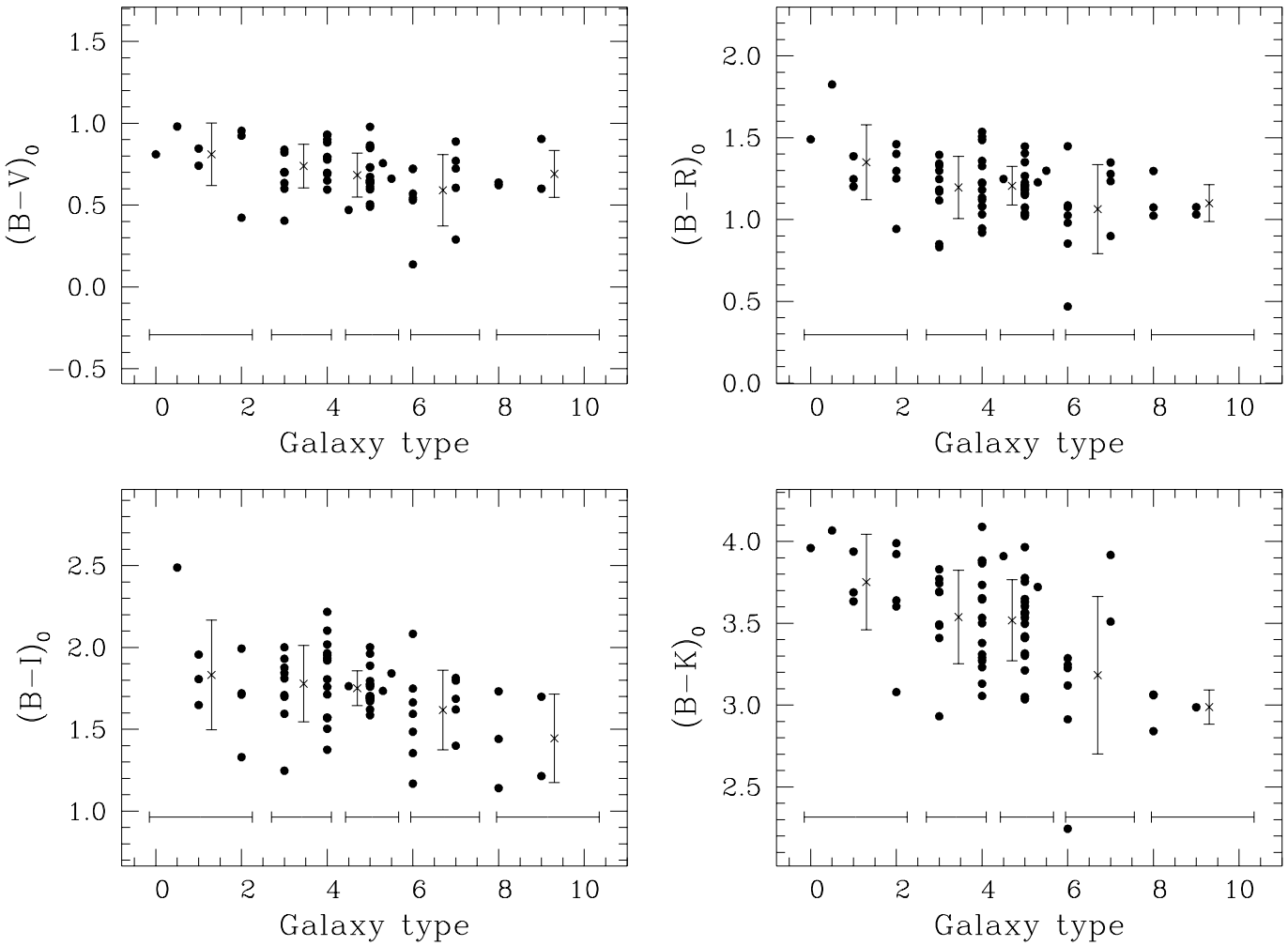

Fig. 9. The Galactic reddening corrected integrated colors of the galaxies as function of morphological type index. The crosses show the values averaged over the bins indicated by the horizontal bars. The vertical bars are the standard deviations on the mean values. Only the galaxies with an error of less than 0.5 mag in their color were used in these diagrams.

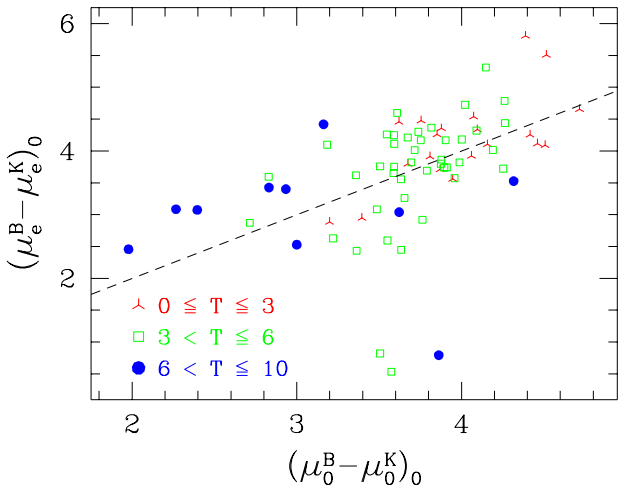

Fig. 10. The central surface brightness B–K color of the disk versus the effective surface brightness B–K color of the bulge. Different symbols are used to denote the indicated morphological type ranges. The dashed line indicates the line of equality.

B–K than the central disk color, which means that the stellar populations probably do not differ very much.

5 Discussion

An important consequence of the color differences in and among galaxies is the implied change in the M/L_λ values. The comparison of the data with the dust and stellar population models indicates that the color gradients in the galaxies of this sample result mainly from population changes and that dust reddening only plays a minor role. The M/L_λ values corresponding to the synthesis models presented in Figs 6 and 7 are listed in Table 2.

In every passband, young populations have much lower M/L_λ values than old populations. Young populations still contain very massive stars, which are very luminous for their mass, but expend their energy quickly. Continually adding in young populations, as done in the exponentially declining and constant SFR BC models, decreases the M/L_λ values drastically. Young massive stars are blue so that this effect is most pronounced in the B passband. The change in M/L_B is

Table 1. The integrated colors for different morphological type ranges using only the photometric observations of Paper I with errors in the colors less than 0.5 mag.

RC3 type	#	$B–V$	#	$B–R$	#	$B–I$	#	$B–H$	#	$B–K$
$0 \leq T \leq 2$	7	0.81 ± 0.19	10	1.35 ± 0.22	8	1.83 ± 0.31	6	3.46 ± 0.21	10	3.75 ± 0.28
$2 < T \leq 4$	14	0.74 ± 0.13	26	1.20 ± 0.19	24	1.78 ± 0.23	6	3.14 ± 0.34	26	3.53 ± 0.28
$4 < T < 6$	19	0.67 ± 0.15	19	1.20 ± 0.13	20	1.75 ± 0.10	10	3.28 ± 0.14	21	3.51 ± 0.26
$6 \leq T < 8$	11	0.59 ± 0.21	11	1.06 ± 0.26	12	1.61 ± 0.23	3	2.96 ± 0.62	8	3.18 ± 0.45
$8 \leq T \leq 10$	4	0.69 ± 0.14	5	1.10 ± 0.10	5	1.44 ± 0.24	0	—	4	2.99 ± 0.09

about a factor of 6-11 between the 2 and 17 Gyr models and a factor of 3-5 between the single burst and the constant SFR BC models.

Metallicity has an entirely different effect on the M/L_λ ratios. The M/L_B values increase with metallicity, while the M/L_K values decrease with metallicity. The turnover point is somewhere between the I and the J passband. This was the motivation for W94 to recommend the I passband for standard candle work and for studies of M/L in galaxies.

The recommendation of the I passband is not entirely obvious, because the choice of optimum passband depends on whether one expects extinction, age or metallicity to have the largest influence on the photometry. If extinction is expected to play a role, the K passband should be used, as the extinction in the K passband is $\sim$4 times less than the extinction in the I passband. The K passband should also be preferred if differences in SFR are expected to be important; see for instance the change in M/L_λ ratios of the different BC models. One should turn to the I and J passbands only when the metallicity differences among the different objects are large.

Table 2. The M/L_λ values in solar units for the models presented in Section 3.2. For the BC models single burst models (s.b.), exponential declining SFH models (exp.) and constant SFR models (cnst.) are listed. The single burst models of W94 are listed for several different metallicities.

age	BC models			W94 models					
Gyr	s.b.	exp.	cnst.	[Fe/H]= –2	–1	–0.5	–0.25	0.0	0.25
				B passband					
2	0.90	0.82	0.30	—	—	—	1.52	1.73	2.42
5	3.13	1.02	0.67	—	—	—	3.32	3.95	5.26
8	4.33	1.42	1.02	2.60	3.39	4.16	5.19	5.96	8.05
12	5.70	2.25	1.43	3.71	4.81	6.26	7.41	8.70	11.95
17	9.91	4.02	1.88	5.01	6.45	8.53	12.28	10.54	17.15
				I passband					
2	1.27	1.25	0.79	—	—	—	1.09	1.03	1.24
5	2.26	1.29	0.91	—	—	—	1.86	2.00	2.21
8	2.82	1.57	1.28	2.34	2.53	2.45	2.67	2.77	3.08
12	3.23	2.07	1.68	3.04	3.30	3.50	3.58	3.60	4.17
17	4.71	2.95	2.13	3.84	4.10	4.39	4.73	4.74	5.54
				K passband					
2	0.43	0.65	0.24	—	—	—	0.52	0.42	0.42
5	0.80	0.62	0.44	—	—	—	0.78	0.72	0.60
8	1.13	0.74	0.62	1.70	1.50	1.16	1.12	0.86	0.75
12	1.15	0.87	0.78	2.10	1.88	1.81	1.35	1.06	0.87
17	1.54	1.13	0.93	2.59	2.21	1.90	1.69	1.29	1.04

What influence do the current observations have on studies depending on M/L_λ ratios? I address two issues here: rotation curve fitting and the TF-relation.

The principle of rotation curve fitting is simple. One tries to explain the distribution of the dynamical mass of a galaxy by assigning masses to its known "luminous" (at whatever wavelength) components. The dynamical mass distributions can be determined from optical rotation curves along the major axis (e.g. Rubin et al. 1985; Mathewson et al. 1992) or, more sophisticatedly, from H I or other two-dimensional velocity fields (e.g. Bosma 1978; Begeman 1987; Broeils 1992). The mass assignment to the H I and other gas components is relatively straightforward, but the mass assignment to the stellar components has proven troublesome. Generally, M/L values have been assigned to the different stellar components (bulge and disk) using the maximum disk hypothesis (van Albada et al. 1985; van Albada & Sancisi 1986). This exercise revealed the "missing mass" problem: the dynamical mass of a galaxy is much larger than the maximum "luminous" mass, with the main discrepancy in the outer regions.

In the game of rotation curve fitting, one often encounters the use of B or at best R passband luminosity profiles. Table 2 clearly illustrates the danger of using these passbands, especially if one considers the color gradients observed here. Independent of whether the observed color gradients are caused by age or metallicity gradients (or by reddening for that matter), the M/L_B ratios will be much higher in the center than in the outer regions. Consequently the "missing mass" discrepancy between inner and outer regions is even larger than estimated by the use of the B passband profiles together with a constant M/L. So what is the optimum passband to be used for rotation curve fitting?

Following the conclusions of Section 3.3, let us assume that the central region of a $T \leq 6$ galaxy consists of old stellar populations with a range in relatively high metallicities, say on average [Fe/H]=0 and t=12 Gyr. It is not likely that the metallicity of the stars in the outer regions is higher than that of the gas. The outer populations are younger than the inner populations and let us assume that their average parameters are [Fe/H]=–0.5 and t=8 Gyr. Table 2 shows that M/L_B changes by a factor 2.09 for those two populations, M/L_I by a factor 1.47, and M/L_K by a factor 0.91. Repeating this exercise for lower-metallicity late-type systems gives similar results. As long as the outer regions of galaxies are younger than the inner regions (and the example used was not very extreme), the K passband is the optimum choice for rotation curve fitting. This

is especially true if extinction plays a role, which is expected to be the case for the highly inclined galaxies normally used for rotation curve fitting.

The M/L effects on integrated magnitudes (as used in the TF-relation) are less trivial. In Section 1 it was argued that the integrated colors are dominated by the central colors of galaxies. In Figs. 6 and 7 the open circles indicate the central colors of the galaxies and are therefore representative of the integrated colors. For the T$\leq$6 galaxies, the central colors follow the same trend as the color gradients within galaxies (as might be expected from Fig. 2) and therefore the same argument as for rotation curve fitting can be applied to recommend the K passband for TF-relation work. Note that the differences in central color in the bins of T$\leq$6 are much smaller than the differences within the galaxies themselves and a small color correction term would be sufficient to translate all galaxies to a common M/L scale. The central colors of T$>$6 galaxies show a different distribution in color-color space. They come in a wide range of ages and metallicities and their M/L_K values can easily differ by a factor of two and by a factor of four in M/L_I. This would introduce an uncertainty of $\sim$0.75 K-mag or $\sim$1.5 I-mag in the TF-relation respectively, if one would simply assume that the TF-relation is tracing the connection between luminous mass and dynamical stellar mass. A two-color correction might then be needed to reduce the scatter in the TF-relation if late-type galaxies are also included in the sample. Because the scatter in the TF-relation is often much smaller than the indicated values, one may conclude that the TF-relation is not simply tracing the connection between luminous mass and dynamical stellar mass, and that the amount of dark matter is varying systematicly with galaxy color. But in short, a shift along one vector in Figs 6 and 7 is sufficient to bring the centers of most T$<$6 galaxies to one point, at least two vectors are needed to bring the centers of the T$\geq$ 6 galaxies to one point.

A large number of galaxy formation and evolution theories predict metallicity gradients (for references see e.g. VE and Matteucci 1989, 1992) and age gradients (Kennicutt 1989; Dopita & Ryder 1994 and references therein) in galaxies. Several predict both at the same time, like viscous galaxy evolution models (Lin & Pringle 1987; Sommer-Larsen & Yoshii 1990), the models of Wyse & Silk (1989) and various gas infall and galaxy merger models. The young, low metallicity late-type systems observed here would be ideal merger candidates to replenish the outer regions of large galaxies with nearly unprocessed gas from which new stars can be formed. A detailed study of all possible models, investigating time scales and metallicity ranges involved, is beyond the scope of this work.

A key question that is not addressed in this investigation is whether the color gradients originate in the arm or in the interarm region, or are present in both regions. High resolution and high signal-to-noise observations are needed to solve this question, and the present data set is not suited for such an investigation. A detailed study of a few large nearby galaxies is in preparation (Beckman et al., private communication).

The current observations have a high enough signal-to-noise ratio to study the central regions of the galaxies in more detail. Several galaxies show circumnuclear activity, which already leave their mark in the color profiles (though one has to be careful not to mistake the seeing differences between the different passbands as a sign for a blue nucleus). Some galaxies are worth mentioning as their activity is clearly visible on the color maps. UGC 89 has a blue ring around the center, cut in two halves by the red dust lane running over the bar. UGC 2368 has a blue nucleus surrounded by a red dust ring coming from the strong bar. UGC 4422 has a blue ring around the nucleus. The highly asymmetric galaxy UGC 5510 probably has a blue nucleus, but is it is barely resolved. UGC 5554 has a blue circumnuclear region and some very blue knots in the arms. UGC 6077 probably has a blue nucleus surrounded by a red (dust?) ring. UGC 7450 (M 100) is known to have central activity (note that the central region was saturated on our R and I images) and is described in detail by Knapen et al. (1995a, 1995b). UGC 12391 and UGC 12614 probably have blue nuclii. UGC 12808 has a blue circumnuclear ring. The galaxies UGC 3066, UGC 4256, UGC 6028, UGC 12614 and UGC 12808 have very blue arms. Most of these galaxies have strong bars, are asymmetric, or are interacting.

In this paper I have showen that broadband color gradients of galaxies provide information on their stellar and dust content. The behavior of the color gradients resembles the properties of the metallicity gradients of galaxies, especially in that the steepness of the gradients show very little correlation with any other galaxy parameter (see e.g. VE). It would be interesting to compare the color gradients with the metallicity gradients of individual galaxies. Even more insight would be obtained if spectroscopy could be used to obtain information on the ages and metallicities of the stellar components and not just on the metallicity of the H II regions.

The amount of dust and its distribution in galaxies is still controversial. New instruments like SCUBA on the JCMT and the ISO infrared satellite enable direct imaging of the coldest dust components. It will be interesting to investigate whether there is a relation between the color gradients observed here and the properties of the dust.

A final point of interest is the behavior of colors and color gradients as function of time. With the refurbished HST accurate surface photometry can be obtained of galaxies at large lookback times. The current sample is an ideal local reference sample for such observations.

6 Conclusions

The stellar and the dust content of a large sample of galaxies was investigated using the color profiles of these galaxies. Data in four optical and two near-IR passbands were combined simultaneously to derive structural properties of the sample as a whole, rather than for individual galaxies. The main conclusions are:

- Almost all spiral galaxies become bluer with increasing radius.
- The colors of galaxies correlate strongly with surface brightness, both within and among galaxies. The morphological type is an additional parameter in this relationship,

because at the same surface brightness late-type galaxies are bluer than early-type galaxies.
– Realistic 3D radiative transfer modeling indicates that reddening due to dust extinction cannot be the major cause of the color gradients in face-on galaxies. The predicted color vectors in color–color space are not compatible with the data, unless the assumed scattering properties of the dust are entirely wrong.
– The color gradients in the galaxies are best explained by differences in SFH as function of radius, with the outer parts of galaxies being on average much younger than the central regions. This implies that the stellar scalelength of galaxies is still growing. The central stellar populations in a galaxy must have a range in metallicities to explain the red central colors of the galaxies.
– A consequence of the population changes implied by the color differences in and among galaxies is that there are large changes in M/L values in and among galaxies. These changes in M/L make the missing mass problem in spiral galaxies as derived from rotation curve fitting even more severe.
– The H and K passbands are recommended for standard candle work and for studies depending on M/L ratios in galaxies.

Acknowledgements. Many thanks to Stephane Charlot and Guy Worthey for providing machine readable versions of their stellar population synthesis results. I thank Edwin Huizinga for discussing and checking the dust models. I would like to thank Erwin de Blok, Thijs van der Hulst, Piet van der Kruit, René Oudmaijer, Penny Sackett and Edwin Valentijn for their stimulating discussions and the many useful suggestions on the manuscript.

References

Aaronson M. 1978, ApJ 221, L103
Andredakis Y.C., van der Kruit P.C. 1992, A&A 265, 396
Aoki T.E., Hiromoto N., Takami H., Okamura S. 1991, PASJ 43, 755
Baade W. 1944, ApJ 100, 137
Begeman K. 1987, Ph.D. Thesis, University of Groningen, The Netherlands
Bershady M.A. 1993, PASP 105, 1028
Bessell M.S. 1979, PASP 91, 589
Block D.L., Witt A.N., Grosbøl P., Stockton A., Moneti A. 1994, A&A 288, 383
Bosma A. 1978, Ph.D. Thesis, University of Groningen, The Netherlands
Broeils A. 1992, Ph.D. Thesis, University of Groningen, The Netherlands
Bruzual G.A., Charlot S. 1993, ApJ 405, 538
Bruzual G.A., Magris G.C., Calvet N. 1988, ApJ 333, 673
Burstein D., Heiles C. 1984, ApJS 54, 33
Bushouse H.A., Stanford S.A. 1992, ApJS 79, 213
Buzoni A. 1989, ApJS 71, 817
Byun Y.I., Freeman K.C., Kylafis N.D. 1994, ApJ 432, 114
Charlot S., Bruzual G.A. 1991, ApJ 367, 126
Cornell M., E., Aaronson M., Bothun G., Mould J. 1987, ApJS 64, 507
de Jong R.S. 1995a, to be submitted to A&A **(Chapter 2)**
de Jong R.S. 1995b, to be submitted to A&A **(Chapter 3)**
de Jong R.S., van der Kruit P.C. 1994, A&AS 106, 451 **(Chapter 1)**
de Vaucouleurs G., de Vaucouleurs A., Corwin H.G., Buta R.J. et al. 1991, Third Reference Catalog of Bright Galaxies (Springer-Verlag, New York) (RC3)
Disney M.J., Davies J.I., Phillipps S. 1989, MNRAS 239, 939
Dopita M.A., Ryder S.D. 1994, ApJ 430, 163
Evans R. 1994, MNRAS 266, 511
Freeman K.C. 1970, ApJ 160, 811
Frogel J.A. 1985, ApJ 298, 528
Gilmore G., King I., van der Kruit P.C. 1989, The Milky Way as a Galaxy (Geneva Observatory, Sauverny-Versoix, Switzerland)
Giovanelli R., Haynes M.P., Salzer J.J., Wegner G., Da Costa L.N., Freudling W. 1994, AJ 107, 2036
Goudfrooij P., Ph.D. Thesis, University of Amsterdam, The Netherlands
Goudfrooij P., Hansen L., Jørgensen H.E., Nørgaard-Nielsen H.U., de Jong T., van den Hoek L.B. 1994, A&AS 104, 179
Green E.M., Demarque P., King C.R. 1987, The Revised Yale Isochrones and Luminosity Functions (Yale University Observatory, New Haven)
Grevesse N., Anders E. 1989, in: Cosmic Abundances of Matter, AIP Conference Proceedings 183, ed. C.J. Waddington (AIP, New York)
Han M. 1992, ApJS 81, 35
Henyey, L.G., Greenstein, J.L., 1941, ApJ, 93, 70
Huizinga J.E. 1994, Ph.D. Thesis, University of Groningen, The Netherlands
Jansen R.A., Knapen J.H., Beckman J.E., Peletier R.F., Hes R. 1994, MNRAS 270, 373
Kennicutt Jr. R.C. 1989, ApJ 344, 685
Kent S.M. 1984, ApJS 56, 105
Kent S.M. 1986, AJ 91, 1301
Kent S.M. 1987, AJ 93, 816
Knapen J.H., Hes R., Beckman J.E., Peletier R.F. 1991, A&A 241, 42
Knapen J.H., Beckman J.E., Heller C.H., Schlosman I., de Jong R.S. 1995a, ApJ submitted
Knapen J.H., Beckman J.E., Schlosman I., Peletier R.F., Heller C.H., de Jong R.S. 1995b, ApJL in press
Kraan-Korteweg R.C. 1986, A&AS 66, 255
Kylafis N.D., Bahcall J.N. 1987, ApJ 317, 637
Lauberts A., Valentijn E.A. 1989, The Surface Photometry Catalogue of the ESO Sky Survey (ESO, Garching) (ESO-LV)
Lin D.N.C., Pringle J.E. 1987, ApJ 320, L87
Maeder A., Meynet G. 1991, A&AS 89, 451
Mathewson D.S., Ford V.L., Buchhorn M. 1992, ApJS 81, 413
Mathis J.S. 1990, ARA&A 28, 37
Matteucci F. 1989, in Evolutionary Phenomena in Galaxies, eds. J.E. Beckman, B.E.J. Pagel (Cambridge University Press, Cambridge), p. 297
Matteucci F. 1992, in Morphological and Physical Classification of Galaxies, eds. G. Longo, M. Capaccioli, G. Busarello (Kluwer Academic Publishers, Dordrecht), p. 245
Nilson P. 1973, Uppsala General Catalog of Galaxies (Roy. Soc. Sci., Uppsala) (UGC)
O'Connell R.W. 1987, in Stellar Populations, eds. C. Norman, A. Renzini, M. Tosi (Cambridge University press, Cambridge), p. 167
Peletier R.F. 1989, Ph.D. Thesis, University of Groningen, The Netherlands
Peletier R.F., Davies R.L., Davis L.E., Illingworth G.D., Cawson M. 1990a, AJ 100, 1091

Peletier R.F., Valentijn E.A., Jameson R.F. 1990b, A&A 233, 62
Peletier R.F., Valentijn E.A., Moorwood A.F.M., Freudling W. 1994, A&AS 108, 621
Pickles A.J. 1985, AJ 296, 340
Renzini A., Buzzoni A. 1986, in Spectral Evolution of Galaxies, eds. C. Chiosi, A. Renzini (Reidel, Dordrecht)
Rieke G.H., Lebofsky M.J. 1985, ApJ 288, 618
Rix H.-W., Rieke M.J. 1993, ApJ 418, 123
Rubin V.C., Burstein D., Ford Jr. W.K., Thonnard N. 1985, ApJ 289, 81
Ryder S.D., Dopita M.A. 1994, ApJ 430, 142
Salpeter E.E. 1955, ApJ 121, 161
Schaerer D., Meynet G., Maeder A., Schaller G. 1993, A&AS 98, 523
Schweizer F. 1976, ApJS 31, 313
Searle L., Sargent W.L.W., Bagnuolo W.G. 1973, ApJ 179, 427
Silva D.R., Elston R. 1994, ApJ 428, 511
Sommer-Larsen J., Yoshii Y. 1990, MNRAS 243, 468
Terndrup D.M., Davies R.L., Frogel, J.A., DePoy D.L., Wells L.A. 1994, ApJ 432, 518
Tinsley B.M. 1980, Fund. of Cos. Phys. 5, 287
Tully R.B., Fisher J.R. 1977, A&A 54, 661
Valentijn E.A. 1990, Nat 346, 153
Valentijn E.A. 1994, MNRAS 266, 614
van Albada T.S., Bahcall J.N., Begeman K.G., Sancisi R. 1985, ApJ 295, 305
van Albada T.S., Sancisi R. 1986, Phil. Trans. (Roy. Soc. London) A320, 447
VandenBerg D.A. 1985, ApJS 58, 711
van der Kruit P.C. 1988, A&A 192, 117
Villa-Costas M.B., Edmunds M.G. 1992, MNRAS 259, 121
Wainscoat R.J., Freeman K.C., Hyland A.R. 1989, ApJ 337, 163
Wevers B.M.H.R., van der Kruit P.C., Allen R.J. 1986, A&AS 66, 505
Witt A.N., 1977, ApJS 35, 1
Witt A.N., Thronson Jr. H.A., Capuano Jr. J.M. 1992, ApJ 393, 611
Worthey G. 1994, ApJS 95, 107
Wyse R.F.G., Gilmore G 1988, AJ 95, 1404
Wyse R.F.G., Silk J. 1989, ApJ 339, 700
Zaritsky D., Kennicutt Jr. R.C., Huchra J.P. 1994, ApJ 420, 87

A Monte Carlo radiative transfer simulations of light and dust in exponential disks

The modeling of dust extinction in extragalactic systems has a long history. The effects of scattering are often ignored or are assumed to be no more than a scaling factor (Disney et al. 1989; Huizinga 1994), which is correct as long as one is not looking at wavelength dependent effects. Therefore, scattering is included in most studies investigating the wavelength dependent effects of extinction (e.g. Kylafis & Bahcall 1987; Bruzual et al. 1988, Witt et al. 1992, Byun 1994)

The Monte Carlo approach followed here is a somewhat "brute force" method, but it has the advantage that it can be used for luminous and dust geometries containing little symmetry. Even though smooth light and dust configurations are applied here, this method can easily be extended to include dust clouds and spiral structure.

A.1 The mathematical method

A Monte Carlo radiative transfer code was used to calculate the light and color distribution of disk galaxies as seen by a distant observer. The Monte Carlo principle as applied to extinction in gaseous nebulae is described in detail by Witt (1977). In the computer model the paths of many ($\sim 10^6$) photons were followed as they traveled through the absorbing and scattering dusty medium. At great distance the photons were collected to produce a galaxy image which was used for further study.

The trajectory of a photon through a dusty medium is determined by random processes. One can characterize these processes by a probability function $p(x)$ on an interval (a, b) such that

$$\int_a^b p(\xi)d\xi = 1. \tag{A1}$$

Using a random number generator, which produces a random number R distributed uniformly in the interval $0 \leq R \leq 1$, one can simulate an event with frequency $p(x)dx$ in the interval $(x, x + dx)$ by requiring

$$\int_a^x p(\xi)d\xi = R. \tag{A2}$$

This equation was used to simulate the birthplace and direction of photons, as well as the scattering properties of the dust. In the following sections, each R will denote a new random number in the interval $0 \leq R \leq 1$.

A.2 The creation of photons

This section describes the creation of photons and the random processes involved in this creation. Rather than creating photons in space with a certain density distribution such as in a real galaxy, the photons were instead created uniformly in space and given an initial intensity weight to produce the exponential light profile. These initial weights were reduced by absorption as the photon moved through the dusty medium.

The models consisted of three-dimensional distributions of stellar light and dust that were chosen independently. For the

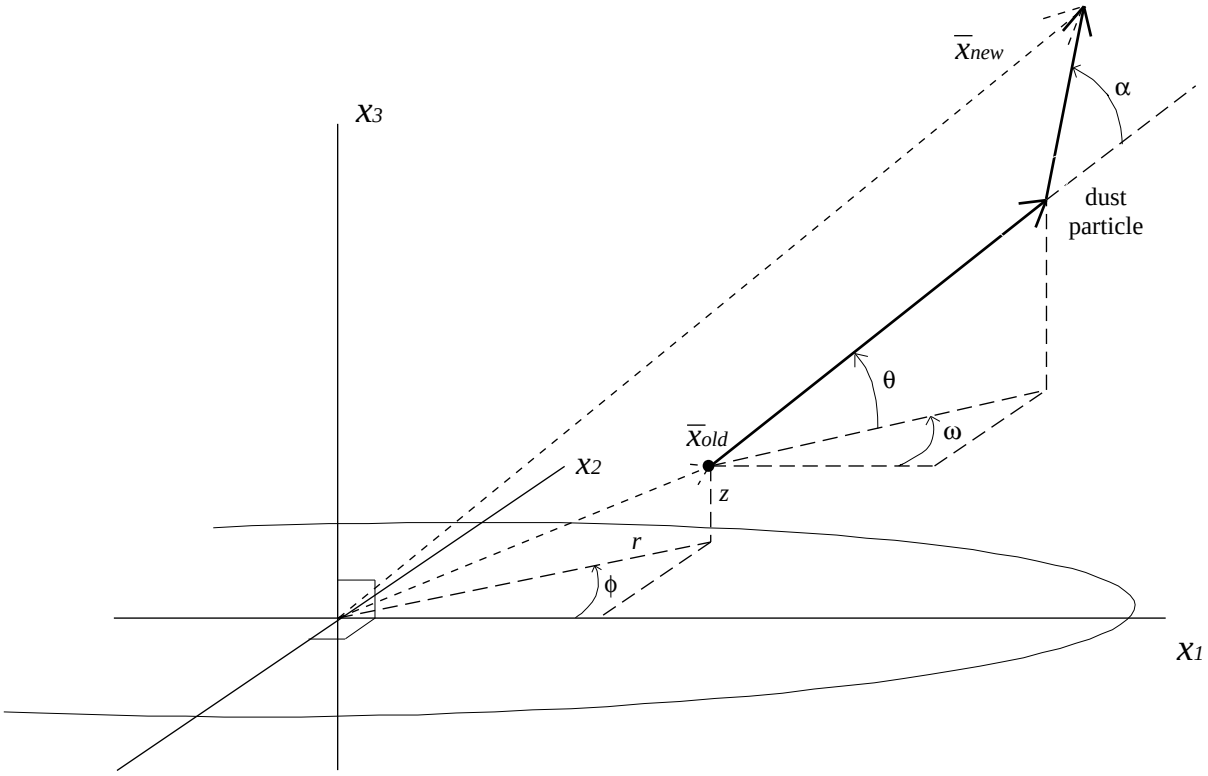

Fig. 11. The definition of the coordinate system. A trajectory with a scattering is indicated for one step size. A "photon beam" starts at $\overline{x}_{\rm old}$ in the direction defined by (ω,θ), scatters off a dust particle over an angle α, and ends at $\overline{x}_{\rm new}$.

stellar light, an axisymmetric disk-like distribution was used, with an exponential intensity behavior in both radial (r) and vertical (z) directions:

$$I(r,z,\phi) = \mathrm{e}^{-(r/h_{\rm s}+|z|/z_{\rm s})}, \tag{A3}$$

where $h_{\rm s}$ and $z_{\rm s}$ are the scalelength and the scaleheight of the stellar distribution respectively, with the coordinate system is as defined in Fig. 11. The luminosity was truncated at seven scalelengths and heights. The exponential behavior of the radial light distribution of disks in spiral galaxies is well established, but the vertical light distribution is more controversial, because extinction effects make measurements difficult. I have used the exponential law vertically instead of (for instance) the sech or sech^2 laws (van der Kruit 1988), because the nearly unobscured light distribution as obtained with near-IR observations often can be well described by such an exponential law (Wainscoat et al. 1989; Aoki et al. 1991). It is not expected that the results obtained here will change significantly if other plausible vertical light distributions are used. Each "photon beam" that was created received an initial weight according to the $I(r,z,\phi)$ of Eq. (A3).

Photons were created at a certain position in the model galaxy using the distribution functions

$$r = 7Rh_{\rm s} \quad z = 7(R-0.5)2z_{\rm s} \quad \phi = 2R\pi, \tag{A4}$$

and thus their initial position in cartesian coordinates was

$$\overline{x} = \begin{pmatrix} r\cos(\phi) \\ r\sin(\phi) \\ z \end{pmatrix}. \tag{A5}$$

The distribution functions of Eq. (A4) create photons uniformly in cylindrical coordinates, but not in cartesian space. The density of created photons is much higher near the center than in the outer regions and a correction factor is needed. To still get an exponential behavior in flux, an additional weight factor of $2\pi r$ was given to the intensity of each created "photon beam". These distribution functions were chosen, because the final model images were azimuthally averaged just as the real observations and in the absence of dust give these distribution functions an equal number of photons at each radius in the face-on case.

At creation, the initial flight direction of the photons was specified by the functions

$$\omega = (2R-1)\pi \quad \theta = (R-0.5)\pi. \tag{A6}$$

The corresponding directional cosines are

$$\Delta\overline{x} = \begin{pmatrix} \cos(\omega)\cos(\theta) \\ \sin(\omega)\cos(\theta) \\ \sin(\theta) \end{pmatrix}. \tag{A7}$$

Again, since this would not give a uniform distribution of flux density in each direction, an extra weight of the form $\cos(\theta)$

was introduced. The initial intensity of a "photon beam" at creation was thus

$$I_0(r,z,\phi,\omega,\theta) = 2\pi r\cos(\theta)\mathrm{e}^{-(r/h_\mathrm{s}+|z|/z_\mathrm{s})}. \quad \text{(A8)}$$

A.3 The dust properties

Let us first define the notation for the basic equations of radiative transfer. A beam of light with intensity I is followed while traveling along a straight line through a dusty medium. Since this medium removes a fraction $\kappa\,ds$ of the incident intensity for each distance ds traveled, the full equation is

$$\frac{dI(s)}{ds} = -\kappa(s)I(s) + J(s), \quad \text{(A9)}$$

where $J(s)$ are the new sources of intensity at point s in the travel direction. κ is the extinction coefficient and consists of an absorption and a scattering part, and their relative importance is normally expressed by the albedo (a)

$$\kappa = \kappa_a + \kappa_s \quad \text{(A10)}$$
$$a = \kappa_s/\kappa. \quad \text{(A11)}$$

While following the light beam through the dusty medium, no new photons were added to the initial beam of photons that was created with intensity $I(0)$, because they are accounted for by the repeating Monte Carlo principle, and $J(s) = 0$. For this single "photon beam" the radiative transfer equation is now

$$\frac{dI(s)}{ds} = -\kappa(s)I(s) \quad \text{(A12)}$$

with formal solution

$$I(x) = I(0)\mathrm{e}^{-\int_0^x \kappa(s)ds}. \quad \text{(A13)}$$

The integral in Eq. (A13) defines optical thickness

$$\tau \equiv \int_0^x \kappa(s)\,ds. \quad \text{(A14)}$$

Since the beam was followed while it scattered through the medium (so no longer on a straight line), there were no losses by scattering along the path of the beam. One still can use Eq. (A13), but with $\kappa_a(s) = (1-a)\kappa(s)$ instead of $\kappa(s)$ as long as the line integral is taken along the path traveled. The extinction coefficient and the albedo are wavelength dependent, which creates reddening of stars and could cause the observed color gradients in the galaxies.

To calculate the absorption along the path traveled, the dust distribution must be defined. The dust extinction coefficient in the models was taken to have a similar distribution as the stellar light, but with a scalelength and scaleheight that were chosen independently:

$$\kappa_\lambda(r,z,\phi) = \kappa_{0,\lambda}\mathrm{e}^{-(r/h_\mathrm{d}+|z|/z_\mathrm{d})} \quad \text{(A15)}$$

where $\kappa_\lambda(r,z,\phi)$ is the local extinction coefficient at wavelength λ and $\kappa_{0,\lambda}$ is the extinction coefficient at $(r=0,z=0)$. In this article *the* optical depth of a system is denoted by the integration of κ_V (κ in the V-passband) along the symmetry axis from $(r=0,z=-\infty)$ to $(r=0,z=\infty)$

$$\tau_{0,V} = \int_{-\infty}^{\infty} \kappa_{0,V}\,\mathrm{e}^{-|z|/z_\mathrm{d}}\,dz = 2\kappa_{0,V}z_\mathrm{d}. \quad \text{(A16)}$$

Using Eq. (A13) one can calculate that a point source located behind the center of the galaxy will have suffered an extinction in the V-passband for an observer located at its other pole of

$$I(z=\infty) = I(0)\mathrm{e}^{-\tau_{0,V}}, \quad \text{(A17)}$$

assuming that all absorbed *and* scattered photons are lost for a point source.

Three parameters are needed to describe dust properties, the relative extinction (τ_λ/τ_V), the albedo (a_λ) and the scattering phase function $\Phi_\lambda(\alpha)$, and all are dependent on wavelength (λ). As there are almost no direct measurements of the dust properties in other galaxies, I decided to use the (also poorly determined) Galactic values. Studies by Knapen et al. (1991) and Jansen et al. (1994) seem to indicate that at least the Galactic extinction curve is applicable to some other galaxies, the other two dust properties have never been measured in extragalactic systems.

For relative extinction, the Galactic extinction properties of Rieke & Lebofsky (1985) were used. The values for the albedo were drawn from Bruzual et al. (1988), as were the values for the scattering asymmetry parameter g_λ. This asymmetry parameter enters in the scattering phase function suggested by Henyey & Greenstein (1941)

$$\Phi_\lambda(\cos(\alpha),g_\lambda) = [(1-g_\lambda^2)/4\pi](1+g_\lambda^2-2g_\lambda\cos(\alpha))^{-3/2} \quad \text{(A18)}$$

where α is the scattering angle between the incident and the deflected photon. The function is such that $g_\lambda = \langle\cos(\alpha)\rangle$, and thus $-1 \le g_\lambda \le 1$. Forward scattering dominates for $g_\lambda > 0$ and $g_\lambda = 0$ results in isotropic scattering. To determine a random deflection angle for a photon with the probability function Φ_λ Eq. (A2) can be used and one finds (Witt 1977)

$$\alpha = \arccos(\{(1+g_\lambda^2) - [(1-g_\lambda^2)/(1-g_\lambda+2g_\lambda R)]^2\}/2g_\lambda). \quad \text{(A19)}$$

The values used for τ_λ/τ_V, a_λ, and g_λ for the different photometric passbands are listed in Table 3.

Table 3. Values used in our scattering model for the dust properties relative extinction (τ_λ/τ_V), albedo (a_λ) and scattering asymmetry (g_λ) as function of photometric passband.

passband	τ_λ/τ_V	a_λ	g_λ
U	1.531	0.68	0.67
B	1.324	0.66	0.59
V	1.000	0.60	0.50
R	0.748	0.53	0.40
I	0.482	0.45	0.29
H	0.175	0.28	0.04
K	0.112	0.20	0.00

A.4 The numerical method

Each photon beam that was created using Eqs. (A4) and (A6) was stepped through the dusty medium. The step size was determined by the local dust density and was chosen in such way that it would give an optical thickness (absorption plus scattering) of 0.03 if there was a constant dust density along the step. This means that the chance of multiple scattering is of order $(0.03a_\lambda)^2$ along a step. This is negligible, as it should be, because only single scattering was incorporated along each step. It is trivial to show that the step size has to be of order

$$\Delta s = 0.03/\kappa(\overline{x}) = 0.03/(\kappa_0 \mathrm{e}^{-(r/h_\mathrm{s}+|z|/z_\mathrm{s})}) \tag{A20}$$

and the new position is (if there is no scattering)

$$\overline{x}_\mathrm{new} = \overline{x}_\mathrm{old} + \Delta\overline{x}\Delta s. \tag{A21}$$

For the actual absorption along a step, one has to use Eq. (A13) with $\kappa_a = \kappa(1-a)$ instead of κ. The integral was at each step approximated by four-point Gauss-Legendre quadrature:

$$\tau_{\Delta s} = \int_{\overline{x}}^{\overline{x}+\Delta\overline{x}\Delta s} \kappa_a(\overline{s})\, d\overline{s} \;\approx\; 0.5\Delta s \sum_{j=1}^{4} w_j\, \kappa(\overline{x} + 0.5(1+x_j)\Delta\overline{x})(1-a), \tag{A22}$$

where the values for w_j and x_j can be found in any handbook on numerical analysis. When there was no scattering during the step, the $\kappa(\overline{x}_4)$ calculated in Eq. (A22) was used to determine the step size with Eq. (A20) in the next step.

If scattering did occur, the step proceeded slightly differently. The chance of scattering during a step can be simulated by requiring

$$\mathrm{e}^{-\tau_{\Delta s} a_\lambda} < R. \tag{A23}$$

In that case the directional cosines of Eq. (A7) were changed by an angle given by Eq. (A19). This left another angle of freedom for the azimuthal change of the direction which was generated by

$$\beta = 2\pi R. \tag{A24}$$

Rotating the initial directional angles ω, θ over the scattering angles α, β gives the new directional cosines

$$\Delta\overline{x}_\mathrm{new} = \begin{pmatrix} \cos(\omega)\cos(\theta)\cos(\beta) & +(\sin(\omega)\cos(\alpha) + \cos(\omega)\sin(\theta)\sin(\alpha))\sin(\beta) \\ \sin(\omega)\cos(\theta)\cos(\beta) & +(-\cos(\omega)\cos(\alpha) + \sin(\omega)\sin(\theta)\sin(\alpha))\sin(\beta) \\ \sin(\theta)\cos(\beta) & -\cos(\theta)\sin(\alpha)\sin(\beta) \end{pmatrix}. \tag{A25}$$

When Eq. (A23) was satisfied and scattering occurred in a step, the photon proceeded a fraction $f = R$ of step size Δs in the old direction, before following the new direction

$$\overline{x}_\mathrm{new} = \overline{x}_\mathrm{old} + (f\Delta\overline{x}_\mathrm{old} + (1-f)\Delta\overline{x}_\mathrm{new})\Delta s. \tag{A26}$$

A.5 Projection on the sky

The steps in the previous paragraph were repeated until $|\overline{x}_\mathrm{new}| > 10h_\mathrm{s}$. All $\tau_{\Delta s}$ of the different steps were added, and the final intensity of the photon beam was $I_\mathrm{end} = I_0 \mathrm{e}^{-\tau_\mathrm{tot}}$. The final intensities were projected on the sky as if the galaxy was being observed from infinity. Due to the axisymmetric nature of the models, one can ignore the ω dependence of the exit direction and rotate all photons over angle ω as if they leave the galaxy in the same direction. The projection on the (y_1, y_2)-plane becomes

$$\overline{y} = \begin{pmatrix} -\sin(\omega) & \cos(\omega) & 0 \\ -\sin(\theta)\cos(\omega) & -\sin(\theta)\sin(\omega) & \cos(\theta) \end{pmatrix} \overline{x} \tag{A27}$$

This procedure of creating photons, stepping through the medium and projecting the exiting photons on the sky was repeated for two million photons. The photons were binned into pixel images in (y_1, y_2) direction and the binning in viewing angle θ direction resulted in ten model images from edge-on to face-on. The binning of photons in the θ direction was in equal steps of b/a, where b/a is the axial ratio of an inclined circle. This has the advantage that each image has approximately equal flux, at least in the case of no extinction. For the analyses discussed in this paper only the face-on images were used, which contained the photons that exited with an angle between 90° and 71.8° (i.e. $1 \geq b/a > 0.95$).

A.6 Testing and the results

The computer program was tested extensively to ensure that the results were reliable. First, a point source emitting all its photons to a pole was placed at the center of the galaxy and the exiting flux was correctly described by Eq. (A17). Tests showed that in the case of no absorption all images at different viewing angle had an equal flux. Tests were made to ensure that the scattering angle phase function was produced correctly and that the angle between the incident and the deflected photon was indeed the required angle. One of the most important tests was the independence of the number of scatterings on step size. If the step size had been too large or if the calculation $\tau_{\Delta s}$ had been incorrect this could not have been the case. The model profiles were tested against the analytic profiles of DDP for the cases with and without scattering. In the case of no scattering (all scattered photons were removed to mimic absorption) the agreement was perfect. Figure 4 shows an excellent agreement between the two models even with scattering, as long as the extinction is high. All test results were correct to within the statistical noise.

For the extraction of the (color)profiles, the same programs as in Paper I were used and the model results can be compared directly with the data. Once a $\tau_{0,V}$ and a set of scalelengths and heights have been chosen for a particular model, $\kappa_{0,\lambda}$ is determined by Eq.(A16) and the corresponding optical depths for the other passbands are determined by Table 3. This model is also useful to study inclination-dependent effects of extinction.

Chapter 5

Conclusions & prospects

Abstract. In this thesis optical and near-infrared surface photometry has been used to perform a statistical study of light and color distributions in and among spiral galaxies. In this chapter I summarize the main results using the six passband surface photometry of 86 face-on spiral galaxies and give some suggestions for future work.

1 The distribution of light

I analyzed the problem of separating the light distribution of galaxies into different components in Chapter 2. A number of decomposition methods were tested and compared and this revealed the two main sources of error:

- The uncertainty in the shape of the bulge profile to be used.
- The uncertainty in the sky surface brightness.

An analysis of the fit residuals shows that the residual variations among the different fit models are small compared to the residuals themselfs. The accuracy of the obtained fundamental parameters can only be improved by increasing the description of the different model components. The most reproducible and representative bulge and disk parameters are obtained by modeling the two-dimensional image of the galaxy with an exponential light profile for both bulge and disk and, when necessary, with a Freeman bar (Freeman 1966)

The fundamental bulge and disk parameters were statistically analyzed in Chapter 3. The observed sample is statistically complete and correctable for selection effects. The K passband observations gave a nearly unobscured view on the galaxies revealing the "old" stellar distribution of the galaxies. The main results from this chapter are:

- Freeman's law (Freeman 1970) of constant disk central surface brightness among galaxies has to be redefined. There is an upper limit to the central surface brightnesses as indicated by Freeman's law, while for lower central surface brightnesses the number density of galaxies decreases only slowly as function of central surface brightness.
- The bivariate distributions in the (μ_0,h)-plane (Fig. 7) indicate that there might be large numbers of small scalelength, low surface brightness galaxies, but this area in the diagram is poorly sampled.
- The Hubble sequence type index correlates strongly with the effective surface brightness of the bulge, much better than with the bulge-to-disk ratio.
- The disk and bulge scalelengths are correlated.
- These scalelengths are not correlated with Hubble type. Hubble type is a lengthscale-free parameter and each type therefore comes in a range of magnitudes (and presumably a range of total masses).

The key figures of Chapter 3 are Figs 5, 7, 8 and 10.

2 The distribution of colors

In Chapter 4 I investigated the dust and stellar content of the sample of galaxies using their color gradients. The sample was used as a whole, no individual galaxies were examined. This has some clear advantages. While it is conceivable that an individual galaxy has a stellar population with a metallicity much higher than the metallicity of the surrounding gas due to a recent merging with a metal poor dwarf, this is very unlikely to be the case for most of the galaxies in a sample. The same holds true for extreme dust distributions. While a number of galaxies could have strange dust properties and distributions, it is unlikely that all galaxies have properties and distribution different from what is observed in edge-on galaxies and especially in our own Galaxy. The main conclusions of Chapter 4 are:

- Almost all spiral galaxies become bluer with increasing radius.
- The colors of galaxies correlate strongly with surface brightness, with lower surface brightness regions being bluer, both within and among galaxies. The morphological type is an additional parameter in this relationship, because at the same surface brightness late-type galaxies are bluer than early-type galaxies.
- The color gradients in the galaxies are best explained by differences in SFH as function of radius, with the outer parts of galaxies being much younger on average than the central regions. This implies that the stellar scalelength of galaxies is still growing. The central stellar populations must have a range in metallicities to explain the red central colors of the galaxies.
- Realistic 3D radiative transfer modeling indicates that reddening due to dust extinction cannot be the major cause of the color gradients in face-on galaxies. The model color vectors in color–color space are not compatible with the data.
- A consequence of the population changes implied by the color differences in and among galaxies is that there are large differences in M/L values in and among galaxies. These changes in M/L make the missing mass problem in spiral galaxies as derived from rotation curve fitting even more severe.

The key figures of Chapter 4 are Figs 2, 6 and 7.

3 Future work

Every study raises more questions than it solves. Some suggestions for future work and observational programs are presented in this final section.

Two problems regarding Freeman's law were not dealt with adequately in the present study. 1) The number density of low surface brightness and small scalelength galaxies is still unknown, as figure 5 of Chapter 3 shows that the present sample is heavily biased against such galaxies. 2) The galaxies of the present sample are probably not randomly distributed in space. The sample may be slightly biased due to the density enhancement of the local supercluster.

Both problems can be circumvented by observing a new sample using careful selection criteria. The new diameter limited sample should be selected from an all sky (or at least half sky) survey from deep photographic plates enabling fainter isophotal diameters to be used (preferably measured and not eye estimated) than the diameters used here. This will shift the selection lines in Fig. 5, Chapter 3 downwards. Using a smaller diameter criterion ($\sim$1–1.5 arcmin) will shift the selection lines to the left. When the sample is limited to only face-on galaxies, it will still contain several thousands of galaxies. By selecting at random one in twenty galaxies one ensures random distribution over the whole sky and combined with the faint limits this ensures that the sample is hardly biased by the local density enhancement. At least several hundreds of galaxies should be observed (surface photometry in the K passband of course, but also their redshifts should be measured) to fill the bivariate distributions, such as Figs 7 and 23, adequately.

The distribution of dust and the amount of extinction it is causing can soon be measured much more accurately at the far infrared bands by the use of ISO and at the sub-millimeter wavelengths by the use of SCUBA at the JCMT. The determination of the scattering properties of dust needs most urgently improvements. The dust scattering properties used in this thesis stem from observations made in the early seventies or from model calculations. Scattering properties of dust in extra-galactic systems have never been measured.

The nature of the color gradients can be better determined when spectroscopy is used to determine the stellar population properties as function of radius. A first indication of the metallicity gradient can be obtained by measuring a number of H II regions, but this gives only information about the metallicity gradient in the current gas fraction. Ideally one would like to obtain the long-slit spectra of the stellar population of the galaxies, concentrating on the absorption lines indicated by Worthey (1994) to be the most affected by age *or* metallicity effects. Such observations would require long observation times, especially for the faint outer parts of galaxies and for low surface brightness galaxies. Maybe the new 8-10 m class telescopes which will become available during the next few years will decrease the demand on the 4 m class telescopes, which could be used to obtain long-slit spectra in reasonable observing times of a statistically significant number of galaxies.

There is a clear need for a systematic survey of broadband optical and in particular near-infrared surface photometry of the large, nearby galaxies. These galaxies have been studied at all wavelengths in great detail and the local physical processes in these galaxies are known in some detail. It is important to know the relation between these local processes and the global light distribution of these galaxies. All galaxies that can in principle be resolved in stars from the ground (like the Magellanic clouds, M 31, M 33 etc.) should be subject of such a survey and could be observed with a small, wide field telescope (like the parking lot camera of Bothun & Thompson 1988).

Once it has been established what fraction of the color gradients is caused by dust, age and metallicity effects, it becomes interesting to examine the physical processes determining the steepness of the color gradient. For this sample no correlation between the steepness of the gradient and any other known galaxy parameter has been found so far. Peletier et al. (1994) showed a very weak correlation with inclination, but this can not be confirmed with this face-on sample.

References

Bothun G.D., Thompson I.B. 1988, AJ 96, 877
Freeman K.C. 1966, MNRAS 133, 47
Freeman K.C. 1970, ApJ 160, 811
Peletier R.F., Valentijn E.A., Moorwood A.F.M., Freudling W. 1994, A&AS 108, 621
Worthey G. 1994, ApJS 95, 107